GRAN SASSO SCIENCE INSTITUTE
SCHOOL OF ADVANCED STUDIES
Scuola Universitaria Superiore

DOCTORAL THESIS

Radon-Induced Lead Isotopes in XENONnT:
Studies on Branching Ratios and Surface Background

PHD PROGRAM IN ASTROPARTICLE PHYSICS: XXXVI CYCLE

Discussed on: 15/04/2025

Author:	*Supervisor:*
Cecilia FERRARI	Prof. Alfredo D. FERELLA

GSSI Gran Sasso Science Institute

Abstract

The XENONnT experiment, a dual-phase liquid Xenon time projection chamber (TPC), hosted in the Laboratori Nazionali del Gran Sasso underground facilities, is designed to achieve unprecedented sensitivity in the direct detection of WIMP dark matter. As the sensitivity of liquid Xenon detectors improves, background contributions from intrinsic radioactive contaminants become increasingly significant. Among these, Radon-induced Lead isotopes ^{212}Pb, ^{214}Pb and ^{210}Pb pose a major challenge, affecting both low-energy electron recoil searches and WIMP detection. These isotopes originate from Radon outgassing and Radon progeny plate-out on detector surfaces, constituting bulk and surface backgrounds through beta decays and subsequent radiation emissions. A precise characterization of their decay properties, deposition mechanisms and impact on the experimental signal region is essential for optimizing background rejection techniques and improving sensitivity to rare-events and Beyond Standard Model physics searches.

Dedicated measurements of the beta decay branching ratios of ^{212}Pb and ^{214}Pb have been performed using XENONnT data, with the aim of significantly reducing systematic uncertainties for future low-energy rare-events electron-recoil searches. The analysis, based on high-statistics ^{220}Rn and ^{222}Rn calibration campaigns, yields ground state branching ratios of $15.28 \pm 0.13^{+0.02}_{-0.33}\%$ and $9.8 \pm 0.3^{+0.8}_{-0.0}\%$ for ^{212}Pb and ^{214}Pb respectively. These improved branching ratios measurements enhance the ability to constrain ^{212}Pb- and ^{214}Pb-induced backgrounds in the electron recoil low-energy region, particularly relevant for searches targeting Solar-pp neutrinos and other Beyond Standard Model studies. Furthermore, the refined measurements of ^{212}Pb and ^{214}Pb ground state branching ratios contribute to the broader field of low-background physics, informing Monte Carlo simulations and improving the accuracy of background models used in rare-event searches.

In addition to bulk Lead contamination, the ^{210}Pb isotope represents a critical background component due to its long half-life (of about 22 y) and its accumulation on detector Teflon surfaces. A novel six-dimensional physics-driven model has been developed to describe the ^{210}Pb surface background in XENONnT, incorporating charge loss effects, refined spatial events distributions and energy deposition simulation. This model, validated against XENONnT science runs SR0 and SR1 data, provides a refined estimate of the ^{210}Pb wall background activity, estimated to be $19.0(10)\,\mathrm{Bq/m^2}$. The improved understanding of the surface background enables the definition of more precise fiducial volumes in future science runs and potentially improve WIMP searches, by gaining exposure.

The impact of these studies extends beyond XENONnT physics goals, providing critical insights for future noble liquid TPCs, such as XLZD, both for refinement of sensitivity studies and for improvements in the materials handling and cleaning procedures. Indeed, on the one hand, the methodology developed for ^{212}Pb and ^{214}Pb Lead isotope characterization offers a framework for assessing and mitigating similar backgrounds, while the direct measurements of their ground state branching ratios provides improved constraints for future rare-events analysis. On the other hand, the advancements obtained in the TPC surface background analysis once more validate the Radon progeny plate-out origins of this background and reveal the importance of the human-factor in the enhancement of its rate. Indeed, as evident by the study results, given the non-uniform spatial distribution observed in the data, the explanation for the modulation of the surface background rate can be related to cleaning and handling procedures of Teflon materials.

By advancing the precision of Radon-induced background characterization and surface event modeling, this Ph.D Thesis represents a major step forward in the optimization of liquid Xenon experiments for fundamental physics searches. The results presented here contribute directly to the improvements of electron recoil backgrounds constraints and optimization of data selection, pushing the discovery potential of both rare-events and direct WIMP dark matter detection, closer to the ultimate sensitivity limit imposed by the neutrino floor.

Contents

Introduction

At the beginning, there was a singularity. Then, suddenly, an exponential expansion gave birth to the universe – an unlinked universe, whose distant regions became causally disconnected due to its rapid growth. As the cosmos evolved, the radiation-dominated epoch emerged. When the expansion rate of the universe matched that of photon recombination, the latter decoupled, giving rise to the first observable imprint of the early universe: the Cosmic Microwave Background (CMB).

This relic radiation has provided a means to study the primordial universe and interpret its evolution. Observations within the ΛCDM model revealed that a significant portion of the universe energy content was missing. To account for this discrepancy, the existence of an additional, non-baryonic form of matter was postulated.

The CMB, however, was not the only clue pointing to this missing component. In the same century, many astrophysicists noted that the combination of known gravitational laws and visible astronomical objects was insufficient to explain the motion of stars and galaxies. Pioneers such as Fritz Zwicky and Vera Rubin proposed the existence of an invisible form of matter—undetectable to their instruments, as well as to current ones – which they called dunkle Materie (dark matter).

Since then, both theoretical and experimental physicists have tried to unravel this mystery, giving birth to the dark matter hunt. The former approached the problem by expanding existing frameworks, such as the Standard Model of particle physics, or by considering already-known astrophysical objects, such as black holes, leading to a vast array of dark matter candidates spanning 89 orders of magnitude in mass. The latter focused on developing new detection techniques to identify potential interactions with these elusive particles.

Among the numerous candidates, the Weakly Interacting Massive Particle (WIMP) emerged as one of the most promising. With a mass in the GeV to TeV range, WIMPs naturally fit the observed dark matter energy density within the ΛCDM framework, assuming an interaction cross-section comparable to that of the weak force. This remarkable theoretical alignment, often referred to as the *WIMP miracle*, sparked a sense of excitement in the scientific community, driving early direct detection experiments to focus on this candidate.

It is within this scientific and historical context that the Xenon dark matter project was conceived. Over the past two decades and across four generations of detectors, the XENONnT experiment has reached unprecedented sensitivity levels, excluding a substantial portion of the WIMP parameter space and weakening the hypothesis of its existence. Achieving this level of sensitivity required not only advancements in detector technology but also a profound understanding of potential background sources, along with the development of purification, distillation and veto systems.

To push the sensitivity of rare-event searches even further, precise background characterization and mitigation are essential. A thorough understanding of background sources and their distinctive signatures is crucial for improving discrimination techniques and refining future detector designs.

This thesis focuses on the characterization of major radioactive backgrounds in XENONnT, aiming to optimize future experiments by providing a more detailed understanding of these contaminants. Specifically, the work targets three Radon induced lead isotopes – ^{212}Pb, ^{214}Pb, and ^{210}Pb – which contribute significantly to the experiment background.

The first two studies, presented in Chapter 4 and Chapter 5, focus on improving the precision of the beta-decay branching ratios of ^{212}Pb and ^{214}Pb. These results are critical for refining background constraints in Solar-pp neutrino searches and other low-energy electron recoil studies, both in XENONnT and similar liquid Xenon experiments.

The third isotope, ^{210}Pb, originates the surface background, which affects all liquid noble gas TPCs. Traditionally, WIMP searches have relied on data-driven templates and fiducial volume cuts to suppress this background contribution. Contrarily, in Chapter 6, a six-dimensional physics-driven model is introduced to describe the behavior of ^{210}Pb on detector surfaces. This model validates the hypothesis regarding the origins of the surface background while reinforcing the understanding of the detector response. This refinement in the modeling of surface background, obtained with this study, will provide valid inputs to future XENONnT analysis for the optimization of fiducial volume selection, pushing the experimental WIMP sensitivity, thanks to the increased exposure.

1

Direct Dark Matter Searches

At the time of this writing, the universe is claimed to be dark and flat, where the ordinary luminous baryonic matter only constitutes the 5% of the total cosmological density budget. All the rest is composed by dark matter (27%) and dark energy (68%) [1]. This is the outcome of the analysis led by Plank's Collaboration on Cosmic Microwave Background (CMB) data survey by assuming the ΛCDM standard model of Big Bang cosmology.

According to the ΛCDM model, the dark matter particles should be able to interact with the ordinary ones. Additionally, given the indirect evidences of the presence of dark matter clustering around galaxies, there may be the chance of directly observing these particles with Earth-based experiments. More specifically, by assuming a physics-motivated distribution of the dark matter particles in the Milky-Way galactic halo and considering a specific dark matter candidate, for example the Weakly Interacting Massive Particle (WIMP), it is possible to predict its expected signal rate in a properly designed particle detector. Eventually, to enhance the dark matter discovery probability, a series of techniques can be employed to reduce the background rate from ordinary matter radiation. At the time of this writing, no experiments searching for direct dark matter interactions have returned a positive result[1], excluding the existence of a large portion of the expected combined mass/cross-section parameter space for WIMPs. Likewise, both accelerators experiments, designed to detect signatures of the SUperSYmmetric (SUSY) model, and indirect searches, probing cosmic rays to detect any possible dark matter annihilation product, obtained null results. All these results combined have lately pushed part of the scientific community in shifting its interest towards different dark matter candidates. However, given that the WIMP hypothesis has not been fully ruled-out, a large part of the community is still focussing its effort in developing and designing more sensitive experiments, reaching unprecedented purity and precision levels. As a result, these improvements opened the opportunity of investigating alternative new physics channels and refining the knowledge of already known physics processes.

This Chapter does not intend to constitute an introductory manual about dark matter and its possible detection methods. About this subject, many comprehensive reviews can be used as reference, such as [3] and [4]. Moreover, for this Thesis purposes, no alternatives to the ΛCDM model (to which recent observation may point to) or modified gravity theory (as a possible alternative explanation to cold dark matter particles) are discussed. This Chapter

---

[1] with the remarkable exception of the DAMA/LIBRA claims [2]

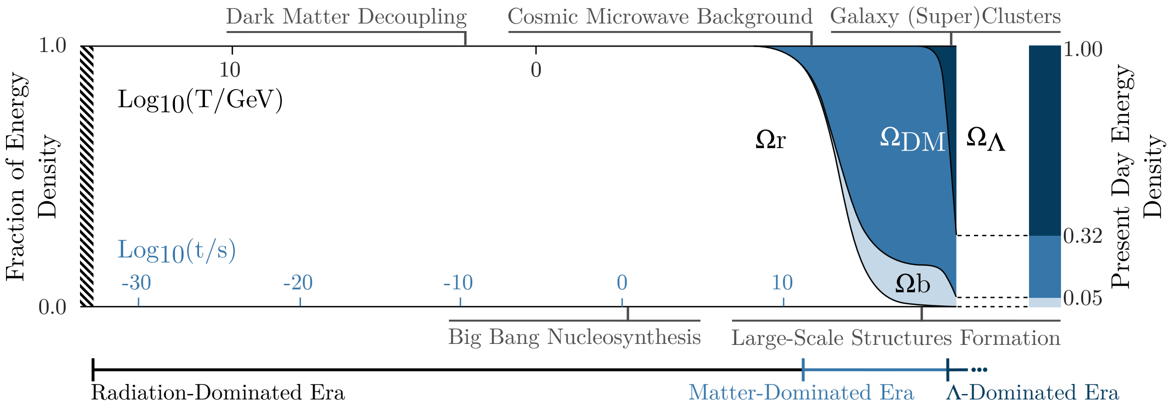

Figure 1.1: (Edited from [5]) A history of the universe reported with both temporal axis (bottom, blue) and temperature one (top, black). The plotted stacked curves represent the radiation energy density contribution (Ω_r in white), the baryon energy density contribution (Ω_b in light-blue), the dark matter energy density contribution (Ω_DM in French blue) and the Λ (dark energy) energy density contribution (Ω_Λ in dark blue). As reported in the bottom of the scheme, the trend of these energy density contributions chronologically defines three different eras: the radiation-dominated Era, the matter-dominated Era and the Λ-dominated Era. The present energy density values are those of [1]. The most important events of interest to this Chapter are labelled in gray.

provides an essential introduction to the physics case that led to the design and construction of the XENONnT experiment, to which the Chapter 2 is dedicated. After a brief introduction to the footprints the presence of dark matter particles has left in the different stages of the expanding universe in 1.1, the particle dark matter properties and the experimental efforts for direct dark matter searches are respectively described in 1.2 and in 1.3.

1.1 The Role of Dark Matter in the Expanding Universe

How the universe was born and how it became the one we can observe nowadays is the bread and butter of cosmologists and, as every other physics field of searches, it is based upon one main model that is continuously probed by means of experimental observations. The most scientifically accepted cosmological model is the ΛCDM Big Bang Theory, that foresees three different eras, as schematically represented in Figure 1.1. These stages are defined after the dominating energy density content in the universe: the radiation-dominated era, the matter-dominated era and the dark energy-dominated era. The variation of the total universe energy density, and thus its transition between these stages, strictly determines the expansion rate of the universe and its history. In formulae, the universe expansion rate $H(t)$ is described by the Friedmann equation that, by assuming a flat Euclidean universe as suggested by several evidences [6], can be written as:

$$H^2(t) = \frac{8\pi G}{3}\rho(t), \tag{1.1}$$

where G is the Newton's constant and $\rho(t)$ is the universe energy density. Thanks to the astronomical observations [1], it is possible to measure the value of the today's expansion rate H_0, also known after the name of Hubble's constant. Assuming $H_0 = 67.32\,\mathrm{km\,s^{-1}\,Mpc^{-1}}$, a critical universe energy density ρ_c, that in a flat geometry equals today's energy density ρ_0,

$$\rho_c = \rho_0 = \frac{3H_0^2}{8\pi G} = 0.852 \times 10^{-29}\,\mathrm{g\,cm^{-3}} \tag{1.2}$$

is obtained.

According to the standard model of the Big Bang cosmology ΛCDM the ratio Ω of the actual (or observed) density ρ_0 to the critical density ρ_c is the sum of three main different contributions: the matter energy density parameter Ω_{m}, the radiation energy density parameter Ω_{r} and the energy density parameter due to the cosmological constant Ω_Λ. In formulae:

$$\Omega = \Omega_{\mathrm{m}} + \Omega_{\mathrm{r}} + \Omega_\Lambda. \tag{1.3}$$

Supposing the universe has a flat geometry, an Ω value equal to 1 is obtained. This implies that Equation 1.3 can be interpreted as how the total universe energy density is shared between the three different components. Moreover, the ΛCDM model interprets the Ω_{m} parameter as the sum of two different contributions: the baryonic matter energy density contribution Ω_{b} and the cold dark matter one Ω_{DM}. The existence of this latter term has been postulated and required as an important ingredient of the ΛCDM model, in order to interpret many cosmological and astrophysical observations. Additionally, the neutrino energy density contribution Ω_ν contributes to the matter or radiation budget according to the considered cosmological time at which Ω is probed.

In this Section, a very brief description of the different universe stages along with the role that the hypothetical cold dark matter particle has played and hence the footprints (indirect evidences) it left behind, is reported. For a more detailed introduction to this physics topic, it is recommended to refer to specific textbooks, such as [6] or [7].

1.1.1 The Radiation-Dominated Era

After the Big Bang that gave birth to the space-time, an inflation era caused a violent expansion of the universe, increasing its size exponentially within a fraction of a second. This rapid expansion helped to smooth out any irregularities in the density of matter and energy, setting the stage for a more uniform radiation-dominated cosmos. Following the period of inflation, the universe continued to expand but at a slower rate. As the universe cooled, protons and neutrons began to combine to form the first atomic nuclei in a process called Big Bang Nucleosynthesis (BBN), primarily producing hydrogen and helium isotopes.

Even if not directly assessable, it is possible to observe second order effects of the primordial light nuclei production and hence infer their abundance in the early universe. This result also sets important constraints to the ordinary matter energy budget content, providing an indirect proof to the dark matter existence hypothesis.

The Big Bang Nucleosynthesis

The BBN process starts at about 1 s after the Big Bang, when the cosmic temperature T reached the threshold of 1 MeV. The synthesis of light nuclei begins with the production of deuterium via $\mathrm{p(n,\gamma)D}$ which becomes efficient once the number of photons per baryon above the temperature of the deuterium binding energy threshold (2.23 MeV) falls below unity at T about 0.1 MeV. After that moment, the formation of other light nuclei starts, following the reaction chains $\mathrm{D(p,\gamma)^3He}$, $\mathrm{^3He(D,p)^4He}$ and $\mathrm{^3He(^4He,\gamma)^7Li}$. The rates of these reactions are determined by the density of baryons n_{b}, that is usually normalized to the relic black body photon density n_γ (fixed by CMB measurements) as $\eta = n_{\mathrm{b}}/n_\gamma$. In Figure 1.2, the theoretical predictions of these light nuclei abundances are shown against a wide range of baryon to photon ratio η and the baryonic matter energy density contribution Ω_{b}.

Primordial light nuclei abundances measurements (light-blue boxes in Figure 1.2) are assessed via astrophysical observations pointing at sources formed at much later epochs with

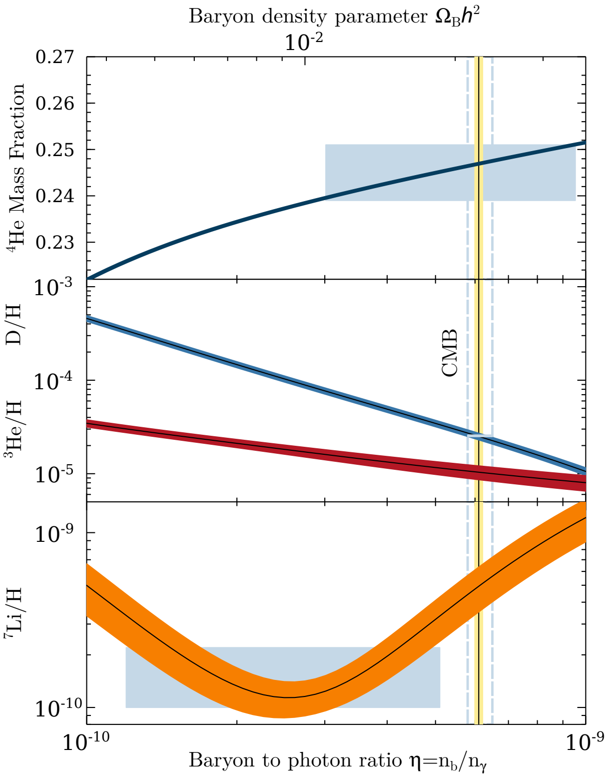

Figure 1.2: (Edited from [4]) The primordial abundances of ^{4}He, D, ^{3}He, and ^{7}Li as predicted by the standard model of Big-Bang nucleosynthesis. Boxes (light-blue) indicate the observed light element abundances. The narrow vertical band (yellow) indicates the CMB measure of the cosmic baryon density, while the wider band (dashed light-blue) indicates the BBN D+^{4}He concordance range.

respect to BBN, even after the stellar nucleosynthesis started. This latter process may alter the measurement of the primordial abundances of light nuclei, since it causes the genesis of heavy elements (*metals*), such as C, N, O and Fe, via light nuclei fusion. Therefore, to experimentally constrain the BBN predictions, it is necessary to exploit low-metallicity astrophysical sites [4]. Since Big Bang Nucleosynthesis (BBN) is the sole production source of deuterium (D), which is entirely processed in the cores of stars, the measured primordial abundance of this isotope is particularly stringent. Furthermore, the η parameter can be determined from the acoustic peaks in the CMB power spectrum. The consistency between η_{CMB} and η_{BBN} (see Figure 1.2) further supports the Standard Big Bang cosmology model. The combination of these measurements, returns a baryon energy density contribution of $\Omega_{\mathrm{b}} = 4.97(3)\,\%$, assuming a Hubble parameter value of $h = H_0/100\ \mathrm{km\,s^{-1}\,Mpc^{-1}} = 0.6732$ from [8]. This result eventually limits the total baryonic contribution to the universe total energy density, suggesting that most of the matter in the universe is made up by a non-baryonic dark component.

1.1.2 The Matter-Dominated Era

As the temperature dropped further, photons decoupled from matter, creating what we now observe as the CMB, and the universe transitioned into the matter-dominated era. After this time, the BBN nuclei were allowed to capture electrons and form the first neutral atoms, leading to the recombination epoch. Over billions of years, the force of gravity pulled matter together to form stars, galaxies, and larger structures, such as galaxy clusters and superclusters.

Both these processes, the photon decoupling and the large structure formation, provide strong evidences in support of the hypothesis of the particle dark matter existence. Moreover, the related cosmological observations set important constraints to its properties as discussed in 1.2.

The CMB Anisotropies

The CMB is a remnant of the primordial universe, that preserves every information (evolved according to the universe expansion rate) of the last scattering surface since the decoupling. CMB shows a perfect black body spectrum today peaked at $T_\gamma = 2.7255(6)\,\mathrm{K}$ [9], presenting anisotropies of the order of 10^{-5}. These anisotropies can be studied via spherical harmonics ($Y_{lm}(\theta, \phi)$) expansion:

$$T(\theta, \phi) = \sum_{lm} a_{lm} Y_{lm}(\theta, \phi). \tag{1.4}$$

Given no preferred directionality and the very weak phase correlations observed in the CMB sky, it is possible to study its features in the l power spectrum:

$$D_l = \frac{l(l+1)}{2\pi} \langle |a_{lm}|^2 \rangle. \tag{1.5}$$

Focussing on temperature power spectrum (TT), its $l = 0$ component corresponds to the black body radiation temperature, while at $l = 1$, the dipole anisotropy is introduced by the Local Group motion with respect to the CMB sky. At higher-order multipoles $l \geq 2$, instead, the anisotropies return information about density perturbations in the early universe.

Figure 1.3 shows the Plank Collaboration results on the TT power spectrum fit considering the minimal ΛCDM model consisting of just six parameters [1]. Among the best fit values, $\Omega_\mathrm{b} h^2 = 0.02237 \pm 0.00015$ and $\Omega_\mathrm{DM} h^2 = 0.1200 \pm 0.0012$ were found, returning $\Omega_\Lambda = 0.685 \pm 0.007$, assuming $\Omega = 1$. These results, given the great precision of ΛCDM model in describing the observed data, once again reinforce the necessity of admitting the existence of a cold dark matter component to explain the early universe stages.

The Large-Scale Structure Formation

The formation of the large-scale structures in the universe is a direct consequence of primordial small density fluctuations that acted as seeds, subsequently evolved under the influence of the gravitational pull. Detailed three-dimensional maps of today's universe, obtained via extensive galaxy redshift surveys, such as the 2-degree Field Galaxy Redshift Survey and the Sloan Digital Sky Survey, reveal that galaxies are not uniformly distributed in space, but are instead arranged in a web-like structure [4]. In recent years, in order to understand how the cosmic-web, in its complexity of filaments and voids, could have been formed, advanced simulations, incorporating various physical processes like gas dynamics, star formation and black hole growth, have been conducted. The Millennium Simulation [10] and the more recent IllustrisTNG simulation have demonstrated the theoretical predictions would not match the observed distribution of the cosmic-web, except for admitting the existence of a dominant cold dark matter component present since the early universe.

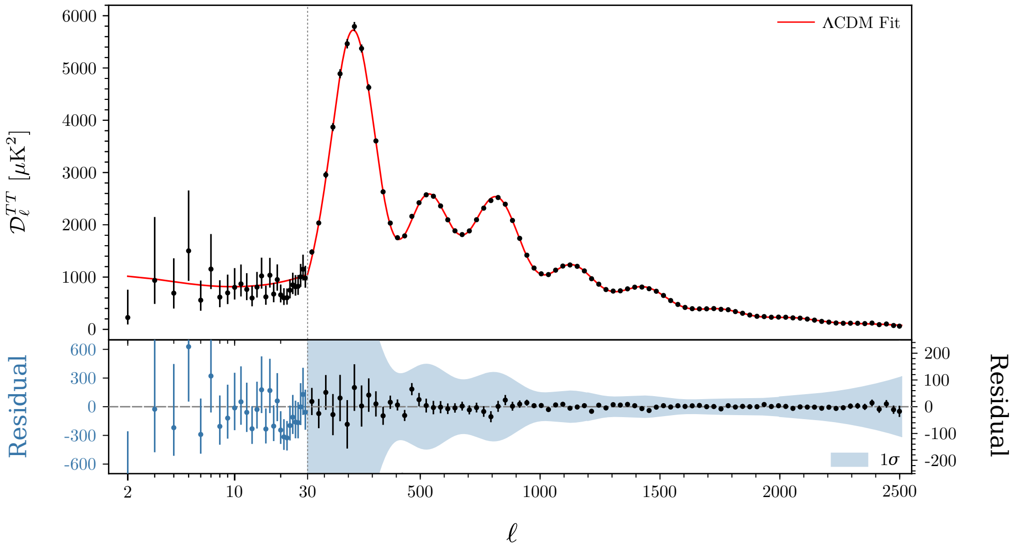

Figure 1.3: (Edited from [9]) Planck 2018 TT power spectrum. The ΛCDM theoretical spectrum best fit to the likelihoods is plotted in red in the upper panel. Residuals with respect to this model are shown in the lower panel. The vertical scale changes at $l = 30$, where the horizontal axis switches from logarithmic to linear. The error bars show $\pm 1\sigma$ diagonal uncertainties, including cosmic variance (approximated as Gaussian) and not including uncertainties in the foreground model at $l \geq 30$. The 1σ region in the middle panel corresponds to the errors of the unbinned data points.

1.1.3 The Dark Energy Dominated Era

Galaxy clusters and superclusters continued to evolve and change under the influence of gravity and dark energy, which drives the expansion of the universe. Many indirect probes to the existence of dark matter can be still observed in today's universe. More specifically, these evidences mainly derives from the missing matter component that is required to justify astrophysical observations of galaxy clusters and superclusters.

Missing Matter Component in Today's Universe

The first modern astronomical observation of missing matter component referred as dark matter, is certainly the one of the Coma cluster by Fritz Zwicky in 1933, reported in [11] and later discussed in [12]. In his study, Zwicky reported the observation of rotational velocities for some galaxies of the cluster, that greatly overcame the expectations considering the computed luminous mass of the cluster. More precisely, by exploiting the virial theorem, a gravitational matter content of about two orders of magnitude greater than luminous matter content of the Coma cluster was found. In later years, thanks to an update of the measured Hubble constant, this discrepancy was reviewed and refined, confirming the existence of a non-null mismatch. This still surviving discrepancy, possibly explained by a missing matter component, nowadays stands as an indirect proof to the existence of dark matter.

A second very famous indirect evidence to the dark matter existence in today's universe was found in Andromeda M31 spiral galaxy [13], and later confirmed with a lager spiral galaxies survey [14], by Vera Rubin and collaborators. By measuring hydrogen spectral lines in several galaxy emission regions, they were able to reconstruct the rotational velocity curves as function of distance from the galactic center. These curves cannot be solely interpreted with the observed luminous matter budget and its distribution. Specifically at large distances (r) from the galactic center ($r \geq 25\,\mathrm{Mpc}$), where the galactic disk gravitational contribution to the rotational velocity drops as $1/r$ according to the Newtonian gravity theory, the observed data points reached a plateau. This mismatch between observed data and theoretical expectations, that is visible and consistent for a very large set of different spiral galaxies, can be recovered once the existence of a non-luminous matter density $1/r^2$ profile (at large distances) is assumed. This missing matter component is nowadays attributed to the presence of dark matter halos.

A third set of astrophysical observations pointing to the existence of a non-luminous matter are performed by exploiting the gravitational lensing effects. With no doubt, the most famous observation is about the 1E 0657-558 merging galaxies cluster, also known as the Bullet cluster [15]. In this specific case, a displacement with 8σ significance between the gravitational lensing measured center of mass and the one deduced with the measured intracluster plasma emitted X-rays is observed. Since the collisionless galaxies matter budget is not enough to explain the detected gravitational lensing effects, also in this case the inclusion of a prevalent dark matter component is necessary to the explanation of the observed phenomenon.

1.2 The Dark Matter Identikit

Each footprint a hypothetical dark matter particle candidate has imprinted in the universe expansion history, partially reveals some of its properties. If we assume that all these observations could be explained by a single dark matter particle, it has to satisfy the following listed main conditions.

Dark or, equivalently, electrically neutral leading to a null or very weak electromagnetic coupling.

Cold or, equivalently, non-relativistic at the moment of its decoupling from the primordial universe particle soup.

Collisionless or, equivalently, much less self-interacting than baryons.

Stable or, equivalently, characterized with a lifetime longer than the age of the universe.

By assuming or partially relaxing these requirements, a dark matter particle candidate zoo spanning a humungous mass range (89 orders of magnitude) can be derived. At low mass values, this range is limited by quantum effects at $1 \times 10^{-22}\,\mathrm{eV}$ ($70\,\mathrm{eV}$) for boson (fermion) candidates, due to its Compton wavelength (the Tremaine-Gunn limit) [4]. At high values, the limit on the mass range derives from the stability against tidal disruption of structures immersed in dark matter halos, which requires a dark matter candidate mass lower than few solar masses [4].

For the introductory purposes of this Thesis, the focus is here directed towards the WIMP candidate. For a more broaden introduction to the other possible dark matter candidates refer to [16].

1.2.1 The WIMP Dark Matter Candidate

The WIMP dark matter candidate is a thermal relic of the primordial universe. The success of this hypothesis, among all possible others for dark matter, has to be attributed to the freeze-out production mechanism that, to explain the cosmology dark matter predicted abundance,

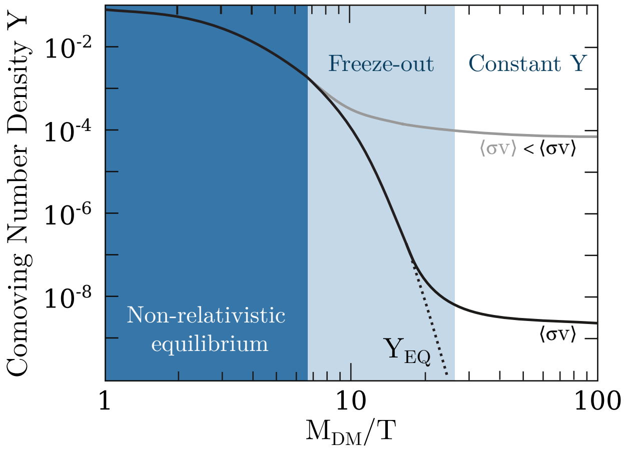

Figure 1.4: (Edited from [5]) Comoving dark matter number density Y as the temperature drops below its hypothetical mass value M_{DM}.

naturally required a candidate mass and cross-section values neatly fitting into the standard model of particle physics. This natural coincidence is also known after the name of *WIMP miracle*.

In few words, the freeze-out mechanism is the hypothesis of a particle relic production due to the prevailing of the universe expansion rate over the one of its interaction with the primordial universe particles thermal bath. A relic of this kind is the CMB, that has been the subject of intense studies [9] and will still be for several future ones [17]. Other two predicted early universe freeze-out relics are the CνB, the cosmic neutrino background, that is the target of proposed future experiments [18] and the WIMP relic. If this dark matter particle existence is assumed, a possible direct detection of it would constitute the observation of the earliest product of our primordial cosmos.

Supposing that in the early hot universe the Standard Model (SM) and WIMP dark matter (DM) species were in thermal equilibrium, the chemical equilibrium was guaranteed by the production (annihilation) processes (DM+DM $\leftrightarrow$ SM+SM), while the kinetic one was regulated by the elastic scattering with SM particles (DM+SM $\leftrightarrow$ DM+SM) [19]. Recasting the Boltzmann equation for annihilation [7], considering the comoving WIMP number density Y, it is possible to get the evolution equation:

$$\frac{\mathrm{d}Y}{\mathrm{d}t} = T^3 \langle \sigma v \rangle \left(Y_{\mathrm{EQ}}^2 - Y^2 \right) \tag{1.6}$$

where Y_{EQ} is the equilibrium abundance and $\langle \sigma v \rangle$ is the thermally averaged annihilation cross-section [7]. At universe temperatures much larger than the WIMP mass $T \gg M_{\mathrm{DM}}$, the reaction proceeds rapidly guaranteeing the chemical equilibrium between species ($Y \sim Y_{\mathrm{EQ}}$). In this limit, the statistical mechanic distribution function (independently of boson or fermion statistics) simplifies and returns $Y \sim Y_{\mathrm{EQ}} \asymp 10^{-1}$ [6]. At the time for which $T \sim M_{\mathrm{DM}}$, Y_{EQ} starts to be exponentially suppressed. Eventually, the WIMP DM number density becomes so little, that the annihilation rate drops below the expansion one. It is at this moment (roughly when $T_{\mathrm{f.o.}} = T \asymp M_{\mathrm{DM}}/10$ [6]) that the freeze-out mechanism produces the WIMP relic, literally freezing Y to its value at the time of this decoupling. Figure 1.4 depicts the comoving WIMP number density Y trend according to the ratio M_{DM}/T.

It is worth noticing that for increasing $\langle \sigma v \rangle$, the freeze-out abundance value decreases while the time (or equivalently the ratio M_{DM}/T) at which the decoupling occurs increases.

All this information can be recast, following [6], to determine the DM energy density contribution as:

$$\Omega_{DM} \sim 0.1 \frac{M_{\mathrm{DM}}}{T_{\mathrm{f.o.}}} \frac{1 \times 10^{-8}\,\mathrm{GeV}^{-2}}{\langle \sigma v \rangle}. \tag{1.7}$$

The observed DM energy density contribution can then be easily reproduced once $\langle \sigma v \rangle \asymp 1 \times 10^{-8}\,\mathrm{GeV}^{-2}$ is assumed. This value for the interaction cross-section is typical of the electroweak interaction scale, conveying the miracle image to the WIMP DM candidate as the perfect missing link between cosmology and particle-physics.

A WIMP DM candidate of this kind has a limited, yet quite extended, mass range (10 GeV-120 TeV) [19]. Within this range and different values of predicted cross-sections, many beyond SM theories lay. The most famous one, predicting the existence of a particle perfectly fitting into the WIMP relic cosmological scenario, is probably the SUSY, that would provide an elegant and simple solution to the SM gauge hierarchy problem [4]. The SUSY model introduces the existence of new particles beyond the SM ones, among which the lightest one (also known after the name of LSP, the lightest SUSY particle) is predicted to be stable and, if electrically and color neutral, it would constitute a perfect WIMP candidate. However, null results from both LHC and direct WIMP searches experiments have led to a rather pessimistic attitude towards the validity of the SUSY paradigm [20].

1.3 Experimental Efforts for Direct WIMP Searches

The WIMP DM paradigm can be tested, probing the existence of such particles, by means of detecting either its production aftermaths at accelerators, or its products of annihilation or decay from the cosmos or, eventually, the effects of its direct interaction in common particle detectors. Very briefly (for an extensive treatment see [3]), the target of these searches are here below listed.

Accelerator-based detection aims to produce DM particles. To this purpose, high-energy pp collisions, lower-energy $\mathrm{e}^+\mathrm{e}^-$ collisions and beam dump experiments are exploited. DM particles can be revealed, for example, by means of missing transverse momentum or energy in processes like $\mathrm{pp} \rightarrow \mathrm{DM} + \overline{\mathrm{DM}} + x$, where x could be of different natures: a hadronic jet, a photon or a lepton generated from the decay of a Z or W boson.

Indirect Detection aims at searching cosmic rays excesses potentially due to DM annihilation or decay processes. To these purposes, galactic and extra-galactic charged particles, photons or neutrinos reaching Earth- and space-based experiments are studied, searching for such signatures.

Direct Detection aims at detecting the recoil interaction of a DM particle with an Earth-based instrumented target. The event produced by a passing DM particle hitting one of the nuclei or electrons of a highly shielded and closely monitored underground detector target, can in principle be observed and recognized as such, if it represents an excess on top of the known expected background. The target material defines the WIMP mass range the experiment is sensitive to. This DM search approach is treated in more details in the following paragraphs.

1.3.1 The ABC of WIMP Direct Dark Matter Detection Approach

Direct DM searches are based on the assumption of an existing DM halo permeating the Milky Way. WIMP particles possibly making up this halo have a non-null probability, according to their foreseen cross-section, of interacting with properly tuned instrumented targets that may detect their passage [21]. The ingredients for such detection to occur are the existence of a DM halo, an expected kinematically-available WIMP signal rate and a tuned particle detector. These three essential requirements are described in the following.

Apparent Milky Way WIMP Wind

Inconsistencies between the measured rotational velocity curves and the baryonic contribution are also observed in the Milky Way [3]. These indirect evidences suggest the existence of a Milky Way DM halo, with a non-null density at the radial position of the Solar system. The value of the local DM density, ρ_0, ranges between 0.2–0.6 $\mathrm{GeV/cm^3}$ according to the selected halo model. For coherency purposes, direct WIMP DM experiments consider the $\rho_0 = 0.3\,\mathrm{GeV/cm^3}$ recommended value derived from a simplified smooth, isothermal, and spherical DM halo called standard halo model [22].

A second aspect of this halo, very important for direct DM searches, is the velocity distribution of its particles. In the rest frame of the galactic center, the velocity distribution is supposed to be an isotropic Maxwell-Boltzmann with a sharp cut-off at the escape velocity ($v_{\mathrm{esc.}}$):

$$f(v) = N \exp\left(-v^2/v_0^2\right)\Theta(v_{\mathrm{esc.}} - v) \tag{1.8}$$

where N is a normalization factor and $v_0 \sim 238\,\mathrm{km/s}$ identifies the most probable velocity. The escape velocity represents the limit above which DM particles prefer to evaporate off the galaxy with respect to maintain their binding status with the halo. $v_{\mathrm{esc.}}$ is estimated to be about 544(35) km/s [23].

Given that direct DM experiments are Earth-based, the laboratory rest frame distribution velocity has to be computed by considering Sun and Earth motions around the galactic center. The Galilean composition, by means of Sun (galactic disk) rotation velocity $v_\odot \sim 220\,\mathrm{km/s}$ and a yearly-averaged Earth one $v_\oplus \sim 29.8\,\mathrm{km/s}$, easily returns the wanted velocity distribution [3]. This relative motion generates an apparent Milky Way WIMP wind which boosts the DM flux potentially perceived by the Earth-based detectors.

As described in the following paragraph, the laboratory rest frame WIMP velocity distribution is fundamental for the computation of the expected signal rate in a counting experiment. Moreover, the characteristic orbital motion of the Earth around the Sun introduces a sinusoidal temporal variation to $f(v)$. In turn, this $\mathcal{O}(5\,\%)$ modulation impacts the computation of the WIMP flux, imprinting a peculiar signature to the expected signal. This characteristic behavior could be exploited for direct DM searches, as firstly described in [24]. A review to annual modulation WIMP experiments can be found in [3].

Basics of WIMP Signal Rate Computation

Given their mass and chargeless nature, WIMPs are expected to scatter off atomic nuclei within the targets. The resulting nuclear recoil (NR) can then be detected with a properly tuned instrumentation. The expected differential rate of WIMP scattering according to the nuclear recoil energy E_{NR} is [3]:

$$\frac{\mathrm{d}R}{\mathrm{d}E_{\mathrm{NR}}} = \frac{\rho_0 m}{M_{\mathrm{N}} M_{\mathrm{DM}}} \int_{v_{\mathrm{min}}} v f_\oplus(v) \frac{\mathrm{d}\sigma}{\mathrm{d}E_{\mathrm{NR}}}\,\mathrm{d}v \tag{1.9}$$

where M_{N} is the nucleus mass, m is the detector total mass, $f_{\oplus}$ is the DM velocity distribution in the Earth reference frame, σ is the WIMP scattering cross-section and $v_{\min}$ is the lower velocity kinematics bound. This latter is easily found, once the nuclear recoil energy is recast in terms of non-relativistic elastic scattering parameters:

$$E_{\mathrm{NR}} = \frac{\mu^2 v^2}{M_{\mathrm{N}}}(1-\cos\theta) = \frac{q^2}{2M_{\mathrm{N}}} \tag{1.10}$$

where $\mu = M_{\mathrm{DM}}M_{\mathrm{N}}/(M_{\mathrm{DM}}+M_{\mathrm{N}})$ is the system reduced mass, θ is the scattering angle in the center of mass-frame and q the transferred momentum. Thus, the lower bound velocity result to be

$$v_{\min} = \sqrt{M_{\mathrm{N}}E_{\mathrm{NR}}/(2\mu^2)}. \tag{1.11}$$

The derivation of $v_{\min}$ in the elastic scattering approximation is only possible by the very low momentum transfer. At higher values of q for which the de Broglie wavelength is comparable or even smaller than the size of the nucleus, this latter would no more respond coherently. In this limit, corrections to the coherence loss are expressed, for example in the interaction cross-section, with the form factor F. The form factor is a function of E_{NR} and is different for DM spin dependent (SD) and independent (SI) interactions. In this latter case, F is the Fourier transformation of the nucleon density and can be approximated with an analytical function proposed by Helm [25]. The WIMP interaction cross-section is hence expressed on the nucleon level and, regardless of the specific underneath coupling nature, it is defined as the sum of spin independent and spin dependent contributions as:

$$\frac{\mathrm{d}\sigma}{\mathrm{d}E_{\mathrm{NR}}} = \frac{M_{\mathrm{N}}}{2\mu^2 v^2}\left(\sigma_{\mathrm{SI}}^{(0)}F_{\mathrm{SI}}^2(E_{\mathrm{NR}}) + \sigma_{\mathrm{SD}}^{(0)}F_{\mathrm{SD}}^2(E_{\mathrm{NR}}),\right) \tag{1.12}$$

where $\sigma_{\mathrm{SI(SD)}}^{(0)}$ represents the SI (SD) cross-section at zero momentum transfer. The SI cross-section in the limit of small momenta transfer is [3]:

$$\sigma_{\mathrm{SI}}^{(0)} \overset{q\to 0}{=} \frac{\mu^2}{\mu_{\mathrm{N}}^2}A^2\sigma_{\mathrm{N}} \tag{1.13}$$

where μ_{N}^2 is the WIMP-nucleon reduced mass, A is the nuclear mass number and σ_{N} is the SI WIMP-nucleon cross-section, which is, along the WIMP mass, the parameter direct DM experiments explore and report as result. It is worth noticing that for WIMP masses well above the full target nuclear mass ($M_{\mathrm{DM}} \gg M_{\mathrm{N}}$), $\sigma_{\mathrm{SI}} \sim A^4$ enhancing the sensitivity of experiments exploiting heavy nuclear targets. However, as a drawback, the large size of high mass number nuclei translates into a heavy suppression of the Helm form factor, which eventually limits the sensitivity enhancement. This can be seen in Figure 1.5, where the differential WIMP signal rate is reported for several target materials. As shown by this plot, within a simplified WIMP interaction mechanism [27], the differential signal rate exponentially decays with E_{NR}. For comparison purposes, in the Figure 1.5 the nuclear recoil energy has been reported in unit of nuclear recoil equivalent keV, keV$_{\mathrm{NR}}$. This energy scale differs from the electronic recoil one due to heat-loss quenching effects.

The spin dependent cross-section derivation involves more complex considerations, as described in [3]. In the limit of small momenta transfer, it is possible to show that:

$$\sigma_{\mathrm{SD}}^{(0)} \overset{q\to 0}{=} \frac{\mu^2}{\mu_{\mathrm{N}}^2}S(q=0)\sigma_{\mathrm{N,SD}}, \tag{1.14}$$

where $S(q)$ represents the collected nuclear response function dependent on the transferred momentum and $\sigma_{\mathrm{N,SD}}$ is the SD WIMP-nucleon cross-section. Differently from the SI case,

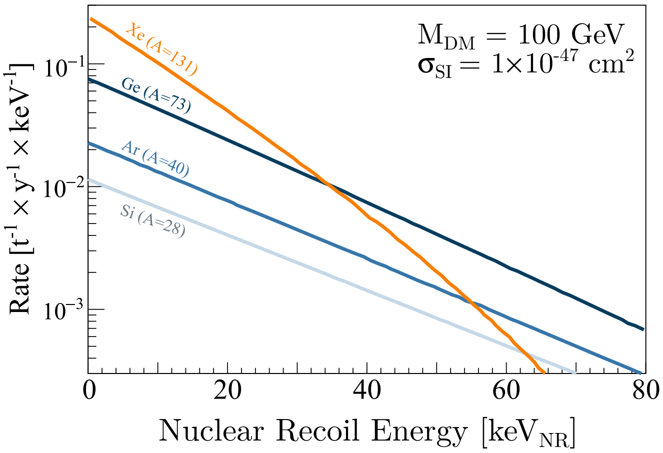

Figure 1.5: (Edited from [26]) Nuclear recoil spectra induced by a $M_{\mathrm{DM}} = 100\,\mathrm{GeV}$ WIMP in various common target materials, assuming a spin-independent WIMP-nucleon cross-section $\sigma_{\mathrm{SI}} = 1 \times 10^{-47}\,\mathrm{cm}^2$. The rate for spin-independent interactions increases with A^2, i.e. prefers heavy target materials. On the other hand, the rate for large nuclei (Xe) decreases at higher energies due to the form factor suppression.

the large WIMP mass approximation does not have the additional enhancement due to the A^2 coherent factor. This translates into a generally weaker experimental sensitivity. Beyond the standard SI and SD models, additional effective Lagrangian terms have been proposed in literature to include alternative nuclear coupling and responses [28].

Common Experimental Techniques

The total energy loss of a recoil in a WIMP detector can be expressed as the sum of the three possible energy deposition channels: excitation, ionization and heat. Given the chargeless WIMP nature, similarly to neutrons, there is an enhanced probability for these class of particles to directly interact with nuclei and deposit more energy in heat channel. This energy loss yields a quenching effect that is correctly assessed by the Lindhard theory in semiconductors [25], while in liquid noble targets a semi-analytical approach is exploited [26].

This quenching effect creates the opportunity of discriminating signal- and background-like events, if two or more energy deposition channels are read out. According to the technology exploited, the experimental sensitivity cover a specific portion of the WIMP vanilla paradigm mass region. These experimental techniques can be classified in two groups according to their WIMP sensitivity mass range: above the GeV scale or at the GeV scale.

Above GeV **scale** the noble-liquid dual-phase time projection chamber (TPC) technology holds the leading sensitivity. Indeed, thanks to the noble liquids properties, such as transparency to their own light, high stopping power and the possibility of looping them into purification systems, plus the easy scalability of the TPC technology, it is possible to explore the WIMP parameter space down to the neutrino fog [29], that ultimately limit their sensitivity. Such technologies are divided into two categories according to the noble element used. Xenon-based dual-phase TPCs are exploited in XENONnT [30], LZ [31] and PandaX-4T [32] experiments. Argon-based technologies will be soon exploited in DarkSide-20k [33], as happened with its predecessor DarkSide50 [34]. Single phase noble-liquid technologies have also been explored, such as the Xenon-based XMASS [35] or the Argon-based DEAP-3600 [36] experiment, leading to less enhanced sensitivities in this specific WIMP mass range.

The GeV **scale** cannot be explored with noble-liquid TPCs classical analysis methods, since the predicted NR energy deposition falls below the experiment kinematic threshold,

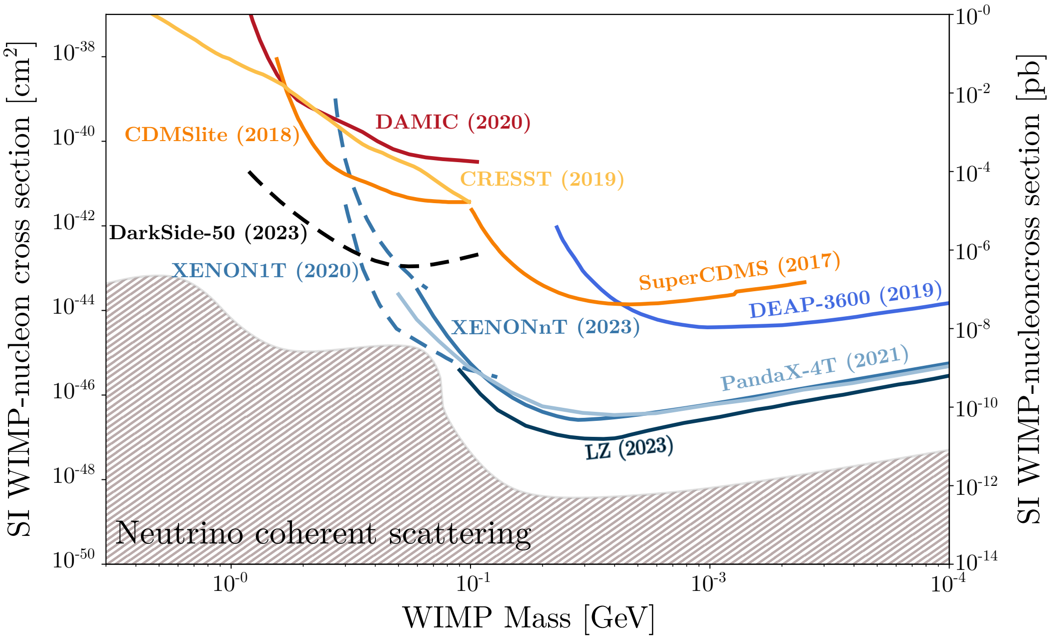

Figure 1.6: (Edited from [4]) Upper limits on the SI DM-nucleon cross-section as a function of DM mass. The blue 90 % confidence limits were obtained with experiments classified to be sensitive in the above GeV scale, while red ones are from experiments sensitive in the GeV scale. Dashed lines represent the exclusion plots obtained with the alternative analyses approach, such as ionization-only or Migdal analyses.

limiting the sensitivity. Therefore, some other analysis channels such as the ionization-only one or the Migdal effect [3] are exploited. Nevertheless, the low temperature calorimeters technique has demonstrated to hold the leading role for WIMP sensitivities in this mass range. Indeed, thanks to the $\mathcal{O}(10\,\text{meV})$ energy needed to produce elementary phonon excitations, low temperature calorimeters based technologies have shown eV-scale energy thresholds and resolutions [3], opening the possibility to explore GeV-scale masses via NR channel. There are two classes of low temperature calorimeters based experiments, according to the energy deposition channel read-out. The first one exploits phonon and charge read-out, such as SuperCDMS [37] and its "lite" configuration CDMSlite [38] utilizing Si and Ge crystal targets. The second one exploits phonon and light read-out, such as CRESST [39] utilizing low temperature scintillating calorimeters [3]. Room temperature silicon-based detectors have also been exploited in the DAMIC experiment [40], leading to similar sensitivities. The main limitation of these crystals based experiments is their kg d exposure, which in turns limit their sensitivity to larger WIMP cross-section values with respect to the t y scale of the noble liquid technologies. This limit might be overcome by exploiting spherical proportional counters gas detectors, such as NEWS-G [41] and future ECuME [3] and DarkSPHERE [42] experiments, or by bubble chambers, such as the PICO [43] and SBC [44] experiments.

To summarize the impact these experiments have in the direct search of the WIMP vanilla DM candidate, Figure 1.6 reports the published SI exclusion limits for several experiments. Beyond the WIMP vanilla paradigm, the scientific community has recently focused its attention towards the sub-GeV mass scale, developing new technologies to push the energy threshold to even lower values and in turn enhance the experimental sensitivity at these low mass values. More comprehensive reviews of the here cited experiments and a treatment of the non-vanilla sub-GeV DM searches can be found for example in [3, 4, 26, 45].

All these technologies to reduce cosmic and environmental radiations must be placed in deep-underground facilities and shielded with appropriate passive or active veto systems, such as the water Cherenkov muon and neutron detector in the specific case of XENONnT [30]. Moreover, purification systems for liquid targets, the definition of a fiducial volume, via 3D position reconstruction, and the discrimination between single- versus multiple-scatters events provide an extra handle to reject a significant fraction of the remaining backgrounds [4].

Ultimately, these experiments will be limited by the irreducible background of neutrinos originating in the atmosphere and in the core of the Sun (gray band in Figure 1.6) known after the name of neutrino fog [3]. The XENONnT [46] and PandaX-4T [47] experiments have already started observing its effect, by detecting solar ^{8}B neutrinos via coherent elastic neutrino-nucleus scattering.

A method to overcome the neutrino fog apparent limit for WIMP dark matter detection has been proposed, among others, by the CYGNUS [48] and the ReD [49] Collaborations. This method relies on imaging nuclear recoil ionization tracks to reconstruct directionality. Indeed, by determining the direction of incoming particles, it is possible to distinguish the solar neutrino background from the WIMP signal, as their sources map different locations in the sky.

2

The XENONnT experiment

Liquid-Xenon (LXe) dual-phase time-projection chamber (TPC) technology holds the worldwide leading sensitivity for direct searches WIMP dark matter (DM) candidate above the GeV mass scale [4]. One of the experiments exploiting this technology is the last stage of the Xenon DM project, XENONnT.

In the last two decades, the Xenon DM project operated four stages of detectors based on the LXe dual-phase TPC technology. With progressively larger mass, lower background and improved sensitivities, these successful experiments (XENON10 [50], XENON100 [51], XENON1T [52] and XENONnT [53]) were all operated in the underground facilities of Laboratori Nazionali del Gran Sasso, in Italy. Figure 2.1 summarizes the Xenon project progression of achievements, in terms of the lowest excluded SI WIMP-nucleon cross-section and exposure, from 2006 up to the time of this writing (2024). For completeness, also projected sensitivities and exposures are reported both for the still-running XENONnT [54] and the foreseen next generation experiments [55].

The unprecedented background levels, obtained thanks to the larger LXe mass, the great effort in material radioassay and the upgrade of the purification systems, create the opportunity of exploiting such a detector not only for the WIMP vanilla direct searches, but also for other exotic physics channels in low- and high-energy ranges and for precision studies of known processes.

In this Chapter, a brief review of the LXe TPC technology working principles, along with a description of the XENONnT experiment, is provided. More specifically, after a description of the suitability of LXe as direct DM searches target and the phenomenology of its scintillation and ionization signals in 2.1, the dual-phase TPC technology working principles are outlined in 2.2 along with its particle discrimination properties. Eventually, the XENONnT experiment and its WIMP DM searches results are reported in 2.3 and 2.4, respectively.

2.1 LXe as Dark Matter Detection Medium

LXe, as other noble liquid elements such as liquid Argon, has been widely exploited as particle detection medium. Indeed, it is exhibits excellent scintillation yields and time response and

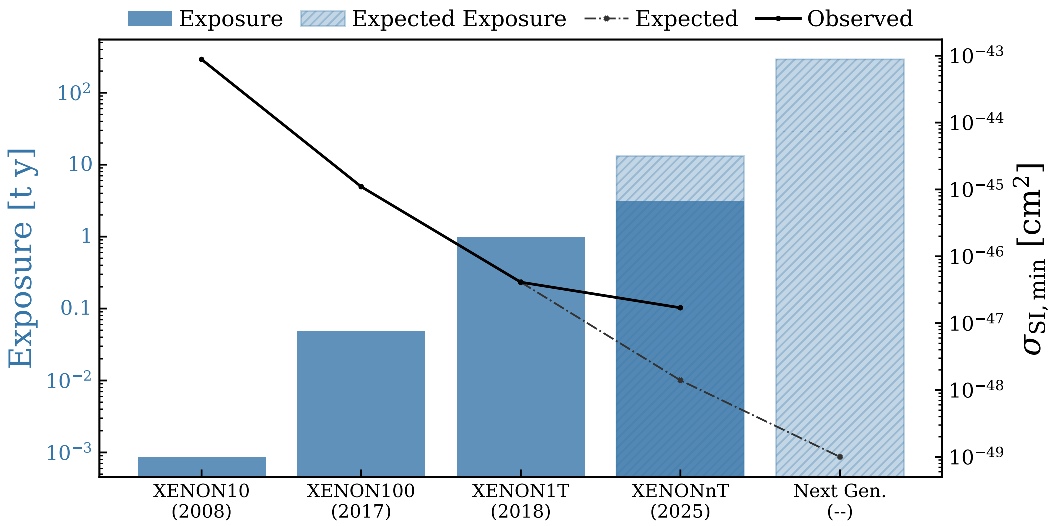

Figure 2.1: Evolution of the Xenon DM project. For each experimental stage (XENON10 [50], XENON100 [51], XENON1T [52] and XENONnT [53]) the total exposure (blue bars, left y-axis) and the lowest excluded value of SI WIMP nucleon cross-section (black dots, right y-axis) are reported. Projections for the full XENONnT project [54] and the proposed next-generation [55] experiment are also reported.

very high stopping power. Furthermore, it provides strong electrical insulation, given the large energy gap between valence and the conduction electronic bands. All these properties, reported in Table 2.1, make LXe a perfect target for TPCs, that can also read its ionization signal, by means of a simple electric field configuration. More on LXe TPC working principles and advantages can be read in 2.2.

In the particular case of direct DM searches, the Xenon atomic mass (A= 131), the highest among the scintillating noble elements, enhances the SI discovery power, see Equation 1.13. Moreover, among the different isotopes composing natural Xenon ($^{\mathrm{nat}}$Xe), ^{129}Xe, with a 1/2 nuclear spin, and ^{131}Xe equals, with a 3/2 nuclear spin, also allow the SD WIMP DM searches.

An additional important feature of $^{\mathrm{nat}}$Xe is that the only unstable Xenon isotopes are ^{124}Xe and ^{136}Xe, both decaying via second-order weak processes, subdominantly impacting the WIMP DM searches region of interest (ROI). This property has a double effect. The first

Table 2.1: (Inspired by [56] and [57]) Physical properties of natural LXe.

Property	Value	Reference
Atomic Number	54	[58]
Atomic Mass	131.293 g/mol	[58]
Content in Dry Air Mass	0.09 ppm	[59]
Boiling point	163.39 K (at 1 bar)	[59]
Density	2.86 g/cm^3 (at 177 K and 1.89 bar)	[60]
Band Gap	9.276 g/cm^3 (at 135 K)	[61]
Dielectric constant	1.95	[62]
Scintillation wavelength	178 nm	[62]
Natural Composition	^{124}Xe (0.095 %) , ^{126}Xe (0.089 %) , ^{128}Xe (1.910 %), ^{129}Xe (26.40 %) , ^{130}Xe (4.071 %) , ^{131}Xe (21.23 %), ^{132}Xe (26.91 %) , ^{134}Xe (10.44 %) , ^{136}Xe (8.857 %).	[58]

is that any possible radioactive contaminant, except ^{124}Xe and ^{136}Xe, polluting the LXe and impacting in the WIMP ROI is potentially removable by exploiting the different chemical and physical properties between this contaminant and Xenon, as for example done in XENONnT experiment for Radon and Krypton contaminants. The second concerns the physics reach of the experiment, that is enriched by the additional studies targeting ^{124}Xe double electron capture and ^{136}Xe double beta decay.

Beyond inner contaminants, external radiation may represent a major background for direct DM searches. Nevertheless, LXe is highly self-shielding. Indeed, thanks to its high atomic number (Z = 54) and density (2.86 g/cm^3 at 177 K and 1.89 bar), LXe is characterized by the highest efficiency in stopping penetrating radiation among all noble liquid elements. As an example, the 46.539 keV gamma transition of ^{210}Bi, following about 80 % of the times the beta decay of ^{210}Pb [63], has a mean free path of about 0.023 cm in LXe, according NIST 2017 database [64]. Chapter 3 and Chapter 6 are dedicated about the origins and importance of ^{210}Pb background in the XENONnT WIMP searches. As a second example, if the 2614.5 keV de-excitation gamma [63], following ^{208}Tl beta decay, is taken into account, its mean free path is about 9.5 cm [64]. Concerning, instead, beta (alpha) particles, the mean free path monotonically increases with energy reaching about 2 cm (0.02 cm) at 10 MeV. The direct consequence of the efficient self-shielding property of the LXe is that, when instrumented with a technology providing position reconstruction, it allows the selection of a large and clean fiducial volume, limiting the amount of discarded mass exposure due to external backgrounds. Indeed, in the case of the XENONnT experiment, the fiducialization for WIMP searches is performed with a geometrical data selection rule that only removes the events occurred within few centimeters from the boarders of the TPC. The specific case of XENONnT fiducialization selection criteria for WIMP studies is further treated in Chapter 6.

2.1.1 Phenomenology of LXe light and ionization signals

Whenever a particle interacts with the LXe medium, it deposits energy either via scattering off electrons (electron recoils, ER) or Xenon nuclei (nuclear recoil, NR). In both cases, the total deposited energy is partitioned into inelastic channel, including ionization ($e^- + Xe^+$) and excitation (Xe^*) processes, and elastic channel, including atomic motion (heat):

$$\frac{\mathrm{d}E}{\mathrm{d}x} = \left(\frac{\mathrm{d}E}{\mathrm{d}x}\right)_{\mathrm{inel}} + \left(\frac{\mathrm{d}E}{\mathrm{d}x}\right)_{\mathrm{el}} . \tag{2.1}$$

The energy deposited in the inelastic channel $E_0 L$ can be further expressed according to the Platzman energy balance [65] as:

$$E_0 L = N_i E_i + N_{ex} E_{ex} + N_i \varepsilon \tag{2.2}$$

where E_0 is the total deposited energy, L the Lindhard factor, N_i/N_{ex} the number of ionized/excited atoms at an average energy cost of E_i/E_{ex} and ε the average energy carried away by single electrons no more able to ionize or excite other atoms being below-threshold [66, 67]. For LXe, ε is about 5 eV[68].

The Lindhard factor L accounts for the quenching of the total deposited energy E_0 according to the nature of the primary interaction. Indeed, in the case of an ER, being the mass of the electron negligible compared to that of the target atoms, the energy lost in the elastic contribution is almost null and hence $L \sim 1$. Differently, in NRs, where the Xenon recoiling nuclei have a velocity comparable to the one of their atomic electrons and hence an effective charge typically lower than unity [69], the Lindhard factor is about $L = 0.15$–0.3 for

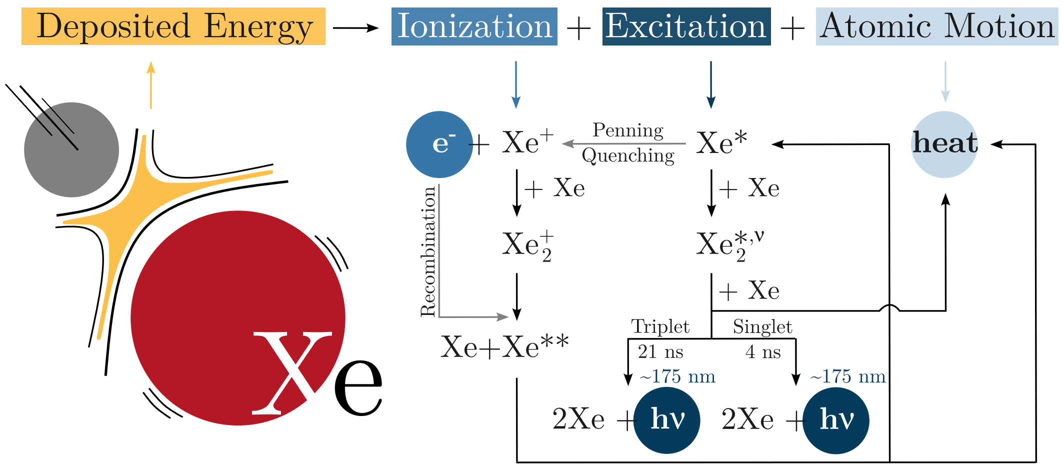

Figure 2.2: (Inspired by [56] and [72]) Schematics of the phenomenology of LXe light and ionization signals, following the description in [67] and in [73].

energies in the range 1–100 keV. More specifically, in the Lindhard-Scharff-Schiøtt theory [70, 71], the quenching factor can be evaluated as:

$$L = \frac{kg(\epsilon)}{1 + kg(\epsilon)}, \tag{2.3}$$

where k is a proportionality constant between the electronic stopping power and the velocity of recoiling nucleus and $g(\epsilon)$ is proportional to the ratio of electronic stopping power to the nuclear stopping power. By using the dimensionless quantity representing the deposited energy ϵ, in turn determined by the target nucleus atomic number Z as $\epsilon = 1.5(E_0/\mathrm{keV})Z^{-7/3}$, $g(\epsilon)$ is parametrized as:

$$g(\epsilon) = 3\epsilon^{0.15} + 0.7\epsilon^{0.6} + \epsilon. \tag{2.4}$$

Even if the potential measurement of the heat channel would represent a great signature for ER/NR discrimination, this latter can still be done by just exploiting ionization and excitation signals, that thanks to their phenomenology presents different yields according to the nature of the primary interaction. This happens thanks to different ionization density of NR with respect to ER events that determines the probability of some sub-quenching and recombination processes to happen. The basics of the production of the detectable signals (low-energy electrons and photons) from ionization and excitation mechanism are schematically represented in Figure 2.2.

Xenon excitation signal is represented by scintillation photons generated after the formation of excited diatomic molecules, called *diatomic excimers*. The relaxation mechanism of diatomic excimers proceeds as described in [73]:

$$\begin{aligned} \mathrm{Xe}^* + \mathrm{Xe} &\rightarrow \mathrm{Xe}_2^{*,\nu} \\ \mathrm{Xe}_2^{*,\nu} + \mathrm{Xe} &\rightarrow \mathrm{Xe}_2^* + \mathrm{Xe} + \mathrm{heat} \\ \mathrm{Xe}_2^* &\rightarrow 2\mathrm{Xe} + h\nu, \end{aligned}$$

where the $\mathrm{Xe}_2^{*,\nu}$ state represent the diatomic excimer with a non-null vibrational excitation ν. This latter is usually released in form of heat, via non-radiative channels, even if a relaxation by means of radiative infrared photons is also possible [74]. The non-vibrational excited Xe_2^* form can either be created in a singlet $({}^1\Sigma_u{}^+)$ or in a triplet $({}^3\Sigma_u{}^+)$ state. The de-excitation of both states produce a vacuum-ultraviolet (VUV) scintillation photon with wavelength

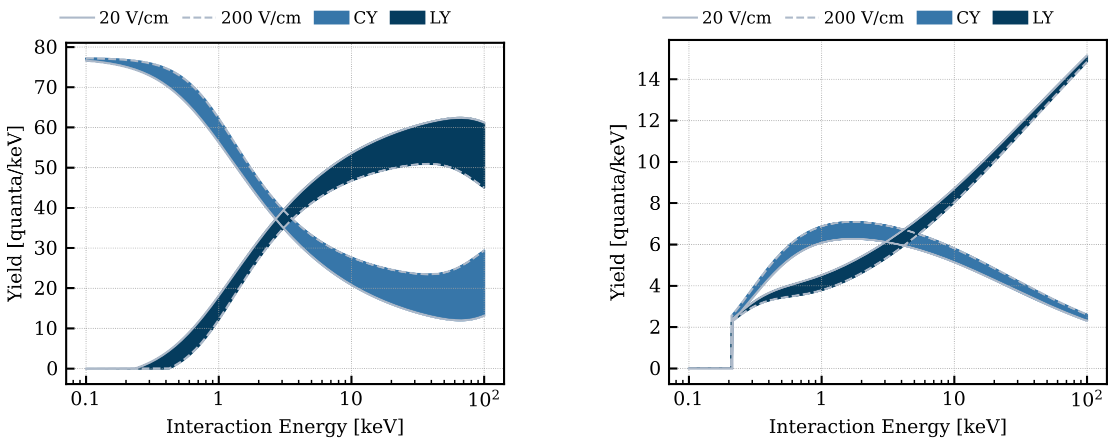

Figure 2.3: (Inspired by [56]) NEST [79] (nestpy v2.4.0 [80]) charge (CY) and light yields (LY) according to the initial energy of the impinging particle, for both ER (left) and NR (right) case. The yields electric drift field dependence is shown by means of bands spanning from the 20 V/cm curves (solid lines) up to the 200 V/cm curves (dashed lines).

$\lambda = 175\,\mathrm{nm}$ [75]. What differs between the two excited states is their relaxation time, that is faster for the singlet ($\tau_1 = 4.3(6)\,\mathrm{ns}$) with respect to the triplet ($\tau_3 = 21(2)\,\mathrm{ns}$) [76]. The ratio between abundance of photons emitted from triplet to singlet components slightly depends on the primary interaction, with a higher singlet component for NR interactions [77]. However, given the small difference between the two characteristic time constants, in LXe-based experiments this discrimination is rarely used.

A second mechanism of generating the scintillation signal is via recombination between liberated electrons and Xenon ions after prompt atom ionization, generating $\mathrm{Xe}^+ + \mathrm{e}^-$. Also in this case excimers are formed following the process [73]:

$$\begin{aligned} \mathrm{Xe}^+ + \mathrm{Xe} &\rightarrow \mathrm{Xe}_2^+ \\ \mathrm{Xe}^+ + \mathrm{e}^- &\rightarrow \mathrm{Xe}^{**} + \mathrm{Xe} \\ \mathrm{Xe}^{**} &\rightarrow \mathrm{Xe}^* + \mathrm{heat}. \end{aligned}$$

Nevertheless, the recombination process can happen only after liberated electrons have thermalized. Considering a thermalization characteristic timescale of $6.5(5)\,\mathrm{ns}$, as measured in [68], the thermalized electrons are able to reach on average a $4.5\,\mu\mathrm{m}$ distance from the production point [78]. This value is about a factor two greater than the Onsager radius for LXe, namely the radius at which the Coulomb energy equals the thermal energy, and it partially favors the escape of such electrons even not in presence of a strong electric field. The measured electron escape probabilities in absence of electric field are however in tension, ranging between 20 % and 70 %, for both ERs and NRs [76].

Many models have been developed to describe the recombination process as a function of the electron stopping power and the applied electric field. In late years, the LXe scientific community embraced the usage of the Noble Element Simulation Technique (NEST) [79] to parametrize the charge yield (CY) and the light yield (LY), describing the number of produced electrons and scintillating photons scaled to the energy of the incident particle. NEST model is based both on the Thomas-Imel box model [81] and on a series of heuristic models, with free parameters optimized with the available measurements. Figure 2.3 reports NEST yields at different interaction energies for both for ERs (beta radiation) and NRs, together with their electric drift field dependence. A more detailed description of NEST model parametrization is provided in Chapter 6, where it is used for modeling and fitting purposes concerning the TPC surface background.

As clearly visible from the plots of Figure 2.3, as the electric drift field increases also CY does at the expense of LY. This happens because with a higher electric drift field the thermalized electrons recombination probability drops and hence less recombination light is generated. This dependence is stronger for ER events where the light contribution from recombination processes is greater. Although there is a conversion between electrons and photons in processes such as the recombination, the total number of quanta is conserved. Therefore, it is possible to recast Equation 2.2 into:

$$E_0 L = W(N_{\mathrm{ph}} + N_{\mathrm{el}}), \tag{2.5}$$

where $N_{\mathrm{ph}} = N_{\mathrm{ex}} + rN_{\mathrm{i}}$, with r being the recombination probability, determined by the electric field, and W the average energy to produce a carrier (either photon or electron). A measured value for W of $13.7(2)\,\mathrm{eV}$ for LXe is assumed [82], even though more recent results point towards a lower value (of about $11.5\,\mathrm{eV}$ [83, 84]).

The only process not conserving the total number of quanta is the bi-exciton quenching, also known as Penning quenching [85], where two excited atoms interact generating an electron-ion pair:

$$\mathrm{Xe}^* + \mathrm{Xe}^* \rightarrow \mathrm{Xe}^+ + \mathrm{e}^- + \mathrm{Xe}.$$

This process reduces the number of total quanta of one unity at each occurrence, since it converts two excited atoms, potentially sources of two photons, in only one electron-ion pair. The probability associated to the occurrence of this mechanism is defined by the density of excitons, which increases with the linear energy transfer (LET) of the interacting particle. Therefore, it is of particular importance for highly ionizing particles, such as very low-energy NRs, alphas or fission fragments, while its contribution is negligible for ER and above-GeV WIMP NR interactions, for which Equation 2.5 holds. This effect is indeed evident in NR calibration data of LXe detectors, such as those collected in XENONnT SR0 campaign [86].

2.2 XENONnT Dual-phase TPC working principles

The TPC technology, invented by David R. Nygren at Lawrence Berkeley National Laboratory in the late 1970s [87], is based on the application of an electric field, occasionally coupled to a magnetic field, to a sensitive volume, usually filled with a gas or liquid target, to reconstruct particles interaction. In the typical cylindrical geometry used for LXe direct DM searches as utilized in XENONnT [30], the TPC is equipped with two arrays of photomultiplier tubes (PMTs) arranged in the top and bottom bases, to read out the scintillation and ionization signals. On top of the Xenon liquid phase, a gaseous Xenon phase (GXe) is present to amplify the ionization signal. Schematically, the working principle of a dual-phase LXe TPC is presented in Figure 2.4.

Whenever a particle interacts in the LXe active volume, scintillation photons via excitation processes, thermalized electrons via ionization processes and heat via atomic motion are generated. Only the first two signals are collectable with the TPC technology, while the information about energy deposited in the heat channel is lost. Excitation and ionization signals are instead read out in two steps. Prompt scintillation light is detected by the PMTs as S1 signal, while thermalized electrons are drifted by an electric field towards the top part of the TPC. Here electrons are extracted with a much higher electric field into the GXe and produce the S2 signal via electroluminescence. The simultaneous readout of the S1 and S2

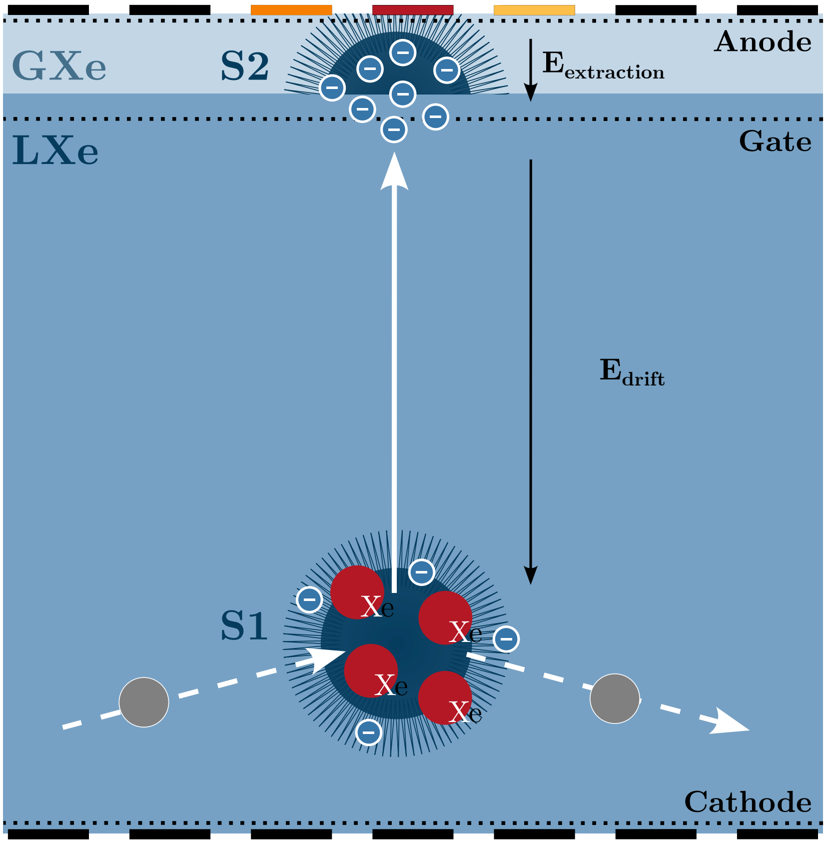

Figure 2.4: (Inspired by [56]) XENONnT LXe dual-phase working principles. The particle interacting within the LXe volume (gray circle) release energy, ionizing and exciting Xenon atoms. Prompt scintillation light is thus produced and detected by the top and bottom photomultiplier tubes (PMT) arrays and registered as S1 signal. Thermalized electrons, produced in the ionization process, are pulled out from the interaction point and drifted towards the LXe/GXe interface where they are later extracted by a higher electric field and produce electroluminescence, detected mainly by the top PMT array as S2.

signals allows the reconstruction of the position at which the event occurred, the determination of the deposited energy in the particle interaction and partial particle identification by exploiting the S1/S2 signature discriminating NR from ER interactions.

Event position reconstruction is performed in two steps: the identification of the (X,Y) position in the TPC horizontal section plane and the determination of the depth (Z) at which the interaction occurred. The (X,Y) position identification is performed via reconstruction of the S2 top PMTs light pattern, which is broadened by electron cloud diffusion that, for a fixed number of carriers, increases with the interaction depth and hence with drift time. The determination of the depth Z of interaction is instead performed by evaluating the temporal difference between the occurrence of the S1 and S2 signals. This can be achieved not only by calibrating the temporal response of the TPC with dedicated runs, but also by means of a uniform and homogeneous electric field throughout the entire TPC length guaranteed by a well-studied field cage design. In the XENONnT experiment, this result is achieved by a field cage design featuring two nested arrays of field shaping rings connected by a resistor chain along the full TPC height [88]. Position reconstruction of events is of particular importance when concerning background sources rejection and modeling. Indeed, if the TPC sensitive target is pure enough, or, as in the case of the XENONnT experiment, continuously purified

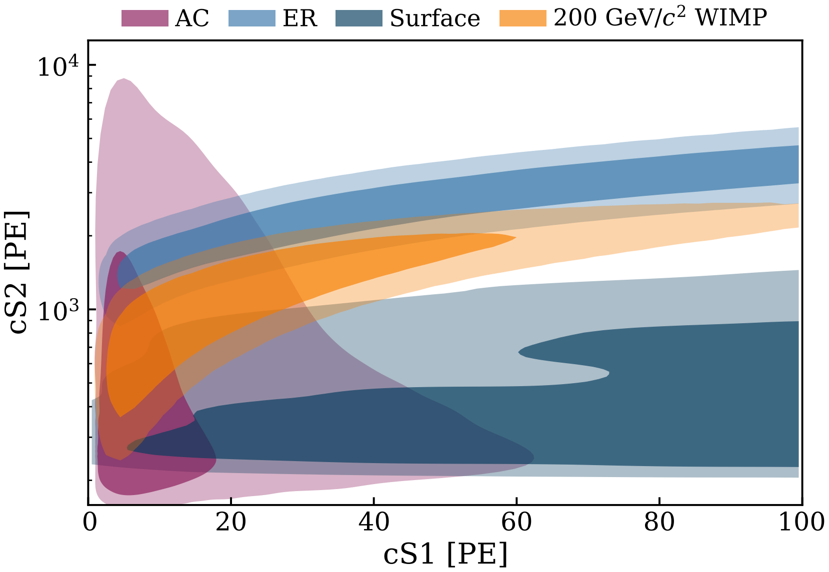

Figure 2.5: (Edited from [89]) XENONnT (S1,S2) observable space with 200 GeV/c^2 WIMP signal and background characteristic responses.

during the operation, the majority of the background is represented by external radiation triggering events in the active detector volume. Given the high stopping power of LXe target, the external radiation hardly reaches the very center of the volume and the resulting signal is characterized by a specific spatial signature according to the external source distribution. In these cases, the easiest approach to drastically reduce the impact of such a background, is to exploit a fiducialization technique, that is the selection of events within an optimized inner geometrical volume (see Chapter 6 for reference).

Events deposited energy is a second feature a LXe dual-phase TPC is able to determine. Indeed, by correcting the S1 snd S2 signals for the temporal and spatial dependence of the detector response (cS1,cS2), plus taking into account the event reconstruction efficiency, it is possible to recast Equation 2.5 as:

$$\mathrm{CES} = W(\frac{\mathrm{cS1}}{g_1} + \frac{\mathrm{cS2}}{g_2}), \tag{2.6}$$

where CES is the reconstructed energy of the event, also known as combined energy scale, while g_1 and g_2 are the ratios between the number of photons or electrons produced with respect to the ones detected. In the case of photons, this ratio represents a detection efficiency, and hence is lower than 1, while in case of electrons it represents the amplification factor, due to the extraction in the GXe phase, and thus it is usually way larger than 1. The computed CES value in Equation 2.6 estimates the deposited energy in a ER event, while for NR interactions the Lindhard factor has to be taken into account, as detailed in 2.1.

Particle identification can also be partially accessed via simultaneous readout of scintillation and ionization signals in a dual-phase LXe TPC. The different probability for quenching sub-processes to occur in the genesis of quanta for ER and NR events induce a larger cS2/cS1 ratio for the first class of events with respect to the second one, as depicted in Figure 2.5, where XENONnT ER band and expected 200 GeV/c^2 WIMP signal (NR) one are displayed. This potentially allows the total rejection of the ER background, while preserving great part of the NR events. Moreover, other backgrounds, such as events induced by the TPC surfaces contamination or accidental coincidences, constituted by randomly paired cS1 and cS2 signals, can be identified by specific signatures in the (cS1,cS2) observable space, and hence partially reduced. This ER/NR discrimination power is further increased if the electric field of both extraction and drift are amplified, thanks to a lower probability of electron-ion recombination. This latter also has the effect of reducing the rate of accidental coincidence background, since, by decreasing the electron drift time, in turn also decreases the maximal event temporal window and hence, fixing the TPC events rate, also the probability of randomly pairing two uncorrelated S1-like and S2-like signals. In order to reduce the surface background impact, instead, a smaller fiducialization volume could be used at the expense of the experimental exposure and hence the WIMP discovery power. Other methods to mitigate this background are for example based on the handling the Teflon panels, currently outlining the TPC of LXe direct DM experiments, such as XENONnT, with some extra precautious in order to limit Radon daughters plate out onto the surfaces. For an overview of current R&D efforts for the LXe dual-phase TPC next generation experiment refer to [90].

2.3 XENONnT experiment at LNGS

Deep underground in Laboratori Nazionali del Gran Sasso, in Italy, more specifically in Hall B, the XENONnT experiment is hosted. This location provides an overburden of about 1500 m of rock, approximately equivalent to 3600 m.w.e., that shields the experiment from cosmic rays, with an effective reduction factor of about 10^6 for cosmic muons. Reducing this background is fundamental for experiments such as XENONnT, not only for detector paralysis issues due to a too high event rate, but also for the cosmogenic neutrons generated within the materials surrounding the sensitive part of the detector. Rock overburden is however not enough for demanded WIMP sensitivities. For this reason the XENONnT experiment is equipped with both other shielding active vetoes and a facility building hosting the liquid and gas purification and handling subsystems [30].

The XENONnT dual-phase LXe TPC detector core is hosted in a cryostat placed at the center of a 700 t water tank (WT), providing a nested configuration of active water-based neutron and muon vetoes (see Figure 2.6). By successively peeling off the layers of the XENONnT *onion*-like detector configuration, the outermost shield is represented by the muon veto (MV). As its name suggests, the MV is primarily dedicated to the detection of cosmic muons that, due to their high energy, survive the shielding provided by the Gran Sasso mountain. At such high energies, Cherenkov light is produced in the MV water medium and later read out by the MV 84 Hamamatsu R5912ASSY 8" PMTs. Beyond vetoing muons that simultaneously trigger events in the MV and in the XENONnT TPC, the MV has the additional purpose of passively shielding the inner detector from external natural radiation.

The second outer shielding detector, immediately surrounding the TPC, is the neutron veto (NV). The NV, optically separated from the rest of the WT thanks to high-reflectivity Teflon panels, in which 120 Hamamatsu R5912-100-10 8" PMTs are mounted facing inwards, has the goal of tagging neutron events in coincidence with the TPC [91]. Cosmogenic neutrons scattering at least once in the TPC have high probability of escaping the LXe volume and, after a moderation step in water, of being trapped by Hydrogen nuclei via neutron capture process. The 2.2 MeV gamma emission, following the neutron capture on Hydrogen, is a highly effective signature, ensuring an enhanced NV tagging efficiency. Other nuclei, such as Gadolinium, present much higher neutron capture cross-sections with respect to Hydrogen. For this reason, the addition of Gadolinium salt during the second science run of XENONnT (SR2) in the WT increased the neutron tagging efficiency from 53 % to about 87 % [92].

Eventually, in the innermost part of the XENONnT WT, the LXe TPC is hosted in a stainless steel double-wall vacuum-isolated cryostat. The cylindrical TPC has a radius of

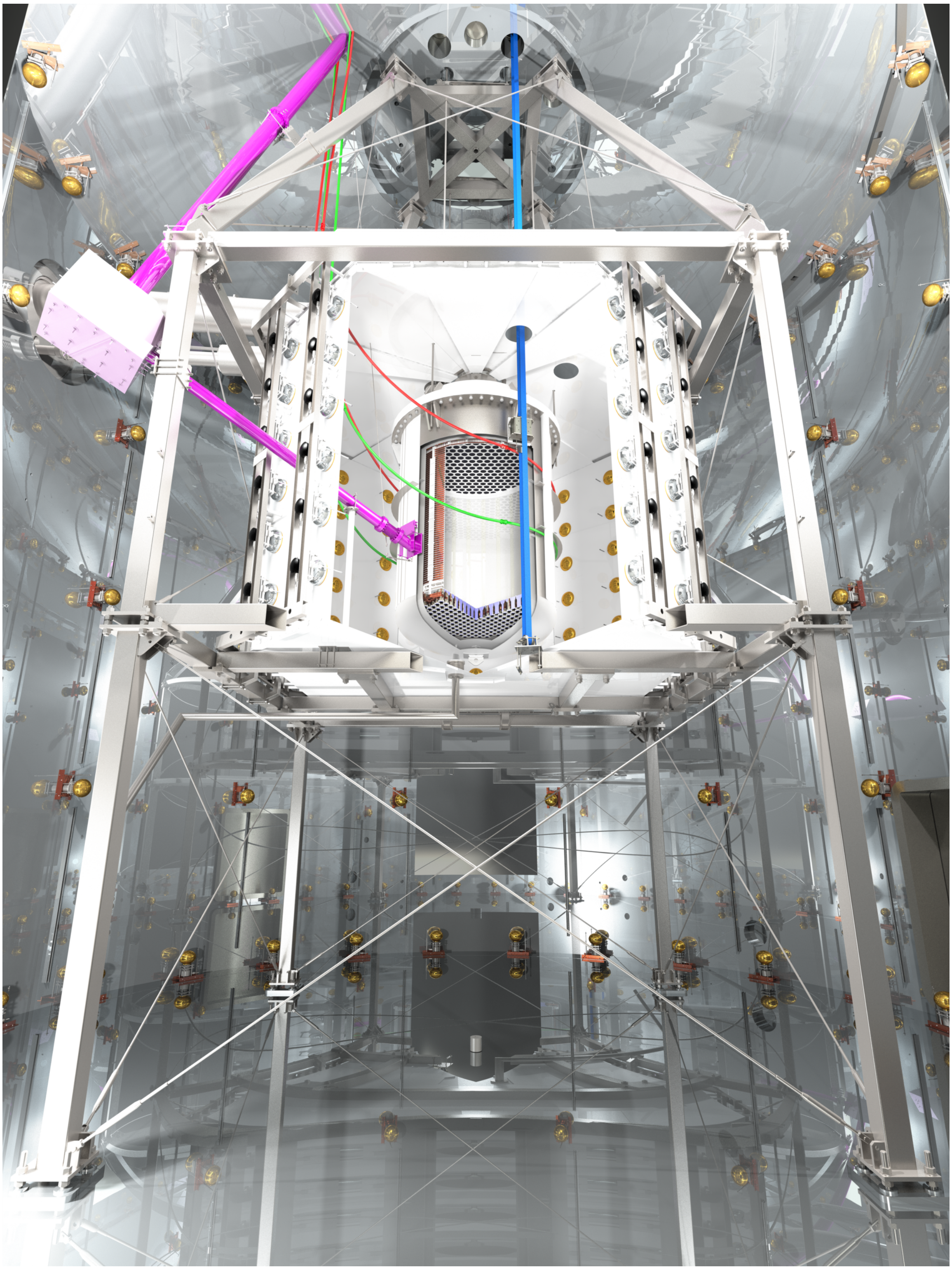

Figure 2.6: (From Collaboration) Rendering of the section of the three nested XENONnT detectors. From the innermost to the outermost: the TPC, the neutron veto and the muon water Cherenkov system.

66.4 cm and a height of about 150 cm. Out of the total 8.6 t of LXe hosted in the cryostat, only 5.6 t are enclosed in the TPC volume outlined by the 48 interlocking vertical PTFE panels designed to compensate for radial thermal shrinkage while guaranteeing light tightness [30]. For light signals readout purposes, 494 (241 + 253) 3" Hamamatsu R11410-21 photomultiplier tubes (PMTs), arranged in a top and bottom arrays, are utilized. The electric field is generated by two stacks of electrode grids, one on the bottom and one on the top of the TPC. The bottom one features the cathode and one screening electrode grid, to protect bottom PMT array from the cathode high voltage, designed to support -30 kV. The top one features a gate, expected to operate at -1.0 kV, the anode, designed to sustain 6.5 kV and eventually, a second screening electrode for PMTs protection. Together, cathode and gate generate the electric drift field through the total 148.6 cm TPC drift length, while gate and anode provide the electric field for electrons extraction within a distance of 0.8 cm. Both the top and bottom screening electrodes are operated at a voltage close to the PMT working one of about -1.5 kV . However, an electrical short between the bottom screen and the cathode, after just two weeks of detector commissioning, prevented the operations to be led in the designed conditions. Thus, for the first science run, the cathode was operated at a voltage of -2.75 kV, while the bottom screen and the gate were respectively set to -2.7 kV and 0.3 kV. Eventually, to mitigate possible burst-like emission of single or few electrons S2 signals, the anode was operated at 4.9 kV [93]. With this electrodes configuration, the operation electric field resulted to be 23 V/cm (about ten times lower than designed), while the average generated extraction field was about 2.9 kV/cm.

Beyond the three nested detectors, the XENONnT experiment proper operations are ensured by other subsystems hosted in a facility building [30]. From the top to the ground floor, in the XENONnT infrastructure (or facility) building, visible in Figure 2.7, the cryogenic system, the gas purification system, the Radon distillation column, the DAQ system, the Krypton distillation column and the liquid purification line are hosted. The optimal operation of these subsystems is ensured by the XENONnT slow control. A more technical description of every subsystem and the XENONnT slow control is provided in [30], and can be also found in specific PhD theses such as [56, 57, 66, 93–95]. For introductory purposes to the author work, in this thesis, only the Radon distillation column, in the next Chapter, is treated in more details.

2.4 XENONnT SR0 and SR1 WIMP Results

After few months of detector commissioning, begun in 2020 during the COVID-19 pandemic, the XENONnT experiment has started taking science data targeting WIMP DM direct detection. Since then, the only occurred downtimes were due to programmed maintenance operations, with the sole exception of a detector malfunctioning provoking the end of the second science run. Up to the time of this thesis writing (end of 2024), two science runs concluded (SR0 and SR1), while a third science run (SR2) is still ongoing. The analysis of the first two science runs led to the exclusion plots of Figure 2.8 [96].

The cumulated exposure of about 3.1 t y, reported in Figure 2.8, is the result of both the LXe mass fiducialization, selecting about 4.00 t out of the 5.8 t total active volume, and the effective live-time corresponding to about 51.4 % of the operation time. This latter reduction for both SR0 and SR1 is dictated by both calibration runs and maintenance periods, reducing the effective exposure from about 1.5 y to only 281.6 d. The periodic calibration runs, as visible in Figure 2.9 referring to XENONnT SR0 and SR1 campaigns, is essential to monitor the detector conditions and characterize its response to different particle interactions. To

Figure 2.7: (Credits to Kexin Liu) Random shifter in LNGS underground Hall B, where the XENONnT experiment is hosted.

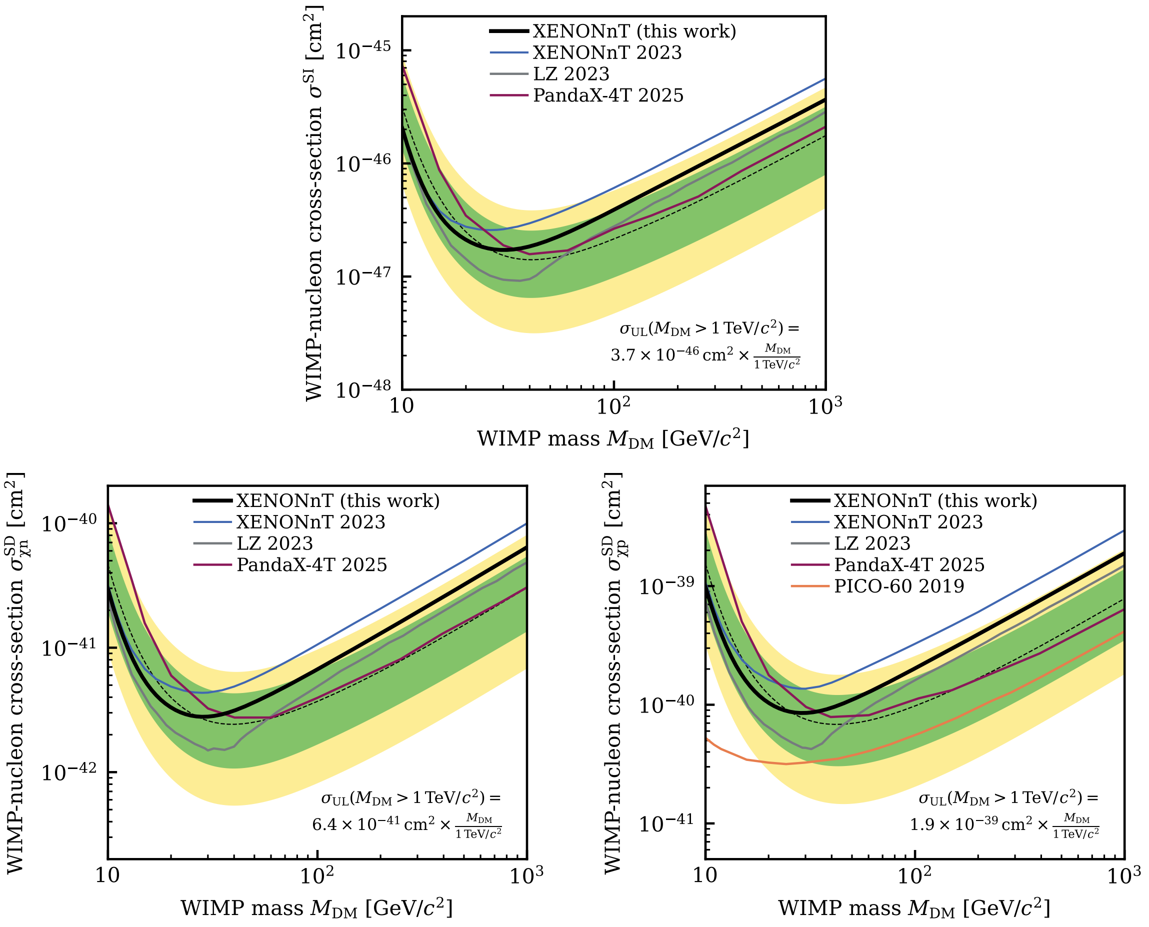

Figure 2.8: (From [96]) (Top) Upper limit on the SI WIMP-nucleon cross-section (90 % C.L.) as a function of the WIMP mass (black line). (Bottom) Upper limits on the spin-dependent WIMP-nucleon cross-section, for the "neutron-only" (left) and "proton-only" (right) cases. In each case, the sensitivity band is indicated by the region containing 68 % (green shaded) and 95 % (yellow shaded) of expected upper limits under the background-only hypothesis as well as their median (dashed line). In addition, published results from XENONnT using only SR0 data [53], LZ [97] and PandaX-4T [98] are shown. For all, a power-constrain limit with a power threshold of 0.16 is used.

this end, different calibration strategies are applied in XENONnT. For the characterization of ER and NR detector responses, also known as ER/NR *band fitting*, calibration runs have been scheduled for SR0 at the beginning and at the end of the science data-taking, while for SR1 accordingly to the availability of the radioactive sources.

2.4.1 Radon Calibrations in XENONnT SR0 and SR1

In order to obtain a full ER detector response characterization of a LXe TPC experiment, few considerations have to be done for the choice of the radioactive sources. For example, an ER source easily uniformly mixing with the LXe volume is preferred, since it allows the full characterization of TPC spatial response. This *internal* calibration can however be only done when the ER source has a sufficiently fast decay time, or it is possible to be distilled by auxiliary LXe circulation systems, to allow the rapid resumption of scientific data-taking. To this end, in the XENONnT experiment, four radioactive sources for ER band characterization have been exploited so far: ^{83m}Kr, ^{37}Ar, ^{220}Rn, ^{222}Rn. These radioactive gaseous sources are

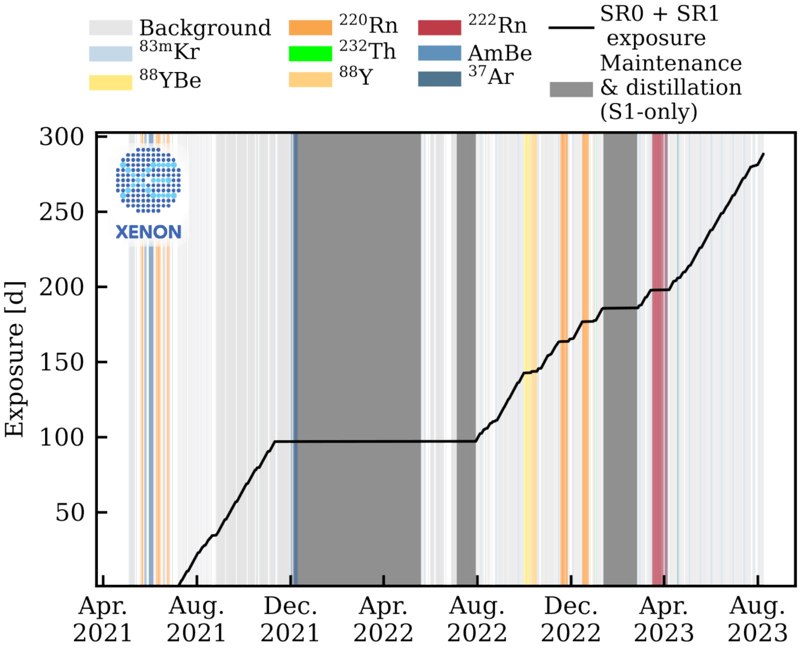

Figure 2.9: (Edited from Collaboration) WIMP SR0+SR1 cumulative Lifetime (black solid line). The growth rate of the science data lifetime is discontinuous due to either foreseen calibration campaigns (represented as colored bands) or general maintenance operations (gray bands).

mixed in the Xenon while flowing in the GXe recirculation system, featuring a calibration source box that serves as an emanation chamber.

The calibration via Radon isotopes allows the introduction of α, β and γ radiation inside the TPC as determined by their specific decay chains, better detailed in Chapter 3. While ^{220}Rn calibration source is produced from Eckert & Ziegler by electroplating ^{228}Th oxide on a platinum [99], ^{222}Rn emanation sample was obtained via implantation of ^{226}Ra ions onto a stainless steel target at the CERN ISOLDE facility [100]. The obtained targets are enclosed in emanation vessels and easily mounted into the calibration source box within the GXe handling system. The injection of Radon isotopes inside the TPC can happen via GXe flow-through, or *flushing*, mode by exploiting a needle valve to provide a regulation, if necessary. Once the Radon injection is terminated, the ^{220}Rn decay rate in the TPC decreases to the background level within few hours [30], while ^{222}Rn demands longer times (given its half-life of about 3.8 d, slightly accelerated in XENONnT thanks to the Radon distillation column) to fully recover the typical science runs event rate.

Differently from ^{83m}Kr and ^{37}Ar, Radon calibration sources provide the full calibration of the ER detector response. Indeed, both ^{220}Rn and ^{222}Rn decay chains feature a Lead beta emitter isotope, respectively ^{212}Pb and ^{214}Pb, that provides a nearly uniform energy spectrum in the WIMP ROI cS1 range, allowing the characterization of the full band. As clearly visible in Figure 2.10, reporting the calibration data taken during SR0 with ^{37}Ar (black points), ^{220}Rn (blue points) and ^{241}AmBe (orange points), Radon data uniformly span the full WIMP ROI cS1 range. A fit to this Radon data-set is thus performed for the detector ER band full characterization, by exploiting the ER emission model described in Appendix A of [89] and in this thesis reported in Chapter 6. To visually show the agreement of the fitted SR0 ER model with ^{220}Rn calibration data, Figure 2.11 is reported, also providing the results of a Poisson χ^2 goodness of fit test performed with the *GOFEvaluation* python package [101].

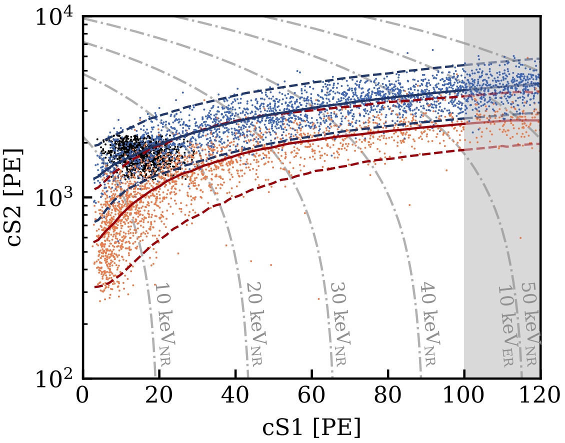

Figure 2.10: (From [53]) SR0 NR and ER calibration data from ^{241}AmBe (orange), ^{222}Rn (blue), and ^{37}Ar (black). The median and the $\pm 2\sigma$ contours of the NR and ER model are shown in blue and red, respectively. The gray dash-dotted contour lines show the reconstructed NR energy (keV$_{\mathrm{NR}}$). Only not shaded events up to a cS1 of 100 PE are considered in the response model fits.

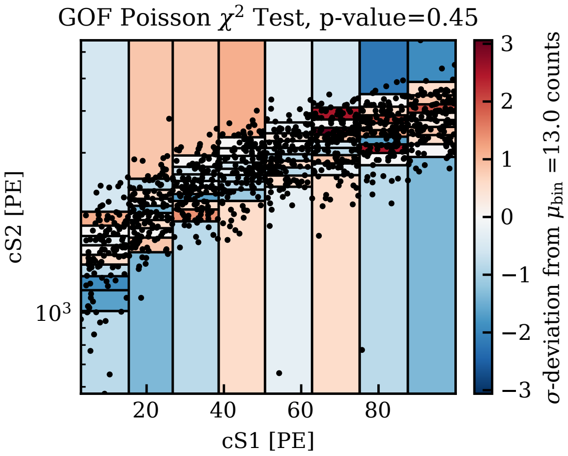

Figure 2.11: Parallel goodness of fit test to the one presented in [89], performed by the author, of SR0 ER model on ^{220}Rn calibration data in WIMP (cS1,cS2) ROI. The analysis has been carried out exploiting the *GOFEvaluation* python package [101]. As in [89], the returned p-value is above the 10 % rejection threshold.

Beyond the basic ER detector response characterization, Radon calibrations are useful to expand the scientific reach of the XENONnT experiment. Indeed, the additional ^{222}Rn calibration of SR1 was suggested and then performed to better constrain the ^{214}Pb contribution, that is the major one, to the total ER dataset. This enhanced understanding of the ^{214}Pb background is crucial for some beyond-WIMP rare-events physics searches in the ER dataset, such as those targeting Solar-pp neutrinos or axions.

Moreover, beyond the constraining and characterization of Lead backgrounds, whose origin is treated in more details in Chapter 3, precision measurements on nuclear transitions can also be achieved. Indeed, spectral shape investigations on ^{214}Bi [102] ground state transition or precision measurements of beta decay branching ratios of ^{212}Pb and ^{214}Pb, here reported in Chapters 4 and 5, have been carried out. With these studies a deeper knowledge of forbidden beta transitions and improvements on precision with respect to the current literature values have been achieved. These studies further demonstrate the vast potential physics reach of LXe TPC technology and hence highlights the importance of a next-generation experiment [29].

3

On the Origin of Lead Backgrounds in XENONnT

The majority of background events in XENONnT WIMP searches is generated by Lead isotopes, more specifically ^{214}Pb, ^{210}Pb and ^{212}Pb. These radioactive nuclei are in turn a product of the ^{232}Th and ^{238}U natural radioactive chains, which are potential natural contaminants of every non-synthetic material. Therefore, to enhance the experimental WIMP sensitivity, all the materials in direct contact with the LXe volume undergone an intense radioassay program and cleaning procedures [103].

The background introduced by ^{232}Th and ^{238}U natural radioactive decay chains inside the XENONnT detector can be grouped into two main categories – since the spontaneous fission is a subdominant process. The first one concerns beta and gamma rays largely produced at the end of these chains, while the second one relates to the high-energy alpha particles that may trigger an (α,n) reaction on Fluorine nuclei present in PTFE (C_2F_4) material. In terms of background contribution, these two categories of events differently impact the region of interest of WIMP searches. The beta/gamma rays increase the rate of ER background by both populating the ER band in the (cS1,cS2) space and the lower cS2 region if the event occurred in the first proximity of the PTFE surfaces. The alpha-generated neutrons, instead, interacting in the LXe active volume may mimic – if not tagged by the neutron veto or rejected by multi-site energy deposition cuts – a WIMP event, lying in the NR band in the (cS1,cS2) space.

In this Thesis the focus is towards the first category of natural radioactivity induced background, which concerns beta and gamma rays mainly originating from Lead isotopes at the end of the ^{232}Th and ^{238}U decay chains. The work presented in the next Chapters is aimed in refining the knowledge on the origins and signatures of these Lead-generated background events. Such improvements will allow developing mitigation techniques for future experiments and upgrading background modeling and rejection tools for the current direct dark matter (DM) analysis.

In this Chapter, after a general introduction about the natural radioactive decay chains in 3.1 and the methods to control their contamination levels in each detector material component in direct contact with the LXe volume in 3.2, the two major mechanism introducing Lead backgrounds inside and in proximity of the LXe active volume are discussed. In 3.3 the Radon outgassing mechanism introducing $^{212/214}$Pb contaminants in the LXe volume is presented, while in 3.4 the Radon progeny plate-out phenomenon is discussed as origin of

Table 3.1: (Edited from [104]) Characteristics of the four natural radioactive decay chains

Longest-Lived Isotope	Half-Life [y]	Final Nucleus	Series Name	Type
^{232}Th	1.42×10^{10}	^{208}Pb	Thorium	$4n$
^{237}Np	2.14×10^{6}	^{209}Bi	Neptunium	$4n+1$
^{238}U	4.47×10^{9}	^{206}Pb	Uranium	$4n+2$
^{235}U	7.04×10^{8}	^{207}Pb	Actinium	$4n+3$

the ^{210}Pb surface background. Finally, in 3.5, a very brief overview about novel strategies to mitigate these background sources is reported.

3.1 ^{232}Th and ^{238}U Natural Radioactive Chains

Natural radioactive decay chains are series of isotopes linked by alpha and beta transitions starting with a very heavy and long-lived progenitor and in most cases terminating with a stable Lead isotope. Since alpha decay is responsible for reducing the mass number (A) by four units, while the beta decay leaves it unchanged, there can only be four independent chains with mass numbers $4n$, $4n+1$, $4n+2$ and $4n+3$, where n is integer. These four series are listed in Table 3.1

The Neptunium series represents an outlier with respect to the others due to two main characteristics. The first one regards the final stable isotope of this chain, ^{209}Bi not belonging to the Lead chemical family. The second one concerns its detectability in nature. It is no more observable in nature given its progenitor short half-life (2.14×10^{6} y) with respect to the Earth's age (about 4.5×10^{9} y [105]).

Except for the Neptunium series, every radioactive chain involves the production of Radon. This gaseous radioactive noble element represent one of the potential break points of these series. Indeed, being volatile, this element has a high probability of escaping its mineral natural sites, breaking the secular equilibrium between the actinides (from U to Ac) and metalloids down to post-transition metals (from At to Tl). The Radon release process, happening from minerals and materials manufactured from rocks and soils, is also known under the name of Radon outgassing mechanism and, among all, is responsible for increasing the air activity in underground caverns and indoor environments.

In the context of XENONnT experiment, as further investigated in 3.3 and 3.4, the Radon outgassing mechanism plays a crucial role. Indeed, Radon outgassing directly introduce ^{214}Pb and ^{212}Pb in the LXe volume, and indirectly causes the deposit of ^{210}Pb on PTFE surfaces. More specifically, the isotopes responsible for these contaminations are ^{222}Rn and ^{220}Rn, that belong to the Uranium and Thorium series, respectively.

3.1.1 Uranium Series

Figure 3.1 shows the Uranium series. This is the longest natural-occurring known series. Beginning with ^{238}U, after an $\alpha\beta\beta$ chain, it features a unique cascade of five successive alpha transitions leading to the production of ^{214}Pb. Then, it proceeds with the $\alpha\beta\beta$ which characterizes the $4n$ and $4n+2$ series, eventually generating the lightest of the Pb radiogenic isotopes.

This series includes both ^{214}Pb and ^{210}Pb, which are responsible for the majority of ER WIMP background and the surface background respectively. Both these two isotopes undergo beta decay into Bismuth, which in turn produces the alpha-emitter ^{214}Po and ^{210}Po. Even

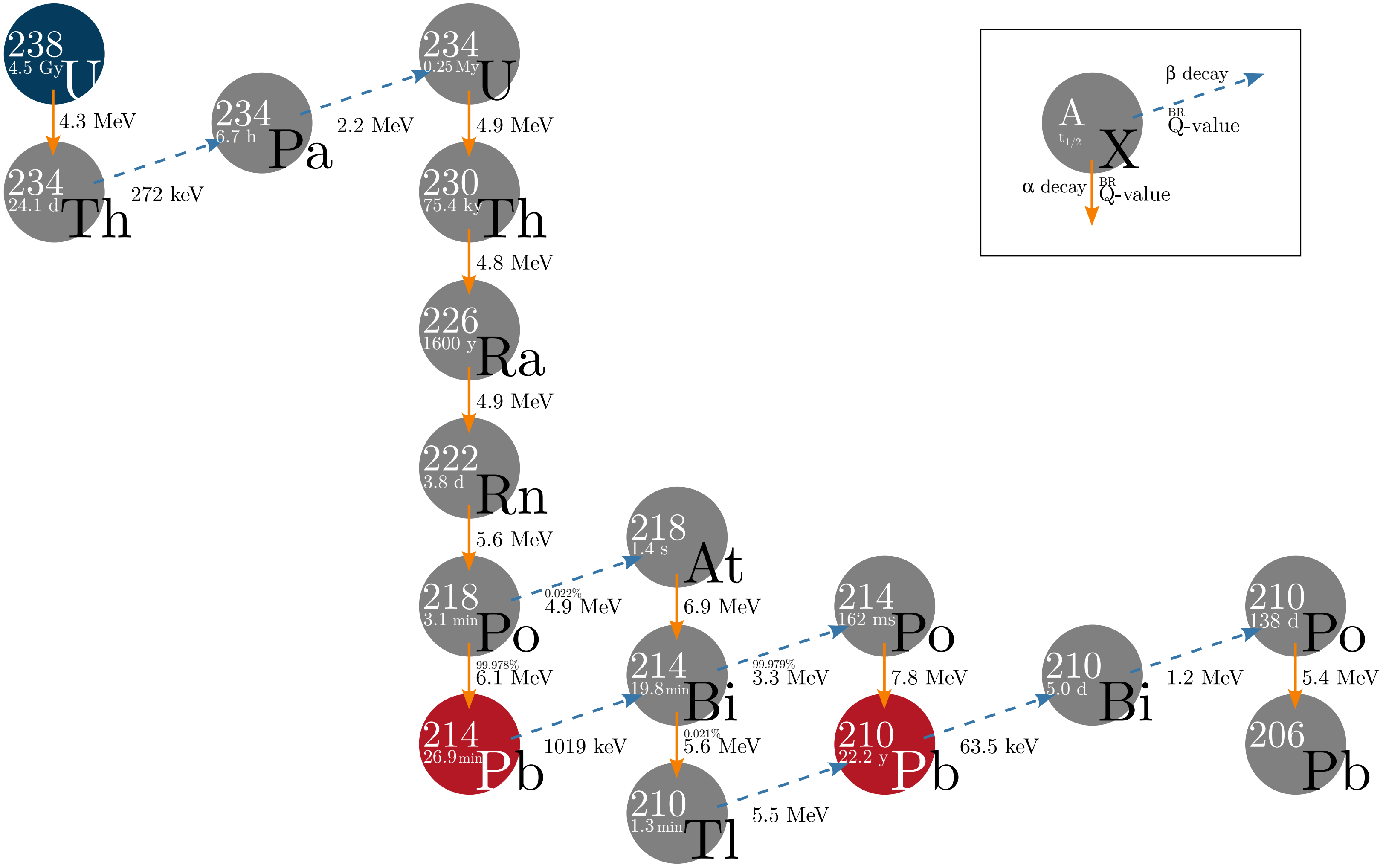

Figure 3.1: ^{238}U natural radioactive chain. As reported in the legend in the top right corner, alpha decays are represented with solid orange arrows, while beta decays are depicted with dashed blue arrows. For each isotope, half-life, Q-value for beta and alpha decays are reported along with their branching ratios. When not specified branching ratios exceed 99.999 %. In red the ^{214}Pb and ^{210}Pb isotopes, responsible for part of ER and of surface background to WIMP searches, are highlighted.

if they decay via beta emission, both ^{214}Bi and ^{210}Bi have a negligible impact on WIMP searches with respect to their Lead parents. Indeed, the first, being followed by the very short-lived ^{214}Po signature, has a very strong signature, featuring monochromatic alpha S1 and S2 signals in the same record window, and hence is easily rejected, while the second, given its beta decay large Q-value, minimally impact the WIMP ROI, whose energy upper limit is of about 10 keV electron-recoil equivalent.

The mitigation strategies to reduce the level of both these Lead contaminants has been studied and refined over the whole Xenon DM project experiments, achieving unprecedented levels of background, which specifically for ^{214}Pb hit values below 1 µBq/kg. This huge achievement opened the possibility to investigate and then exploit a ^{222}Rn source for detector calibration and a refined study on ^{214}Pb decay properties (see Chapter 5 for more details).

3.1.2 Thorium Series

Figure 3.2 shows the Thorium series. Geophysical evidences [106] state that also this series has as progenitor a Uranium isotope, the alpha emitter ^{236}U, constituting the immediate parent of ^{232}Th. However, given its life-time of 2.3×10^7 y [63], comparable to one-hundredth times the age of the Earth, it is no more observable in nature.

This series includes ^{212}Pb which also contribute to the WIMP analysis ER background by means of ^{220}Rn outgassing from structural materials. However, given ^{220}Rn short half-life, the penetration level of ^{212}Pb is drastically reduced with respect to ^{214}Pb, slightly impacting WIMP analysis. The characteristic short half-life of ^{220}Rn not only reduces the possible ^{212}Pb activity in LXe active volume contamination but also allows the usage of a ^{220}Rn source for calibration purposes, via injection given the possible fast recovery of detector condition. The ^{220}Rn calibration data-sets have also been used for nuclear decay properties inference (see Chapter 4 for more details).

3.2 XENONnT Material Radiopurity Control

The easiest way to introduce radioactive isotopes inside a low-background detector is via material contamination. Indeed, the low-energy ^{214}Pb, ^{212}Pb and ^{210}Pb beta/gamma events populating the (cS1,cS2) region of interest for WIMP searches, directly originate from ^{238}U and ^{232}Th natural radioactive chains. These contaminants may be present in detector structural materials or indirectly from their volatile Radon daughters, whose progeny has an enhanced probability to stick on detector PTFE surfaces. The control on these radioactive contaminants in the materials exploited in building XENONnT detector has been achieved by means of three different techniques: the radioassay program, the ^{222}Ra emanation measurements and the surface cleaning procedures.

In the following these three procedures are briefly described, while for a comprehensive review of the XENONnT materials contaminants refer to [103].

3.2.1 The Radioassay Program

The radioassay program, aimed to measure the radionuclide concentrations in the detector materials, was conducted by means of two complementary techniques: gamma-ray spectroscopy and mass spectrometry. The first was performed by exploiting germanium crystal detectors (HPGe) facilities in LNGS, Max Planck Institut für Kernphysik in Heidelberg and Vue-des-Alpes underground laboratory in Switzerland. This technique has been applied for

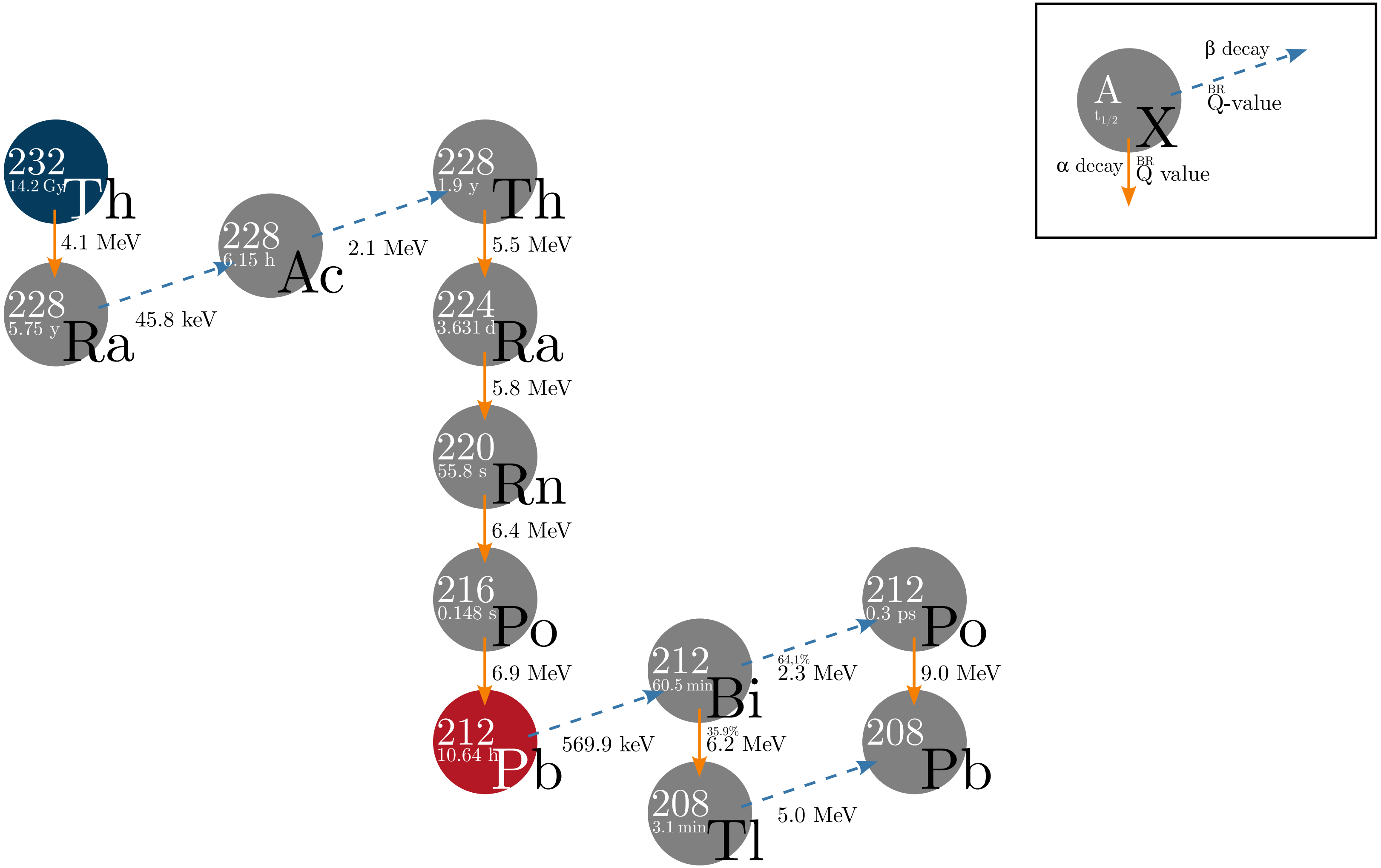

Figure 3.2: ^{232}Th natural radioactive chain. As reported in the legend in the top right corner, alpha decays are represented with solid orange arrows, while beta decays are depicted with dashed blue arrows. For each isotope, half-life, Q-value for beta and alpha decays are reported along with their branching ratios. When not specified branching ratios exceed 99.999 %. In red the ^{212}Pb isotope, partially responsible for ER background to WIMP searches, is highlighted.

Table 3.2: (Edited from [103]) Measured activities of radioactive isotopes in PTFE pillars and panels used in XENONnT TPC barrel construction. All activities are reported in mBq/kg.

Component	Method	^{238}U	^{235}U	^{226}Ra	^{228}Ra	^{228}Th	^{40}K	^{60}Co	^{137}Cs
Panles	HPGe	< 1.0	< 0.07	0.15(3)	< 0.1	< 0.08	0.08(3)	–	< 0.05
	ICP-MS	0.15(7)	–	–	0.03(2)	–	–	–	–
Pillars	HPGe	< 0.8	< 0.05	0.04(1)	< 0.06	< 0.04	< 0.42	–	< 0.01
	ICP-MS	0.26(9)	–	–	0.10(2)	–	–	–	–

the measurement of a wide range of gamma emitters, potentially present in materials samples with mass ranging from few grams up to 100 kg. The Inductively Coupled Plasma Mass Spectrometry (ICP-MS) was used as a complementary technique to measure the amount of long-lived radionuclides present in the materials samples. The results of this radioassay program concerning PTFE pillars and panels, which will be further discussed in Chapter 6, are reported in Table 3.2.

This study has been fundamental for the XENONnT materials selection and the optimization of the Xenon handling and purification systems. In the particular case the Radon distillation system, an additional ^{222}Rn emanation measurement campaign was required to improve its design [103].

3.2.2 ^{222}Rn Emanation Measurements

The emanation rate of ^{222}Rn from detector components cannot be directly inferred from gamma-screening, given the unknown Radon diffusion and potential inhomogeneous distribution of its mother isotope ^{226}Ra. Therefore, in the material selection campaign for the XENONnT construction, which aimed to a ^{222}Rn activity concentration of 1 µBq/kg or lower, a Radon emanation measurement was performed. This study involved a common technique based on adsorbent traps to collect Radon and proportional counters for the measurement [107]. Moreover, these analyses were refined by means of electrostatic Radon monitors and 2-stage extraction method, in order to bypass Xenon outgassing problems. The results of this study were crucial for the optimization of the Radon distillation system – further described in 3.3 – and to estimate the expected overall ^{222}Rn emanation rate in XENONnT detector [103].

3.2.3 The Surface Cleaning Process

The surface cleaning process for the XENONnT detector involves several critical steps aimed at ensuring cleanliness and preventing contamination that could compromise the detector's operation. These steps include thorough cleaning, chemical treatment, and storage procedures, all conducted in controlled environments to minimize the risk of re-contamination. Two cleanrooms with a certified ISO-6 classification, one above ground (AG-CR) and one underground (UG-CR), were utilized for this scope. The AG-CR, equipped with HEPA filters and laminar airflow, was used for large-scale material cleaning, while the UG-CR, built inside the water tank, ensured a clean environment for detector assembly underground [103].

Cleaning procedures vary according to the material, with PTFE receiving particular attention due to two main reasons: its closeness to the LXe active volume, for example the XENONnT TPC barrel is outlined by PTFE pillars and panels, and its susceptibility to attract positively charged Radon daughters, which can lead to plate-out contamination. The cleaning procedure for PTFE and other plastics involved several steps aimed at effectively removing contaminants while preserving the material integrity. Additionally, in order to improve the vacuum ultraviolet light reflectivity, PTFE panels surfaces supposed to face the inner TPC volume, were treated with a diamond-tipped tool. This process also allowed the reduction of ^{222}Rn-induced surface activity, since during this operation up to 1.5 mm of surface layer was removed. More specifically, the diamond-shaved PTFE panels surfaces showed a reduction of about 20 mBq/m^2 compared to the activity detected from untreated surfaces of about 126 mBq/m^2 [103]. Following the procedure described in [103], after an initial cleaning with neutral soap in an ultrasonic bath – not used for PTFE panels to avoid damaging the diamond-shaved surfaces – the plastic materials undergone immersion in a nitric acid solution. The acid solution effectively dissolves impurities and facilitates their removal from the material surface. Thorough rinsing with deionized water followed each cleaning step to ensure the complete removal of residual contaminants and cleaning agents. Additionally, the use of dedicated nitrogen flushed container boxes helped to prevent re-contamination of PTFE and other plastic surfaces with Radon daughters or other impurities. This procedure has demonstrated to reduce by a factor two at most the contamination of ^{210}Pb and ^{210}Po on PTFE and plastic surfaces [108].

3.3 Radon Outgassing Contamination and the Radon Removal System

Detector materials continuously emanate ^{220}Rn and ^{222}Rn. Their impact on the WIMP background deeply differs due to their half-life and hence their grade of penetration inside the LXe active volume. Indeed, ^{222}Rn, with a half-life of about 3.8 d, disperses in the full TPC volume more homogeneously with respect to ^{220}Rn, whose half-life is only about 55.6 s. Emanated ^{220}Rn and ^{222}Rn contribution to the WIMP searches background level is only due to the lowest part of their decay chains involving beta emissions. More specifically, the major contribution is given by ^{214}Pb, from ^{222}Rn, and ^{212}Pb, from ^{220}Rn, beta decays respectively to ^{214}Bi and ^{212}Bi ground states that populate the ER band. The subsequent Bismuth decays are in the majority of cases not temporally resolved as two separate events by the XENONnT DAQ system from the alpha events of the short-lived Polonium isotopes following in the chain (see Figures 3.1 and 3.2 as references). Moreover, for the Uranium series, even if the Bi-Po event does not end on a stable isotope, it leads to the creation of ^{210}Pb, with a half-life of about 22.2 y, that negligibly contributes to the WIMP searches background level.

The location of the potential Radon sources in the cryostat and the adjacent Xenon handling facility, such as cryogenic and purification subsystems, are revealed by Radon emanation measurements (already briefly described in the previous Section). The relative location of these sources with respect to those of the detector and the Radon removal system define their classification. Following the purification flow of Xenon in the XENONnT experiment, the sources that might directly introduce the contaminants inside the TPC are classified as type 1, while those that corrupt the Xenon volume passing through the Radon Removal System (RRS) before entering the detector are of type 2. Moreover, type 1 sources are further grouped into two classes if they are in direct contact with the LXe phase (type 1a) or the gaseous one (type 1b). In Table 3.3, the list of Radon emanating sources along with their classification and ^{222}Rn activity concentration per kilogram is reported.

The XENONnT RRS, which working principle is briefly described in the following paragraph, can achieve a reduction of a factor two in the ^{222}Rn activity concentration due to type 1a sources, if a process flow of 62 kg/h (175 slpm) and a 8.4 t Xenon inventory are assumed. Moreover, an additional factor two is gained when type 1b Radon sources can be converted in type 2 sources by extracting the polluted GXe from the detector, processing it through

Table 3.3: (Edited from [109]) Radon source classification and activity concentration in XENONnT assuming a 8.4 t Xenon inventory

Type	System	^{222}Rn Activity [µBq/kg]
Type 1a	LXe TPC	1.11
	Inner Vessel	0.3
	GXe PUR	0.21
	LXE PUR (bypassing RRS)	0.344
	RRS-outlet	0.19
Type 1b	CRY	1.36
	Cables	1.85
Type 2	RRS-inlet	0.3
	LXE PUR (via RRS)	0.086

the RRS and finally re-inject it in the TPC as LXe.

3.3.1 The Radon Removal System Working Principles

The core of the RRS is a distillation column where the Radon removal takes place. Its working principle is based on the difference in vapor pressure between these two noble gasses, which provides the possibility of extracting purified Xenon in gaseous phase, while trapping Radon atoms in the lowest part of the column. Given ^{222}Rn short half-life, of about 3.8 d, this isotope will eventually decay without the need of extraction. This makes the Radon removal procedure a Xenon-loss free process.

The Radon distillation column operates in a continuous mode. As in the scheme illustrated in Figure 3.3, the RRS column is fed with both GXe and LXe according to the selected operation mode. When LXe operation mode is enabled, type 2 and 1a, if extracting LXe at high flow from the cryogenic system, sources are tackled. The LXe, while flowing towards the bottom part of the column, is heated by the Xenon vapor drifting upwards against the pressure gradient. Xenon, being about ten times more volatile than Radon for a large range of temperature values, tends to leave the liquid phase by populating the gaseous one while drifting towards the reboiler, positioned at the bottom part of the column. In this way, the separation between a highly-purified gaseous phase and a Radon-concentrated liquid one is achieved, by collecting the former at the head of the column and the latter in its lowest part. The so-obtained purified GXe is extracted via a compressor, which pumps it into the reboiler bottom vessel. By flowing in a closed loop into the top part of the reboiler, it also serves as a heater to the Radon-concentrated condensed LXe which can in turn be purified, via evaporation. Eventually the nearly-Radon-free GXe is condensed in the bottom part of the reboiler and fed back into the XENONnT cryogenic system. The GXe operation mode, instead, purifies the Xenon polluted by type 1b sources. This Xenon enters the Radon distillation column from the cryogenic system and follows the same path described before for LXe.

Emanated Radon from type 1b sources is removed with an efficiency close to 100 % by exploiting the RRS in GXe-only mode. This reduces the total Radon activity concentration of about a factor two. Moreover, when operating also in the LXe mode, the RRS can potentially achieve an extra factor two in Radon concentration reduction when the entire 8.5 t Xenon volume is exchanged every 5.5 d.

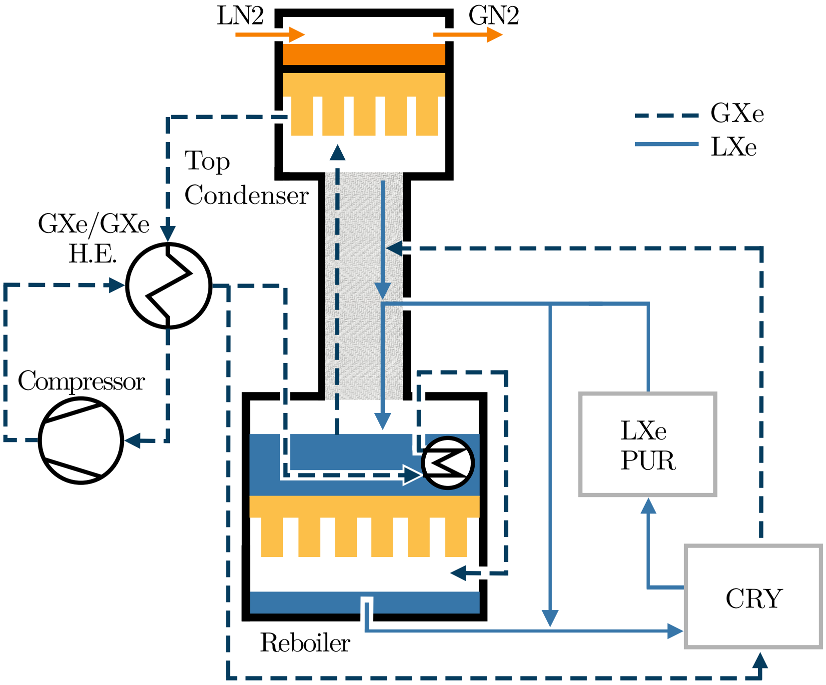

Figure 3.3: (Edited from [109]) Basic layout of the Radon distillation system. The GXe lines are depicted in dashed dark blue, while LXe ones are in solid light blue. For both the flux direction is indicated with arrows. Other XENONnT subsystems, such as the cryogenic (CRY) and LXe purification (LXe PUR) ones, connected to the Radon distillation column are represented with gray boxes.

3.4 Radon Progeny Plate-out Phenomenon on PTFE Reflecting Surfaces

When designing a detector for rare-event physics whose energy region of interest is near the detector threshold, any possible solution to enhance the signal detectability has to be considered. What defines the XENONnT low energy threshold (close to 1 keV) is the limited number of primary scintillation photons detected as S1 signal. This is why the amount of light reaching the PMT arrays has to be maximized. A method to enhance the light collection efficiency exploits high-reflectivity surfaces at the cylindrical edges of the TPC. PTFE material has demonstrated high performances in reflection of a range of vacuum ultraviolet light compatible with Xenon wavelength, of about 175 nm. Indeed, depending on the surface finishing and the surrounding medium, the reflectivity of PTFE is measured to be 37–100 % [110].

The PTFE surfaces, beyond their optical properties, represent a drawback for the experiment. Indeed, they are also responsible for introducing an additional Radon-generated contaminant inside the detector, ^{210}Pb. This isotope accumulates on PTFE surfaces in the detector construction phase, when exposed to Radon-laden air. Indeed, Radon daughters may plate-out onto the surfaces by nuclear recoil in an alpha decay process.

The Radon-daughters plate-out phenomenon is a very well-known effect, whose drawbacks are also observed in many other low-background experiments [111]. However, for those utilizing PTFE materials to outline the active section of the chosen liquid target, this mechanism might produce more background events than expected. Indeed, given the PTFE high probability of carrying negative charges due to triboelectric effect [112], and the likewise high chance Radon daughters have to be positively charged (about 90 % [113]), the plate-out of these latter into the PTFE surfaces is enhanced.

The Radon-daughter contamination level also depend on the activity of this radionuclide in the air to which the surfaces are exposed. This is an additional motivation which stresses the importance of utilizing a high standard classified cleanroom, when the detector is assembled underground. Indeed, if the typical activity of Radon in the air is about 10–100 Bq/m^3, in the underground facilities it can increase to several thousand of Bq/m^3 [111], enhancing the plate-out rate probability. For the XENONnT detector construction phase, as already discussed in Section 3.2, an ISO-6 cleanroom was used [103].

Certainly, the PTFE surfaces may be corrupted also before the detector assembly phase, by means of air exposure during production, transportation and storage. However, as already discussed in Section 3.2, these surfaces have been treated, cleaned and stocked in Nitrogen flushed boxes. The exploited cleaning procedures, demonstrated the possibility of halving the ^{210}Pb contamination and removing up to ten times more that of ^{212}Pb. Moreover, the diamond-shaving process reduces even more the presence of these isotopes by removing the first 1.5 mm surface layer. The storage procedure eventually preserves the cleaned status of PTFE surfaces until the detector assembly phase [30].

3.5 Mitigation efforts for future generation experiments

For next-generation experiments LXe direct DM WIMP searches demand a great suppression of the Uranium generated Lead backgrounds [29]. More specifically, a reduction by one order of magnitude in outgassed ^{222}Rn concentration is demanded. Additionally, the PTFE contamination may play another crucial role if a telescopic design is foreseen in a multi-stage experiment. Indeed, the rate of surface background defines the fiducial volume used for analysis. If the surface-to-bulk ratio is not optimized, which happens only for an equilateral cylinder TPC, a high-rate of surface background may strongly limit the analysis volume and hence the experiment sensitivity.

The reduction of ^{222}Rn easily gained by scaling the mass which goes as $m^{-1/3}$ where m is the LXe detector mass if equilateral cylinder TPC is assumed, is not enough to reach the desired ER background levels (see Figure 3.4). Therefore, different efforts towards developing novel ^{222}Rn mitigation strategies are being investigated. One of the most promising is represented by copper coating of stainless-steal surfaces. Indeed, by covering the Uranium polluted stainless steal surfaces with just 5 µm electrochemically plated Copper, reduction factors of about 130 and 1500 have been observed for ^{220}Rn and ^{222}Rn outgassing rates, respectively [116]. These results clearly meet the requirement of a future large-scale experiment. However, several aspects of this technique still require further investigation, including its scalability and the radiopurity of the coating layer. A second potential method to drastically reduce the Radon background, currently under study at Münster University, is the LowRAD distillation project, that aims in upgrading the distillation systems already in use in the XENONnT experiment [117]. More specifically, the upgrades targets the need of an increased Radon column throughput flow, up to about 750 kg/h, by means of a novel heat pump concept able to provide approximately 20 kW of heating and cooling power for the evaporation and liquefaction.

Concerning the PTFE panels, the current investigations have been focussing on the possibility of reducing the pillars and panels thickness, addressing the need of reduction of NR background to WIMP searches, required for the next-generation experiment. Indeed, the reduction of PTFE material will decrease the number of Fluorine nuclei potentially targets for the (α,n) reaction. The current thickness of PTFE panels has been chosen to optically decouple the instrumented LXe active volume from the skin one that lays inside the cryostat

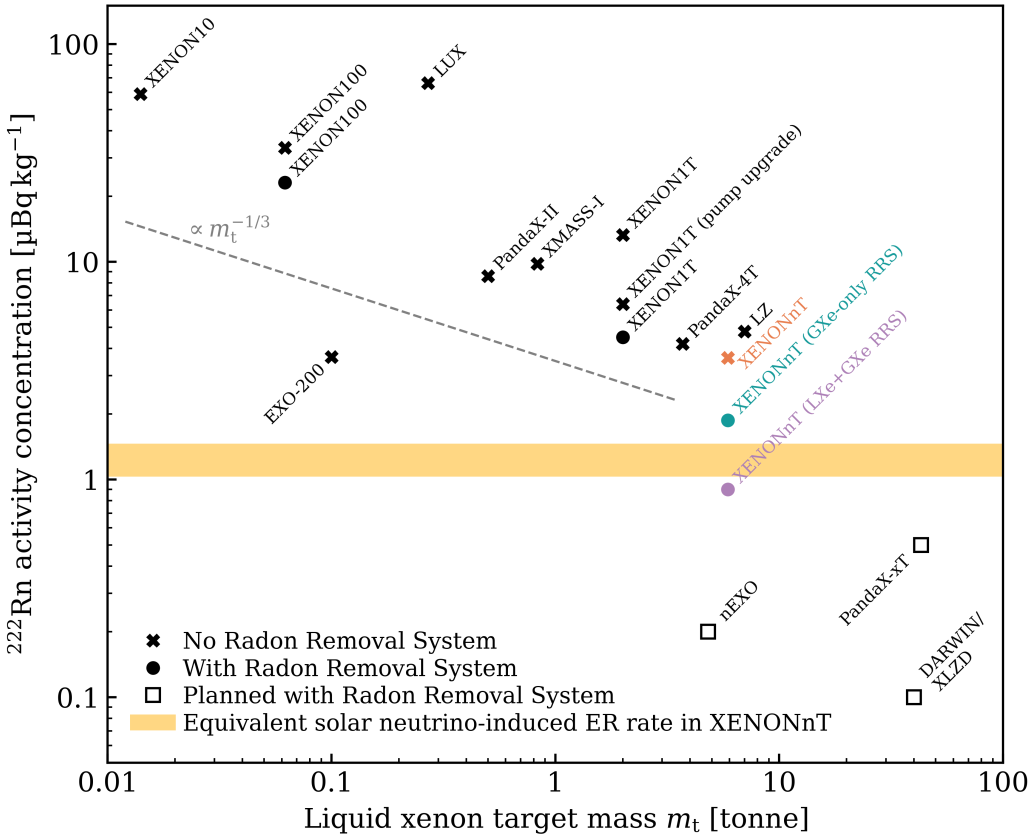

Figure 3.4: (From [114] and [115]) Yamashita plot on ^{222}Rn activity concentration in LXe-based experiments againts their target masses. Achieved ^{222}Rn concentrations of current and past LXe-based experiments are marked as filled circles and crosses. They roughly follow a $m^{-1/3}$ dependence (dashed gray line) expected from the reduction in surface-to-volume ratio. The demanded radon concentrations in next generation experiments (open squares) heavily deviate from the $m^{-1/3}$ trend, thus requiring novel radon mitigation strategies.

but outside the TPC. To better address this issue a study on VUV light PTFE transmittance has been conducted [118]. The obtained results show that few mm PTFE thickness would be sufficient to optically decouple detector regions from each other, reducing the (α,n) reaction and hence the foreseen NR background.

4

^{212}Pb Branching Ratios Measurement

XENONnT is a low-background experiment for direct WIMP searches. Nevertheless, thanks to its unprecedented levels of radiopurity, this experiment can also be exploited for nuclear physics studies. Indeed, by operating the Radon Removal System (see Chapter 3) and having carefully selected the experiment structural materials, the nuclear physics energy region of interest (up to about 3 MeV) is clean enough to perform precision measurements, such as ^{214}Bi first forbidden ground state or ^{136}Xe double beta decay spectral shape analyses.

Among these studies, the measurement of ^{212}Pb branching ratios to ^{212}Bi excited states with the signals and backgrounds model technique demonstrates the feasibility of utilizing such a low-background experiment to access with enhanced precision these nuclear transition values. This study, thanks to a simulation and a background modeling software *ad hoc* developed, accesses the ^{212}Pb nuclear transition values via a binned fitting procedure exploiting the ^{220}Rn calibration data-set.

This Chapter presents the methodology and the results of the ^{212}Pb branching ratios study. Firstly, the physics goal is addressed in 4.1, by presenting the current status of the existing literature. Then, after a detailed description of the modeling and inference procedure in 4.2, the data selection criteria and the simulated cut efficiency curves are presented in 4.3. Eventually, the background and signal components along with the results and a discussion about possible systematic sources are respectively presented in 4.4 and 4.5. Unless otherwise specified, all material presented in the following Chapter is original and has been produced by the author of this Thesis.

4.1 ^{212}Pb Branching Ratios Measurement with XENONnT

When a nucleus decays via beta emission, there is a non-negligible probability of producing an excited daughter nucleus. This latter eventually transitions to its ground state via gamma emission, typically occurring on the electromagnetic timescale (10^{-12} s). The set of probabilities associated with the production of the daughter nucleus in specific excited states defines the beta decay scheme of an isotope. Except very atypical cases (see the ^{14}C [119] as an example), this latter is at first order determined by the variation of the total nuclear quantum numbers. Specifically, the variation of nuclear angular momentum (J) and parity

Table 4.1: (Edited from [120]) Selection rules for nuclear beta decay

Decay Type	ΔJ	$\Delta\pi$
Superallowed	$0^+ \to 0^+$	$+$
Allowed	$0, 1$	$+$
First forbidden	$0, 1, 2$	$-$
Second forbidden	$1, 2, 3$	$+$
Third forbidden	$2, 3, 4$	$-$
Fourth forbidden	$3, 4, 5$	$+$

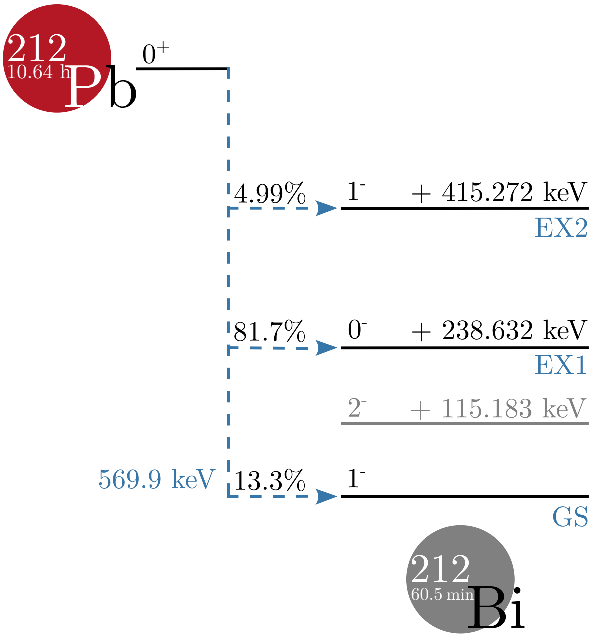

Figure 4.1: ^{212}Pb decay scheme, reporting the Q-value (in blue on the bottom left of blue dashed decay path), ^{212}Bi energy level labels (in blue below the solid black line), their relative branching ratios (above blue dashed arrows), their excitation energy values (in black above the relative level line) and nuclear quantum numbers for angular momentum and parity (reported in the form J^π always on the relative level line). All values in the scheme are taken from [63].

(π) identifies different classes of beta transitions, here reported in Table 4.1. Where the ground-state-to-ground-state transition requires significant changes in angular momentum and/or parity (forbidden transition), there is, if feasible, a large probability for the parent nucleus to access the daughter isotope excited states, reducing the total quantum numbers variation.

^{212}Pb undergoes beta decay into ^{212}Bi. As deducible from the scheme in Figure 4.1, the transition onto any possible accessible state of Bismuth daughter nucleus requires a nuclear momentum and parity variation with respect to the Lead parent isotope, resulting in three different first forbidden beta decays. For the sake of simplicity, in the following these three different transitions from ground to the most energetic Bismuth state will be respectively labeled as GS, EX1 and EX2 (see Figure 4.1 as illustrative reference).

All the values reported in the decay scheme of Figure 4.1 are the recommended ^{212}Pb nuclear values reported in [63] by the laboratoire national de métrologie et d'essais-Laboratoire National Henri Becquerel (LNHB). Another common reference, in this field of study, is the Nuclear Data Sheet (NDS) [121]. Table 4.2 reports as a comparison the LNHB and NDS

Table 4.2: Comparison between LNHB ^{212}Pb nuclear recommended values from [63] and NDS ones from [121].

	LNHB (Q-value 569.9(19) keV)		NDS (Q-value 569.1(18) keV)	
	BR [%]	Excitation Energy [keV]	BR [%]	Excitation Energy [keV]
GS	13.3(11)	0	13.7(10)	0
EX1	81.7(11)	238.632(2)	81.5(10)	238.632(2)
EX2	4.99(21)	415.272(11)	5.01(7)	415.272(11)

recommended values for transition Q-value, branching ratios and excitation energy levels for ^{212}Pb beta decay.

The recommended values for ^{212}Pb to ^{212}Bi beta decay branching ratios reported in both references are indirectly calculated from gamma and internal conversion intensities. These latter are either theoretically estimated, as in [122], or experimentally measured, such as in [123], where silicon- and germainum-based detectors have been exploited. The last updates of these measurements have been done in the 90s [124].

The novelty of measuring these values with the XENONnT experiment stands in two different aspects. Firstly, the technique differs from the simple gamma spectroscopy used for the literature reference values and relies on signal and background models method for the full beta(+gamma) ^{212}Pb spectrum. Secondly, this measurement represent a direct assessment to the ^{212}Pb beta decay branching fractions. This results particularly interesting for the ground state branching ratio estimate, since a direct measurement would reduce its relative uncertainty (currently about 7.7 %, as stated in Table 4.2).

4.2 The high-energy modeling and inference framework

Being the XENONnT experiment optimized for low-energies (1–10 $\mathrm{keV_{ee}}$) WIMP nuclear recoil signal searches, an *ad hoc* fitting framework for higher energy ranges was developed for the scope of nuclear physics studies, such as the ^{212}Pb branching ratio analysis or the nucleon disappearance search, already reported in [56]. Moreover, differently from dark matter searches where the disentangled information of energy released in ionization and excitation channels is of primary importance for background rejection, high energy nuclear physics studies can be performed in the combined energy scale (CES) observable. This observable is built by means of a linear combination of the excitation (cS1) and ionization (cS2) signals. More specifically, we can write:

$$\mathrm{CES} = W\left(\frac{\mathrm{cS1}}{g_1} + \frac{\mathrm{cS2}}{g_2}\right), \tag{4.1}$$

where $W = 13.7$ eV is the mean energy to produce a charge or light quanta (assumed to be equal to 13.7 eV), g_1 is the photon detection efficiency and g_2 the charge amplification. These latter two parameters are extracted by a common procedure exploiting calibration and activation monochromatic sources, from ^{37}Ar K-shell transition at 2.96 keV up to ^{12}C nuclear gamma de-excitation at 4.439 MeV. Each of these monochromatic sources, present monochromatic S1 and S2 responses that can be fit with skewed Gaussian distributions. These fits return the values for the light (L_y) and charge (Q_y) yields for each source and constitute a point in the calibration plot, also known after the name of Doke plot. As an example, Figure 4.2(a) reports the Doke plot for the first XENONnT science run SR0.

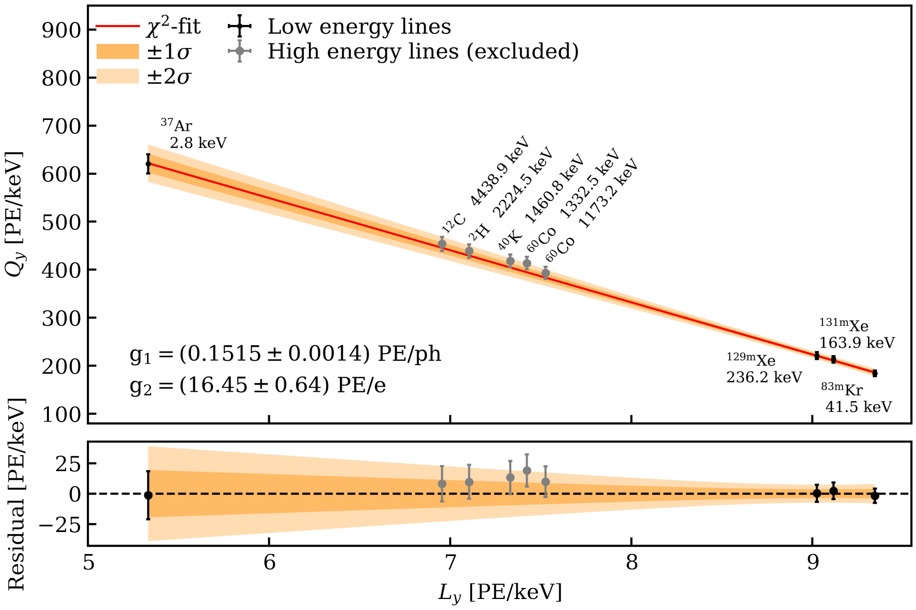

(a) (Edited from [86]) SR0 Doke plot.

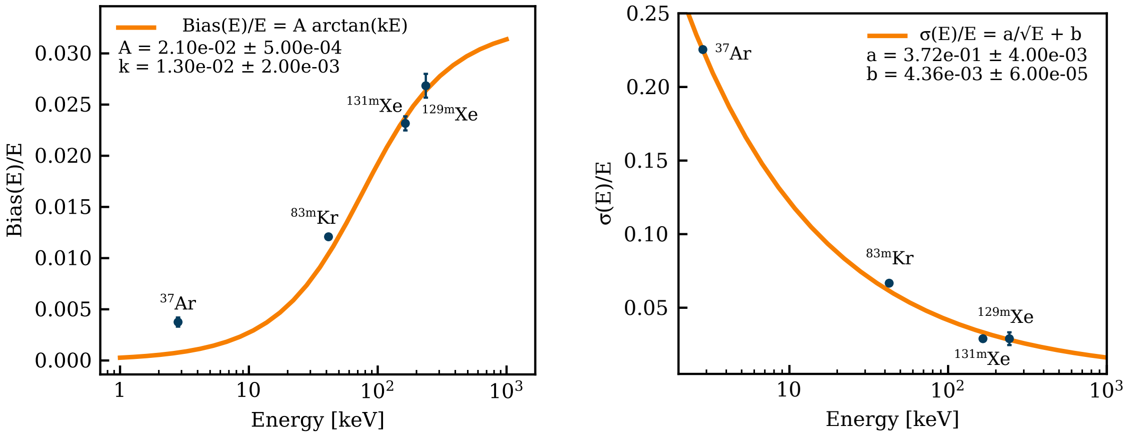

(b) SR0 CES bias, defined as Bias = CES − E_{True}. Arctangent fit function was empirically chosen.

(c) SR0 monochromatic sources energy resolution accessed via skewed-Gaussian peaks fit.

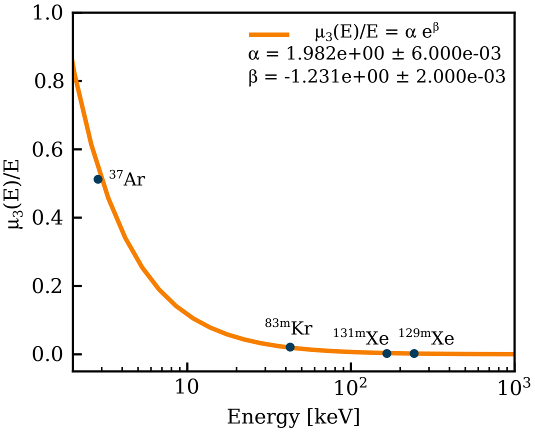

(d) SR0 monochromatic sources energy skewness accessed via skewed-Gaussian peaks fit.

Figure 4.2: (Edited from [86]) SR0 XENONnT detector response calibration functions in the true Energy variable. Doke plot (a), the energy bias (b), the resolution (c) and the skewness (c) obtained by studying the nearly-monochromatic peaks of ^{37}Ar, ^{83m}Kr, ^{131m}Xe and ^{129m}Xe.

One may wonder how it is possible for such an optimized WIMP detector to allow the study of such a wide energy range. The answer is that the XENONnT analysis tools rely on PMT/ADC saturation correction algorithms that have been refined by exploiting the low-gain PMT channels optimized for the high-energy read-out [86, 125]. Despite the visual agreement (see Figure 4.2(a)) of the high-energy sources points within the linear interpretation of the detector response, once the CES observable is compared with the true energy scale, a bias towards higher values shows up, as clearly reported in Figure 4.2(b). In order to take into account this feature in the modeling and fitting procedures in the CES observable space, a parametric arctangent model constrained to equal 0 at 0 keV is optimized against the observed bias, as described in [86]. The bias function hence results:

$$\mathrm{Bias}(E)/E = A \arctan{(kE)}, \tag{4.2}$$

where A and k are optimized via fit procedure.

Moreover, by analyzing in the CES space the monochromatic sources by means of skewed-Gaussian fit it is also possible to give an estimate of the resolution and skewness trends with respect to the true energy. The first (see Figure 4.2(c) as reference), as expected is the linear combination of the statistics term and the constant one:

$$\sigma(E)/E = a/\sqrt{E} + b, \tag{4.3}$$

where a and b are optimized by the fitting procedure. The electronic noise contribution, scaling as E^{-1}, is assumed negligible. Instead, the skewness is important below 30 keV (see Figure 4.2(d) as reference), where the detector response is not purely Gaussian. The variation of the skewness parameter with respect to energy is interpolated with an exponential function:

$$\mu_3(E)/E = \alpha e^{\beta}, \tag{4.4}$$

where α and β are optimized via fit procedure.

4.2.1 The Backgrounds and Signal modeling Module

Background and signal models are built starting from an input that can either be a theoretical value/template or the result of a simulation. The theoretical value/templates are exploited if a monochromatic source or a specific theory model for any contribution has to be taken into account. The simulation-driven model is exploited in all other cases and is produced via GEANT4. By exploiting the output of the tailored GEANT4-based Collaboration Monte Carlo software as input to the *epix FastSim* simulator [56, 126–128], is possible to cluster the energy depositions and give a raw estimate of the S1 and S2 signals via NEST model. Indeed, as better detailed in [127] an empirical match between observed data and *epix* prediction for S1 and S2 signals was found once the energy depositions simulated in GEANT4 were grouped in clusters within bubbles of space and time radii of 5 μm and 10 ns. After the energy depositions clustering step the *FastSim* module reconstructs the simulation template in the true energy (E_{True}) observable space. A novel method based on more physics-driven lineage clustering is now under investigation and could further improve the quanta generation mechanism interpretation of the XENONnT detector response.

The resulting theoretical or simulated spectra are then the input for the model generator module, as illustrated in the scheme of Figure 4.3. After the rebinning operation to match the user analysis configurations in CES space, the template is smeared with the detector response function, represented by a skewed-Gaussian distribution with resolution and skewness as in Figures 4.2(c) 4.2(d). In order to move from E_{True} into the CES observable space, the bias

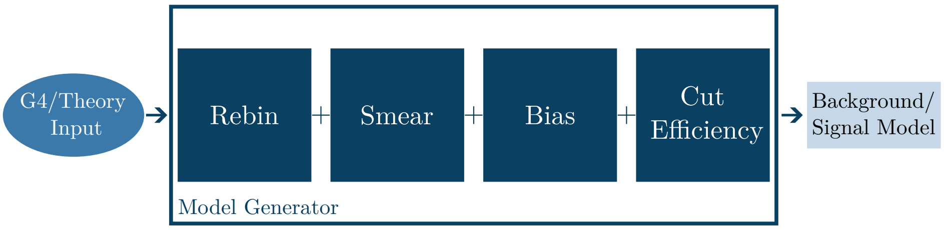

Figure 4.3: Scheme for background/signal model generator module of the high-energy CES modeling and inference software. The oval box represents the input object, square ones symbolize the modules blocks and the rectangular box depicts the output.

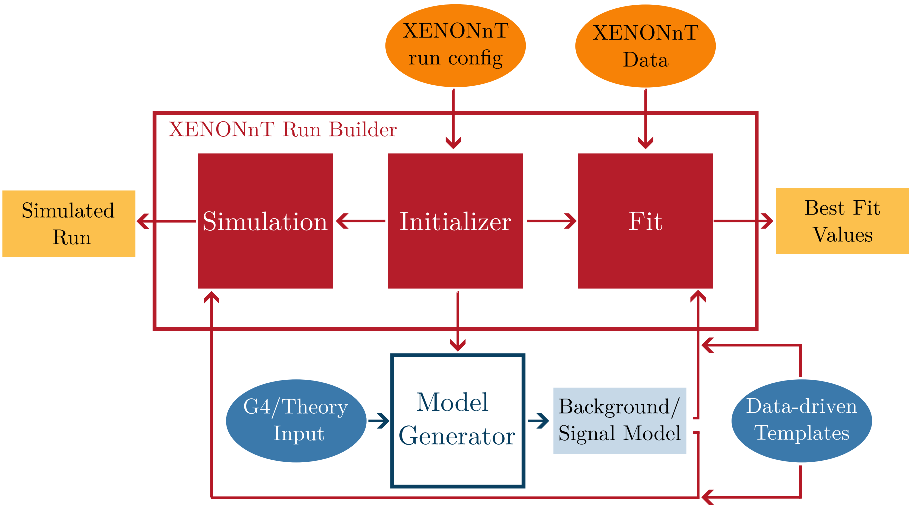

Figure 4.4: Scheme for XENONnT run builder module. The oval boxes represent input objects, square ones symbolize the modules blocks and the rectangular boxes depict the outputs.

function of Figure 4.2(b) is applied. Finally, the template is multiplied by the cut efficiency, determined with a dedicated study.

The obtained background or signal model represents only one component in the contribution list that the user provides as input to the XENONnT run builder module, that also handles simulation and fitting processes. The run builder module is further discussed in the following paragraph.

A future upgrade for the model generator module foresees the inversion of the first two stages. Rebin and smear operations could be swapped in order to provide more reliable modeling also in the neighborhood of the low energy threshold. For the purpose of ^{212}Pb branching ratios measurement, this upgrade was found to apport negligible differences in the study outcome, while heavily increasing the computational costs of the fit procedure.

Additionally, it is possible to include data-driven models, that do not require the detector response folding process. For this reason, these templates are prompted to the XENONnT run builder module bypassing the model generator one. This feature is of crucial importance for this study as better explained later in this Chapter.

4.2.2 The Fitting Procedure

The fitting procedure is handled by the XENONnT run builder module of the high-energy modeling and inference framework. Beyond fitting, this module can also generate simulated XENONnT data for sensitivity studies. In Figure 4.4, the scheme of this module is provided.

The user-defined XENONnT run configurations in input to this module are:

- `components`: list of background and signal components contributing to the run to simulate or analyze,
- `activity`: dictionary providing the (expected) activities and related uncertainties for each component,
- `efficiency`: dictionary specifying the cut efficiency for each component,
- `livetime`: XENONnT run livetime,
- `mass`: LXe mass of the considered XENONnT fiducial volume (FV),
- `ROI`: lower and upper limits for the energy region of interest for the study,
- `energy step`: bin width value.

Some other extra sets of user-defined configuration inputs are available and set for this analysis to the default SR0 values in the initialization process.

The fit module proceeds with building a binned logarithmic likelihood exploiting the iMinuit package. This log likelihood, being in its default configuration set to the Poisson likelihood chi-square (χ^2_λ) of [129], allows the inclusion of constraints useful for XENONnT data fit where the contamination levels of some components can be known by parallel analyses with good precision. Moreover, in order to dump potential systematic effects, some nuisance parameters can be included and optimized in the fit procedure. However, in this case, the fit block will access the model generator module more often, increasing the required computational cost. This problem can be bypassed in future releases by including anchor points for nuisance parameters that can greatly reduce the time of execution.

4.3 Data selection and cut efficiency curves

For the ^{212}Pb branching ratios study the XENONnT first science run (SR0) along with its ^{220}Rn calibration campaign is exploited (refer to Chapter 2 for a brief description of the XENONnT calibration system and procedures). However, differently from what is represented in Figure 4.5, only about half of the full ^{220}Rn calibration data-set can be exploited for this study. This is a consequence of the usage of a DAQ low-pass filter that was exploited to reduce the data acquisition rate, without affecting the low-energy range for WIMP ER band calibration.

In order to perform the ^{212}Pb branching ratios measurement, the selected data-sets have to be further cleaned in order to remove spurious nonphysical pulses and reduce undesired backgrounds. To this purpose, an optimized list of selection rules (in the following referred as *cuts*), has been investigated. Among these, the choice of the analysis fiducial volume, which is the geometrical cut applied to reduce the impact of external backgrounds, is firstly described. Then, the quality cuts, selecting specific sub-sets of events based on the properties of their S1 and S2 signals, are discussed.

4.3.1 Fiducial volume optimization

The ^{212}Pb signal is uniformly distributed in the whole TPC. This is a consequence of the homogeneous diffusion of ^{220}Rn calibration source in the LXe volume (see Chapter 2 for a brief

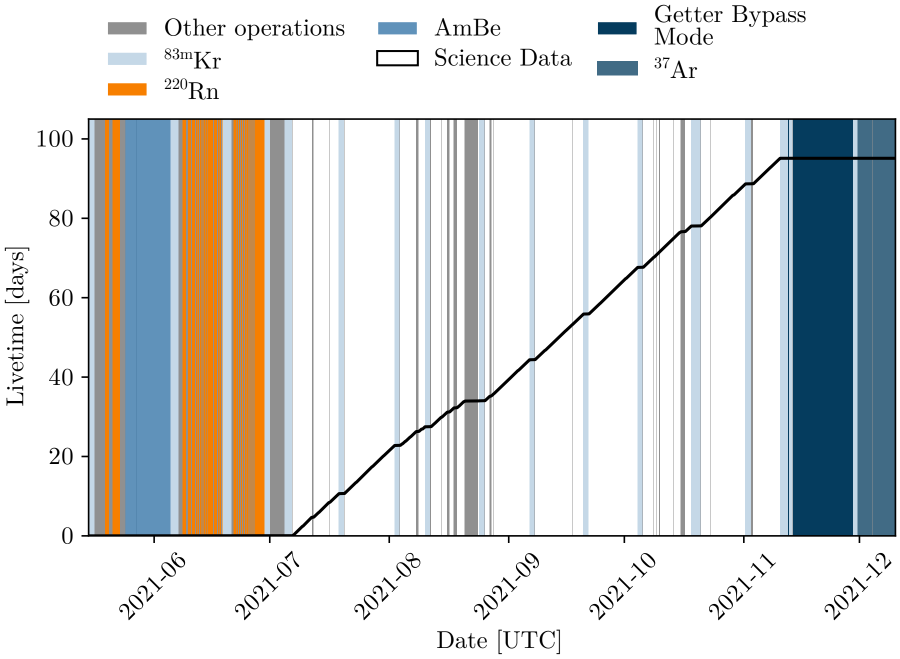

Figure 4.5: (Edited from [86]) WIMP SR0 cumulative Lifetime (black solid line). The growth rate of SR0 lifetime is discontinuous due to either foreseen calibration campaigns (represented as colored bands) or general maintenance operations (gray bands).

description of the calibration system). This signature does not characterize every radioactive background polluting the energy region of interest to this study. Indeed, the XENONnT cryostat along with other structural materials, surrounding the LXe active volume, introduces several radioactive contaminants that trigger events inside the TPC. Among these, there are evidences of ^{232}Th and ^{238}U radioactive chains contributions as well as ^{60}C and ^{210}Pb. All these backgrounds are generally referred as *material* or *wall* backgrounds, according to the analysis. XENON studies refer to *material background* when a ROI upper limit exceeds 50 keV where radioactive contaminants from cryostat dominate. Otherwise, for example in WIMP searches, it is labelled as wall or *surface* background and it is mainly due to ^{210}Pb plated onto the Teflon panels outlining the TPC borders [130]. For a more comprehensive and detailed description of the wall background, refer to Chapter 6.

For the WIMP studies [131] the surface background is modeled with a data-driven approach by exploiting unblinded side-bands and its impact is reduced by means of the FV cut. Conversely, for the ^{212}Pb branching ratio studies it is possible to apply an alternative technique. Since, for this particular study, the signal is produced by the ^{220}Rn calibration source, the SR0 runs collected for WIMP searches can be used as a template for every constant XENONnT background. To do so, the SR0 background data-set is cleaned by means of the same quality cuts and binned in the CES observable space in the same manner as the ^{220}Rn calibration one.

With this method, one could think that, given the large lifetime of radioactive isotopes from material background, every contribution with non-uniform spatial distribution is fully modeled. However, the ^{220}Rn source itself generates two spatial dependent background, in the following referred as *Bismuth* (or ^{212}Bi) *skin* and ^{212}Pb *PTFE*.

The Bismuth skin source-induced background is due to the production of ^{212}Bi and its daughter decay chain from the decay of ^{212}Pb. ^{212}Bi, as reported in Figure 3.2, can either decay via beta or alpha transitions respectively into ^{212}Po (with a branching ratio of about 64.1 %) and ^{208}Tl (with a branching ratio of about 35.9 %). In principle, also the first decay mode of ^{212}Bi and the beta decay of ^{208}Tl could contribute as backgrounds in the energy region for ^{212}Pb study. However, on the one hand, the first is vetoed by the subsequent alpha decay of ^{212}Po. Indeed, the short half-life of ^{212}Po (0.3 ps), the narrow mean free path of alpha particles in LXe and the architecture of the XENONnT event reconstruction algorithm cause the reconstruction of ^{212}Bi S1 and S2 pulses in the same analysis window of the following ^{210}Po alpha decay. Therefore, this distinct signature can be exploited as veto and prevent the reconstruction of ^{212}Bi bulk events inside the ^{212}Pb study energy region of interest. On the other hand, the TPC bulk ^{208}Tl contribution is similarly vetoed by the daughter nucleus gamma de-excitation cascade which in the 99.8 % of cases generates the characteristic 2615 keV gamma. Simulations of this possible background contributions, have excluded the ^{208}Tl contribution in the ROI of ^{212}Pb study.

This rejection of ^{212}Bi events occurs for events inside the TPC volume. However, when these decays happen just outside the Teflon walls but still inside the cryostat, they constitute the Bismuth skin background. Indeed, even if the alpha and beta particles emitted in the ^{212}Bi decay can hardly penetrate the Teflon wall or survive the high grammage of LXe material, the gammas emitted in the following de-excitation processes have a non-negligible probability of triggering events inside the XENONnT TPC. Therefore, the consequent signature in the CES observable space will be the presence of these isotopes gamma peaks lying upon a continuous background coming from multiple site energy losses.

A second source-induced background is due to ^{212}Pb isotope plating out into Teflon surfaces. This phenomenon, enhanced by the high probability Radon daughters have to be positively charged and the Teflon triboelectric effect [112], generates a ^{212}Pb source layer at the borders of the TPC. The consequences of this accumulation are similar to the Bismuth skin in terms of spectra shape, except for its proximity to the active LXe volume, which introduce more events at lower energies.

Bismuth skin, ^{212}Pb plate-out on Teflon and materials contribution, included in SR0 background model, are not the only spectral components in the ^{212}Pb study energy region of interest showing a spatial dependence. Indeed, the same feature is associated with the emission of a gamma consequently to the beta decay of ^{212}Pb when occurring in the proximity of TPC borders. In particular, the emitted gamma may escape the instrumented LXe volume introducing a slight spatial dependence on the shape of the ^{212}Pb energy spectrum.

These spatial dependent components may eventually affect the evaluation of the ^{212}Pb beta decay branching ratios, if not correctly modeled. More specifically, since the target of this study is to achieve for the first time via direct assessment a more precise measurement of the ^{212}Pb ground state branching ratio, the impact of these spatial backgrounds has to be evaluated and as much as possible limited in its specific region of interest. However, at the same time, it is worth to optimize the FV so that the estimated relative uncertainty of the ^{212}Pb ground state branching ratio is minimized. For these reasons, in order to find the optimal compromise between analyzing the largest possible statistics and rejecting the most significant potentially-harmful background, the following figure of merit is defined [132]:

$$\mathrm{FOM} = \frac{S}{\sqrt{S+B}} \propto \frac{M}{\sqrt{\sum_{i \in \mathrm{ROI}} N_i}}, \tag{4.5}$$

where S and B are the signal and background rates. Being the signal homogeneously distributed in the active volume, the FOM is proportional to the considered LXe mass M, scaled by the square root of the sum over i of the N_i, the full ^{220}Rn calibration run template i-th bin counts in the ground state-only ROI. This latter is defined to range between the

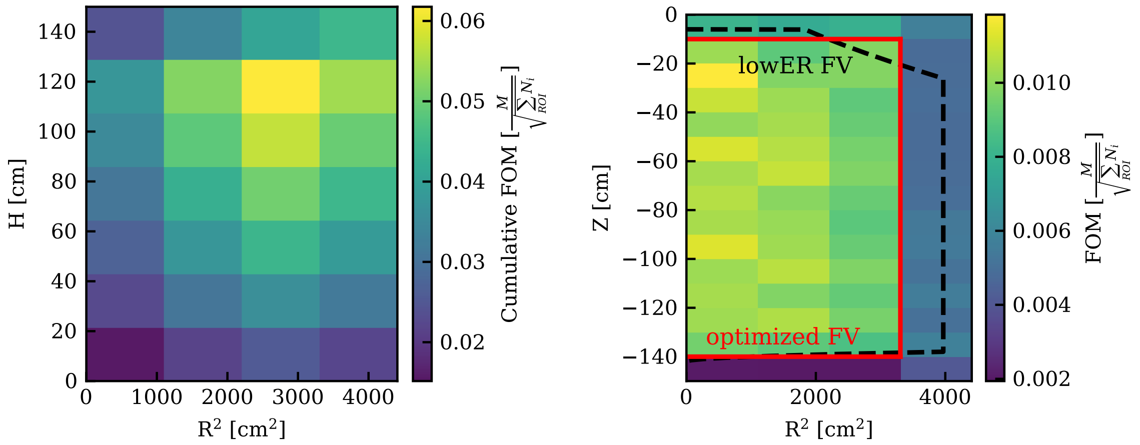

(a) FOM for cylindrical FV different heights and radii.

(b) Optimized FV.

Figure 4.6: Fiducial volume optimization by maximization of FOM of Equation 4.5. Left (Figure (a)) FOM computed for different cylindrical volume data selections; the computed FOM is referred to the cylindrical fiducial volume with radius and height indicated by the top-right corner of each rectangle. Right (Figure (b)) FOM computed in equal-mass TPC portions (color map), optimized fiducial volume for ^{212}Pb branching ratios analysis (red solid line) and low-energy electron recoil analysis FV [133].

arbitrarily-chosen analysis low CES limit, 30 keV, and the ^{212}Bi first excited state energy gap, 1-σ smeared and biased accounting the detector response, at about 244 keV. In order to account both S and B components, the considered template include the full simulation of ^{212}Pb (with branching ratios set accordingly to the Collaboration default values), the Bismuth skin and the SR0 background model. Other background contributions, such as $^{131\text{m}}$Xe, were not included given their very strong signature in the CES observable space, while ^{212}Pb PTFE was not considered since its presence was discovered in a later step.

For simplicity, the FV is constrained to be cylindrical and centered in the TPC center. Therefore, by varying its height and radius, a set of LXe masses and spatial-dependent background rates are obtained. The FOM computed for a set of cylinders with squared radii (heights) extending from 0 cm^2 (cm) up to the TPC borders 4408.96 cm^2 (150 cm) is depicted in Figure 4.6(a). The raw discretization used in binning the full TPC volume has been exploited not to be biased by any statistical fluctuation of the templates. As deducible by this plot, the FOM reaches its maximum for a FV characterized by a radius 3306.0 cm^2 of and a height of 130 cm. Figure 4.6(b) reports this optimized FV, compared to the low energy electron recoil analysis of [133] and the FOM computed for each identical-mass TPC portion, which highlights the impact of spatial-dependent backgrounds as the radius and height increase.

The estimation of the FV LXe mass cannot be simply obtained by computing the geometrical volume and the LXe density given the pressure and temperature conditions. This happens because of the charge insensitive volume that makes the TPC blinded to the events occurring in its bottom corners [130]. (A better description of this feature in provided Chapter 6). Therefore, in order to estimate the active mass enclosed inside the chosen FV, a conservative approach of geometrical scaling the low-energy electron recoil one was adopted. The analysis returned a LXe fiducial mass of 3.71(12) t. The obtained a FOM improvement, with respect to the full TPC volume one, of about 30 % was gained. For completeness, Table 4.3 summarizes all the optimized FV details.

Table 4.3: ^{212}Pb optimized fiducial volume details.

R^2 [cm^2]	Z_{low} [cm]	Z_{high} [cm]	LXe Mass [t]
3306.0	-140.0	-10.0	3.71

4.3.2 Cut efficiency single states and background curves

The fiducial volume selection, reducing the effects of spatial-dependent background, is not enough to clean the data-sets for ^{212}Pb branching ratios measurement. Indeed, on top of this, other selection rules have to be applied to limit the number of non-physical or misreconstructed events while reducing other sources of backgrounds. To do so, a sub-set of selection rules exploited in the low-energy electronic recoil new-physics searches [133], have also been utilized for this study. The selected cuts are the result of a compromise between analyzing the majority of the statistics while assuring pure enough data-sets in order to achieve a clean ^{212}Pb analysis. In Table 4.4 the list and a brief summary of the used data quality and prior selection rules (cuts) are reported.

Commonly, the cut acceptance is evaluated via data-driven approach and estimated by considering the effects the selection rules have on a gamma peak whose energy is close to or inside the ROI. However, this approach cannot be exploited for this analysis for two main reasons. The first one is that the expected cut acceptance is not constant throughout the full ROI, due to the energy and topology dependence of some selection rules. The second one is proper of this analysis: the acceptance of the three ^{212}Pb spectra, which differs due to the different event topologies, cannot be estimated by the cumulative observed ^{212}Pb calibration spectrum, where these components are overlapped. For these reasons, this analysis exploits simulation-driven cut acceptance curves.

To do so, full simulations of ^{212}Pb first and second excited states, ^{214}Pb full spectrum, Bismuth skin and electrons with energy uniformly distributed in 0–750 keV were performed. The choice of using electrons instead of simulating the ^{212}Pb ground state spectrum (pure beta decay) was done in order to obtain enough statistics in the full ROI and also to exploit the same so-obtained cut acceptance for other background components featuring single electron recoil events (caused by either beta or gamma particles).

The cut acceptance curves are then computed by means of the ratio of binned simulation templates after and before the application of the quality cuts, reported in Table 4.4. Given that the simulated templates do not cover the full ROI of this study, these curves have been constrained to 1 in the bins where 0 counts were found. Moreover, since the cut relative to the top PMT fraction of cS2 area has been developed as a quality cut on data, it cannot be applied on simulations and hence its impact is estimated from the data-sets exploiting the $N-1$ approach (see Figure 4.7 as reference) and then convolved with the cut acceptance computed by templates ratio. The $N-1$ method, aims in computing the cut acceptance of a single cut by means of the ratio between the binned histograms after the application of all selection rules and the one obtained excluding the application of that specific cut.

By following this approach, the ^{212}Pb two excited states, the electrons, the Bismuth skin and the full-spectrum ^{214}Pb cut acceptance curves are calculated and eventually smoothed with a moving average technique. Figure 4.8 represents these curves, where the uncertainties are computed with the Clopper-Pearson method [134], defined by the number of events per bin, then accordingly modified by the smoothing procedure. On top of these curves, in order to get the full signal and background efficiencies, the estimated detection efficiency and S2 signal threshold acceptance, which differs from 1 only in the neighborhood of the XENONnT low-energy threshold (lower than 1 keV), are multiplied.

Table 4.4: (Inspired by [56]) Data selection adopted in the ^{212}Pb branching ratios analysis. The table reports the name of the cuts and their description. Cuts highlighted in dark gray are used as prior selections for both simulations and observed data, those highlighted in light gray are used as pre-selections for data only and those that are not highlighted are used as quality cuts. Upon these latter the cut acceptance is computed. For the electrons cut acceptance only the cut_s2_single_scatter was used as a quality selection rather than a prior one.

Cut name	Description
cut_daq_veto	Rejects events that are too close to a hardware veto start or stop.
cut_run_boundaries	Removes events that are too close to the boundaries of a data acquisition period (a run), for which some event information could be lost.
cut_main_is_valid_triggering_peak	Selection which ensures that at least either the main S1 or main S2 is considered a triggering peak. Otherwise, this is most likely an accidental coincidence.
cut_interaction_exists	Simple cut to select (S1; S2) events.
cut_s1_tightcoin_3fold	Selects events with at least 3 PMTs contributing with hits within tight symmetrical range of 50 ns from the peak center.
cut_fiducial_cylinder_3700kg	Selects the events inside the optimized fiducial volume.
cut_s2_single_scatter	Based on the size of the alternative reconstructed S2, it rejects MS events.
cut_cs2_area_fraction_top	Selects physical S2, using the area fraction top as a criterion to suppress gas events and S1-S2 misidentification.
cut_s1_max_pmt	Rejects events in which a PMT contributes most of the entire S1 area, mainly due to spurious PMT light emission or PMT after-pulses. It effectively rejects AC events. The selection threshold varies with the depth of the TPC: Towards the bottom of the TPC, events are more localized, and the threshold is less rigid.
cut_s1_single_scatter	Checks if an alternative S1 in an event waveform exist to form a valid S1 and S2 pair. If so, the event is removed. The selection rejects misreconstructed events and MS.
cut_s1_naive_bayes	Checks how probable the reconstructed S1 is a true S1. The probability is assigned by a Naive Bayes Classifier, a supervised machine learning algorithm trained on simulations, which classifies peaks as S1-like or S2-like. It targets misreconstructed events and rejects AC events at low S1 areas.
cut_s2_width_wire_modeled_low_er	Rejects events with unusual S2 width for the position where they have been reconstructed. Due to the presence of perpendicular wires, which distorts the electron cloud trajectory, the rejection threshold has two definitions depending on whether the events are reconstructed near or far from the wires. It rejects MS, AC and non-physical events.
cut_s2_naive_bayes	Identical to the S1-based cut, but based on S2 features. It rejects events with poorly reconstructed S2s.

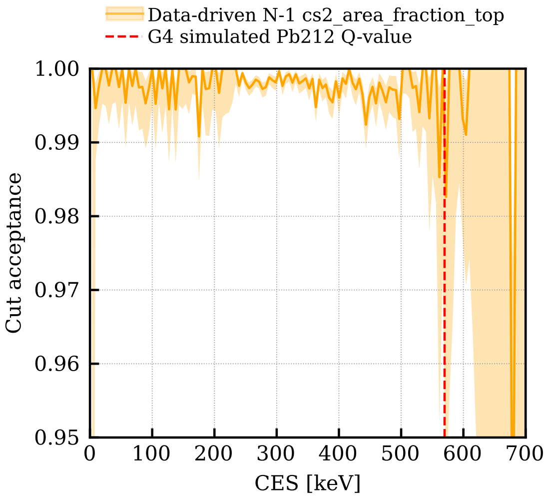

Figure 4.7: SR0 data-driven cut acceptance of cut_cs2_area_fraction_top obtained via background subtraction method of Equation 4.6.

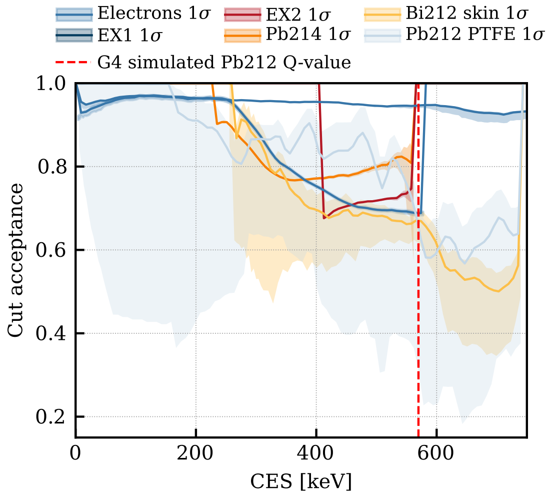

Figure 4.8: Cut acceptance curves for signal and background components for ^{212}Pb analysis. Outside the existence domain of the signals components the acceptance is set to one.

In order to prove the reliability of this approach, beyond the thorough validation of the XENONnT Monte Carlo tools against calibration data across extended energy ranges [56], an extra simulation of ^{212}Pb full spectrum, with branching ratios fixed to the Collaboration default values, has been performed. The cut acceptance obtained with this simulation can be directly compared with the data-driven one by exploiting both SR0 science and ^{220}Rn calibration data. Assuming that the ^{220}Rn calibration data-sets is composed by both ^{212}Pb and background contributions, in order to obtain the data-driven cut efficiency of solely ^{212}Pb spectrum ϵ_{Pb}, the following bin-wise computation has to be performed:

$$\epsilon_{\text{Rn},i} = \epsilon_{\text{Pb},i} s_i + \epsilon_{\text{bkg}_{,i}}(1 - s_i) \;\rightarrow\; \epsilon_{\text{Pb},i} = (\epsilon_{\text{Rn},i} - \epsilon_{\text{bkg}_{,i}}(1 - s_i))\frac{1}{s_i}, \tag{4.6}$$

where $\epsilon_{\text{Rn},i}$, $\epsilon_{\text{bkg}_{,i}}$ and s_i are respectively the data-driven cut acceptance obtained from the ^{220}Rn calibration data, the one computed for SR0 background data and the ^{212}Pb signal fraction in the i-th bin. This latter can be computed by assuming that in each bin the contribution due to the background is that obtained by scaling the SR0 background template for the relative lifetimes of the two data sets.

The obtained data-driven cut acceptance, compared to the simulation-driven one is represented in Figure 4.9(a). After the application of the moving average for smoothing purposes, the simulation- and data-driven curves ratio, plotted in Figure 4.9(b), is obtained. The 2.2(6) % average shift of ratio from 1 can be explained by looking at a more detailed comparison into the cut-by-cut acceptance curves, computed with the N-1 method, reported in Figure 4.10. This discrepancy is likely introduced by both cut_s1_single_scatter 4.10(b) and cut_s2_width_wire_modeled_low_er 4.10(e) effects and by the cuts correlations, that are not present for the ^{212}Pb simulations but show up in the observed data-sets.

4.4 Background and signal model components

As stated in previous paragraphs, in order to constrain the background contributions, the ^{212}Pb branching ratio analysis exploits both the ^{220}Rn calibration and WIMP science (also

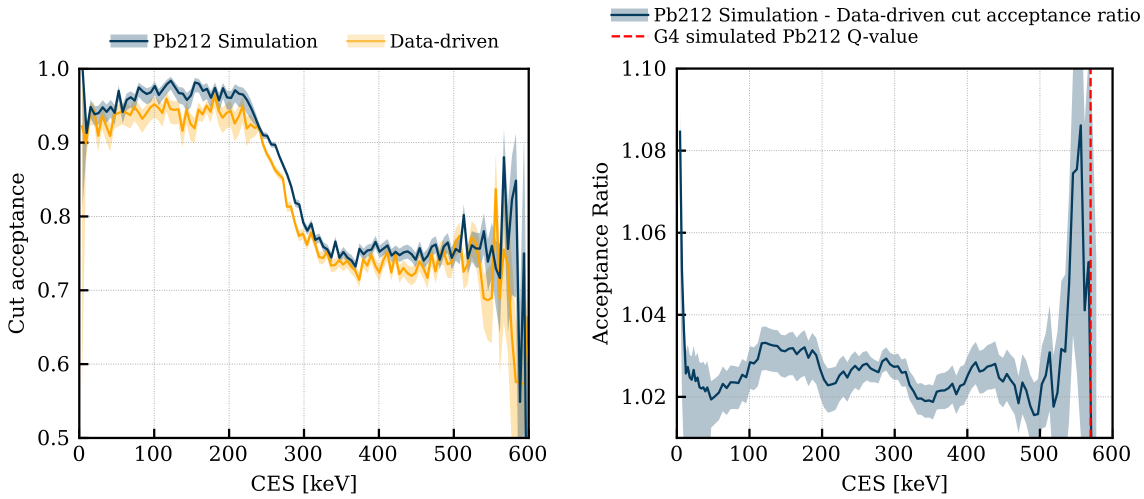

(a) Simulation- and data-driven cut acceptance curves comparison.

(b) Simulation- and data-driven cut acceptance curves smoothed ratio.

Figure 4.9: Simulation- and data-driven cut acceptance curves for ^{212}Pb spectrum, their comparison (a) and their ratio after moving average smoothing approach (b).

labeled as background) data-sets. In Figure 4.11, these two data-sets are binned and compared in the CES observable space. By exploiting SR0 background runs as a template, every constant (or long-lived compared to the experimental lifetime) background contribution is included in the ^{212}Pb branching ratios analysis fit. However, this is not enough to fully model the background contributions to this study. Indeed, XENONnT detector is also polluted by time-dependent backgrounds, which can be subdivided into two classes. The first one is introduced by calibration campaigns while the second one relates with the purification operations.

To the first class belong $^{129\text{m}}$Xe, $^{131\text{m}}$Xe, ^{133}Xe (activated during the AmBe calibration campaigns) and $^{83\text{m}}$Kr (injected during Krypton calibration runs) backgrounds. These isotopes activity can be traced during the whole SR0 lifetime by studying their contribution in specific CES windows. The results of this analysis for neutron-induced backgrounds are reported in Figure 4.12. Given the faint activity of ^{133}Xe, see Figure 4.12 as reference, in both ^{220}Rn calibration and SR0 background runs, it is possible to neglect its contribution for the ^{212}Pb branching ratio study. Concerning ^{83m}Kr instead, given its strong signature in the CES space (peak at around 40 keV), its contribution was included in the fit model without any constraint.

To the second class of time-dependent backgrounds belong ^{214}Pb and ^{85}Kr isotopes, which should be constantly removed respectively by the RSS and the Krypton distillation systems. However, depending on the commissioning and maintenance of these systems, these isotopes activities may vary during the data-taking. During SR0, the Radon column was operated in GXe-only mode and hence the ^{222}Rn background was reduced by about 50 % (see Chapter 3 as reference). However, the RSS system was only switched on after the ^{220}Rn calibration campaign. This hence requires the inclusion of ^{214}Pb component in the fit model. Moreover, it is possible to estimate the activity of this isotope by studying the rate of the alpha peaks generated in the radioactive chain. The result of this analysis, reported in Figure 4.13, can be used to constrain the ^{214}Pb contribution in the fit model. Concerning ^{85}Kr, instead, no strong evidences of its presence were found in the fit procedure and hence, also supported by the ones collected by pipette measurements, it was decided to be removed from the model

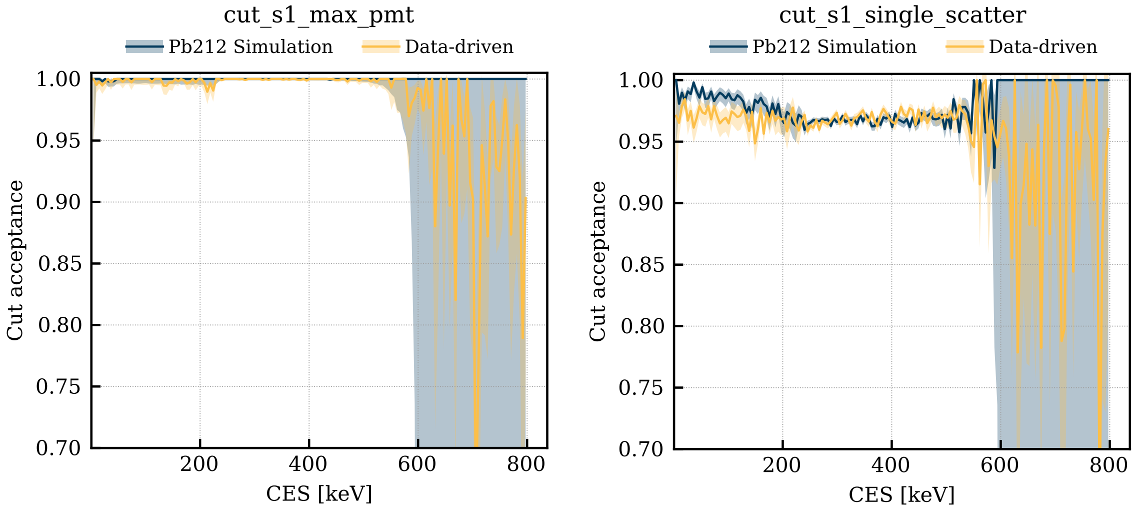

(a) cut_s1_max_pmt N−1 cut acceptance

(b) cut_s1_single_scatter N−1 cut acceptance.

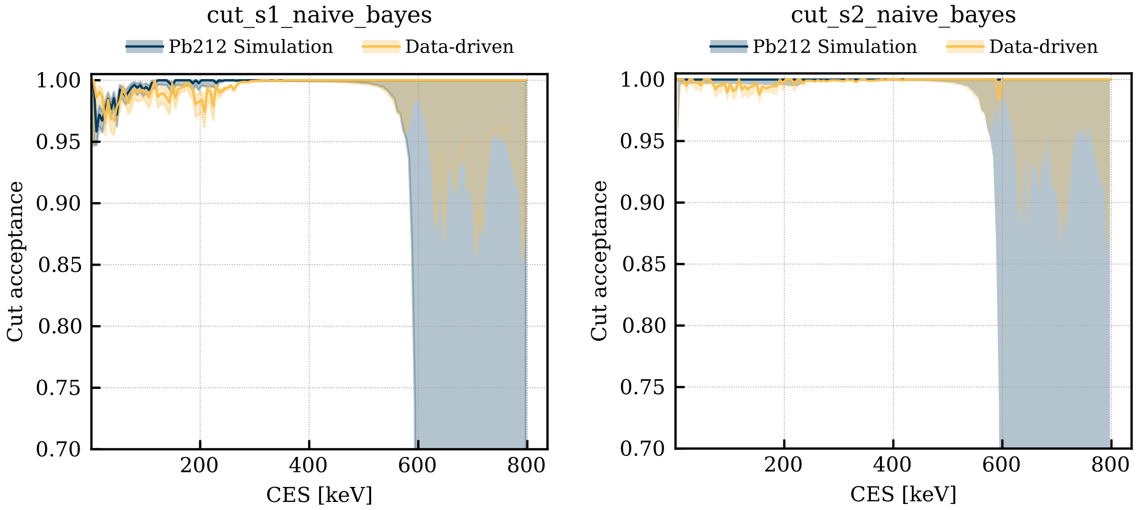

(c) cut_s1_naive_bayes N−1 cut acceptance.

(d) cut_s2_naive_bayes N−1 cut acceptance.

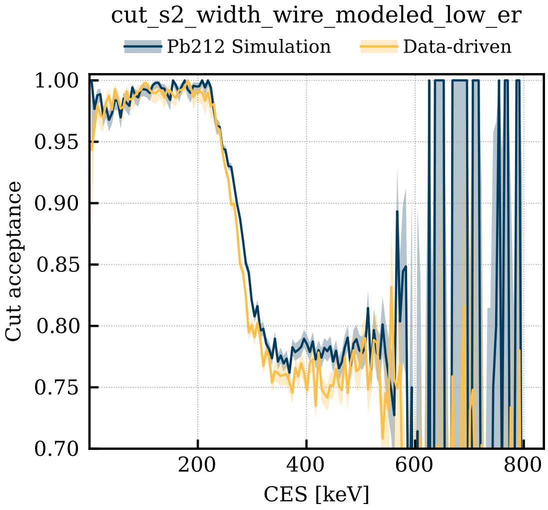

(e) cut_s2_width_wire_modeled_low_er N−1 cut acceptance.

Figure 4.10: N-1 simulation- and data-driven cut acceptances comparison for ^{212}Pb full spectrum.

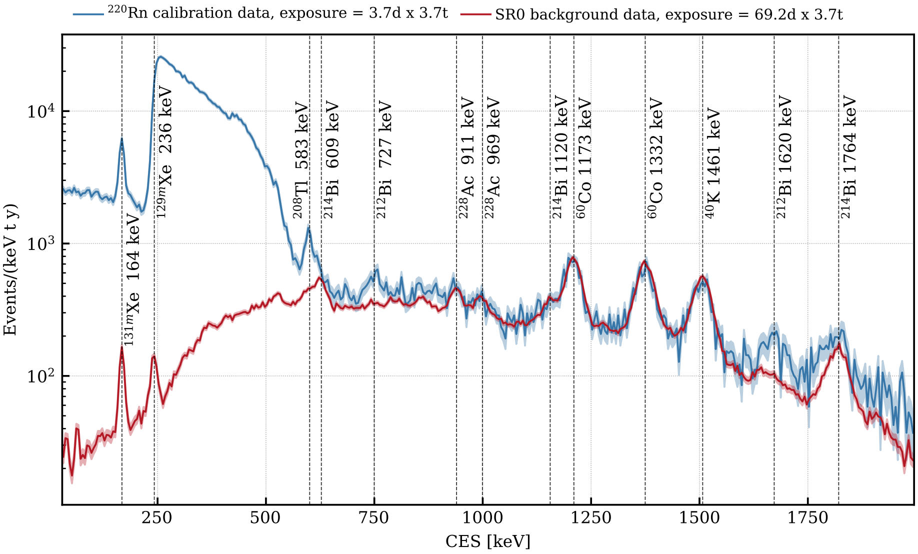

Figure 4.11: XENONnT SR0 ^{220}Rn calibration (in blue) and background data (in red) scaled for the relative exposures and binned in the CES space. The most relevant gamma peaks are marked with a black dashed line and labeled with the respective isotope and energy.

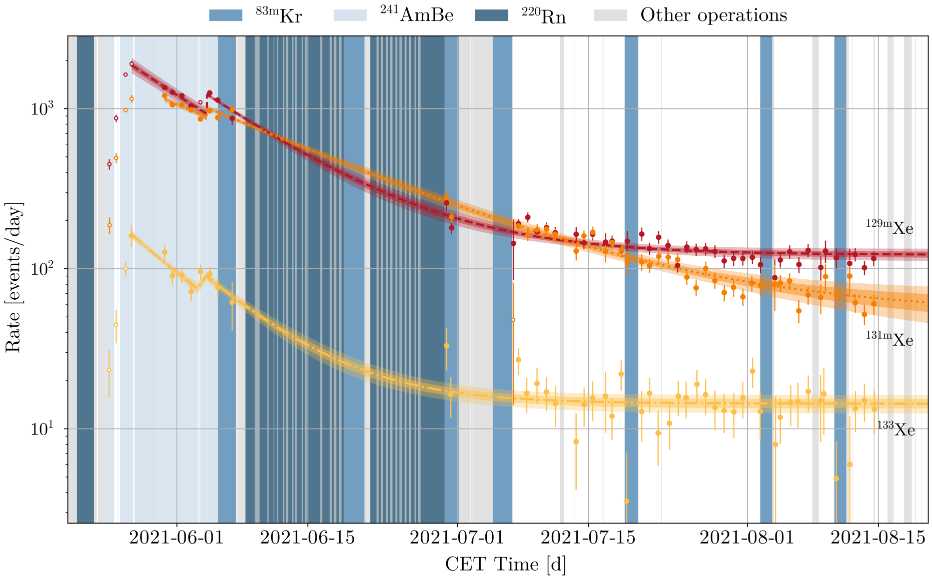

Figure 4.12: (Edited from [56]) Temporal evolution model with 1 and 2σ band uncertainties of neutron-induced background rate based on an exponential plus linear background fit of $^{129\mathrm{m}}$Xe (red), $^{131\mathrm{m}}$Xe (orange), and ^{133}Xe (yellow). The rate was extracted in specific CES windows given by the energy of the peak $\pm 2\sigma_{CES}$, where σ_{CES} is given by the energy resolution. For ^{133}Xe, which has no peak, the region within 80–120 keV was used. The Poisson standard deviations were used as uncertainties for the extracted rate. The calibration periods, e.g., ^{241}AmBe, are shown as reported in the legend.

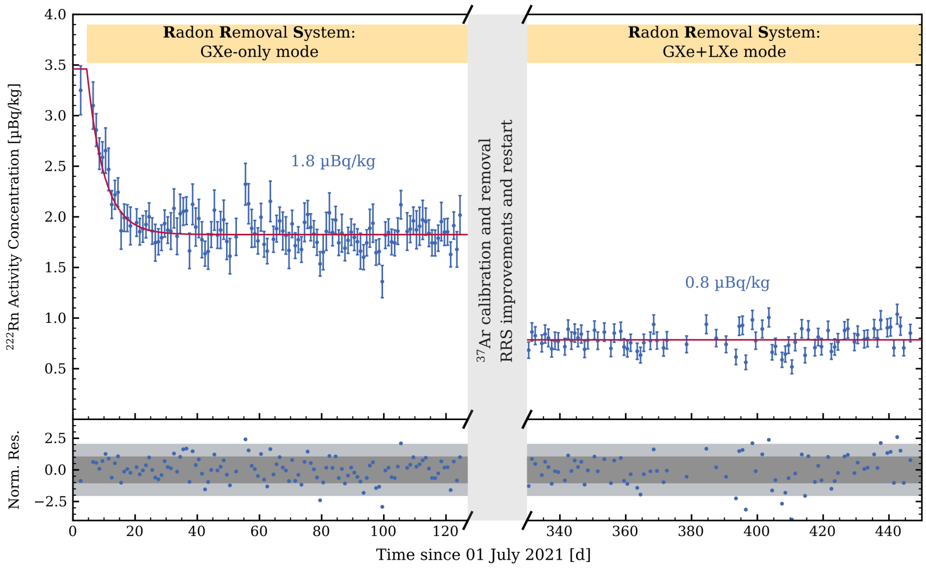

Figure 4.13: (Edited from [114]) ^{222}Rn activity concentration as a function of time. Three time periods can be observed: No Radon removal at the beginning of SR0, Radon Removal System (RRS) in GXe-only mode (During SR0), and RRS in GXe+LXe mode (During SR1).

contribution list.

As far as signal components are concerned, a theoretical model for the ^{212}Pb ground state pure beta spectrum as well as two GEANT4-based templates for the excited states have been exploited. The ^{212}Pb ground state spectral shape, taken from [135], represents an improved model with respect to the GEANT4 version. Indeed, by means of large-scale shell-model calculations and the inclusion of atomic screening and exchange effects, this model show a 12.1–19.0 % difference in a range 1–15 keV with respect to the version computed assuming an allowed decay, which is very similar to the one considered in the GEANT4 electron energy generation. In this analysis, even if the two ^{212}Pb beta decays to the ^{212}Bi excited states are first-forbidden as the pure beta one, these latter templates were computed starting from GEANT4 simulations. As remarked at the end of this Chapter, a future update of this study could be the usage of first-forbidden beta shape models also for these decays.

4.5 Branching Ratios Results from the Fit

Once the model components are set, the fit to data can be performed. In this section, a review of the statistical framework and the computation of the final measurements along with a discussion on possible systematic source are presented.

4.5.1 The statistical framework and likelihood construction

For the fitting procedure the Poisson chi-square likelihood, described in [129], was exploited. Starting from the assumption that the count of the i-th bin follows a Poisson statistics and that the bins counts are statistically independent of each others, we can write the Poisson likelihood as:

$$L_P = \prod_i \exp(-y_i) \frac{y_i^{n_i}}{n_i!} \tag{4.7}$$

where y_i are the number of events predicted by the model in the i-th bin and n_i are the observed ones. By exploiting the goodness-of-fit likelihood ratio test theorem, it is possible to define the following χ^2 test statistics:

$$\chi^2_P = -2\ln\lambda = -2\left[\ln L_P(m_i;n_i) - \ln L_P(y_i;n_i)\right], \tag{4.8}$$

where m_i are defined as the true (unknown) values for n_i. Being the first term independent of y_i, the minimization process of χ^2_P also maximizes the Poisson likelihood function L_P of Equation 4.7. By replacing the unknown m_i by the i-th bin model-indpendent maximum likelihood estimation (n_i), it is possible to define the Poisson likelihood chi-square as:

$$\chi^2_\lambda = 2\sum_i \left[y_i - n_i + n_i \log\left(\frac{n_i}{y_i}\right)\right]. \tag{4.9}$$

As defaults for this analysis the data and the model have been binned considering an ROI of $[30, 620]$ keV and a bin width of 2 keV. These arbitrary choices have been made on physics bases. On the one hand the ROI choice was dictated by the reduction of the accidental coincidence background, impacting the low energy range, while at high-energy ranges the limit was set to be larger than the ^{212}Pb beta decay Q-value (see Table 4.2) and then the ^{208}Tl gamma peak (see Figure 4.11) to better constrain the Bismuth skin background. On the other hand, the choice of the bin width was driven by the capability of the detector response model to correctly reproduce the peaks line shapes. Given the arbitrary nature of these two analysis configurations, the impact of their configuration values on the ^{212}Pb branching ratios measurement has been checked and reviewed at the end of this Chapter.

The minimization of χ^2_λ returns the best fit values for the rate multipliers, which scale the initialization activity of the different fit components of the model. Beyond these, some other nuisance parameters to include potential systematic effects due to detector response interpretation and cut acceptance computation are also optimized. More specifically, the considered nuisance parameters are: A and k from the energy bias calibration curve (see Figure 4.2(b) and Equation 4.2) with the additional c parameter to better fit the offset, a and b from the energy resolution calibration curve (see Figure 4.2(c) and Equation 4.3), α and β from the skewness calibration curve (see Figure 4.2(d) and Equation 4.4) and one parameter for each cut efficiency curve scaling it between its $\pm 1\sigma$ band artificially enlarged by a factor 3, to partially reduce the potential systematic introduced by the simulation-data mismatch. When, the cut efficiency shape parameters equal -1, the efficiency curves collapses to the (-1σ) curve, when instead they equal $+1$, the efficiencies hit the $+1\sigma$ limit. When equal to 0, the curves are identical to the input ones.

Moreover, the Likelihood was penalized with additional terms. In particular, Gaussian constraints where introduced for $^{131\mathrm{m}}$Xe, $^{129\mathrm{m}}$Xe and ^{214}Pb rate multipliers, according to the analysis presented before and illustrated in Figure 4.12, and for SR0 background template, by considering as relative variance the Poisson one of this data-set full statistics. Additionally, other Gaussian constraints have been exploited for nuisance parameters both for the detector response ones, considering the uncertainties of the input parameters reported in Figures 4.2(b), 4.2(c) and 4.2(d), and for the efficiency ones maximizing the probability at 0.

In order to give a better initialization for the parameters in the model, a pre-fit of the same ^{220}Rn calibration data-set was performed by exploiting the full ^{212}Pb spectrum (with branching ratios set to the Collaboration default values). With the obtained activities, the rate multipliers for the different contributions have been set, while the nuisance parameters have been initialized either with their side-analyses best-fit values or to 0 for efficiency modifiers. It is hence worth to notice that the three ^{212}Pb signal spectra have been all initialized with the same activity value.

Table 4.5: ^{212}Pb branching ratios study fit results. Gray highlighted entries mark nuisance parameters.

Parameter	Best Fit Value	Hesse Error
^{212}Pb GS	0.1585	0.0013
^{212}Pb EX1	0.8154	0.0027
^{212}Pb EX2	0.0462	0.0015
^{214}Pb	1.00	0.04
^{83m}Kr	0.0	0.11
^{129m}Xe	1.97	0.06
^{131m}Xe	1.0002	0.0017
^{212}Bi skin	1.07	0.05
SR0 background	1.0000	0.0035
A	0.02	0.02
k	0.01	0.38
a	0.374	0.010
b	2.4e-3	0.7e-3
α	1.9819	0.0030
β	-1.2318	0.0016
ϵ_{Bi}	0.000	0.012
$\epsilon_{\text{Electrons}}$	0.004	0.017
ϵ_{PbEX1}	0.01	0.6
ϵ_{PbEX2}	0.01	0.32
ϵ_{Pb214}	-0.0	0.4

By applying all the above considerations, the Poisson likelihood chi-square, penalized with the constraint terms, was minimized and the results summarized in Table 4.5 and illustrated in Figure 4.14 were obtained. For visualization purposes, in the Figure 4.14(a), all backgrounds sources (^{214}Pb, ^{83m}Kr, ^{129m}Xe, ^{131m}Xe ,^{212}Bi skin and SR0 background) have been summed together in the *Background* contribution.

To better illustrate the meaning of the values obtained for the nuisance parameters in the fit procedure, Figure 4.15 is reported. From these plots it is possible to deduce that the optimized detector response curves, as determined with the ^{212}Pb analysis best-fit values, are compatible with the nominal ones also used in other studies. In order to give a more solid idea about the outcome of this study a simple goodness of fit test was performed, by following the indications reported in [129]. By exploiting the *GOFevaluation* python package [101], with an observed Poisson chi-square value of about 342.9, we computed a p-value of about 0.03.

4.5.2 The Branching Ratios Estimation and Potential Systematic Sources

The ^{212}Pb BRs can be extracted from the best-fit values if the signal models rate multipliers. This is done by considering the parameters fit covariance matrix, obtained from the Likelihood chi-square Hessian, supposing the Likelihood has a nearly-paraboloid shape in the neighborhood of its minimum, and renormalizing their sum to 1. In formulae, for the ^{212}Pb state i (where i runs over [GS,EX1,EX2]), the branching ratio (BR_i) and its uncertainty

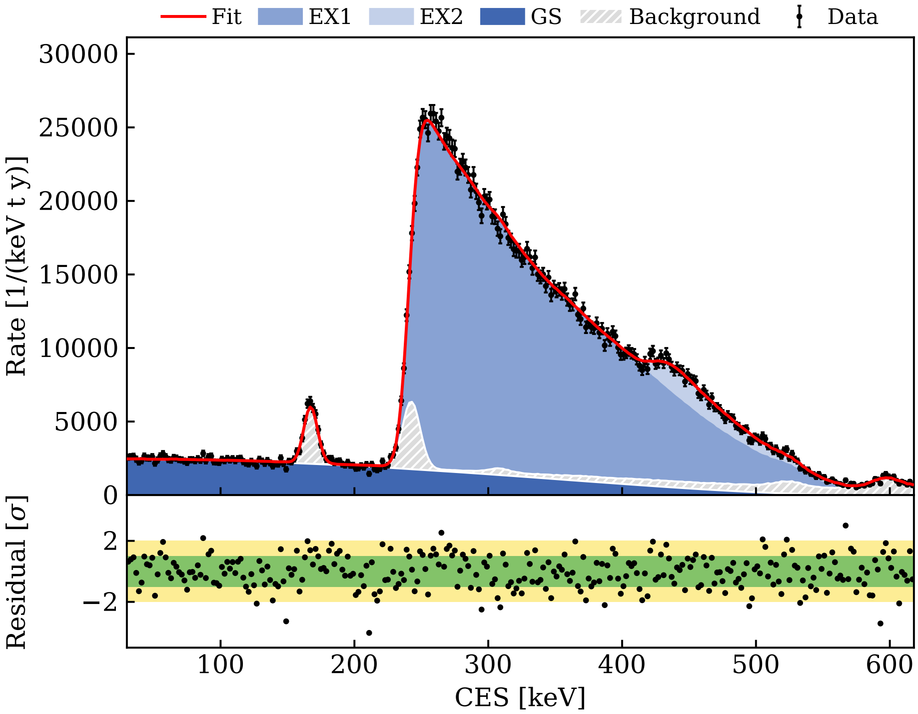

(a) ^{220}Rn binned data-set fit. Fit model components are stack and non-signal contributions are grouped in the *Background* template (gray).

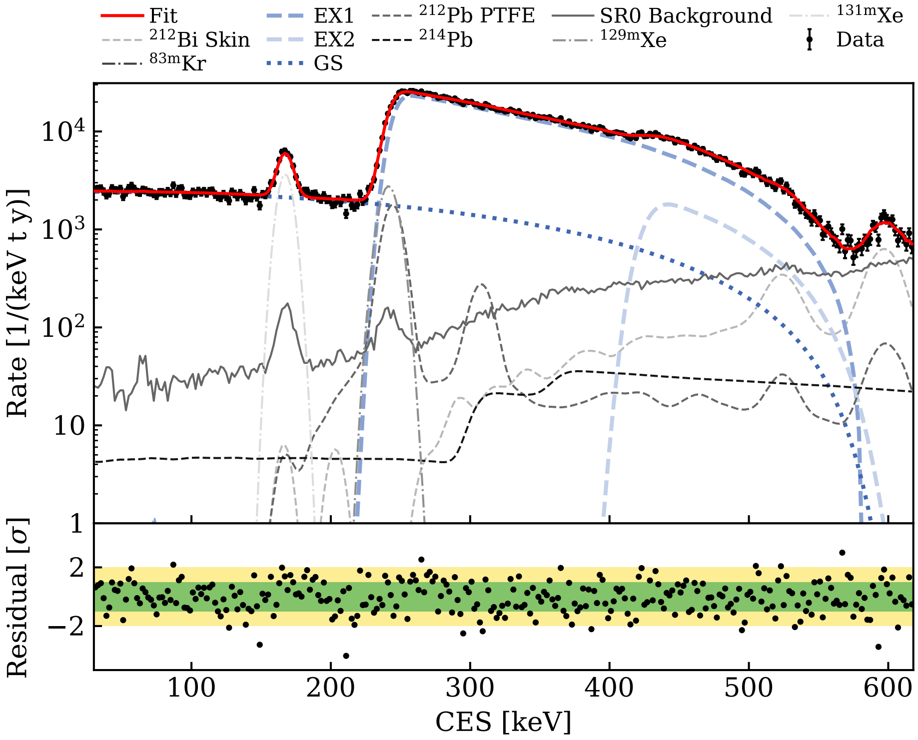

(b) ^{220}Rn binned data-set fit in y-axis log scale. Fit model components are depicted in blue shades if signal contributions or in gray shades if background ones. Additionally, dashed lines represent fit model components from GEANT4 templates, dash-dotted ones refer to peak components, dotted line depicts the theory model (^{212}Pb ground state) and solid one labels the data-driven template (SR0 background).

Figure 4.14: Final result of ^{212}Pb branching ratio analysis. ^{220}Rn binned data-set fit showed for linear (a) and logarithmic (b) y scale.

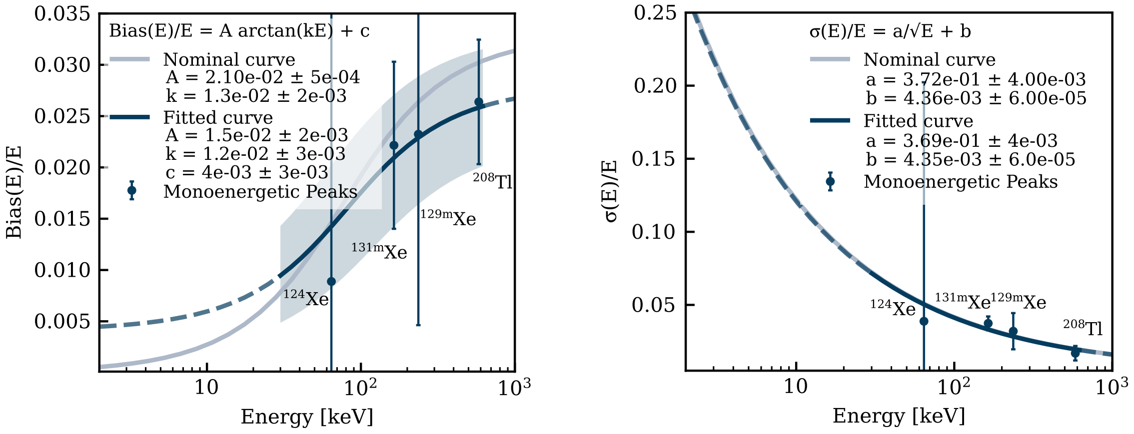

(a) Fit CES bias.

(b) Fit energy resolution.

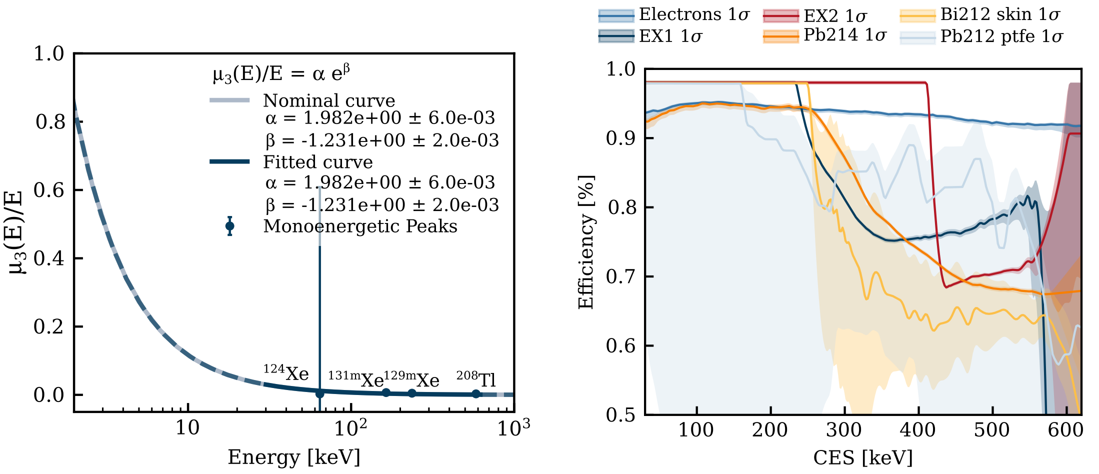

(c) Fit energy skewness.

(d) Fit efficiency curves.

Figure 4.15: Detector response and model components efficiency curves. Figures (a) (b) (c) show the curves with nuisance parameters set to best-fit values (solid blue in analysis ROI, dashed blue outside the ROI), compared to the nominal ones (solid light-blue curves.). Figure (d) shows the cut efficiency curves and their 1σ band for different model contributions multiplied for their best-fit value nuisance modifiers. Efficiency curves here reported are sampled in the fit model templates bin centers.

Table 4.6: Results of the ^{212}Pb branching ratios analysis. The reported uncertainties are here only determined by the analyzed statistics.

^{212}Pb state	Branching Ratio [%]
GS	15.28 ± 0.13
EX1	80.1 ± 0.2
EX2	4.62 ± 0.18

(σ_{BR_i}) result to be:

$$\mathrm{BR}_i = \frac{\mathrm{RM}_i}{\Sigma} \tag{4.10}$$

$$\begin{aligned}\sigma^2_{\mathrm{BR}_i} &= \sigma^2_{\mathrm{RM}_i}\frac{(\Sigma-\mathrm{RM}_i)^2}{\Sigma^4}\\ &+\sum_{j>i}\left(\sigma^2_{RM_j}\frac{(RM_{GS})^2}{\Sigma^4} + -2\sigma_{ij}\mathrm{RM}_i\frac{\Sigma-\mathrm{RM}_i}{\Sigma^4} + 2\sum_{k>j}\sigma_{jk}\frac{(\mathrm{RM}_i)^2}{\Sigma^4}\right)\end{aligned} \tag{4.11}$$

where $\Sigma = \sum_l \mathrm{RM}_l$, RM_i is the best fit rate multiplier value of the ^{212}Pb state i. This computation lead to the ^{212}Pb branching ratios measurement reported in Table 4.6

This measurement method may be affected by systematic uncertainties or biases introduced by the configuration choices arbitrarily done, such as the bin width or the ROI considered, or set as a result of an optimization process, such as the choice of the selected fiducial volume. For this reason this analysis is repeated for different settings of these configurations. The results in terms of GS, EX1 and EX2 branching ratios are reported in Figures 4.16, 4.17 and 4.18. In a very conservative way, we consider as systematic uncertainty introduced by each configuration setting (bin width, ROI, FV and data-set livetime) the maximum difference between the reference measurement and the other measurements, requiring a maximum 2σ migration for nuisance parameters from the reference ones. As an example, we here report in Figure 4.19 the results of the fit of the data binned with 1 keV bin width and considering the 2 t FV. In both these cases, the migration of the energy bias k and c parameters does not meet the requirement, making the fit less reliable. Thus, the 1 keV bin width and 2 t FV measurements are not considered for the estimation of the systematic uncertainties.

Eventually, these systematic uncertainties are combined to get the estimate of the total systematic uncertainty of the measurement. The final results quoting systematic uncertainties are:

$$\mathrm{BR}_{\mathrm{GS}} = 15.28 \pm 0.13(\mathrm{stat})^{+0.02}_{-0.33}(\mathrm{sys})\,\% \tag{4.12}$$

$$\mathrm{BR}_{\mathrm{EX1}} = 80.1 \pm 0.2(\mathrm{stat})^{+0.5}_{-0.2}(\mathrm{sys})\,\% \tag{4.13}$$

$$\mathrm{BR}_{\mathrm{EX2}} = 4.62 \pm 0.18(\mathrm{stat})^{+0.22}_{-0.17}(\mathrm{sys})\,\% \tag{4.14}$$

For a more illustrative representation of these results compared to the literature values of Table 4.2, Figure 4.20 is reported. Quantitatively, by comparing, by means of the Z-test statistics, these measurements to the combined literature values, obtained via weighted average, the results reported in Table 4.7 are obtained. The literature combined values were exploited in this test given the great agreement between the two references.

4.5.3 Discussion on Results

The results obtained in this work represent the first direct measurement of the ^{212}Pb branching ratios to the ^{212}Bi ground and excited states. Specifically, by directly accessing these

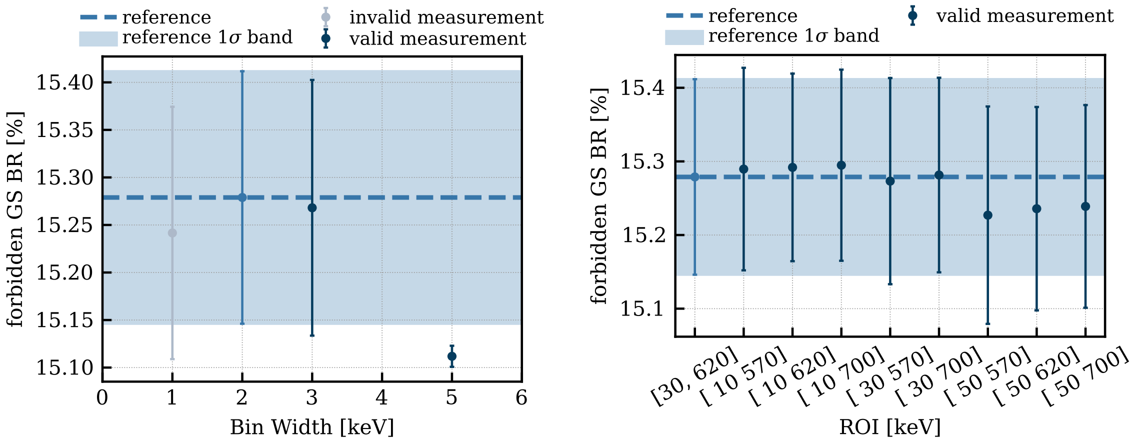

(a) GS BR measurement for different bin width.

(b) GS BR measurement for different ROI.

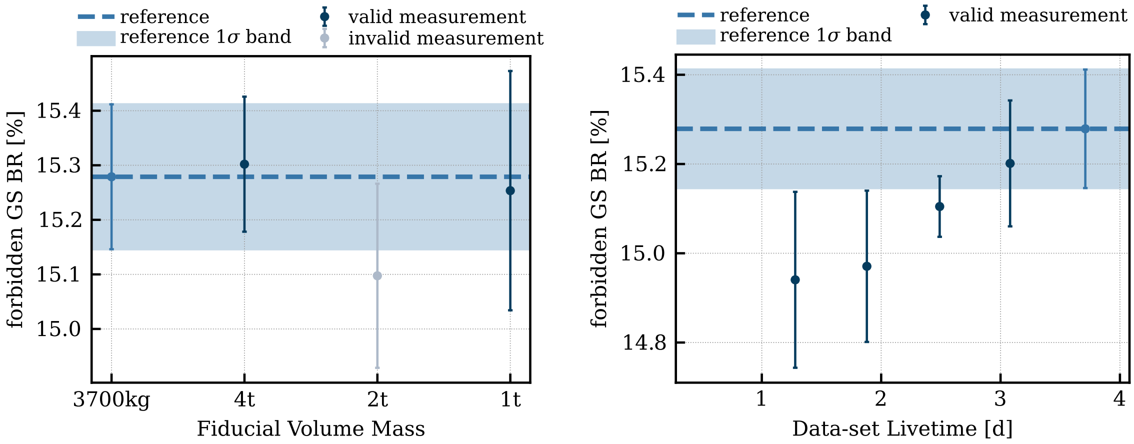

(c) GS BR measurement for different FV.

(d) GS BR measurement for different data-set livetimes.

Figure 4.16: ^{212}Pb GS branching ratios measurements with different bin width, ROI, FV and data-set livetime configurations settings for the fit (dark blue points). Reference measurements are reported as light-blue points and dashed horizontal lines, along with their light-blue 1σ band.

Table 4.7: Z-test statistics for ^{212}Pb branching ratios result compared to the combined literature values, including systematic uncertainties.

^{214}Bi state	Z-test statistics
GS	2.16
EX1	-1.69
EX2	-1.67

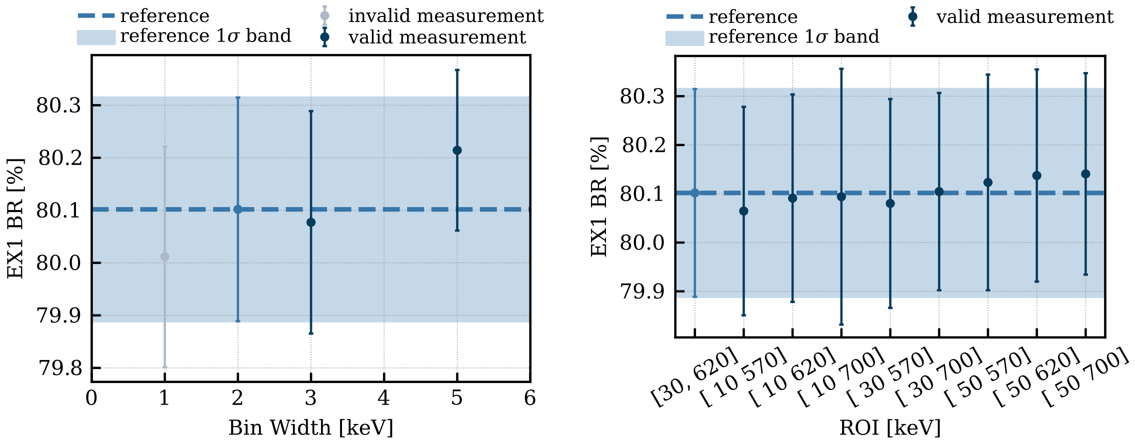

(a) EX1 BR measurement for different bin width.

(b) EX1 BR measurement for different ROI.

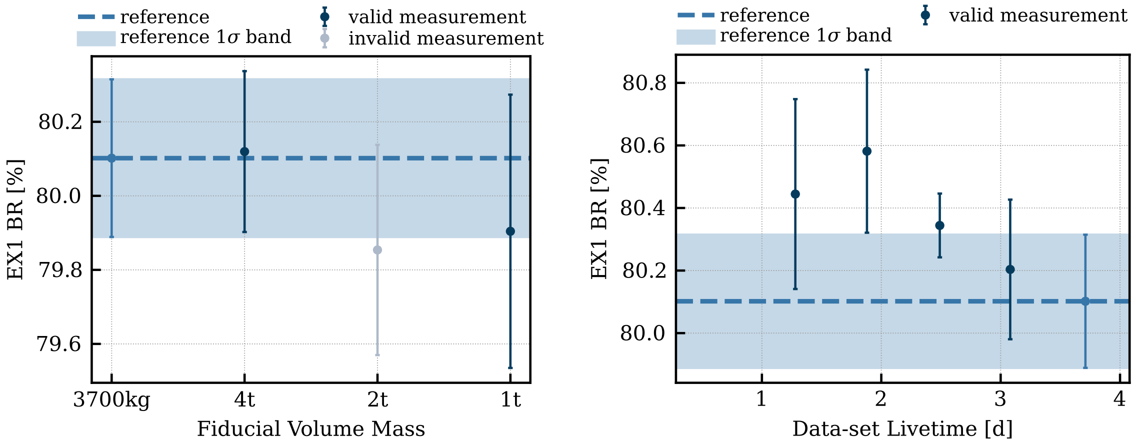

(c) EX1 BR measurement for different FV.

(d) EX1 BR measurement for different data-set livetimes.

Figure 4.17: ^{212}Pb EX1 branching ratios measurements with different bin width, ROI, FV and data-set livetime configurations settings for the fit (dark blue points). Reference measurements are reported as light-blue points and dashed horizontal lines, along with their light-blue 1σ band.

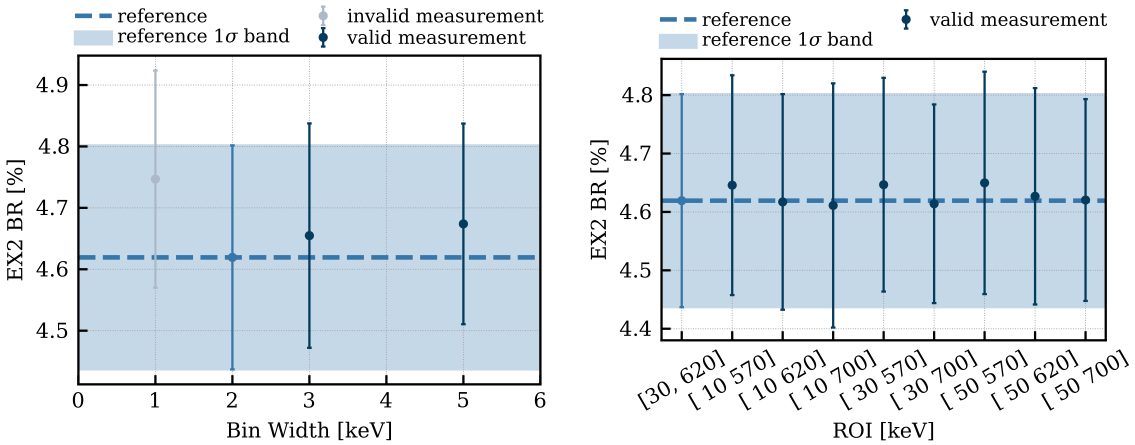

(a) EX2 BR measurement for different bin width.

(b) EX2 BR measurement for different ROI.

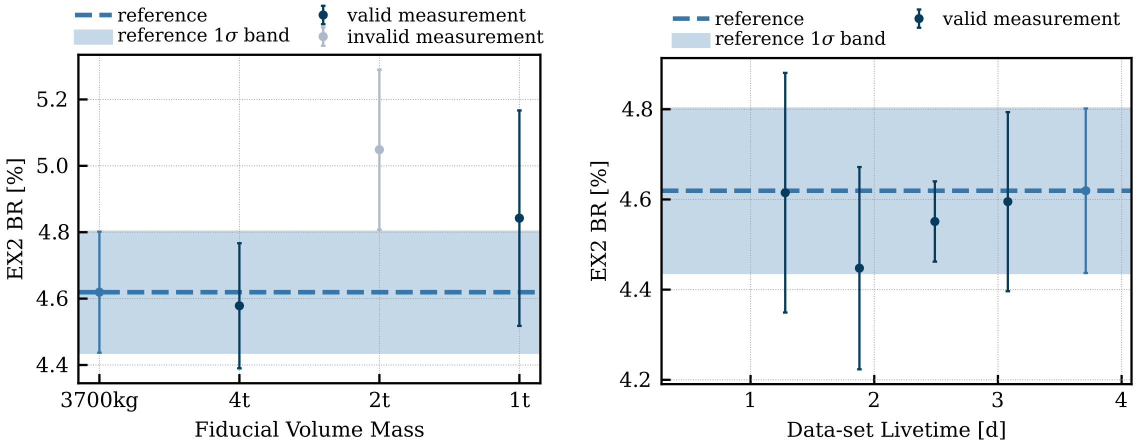

(c) EX2 BR measurement for different FV.

(d) EX2 BR measurement for different data-set livetimes.

Figure 4.18: ^{212}Pb EX2 branching ratios measurements with different bin width, ROI, FV and data-set livetime configurations settings for the fit (dark blue points). Reference measurements are reported as light-blue points and dashed horizontal lines, along with their light-blue 1σ band.

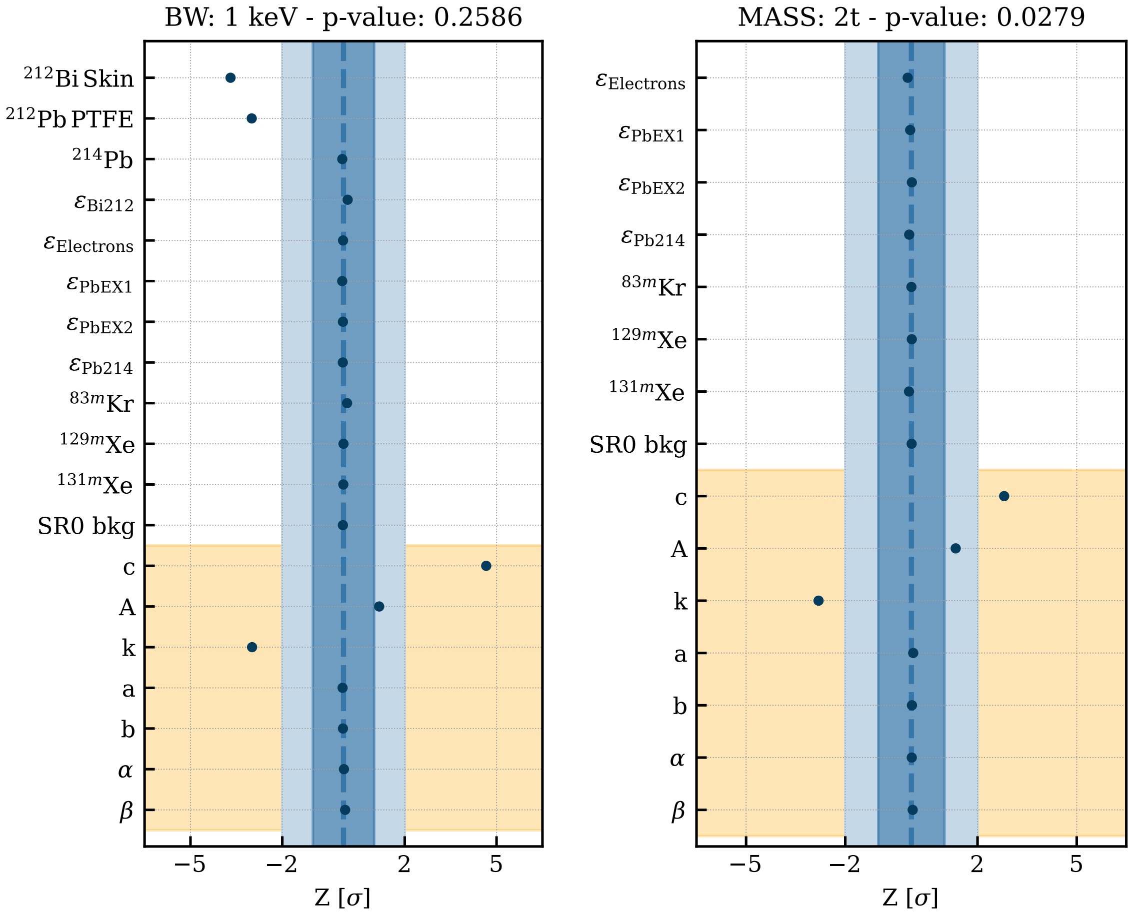

(a) 1 keV bin width.

(b) 2 t FV.

Figure 4.19: Results of ^{212}Pb fit considering 1 keV (a) bin width and 1 t (b) FV. The migration of the energy bias nuisance parameters k and c, above 2σ, reject the possibility of using the 1 keV bin width and 2 t FV measurements in the computation of the systematic uncertainty.

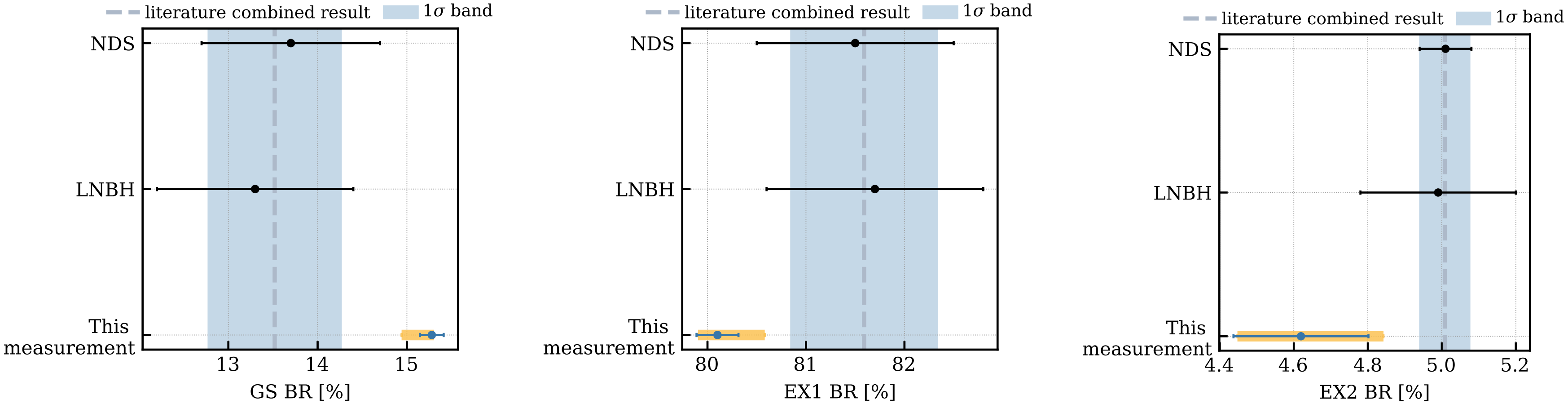

(a) GR BR literature comparison.

(b) EX1 BR literature comparison.

(c) EX2 BR literature comparison.

Figure 4.20: ^{212}Pb GS, EX1 and EX2 branching ratio measurements compared to the literature values of Table 4.2 (black points). This work measurements are reported with light-blue points, light-blue statistical uncertainties and yellow error bars for systematic ones. Combined literature value is represented with vertical gray dashed lines and light-blue bands for their uncertainties.

values from the data, we achieved an enhanced precision on the branching ratio to the ^{212}Bi ground state, by reducing its relative uncertainty of about one order of magnitude if considering only the statistical error, from about 7.7 % to about 0.85 %, or of about a factor three if considering also the systematic uncertainty, from about 7.7 % to about 2.2 %.

Beyond the relative uncertainty refinement, the advantage of a direct measurement, such as the one described in this Chapter, mainly concerns the reduction of the possible systematic, via concurrent assessment of the rates of the three decay modes of ^{212}Pb. Indeed, the only source of systematic uncertainties, as visible in Figure 4.20, are probably due to slight mismodeling of signal and background components made evident when performing the measurement in different FVs and selecting sub-data-sets. This latter test has indeed remarked the possibility of an either missing or mismodeled background component characterized by a non-constant behavior. Although, thorough checks, for simplicity here not reported, tend to favor the mismodeling hypothesis with respect to a missing component.

As far as the literature compatibility is concerned, the study results present a deviation of about 2σ for all the three ^{212}Pb BRs. This outcome as well as the modeling and fitting framework was thus subject to several checks all agreeing with the reported results. Further proofs to the reliability of the presented analysis and results might be obtained in future XENONnT studies, improving the statistics, by including other ^{220}Rn calibration data-sets from SR1 and SR2 and exploiting the theory models for EX1 and EX2 beta energy spectral shapes recently published [136]. Indeed, this second improvement can introduce non-negligible effects to this analysis, given the observed deviation between GEANT4 and first-forbidden spectral shapes for ^{212}Pb GS decay.

Furthermore, this analysis proved the feasibility of high-precision nuclear physics measurements using an experiment à la XENONnT, thanks to the extremely low background rate together with the sophisticated knowledge of the detector response. With such techniques, the standards of sensitivities achieved with common instruments exploited for nuclear precision physics were met and overcome. This analysis, along with other recent studies exploiting low-radioactivity techniques [102, 137–139], underlines the importance of refined precision nuclear measurements. Indeed, as the advancements in the rare-events searches experimental techniques push the discovery power to new levels, very precise knowledge on the remaining background contributions is demanded. This is exactly the case of Solar-pp neutrino searches in the XENONnT ER band. Indeed, the current literature on ^{214}Pb beta decay transition is not precise enough for the Solar-pp neutrino searches. For this reason, as reported in the next Chapter, a direct assessment of the ^{214}Pb branching ratios was performed, overcoming the precision and the tension present in literature.

5

^{214}Pb Branching Ratios Measurement

^{214}Pb undergoes beta decay into ^{214}Bi. Similarly to the study presented in the Chapter 4, where the measurement of the ^{212}Pb branching ratios to the ^{212}Bi ground and excited states is reported, the study on ^{214}Pb is here outlined. Given that the very same modeling and fitting framework described in the previous Chapter is also used for the inference of this study, in the following only the discussions on the physics case and on the results are reported. More specifically, in 5.1 the impact of ^{214}Pb ground state branching ratio uncertainty on the XENONnT experiment physics searches in the electronic recoil channel is discussed. Then, in 5.2 a discussion of the sensitivity study that led to the ^{222}Rn calibration of XENONnT TPC during SR1 is presented. Finally, after 5.3 and 5.4 where data selection and signal and background modeling are presented, the results of this study are detailed in 5.5. Unless otherwise specified, all material presented in the following Chapter is original and has been produced by the author of this Thesis.

5.1 On the Impact of ^{214}Pb on XENONnT Electron Recoil Physics Searches

Beyond WIMP direct dark matter searches, the potential XENONnT rare-events physics reach is vast. Part of these studies, given the expected interaction nature of the hunted particles, are based on specific signal searches within the electron recoil data-set. Such studies hence require the deep knowledge of the electron recoil backgrounds.

For example, the electronic recoil new-physics studies in the low-energy range (below 20 keV) published in [133], primarily motivated by the observation of the XENON1T excess [140], were based on specific signals searches on top of a physics-motivated and constrained background model. This background model fitted up to 140 keV, is presented in Figure 5.1. As clearly visible in this plot, the major contribution to the ER background is, below 35 keV, ^{214}Pb.

For topological reasons, ^{214}Pb contribution in this low-energy region, as in the ^{212}Pb case already treated in Chapter 4, is only due to its pure beta decay channel leading directly to the ^{214}Bi ground state. Thus, to constrain this background in the fit procedure, two pieces of information are needed: the total ^{214}Pb expected activity, which can be estimated from alpha peaks originated within the ^{238}U decay chain, and the value of ^{214}Pb beta decay branching

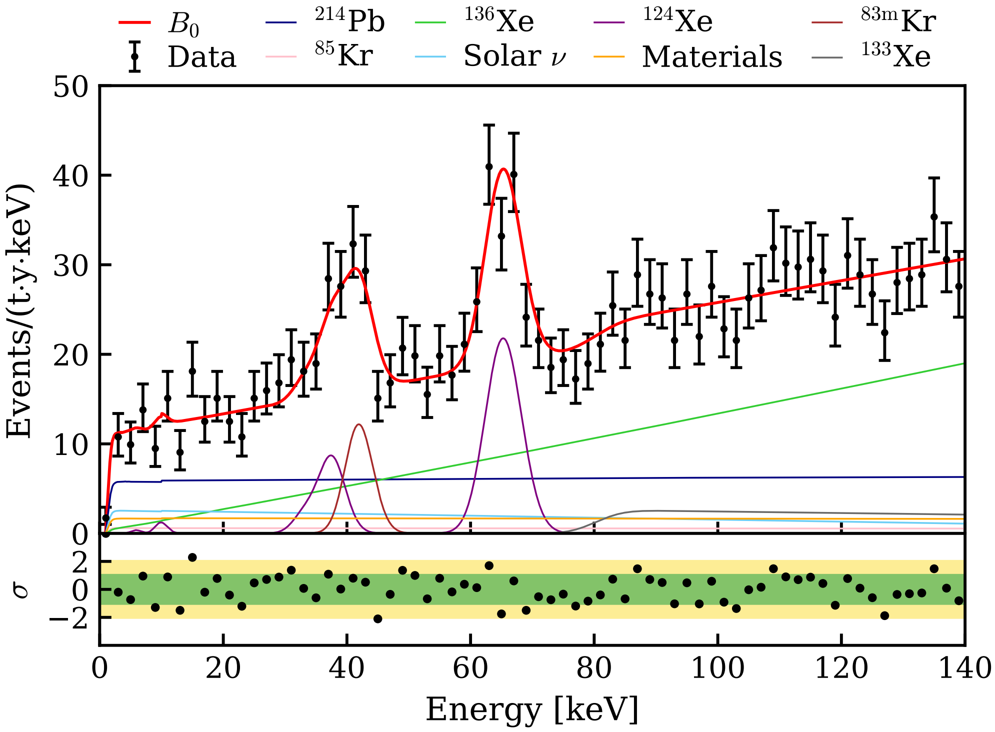

Figure 5.1: (From [133]) Fit to [electron recoil] SR0 data using the background model B0 of [133]. The fit result is the red line. The subdominant AC background is not shown.

ratio (BR) to the ground state (GS). In the specific case of [133], a ^{214}Pb GS BR of 12.7 % from [141] was assumed.

However, the ^{214}Pb GS BR value of [141], assumed in the study reported in [133], is far from being a good constrain for searches aiming to reach better sensitivities. Indeed, the relative uncertainty of ^{214}Pb GS BR reported in [141] (12.7(9) %), is about 7 %. The direct consequence of this high relative uncertainty is its propagation into the final sensitivities and hence results of rare events searches in the electronic recoil band. One of these studies targets the detection of Solar-pp neutrinos with the XENONnT SR1 data, which benefitted by the usage of the RRS (see Chapter 3) in the LXe+GXe mode, reducing from SR0 the ^{214}Pb contribution by about a factor 2 (see Figure 4.13). Collaboration sensitivity studies for Solar-pp neutrinos revealed that in order to claim an observation in the ER channel, with the achieved SR1 levels of background, a ^{214}Pb GS BR relative uncertainty less than 3% is required. This hence translates into a factor 2 improvement in the ^{214}Pb GS BR precision, possibly achievable with a XENONnT direct measurement.

The 7 % ^{214}Pb GS BR relative uncertainty is not the only critical feature this background brings inside these studies. Indeed, different literature references point to very different values as references for the ^{214}Pb GS BR. For example, as reported in Table 5.1, the values quoted in LNHB and NDS, exploited here as major references for nuclear transitions values, show a tension of about 4.7 σ. The nature of this large tension could be at first order attributed to the high multiplicity of ^{214}Pb beta decay scheme, illustrated in Figure 5.2, which increase the complexity in the $P(\gamma + \text{ce})$ computation, which takes into account both gamma-ray (γ) energy balances and recommended internal conversion coefficients (ce) [142].

To improve ER studies sensitivity and push the discovery power for Solar-pp neutrinos ER signal, a better constrain on ^{214}Pb GS BR is thus demanded. To this end, the collection of a SR1 ^{214}Pb enhanced-rate data-set was proposed, with the aim of directly fitting its GS

Table 5.1: Comparison between LNHB ^{214}Pb nuclear recommended values from [63] and NDS ones from [141]. Energy levels with expected BR smaller than 1 % are here not reported.

	LNHB (Q-value 1019(11) keV)		NDS (Q-value 1018(11) keV)	
	BR [%]	Excitation Energy [keV]	BR [%]	Excitation Energy [keV]
GS	9.2(7)	0	12.7(9)	0
EX1	41.09(39)	295.224(2)	39.0(5)	295.2236(19)
EX2	46.52(37)	351.932(2)	44.5(7)	351.9323(21)
EX3	1.047(17)	533.66(2)	1.063(18)	533.672(14)
EX4	2.762(22)	839.00(4)	2.75(8)	838.994(22)

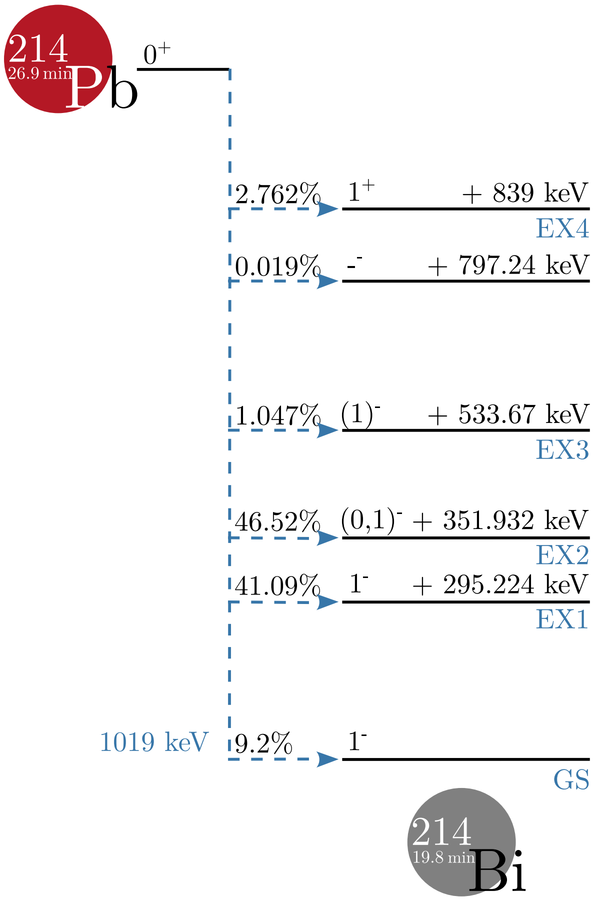

Figure 5.2: ^{214}Pb decay scheme. Branching ratios, energy values and nuclear quantum numbers for angular momentum and parity. All values in the scheme are taken from [63].

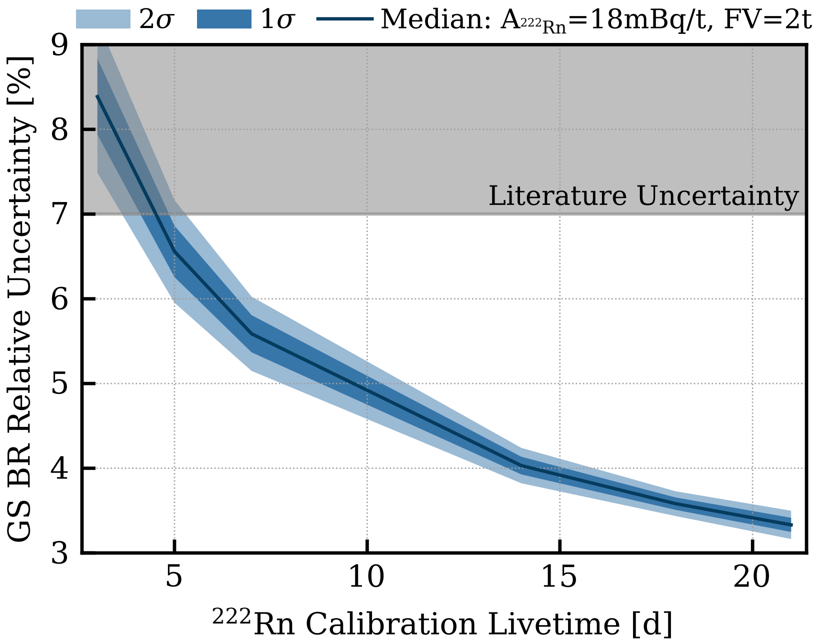

Figure 5.3: Sensitivity study for ^{222}Rn integrating the Q-5 filter in the LXe purification loop. The median sensitivity points have been obtained by simulating 100 calibration runs per livetime with the specifications reported in the figure legend. The 7 % literature reference is reported with a gray solid line.

BR, as was already performed in SR0 for ^{212}Pb (see Chapter 4).

With this aim, two different methods to obtain an enhancement of ^{214}Pb activity in the XENONnT TPC were proposed. The first foresaw the inclusion of the high-efficiency O_2 Engelhard Q-5 purifier [30] filter in the LXe purification loop, utilized in the commissioning phase to boost the LXe purification and later substituted by a filter filled with St707 SAES pills, featuring a reduced radon emanation rate, for cleaner data taking campaigns. The second method proposed involved the usage of a ^{222}Rn calibration sample, already studied in [100], to be placed in the calibration emanation box of the XENONnT GXe loop.

Both these methods were thought to be valid for reaching an enhancement of ^{214}Pb activity, with the aim of improving its GS BR precision. The choice of the method was eventually taken based on the sensitivity studies presented in the next paragraph, where a desired 3 % was targeted.

5.2 Sensitivity study for ^{222}Rn Calibration of XENONnT TPC

In order to understand the feasibility of the ^{214}Pb GS BR direct evaluation with XENONnT enhanced data-set, a sensitivity study was demanded. To this end, the modeling and inference software detailed in Chapter 4 was exploited.

Given the easier realization of the ^{214}Pb enhanced-rate data-set via integration of the Q-5 filter in the LXe purification loop, the sensitivity study aimed, in first instance, to tackle the feasibility of the ^{214}Pb GS BR inference with the ^{214}Pb activity provided with this method, which was expected to be around 18 mBq/t (about 20 times the SR1 nominal value). By considering several data-set lifetimes and for each simulating and fitting 100 runs, the sensitivity curve reported in Figure 5.3 was obtained.

Figure 5.4: (Credits to Florian Jörg, March 2023) XENONnT calibration system source box, with the ^{222}Rn emanating sample (in the center of the picture) just installed by Florian Jörg, Ying-Ting Lin and the author.

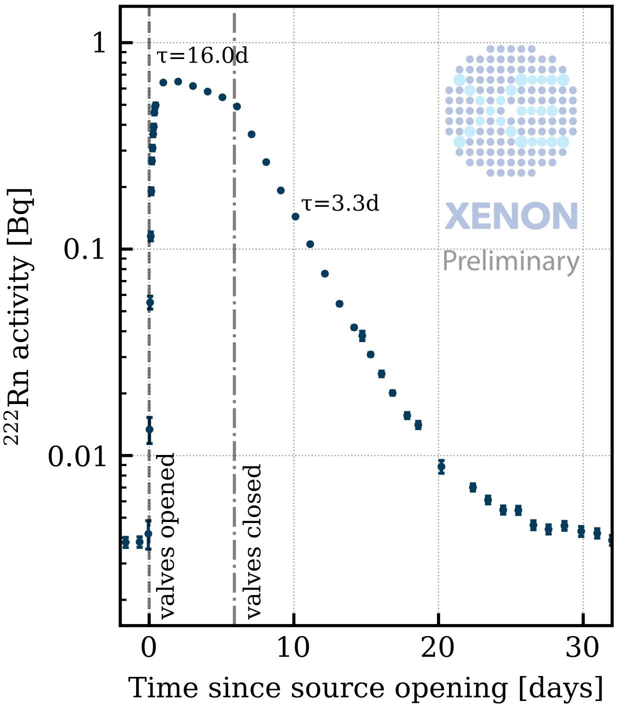

Figure 5.5: (From Collaboration - Ying-Ting Lin) Alpha rate during ^{222}Rn SR1 calibration run, as a function of time. Dashed (dash-dotted) vertical line indicates the time of calibration box valves opening (closing) operations.

This study revealed that by exploiting the Q-5 filter integration, an improvement of the GS BR relative uncertainty with respect to the literature could have been obtained only after 5 d of data taking. Moreover, according to the obtained results the 3 % threshold could never be hit within three weeks of calibration campaign. Thus, the Q-5 filter method was found not to satisfy the desired relative uncertainty threshold while limiting the calibration lifetimes up to few days, that was demanded by the concurrent WIMP analysis.

Therefore, the ^{222}Rn method via calibration sample integration in the GXe loop was chosen, given the estimated activity of 2 Bq yielding to a shorter calibration campaign. The benefits of this approach, with respect of the Q-5 filter one, included:

- a higher radon emanation rate, enabling faster ^{214}Pb statistics collection,
- the absence of contamination risk from Radium-containing dust,
- an improved calibration reliability, given the possibility of an offline characterization of the Radon emanation activity,
- the standardization of the ^{222}Rn calibration procedure for future XENONnT science runs.

For these reasons, in March 2023 the ^{222}Rn calibration sample was mounted in the emanation box (see Figure 5.4) and the calibration campaign took place soon after, so not to spoil the activated source. An on-line alpha-rate monitoring analysis (see Figure 5.5) carried out by the collaboration returned an injected ^{222}Rn activity of about a factor 200 with respect to the SR1 ^{222}Rn background levels. The higher ^{222}Rn activity reached in the TPC with this

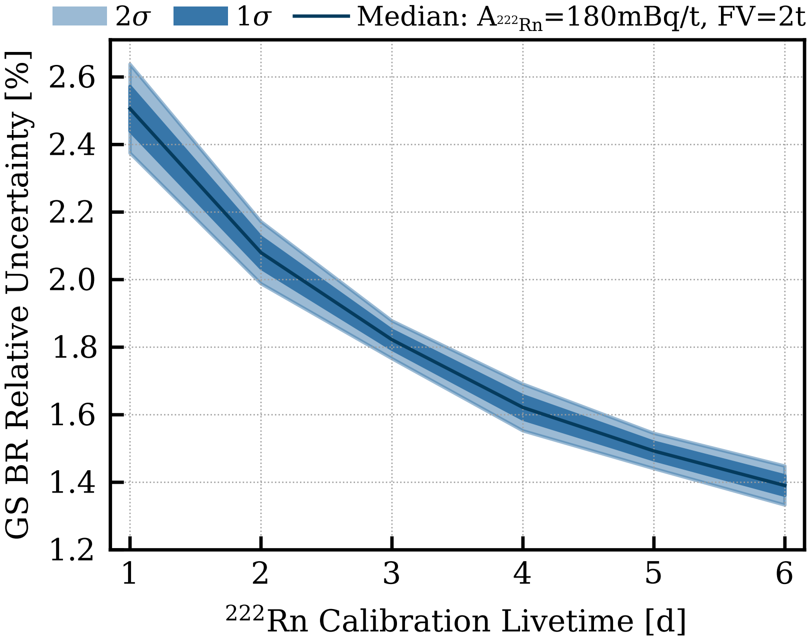

Figure 5.6: Sensitivity study for ^{222}Rn emanating sample in calibration source box. The median sensitivity points have been obtained by simulating 100 calibration runs per livetime with the specifications reported in the figure legend.

method allowed for a shorter calibration period while still providing sufficient statistics for improved GS BR measurements.

By repeating the sensitivity study with the maximum alpha-rate inferred ^{222}Rn activity, it was possible to predict the expected improvement of the ^{214}Pb GS BR relative uncertainty. The results of this updated analysis are reported in Figure 5.6. These results stated that with only few days with this high rate calibration sample, it was possible to improve the literature relative uncertainty by factor beyond 3, by overcoming the set 3 % threshold in less than one day.

These studies have been obtained with the signal and background models presented in Figure 5.7 (representing a simulation example of a 180 mBq/t ^{222}Rn calibration run of 7 days), where only two components for the ^{214}Pb signal have been utilized. After the refinement of ^{212}Pb study of Chapter 4, where every possible decay mode was integrated into the signal modeling, also the ^{214}Pb analysis was modified accordingly. This increased the complexity of the study leading to a worsening of the relative uncertainty of the GS BR in the final inference, mainly due to the increased correlations among the signal spectra rate multipliers. Moreover, the simulations performed for the sensitivity study considered an activated background (constituted from $^{131\text{m}}$Xe, $^{129\text{m}}$Xe and^{133}Xe) rate comparable to that observed in SR0, since SR1 ^{241}AmBe calibration was not yet performed and activated background s rates were not predictable. Unfortunately, the final observed SR1 rate was much higher than expected slightly impacting on the resulting ^{214}Pb GS BR relative uncertainty.

5.3 Data Selection and Cut Efficiency Curves

In this study both the SR1 ^{222}Rn calibration and background data-sets have been exploited. After the sensitivity studies, rejecting the hypothesis of utilizing the integration of the Q-5

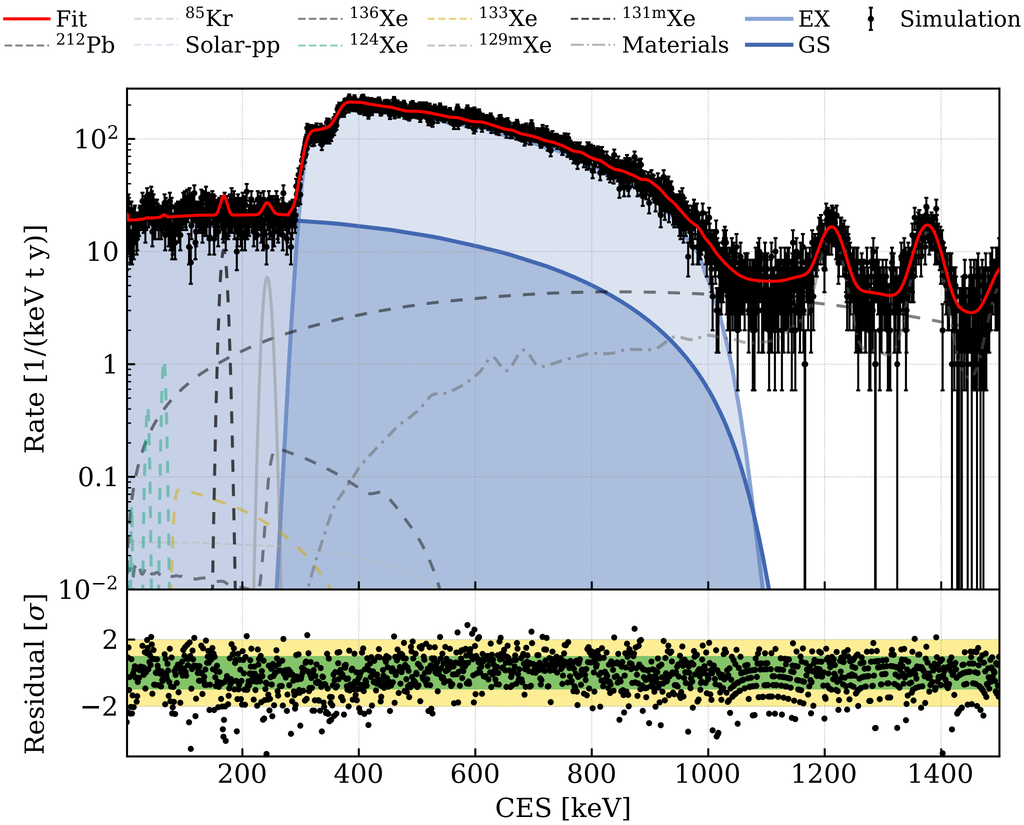

Figure 5.7: Example of simulated data for ^{214}Pb GS BR sensitivity studies relative to a ^{222}Rn activity of 180 mBq/t and 7 days of calibration. Signal models for the ground state (GS) and the cumulative excited states (EX) are represented with blue and light-blue solid lines filled templates. The background components, considered at the time of the sensitivity studies with the same activity observed in SR0 data, are reported with dashed and dash-dotted lines. A deeper investigation of the XENONnT ^{222}Rn calibration data revealed the presence of other components that were later included in the background model. The non-perfect Gaussian behavior of the residuals is due to the difference between simulations and fitting frameworks, where the first included a full ^{214}Pb GEANT4 spectrum, while the second utilized the GS theoretical forbidden spectrum of [135] and, as EX template, the GEANT4 ^{214}Pb full spectrum subtracted by the GS allowed version contribution as the EX template. The background contribution labelled as Materials is the simulated template comprehensive of every detected radioactive contaminant in the materials surrounding the TPC, as reported in [56].

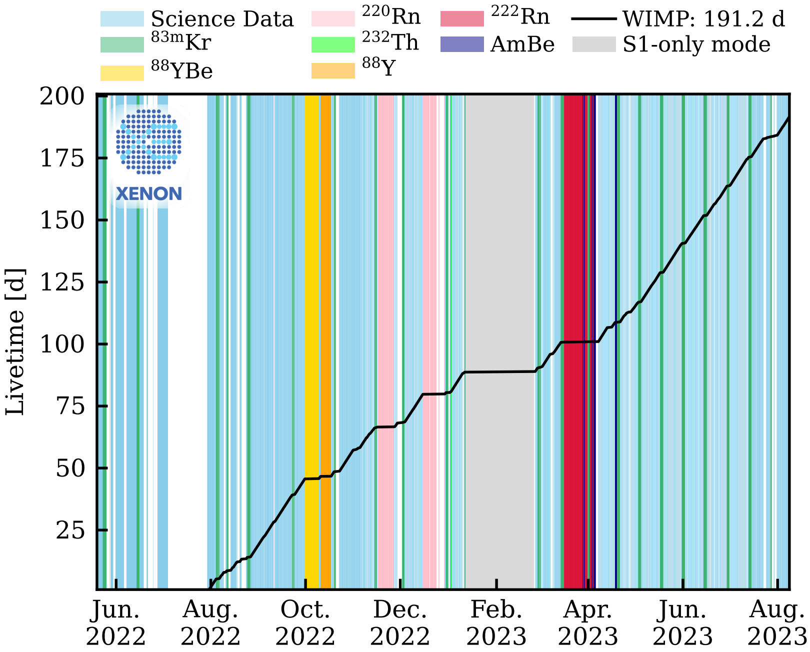

Figure 5.8: (From Collaboration) WIMP SR1 cumulative lifetime (black solid line). The growth rate of SR1 lifetime is discontinuous due to either foreseen calibration campaigns (represented as colored bands) or general maintenance operations (gray bands). ^{222}Rn calibration campaign (red band) was closely followed by and ^{241}AmBe one.

filter, the ^{222}Rn calibration campaign was performed by means of ^{222}Rn emanation sample. Given that the predictions were suggesting that with only few days of data taking enough precision on ^{214}Pb GS BR could have achieved, an ^{241}AmBe calibration campaign was performed soon after with the aim of reducing WIMP analysis dead-time. These operation timings can be deduced from Figure 5.8, where the SR1 campaign and WIMP analysis livetime are illustrated.

As in the ^{212}Pb analysis, the data selection for this study closely followed that of the corresponding science run WIMP search. Thus, data-sets were selected with a first rejection of runs tagged as *messy* or including some labels referring to possible warm or hot spot bursts as described in [89].

Moreover, in order to limit the impact of source-induced background with strong spatial dependence, a fiducial volume (FV) selection was exploited. As performed already for the ^{212}Pb analysis, the FV was designed accordingly to the optimization of the following figure of merit (described in [132]):

$$\mathrm{FOM} = \frac{S}{\sqrt{S+B}} \propto \frac{M}{\sqrt{\sum_{i\in \mathrm{ROI}} N_i}}, \tag{5.1}$$

where S and B are the signal and background rates. Since the S is supposed to be uniform within the TPC, it results proportional to the considered mass M. The denominator, instead, can be computed by considering both the signal and background components affecting the ^{214}Pb GS ROI. For this analysis, the N template was obtained by summing up the contributions of the simulated ^{214}Pb full spectrum, the SR1 background template properly scaled and the simulated source-induced background contributions. These latter, similarly to the case of ^{212}Pb, are due to ^{214}Bi in the outer TPC LXe layer, labelled as ^{214}Bi *skin*, and to ^{214}Pb plated-out onto the PTFE panels at the border of the TPC, labelled as ^{214}Pb *PTFE*.

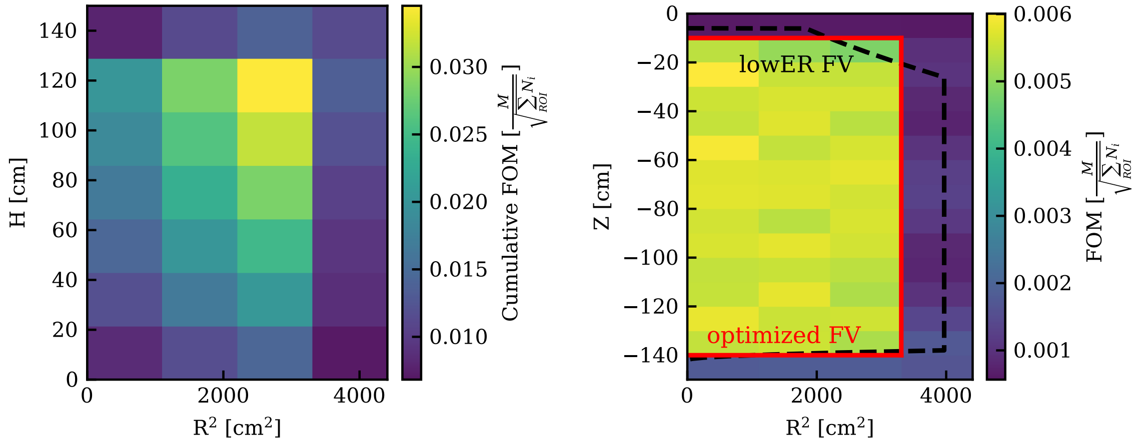

(a) FOM for cylindrical FV different heights and radii.

(b) Optimized FV.

Figure 5.9: Fiducial volume optimization by maximization of FOM of Equation 5.1. Left (Figure (a)) FOM computed for different cylindrical volume data selections; the computed FOM is referred to the cylindrical fiducial volume with radius and height indicated by the top-right corner of each rectangle. Right (Figure (b)) FOM computed in equal-mass TPC portions (color map), optimized fiducial volume for ^{212}Pb branching ratios analysis (red solid line) and low-energy electron recoil analysis FV [133].

The result of this maximization returned the same exact cylindrical volume of ^{212}Pb analysis, corresponding to 3.71(12) t of LXe. In Figures 5.9(a) and 5.9(b) this result are reported.

On top of this first geometrical selection, some quality cuts, listed in Table 5.2, have been applied to clean the ^{222}Rn calibration and SR1 background data-sets. As already done with SR0 data [56], the S2 single scatter prior cut was validated for extended CES energy ranges with respect to the standard WIMP ROI. The result of this study exploiting SR1 data and simulations is presented in Figure 5.10. As evident from this plot, the simulated points present a relative bias with respect to the data. This reinforces the evidences already presented in other SR1 studies [102]. For this reason, the CES bias nuisance offset parameter optimized in the fit was also used to reshape the cut efficiency curves in the fit procedure. Beyond the possible CES bias offset, the discrepancies visible in Figure 5.10 can also be explained by the fact that simulations only take into account the ^{214}Pb signal, while in the subtracted data-set some non-constant background could play a non-negligible role.

The final cut acceptances, taking into account the cuts listed in Table 5.2, in SR1 CES space, are illustrated in Figure 5.11. It is worth noting that, due to the variation of the electric field settings, SR1 CES differs from the one computed in SR0. Once again, also in this case, it is clearly visible the presence of a bias between the two curves, reinforcing the need of reshaping the cut acceptance curves in the fit procedure.

5.4 Background and Signal Model Components

The ^{222}Rn calibration data-set compared to the SR1 background data, both after the application of the FV and quality cuts selection rules, are shown in Figure 5.13.

As in the ^{212}Pb analysis presented in the previous Chapter, also in this case the science run background data have been used as template for constant backgrounds. Neutron sources activated backgrounds (^{131m}Xe, ^{131m}Xe and ^{133}Xe) are included in the fit with the purpose of reducing the impact of their rate in the SR1 background. This happens since, differently from

Table 5.2: (Inspired by [56]) Data selection adopted in the ^{214}Pb branching ratios analysis. The table reports the name of the cuts and their description. Cuts highlighted in dark gray are used as prior selections for both simulations and observed data, those highlighted in light gray are used as pre-selections for data only and those that are not highlighted are used as quality cuts. Upon these latter the cut acceptance is computed. For the electrons cut acceptance only the cut__s2__single__scatter was used as a quality selection rather than a prior one.

Cut name	Description
cut__daq__veto	Rejects events that are too close to a hardware veto start or stop.
cut__run__boundaries	Removes events that are too close to the boundaries of a data acquisition period (a run), for which some event information could be lost.
cut__main__is__valid__triggering__peak	Selection which ensures that at least either the main S1 or main S2 is considered a triggering peak. Otherwise, this is most likely an accidental coincidence.
cut__interaction__exists	Simple cut to select (S1; S2) events.
cut__s1__tightcoin__3fold	Selects events with at least 3 PMTs contributing with hits within tight symmetrical range of 50 ns from the peak center.
cut__fiducial__cylinder__3700kg	Selects the events inside the optimized fiducial volume.
cut__s2__single__scatter	Based on the size of the alternative reconstructed S2, it rejects MS events.
cut__s1__max__pmt	Reject events in which a PMT contributes most of the entire S1 area, mainly due to spurious PMT light emission or PMT after-pulses. It effectively rejects AC events. The selection threshold varies with the depth of the TPC: Towards the bottom of the TPC, events are more localized, and the threshold is less rigid.
cut__s2__width	Reject events with unusual S2 width for the position where they have been reconstructed. Due to the presence of perpendicular wires, which distorts the electron cloud trajectory, the rejection threshold has two definitions depending on whether the events are reconstructed near or far from the wires. It rejects MS, AC and non-physical events.

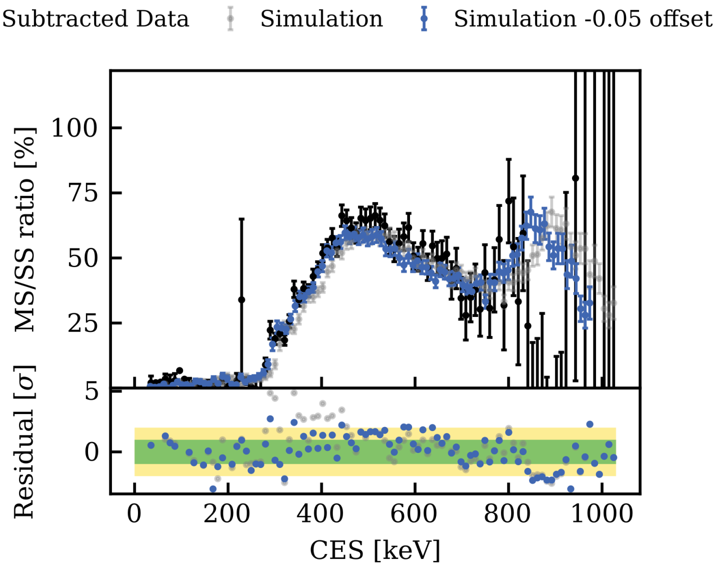

Figure 5.10: The MS-SS ratio as a function of the CES from ^{214}Pb data (black) subtracted from SR1 constant background contribution, full chain simulation (gray points) and its shifted version (blue points) is shown. The residual between the data and simulation (gray points) and data and shifted simulation (blue points) are shown in the bottom panel. In the highest energy region the data points relative error increases because of the low statistics.

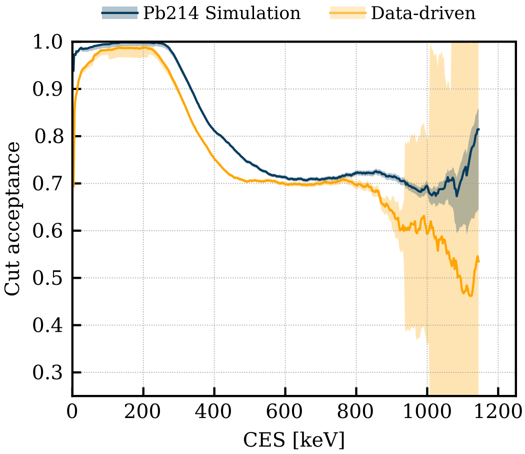

Figure 5.11: Simulation- and data-driven cut acceptance curves comparison for ^{214}Pb.

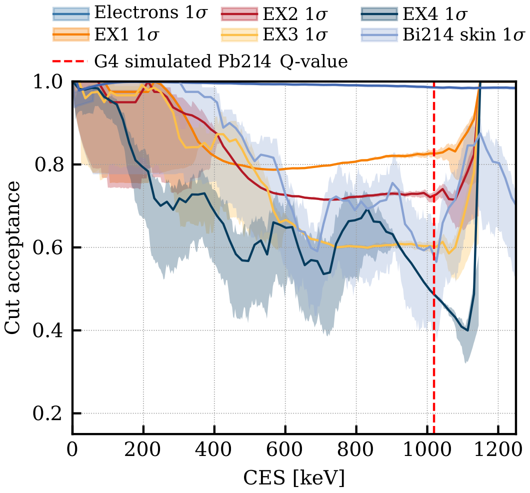

Figure 5.12: Cut acceptance curves for signal and background components for ^{214}Pb analysis.

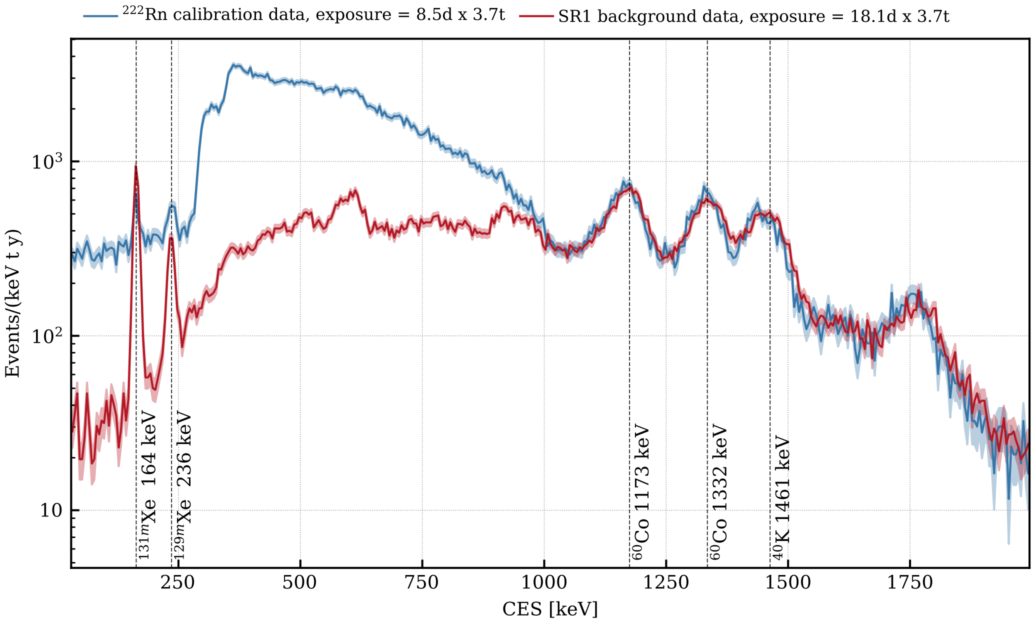

Figure 5.13: XENONnT SR1 ^{222}Rn calibration (in blue) and background data (in red) binned in the SR1 CES space. The most relevant gamma peaks are marked with a black dashed line and labeled with the respective isotope and energy.

SR0, the ^{241}AmBe neutron calibration was performed after the Radon one, re-activating the Xenon backgrounds. This translates into a much higher rate of $^{131\mathrm{m}}$Xe, $^{131\mathrm{m}}$Xe and ^{133}Xe in SR1 background data with respect to the ^{222}Rn calibration, as visible in Figure 5.13, particularly for $^{131\mathrm{m}}$Xe peak.

Furthermore, two source-induced backgrounds are considered in the fit model. The first, denoted ^{214}Bi skin, is generated by ^{214}Bi isotopes which decay in the LXe hosted in the cryostat but outside the TPC. The second, denoted ^{214}Bi skin, is due to ^{214}Pb plating out on the Teflon surfaces. Given its subdominance with respect to the former, this latter model template was built considering the Electrons cut efficiency of Figure 5.12.

As far as signal modeling is concerned, differently from what illustrated in Figure 5.2, only five different spectra and hence decay modes were considered. Indeed, the decay mode with the smallest predicted branching ratio was not included in the model, not only because of the possible reduced sensitivity, given the statistics collected, but also because of the two main literature references that do not agree on its existence. Among the five considered spectra, one represents the GS decaying mode modeled via theoretical template from [135], while the others are GEANT4 simulated templates of the decay modes labeled in Figure 5.2 with blue tags from EX1 to EX4.

5.5 Branching Ratio Results from the Fit

Once the model components are set, the fit on data can be performed. The very same statistical framework and computation of the final measurements performed in the previous Chapter have also been exploited in this case. With the best-fit signals rate multipliers

Table 5.3: ^{214}Pb branching ratios study fit results. Gray highlighted entries mark nuisance parameters.

Parameter	Best Fit Value	Hesse Error
^{214}Pb GS	0.095	0.003
^{214}Pb EX1	0.416	0.007
^{214}Pb EX2	0.417	0.009
^{214}Pb EX3	0.019	0.006
^{214}Pb EX4	0.028	0.005
^{83m}Kr	0.0	0.05
^{129m}Xe	-30	8
^{131m}Xe	-15.4	0.7
^{133}Xe	-2	6
^{214}Bi skin	0.38	0.19
^{214}Pb PTFE	0	30
SR1 background	1.000	0.004
A	0.0067	0.0004
k	0.020	0.012
c	-0.0097	0.0005
a	0.38	0.03
b	0.004	0.002
α	1.982	0.009
β	-1.231	0.005
ϵ_{Bi}	0.0	0.8
$\epsilon_{\text{Electrons}}$	0.0	0.8
ϵ_{PbEX1}	0.0	1.4
ϵ_{PbEX2}	0.00	0.03
ϵ_{PbEX3}	1.0	0.3
ϵ_{PbEX4}	0.0	0.8

reported in Table 5.3 it is possible to compute the BRs exploiting the following relation:

$$\text{BR}_i = \frac{\text{RM}_i}{\Sigma} \tag{5.2}$$

$$\begin{aligned} \sigma^2_{\text{BR}_i} &= \sigma^2_{\text{RM}_i}\frac{(\Sigma - \text{RM}_i)^2}{\Sigma^4} \\ &+ \sum_{j>i}\left(\sigma^2_{RM_j}\frac{(RM_{GS})^2}{\Sigma^4} + -2\sigma_{ij}\text{RM}_i\frac{\Sigma - \text{RM}_i}{\Sigma^4} + 2\sum_{k>j}\sigma_{jk}\frac{(\text{RM}_i)^2}{\Sigma^4}\right), \end{aligned} \tag{5.3}$$

where $\Sigma = \sum_l \text{RM}_l$, RM_i is the best fit rate multiplier value of the ^{212}Pb state i. The measured ^{214}Pb BRs results are reported in Table 5.4.

In order to give a more solid idea about the outcome of this study a simple goodness

Table 5.4: Results of the ^{214}Pb branching ratios analysis. The reported uncertainties are here only determined by the analysed statistics.

^{212}Pb state	Branching Ratio [%]
GS	9.8 ± 0.3
EX1	42.6 ± 0.8
EX2	42.8 ± 0.9
EX3	1.9 ± 0.7
EX4	3.0 ± 0.5

Table 5.5: Z-test statistics for ^{214}Pb branching ratios result compared to the literature values of LNHB and NDS, including systematic uncertainties.

^{214}Bi state	LNHB Z-test statistics	NDS Z-test statistics
GS	0.79	-2.41
EX1	1.70	3.82
EX2	-3.82	-1.49
EX3	0.85	0.84
EX4	0.26	0.28

of fit test was performed, following the indications reported in [129]. By exploiting the *GOFevaluation* python package [101], with an observed Poisson chi-square value of about 230.8, we computed a p-value of about 0.074. For completeness the result of this fit are reported in Figure 5.14.

5.5.1 The Branching Ratio Estimation and Potential Systematic Sources

This measurement method may be affected by systematic uncertainties or biases introduced by the configuration choices arbitrarily done, such as the bin width, the ROI considered or the data-set selected, or set as a result of an optimization process, such as the fiducial volume selection. For this reason this analysis is repeated for different settings of these configurations. For the sake of simplicity, only the results for the GS BR case are reported in Figures 5.15. In a very conservative way, we consider as systematic uncertainty introduced by each configuration setting (bin width, ROI, FV and data-set runs selection) the maximum difference between the reference measurement and the other measurements, requiring migrations of nuisance parameters up to 2σ from the reference ones. The measurements not meeting this requirement were referred in Figures 5.15 as invalid. For example the measurement obtained with 7 keV bin width and 1 t FV, given the migration of the energy bias c nuisance parameter (see Figure 5.16) were excluded from the computation of the systematic uncertainties.

Eventually, these systematic uncertainties are combined to get the estimate of the total systematic uncertainty of the measurement. The final results quoting systematic uncertainties are:

$$\mathrm{BR_{GS}} = 9.8 \pm 0.3(\mathrm{stat})^{+0.8}_{-0.0}(\mathrm{sys})\,\% \tag{5.4}$$

$$\mathrm{BR_{EX1}} = 42.6 \pm 0.8(\mathrm{stat})^{+1.9}_{-0.2}(\mathrm{sys})\,\% \tag{5.5}$$

$$\mathrm{BR_{EX2}} = 42.8 \pm 0.9(\mathrm{stat})^{+0.1}_{-0.9}(\mathrm{sys})\,\% \tag{5.6}$$

$$\mathrm{BR_{EX3}} = 1.9 \pm 0.7(\mathrm{stat})^{+0.2}_{-1.0}(\mathrm{sys})\,\% \tag{5.7}$$

$$\mathrm{BR_{EX4}} = 3.0 \pm 0.5(\mathrm{stat})^{+0.3}_{-0.9}(\mathrm{sys})\,\% \tag{5.8}$$

For a more illustrative representation of these results compared to the literature values of Table 5.1, Figure 5.17 is reported. Quantitatively, by comparing, by means of the Z-test statistics, these measurements to the literature values reported in LNHB and NDS we get the results reported in Table 5.5. From these values, it is possible to state that this study ^{214}Pb GS BR measurement presents a greater agreement with LNHB reference value, from which it differs by only 0.79σ. Although there is this strong agreement at the GS level, for the excited states BRs, except for EX4 characterized in this measurement by a large statistical error, no strong preference among the two references is found.

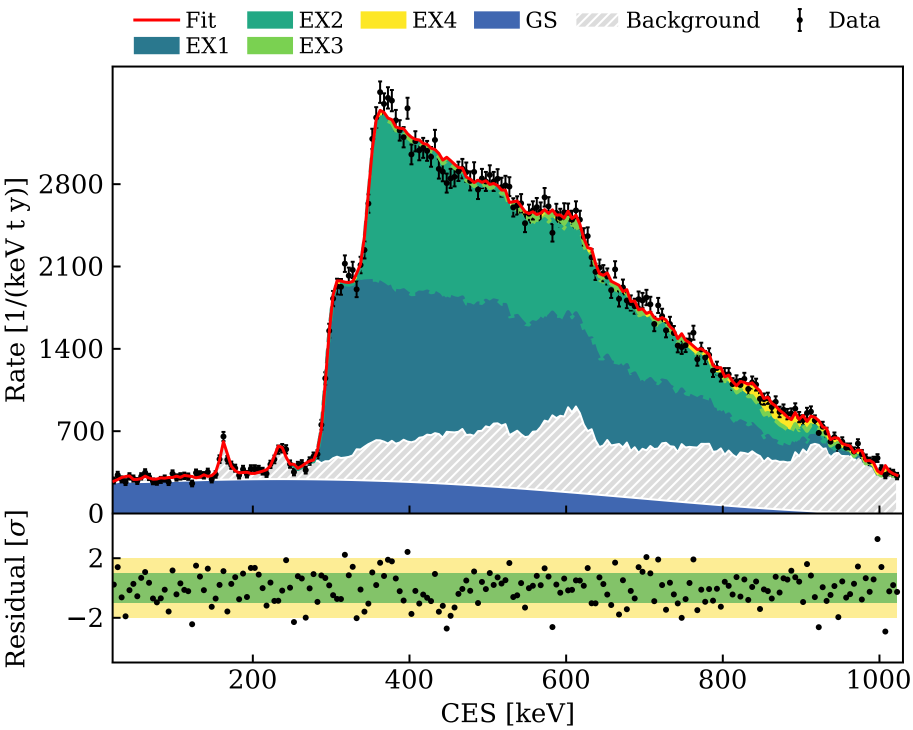

(a) ^{222}Rn binned data-set fit. Fit model components are stack and non-signal contributions are grouped in the *Background* template (gray).

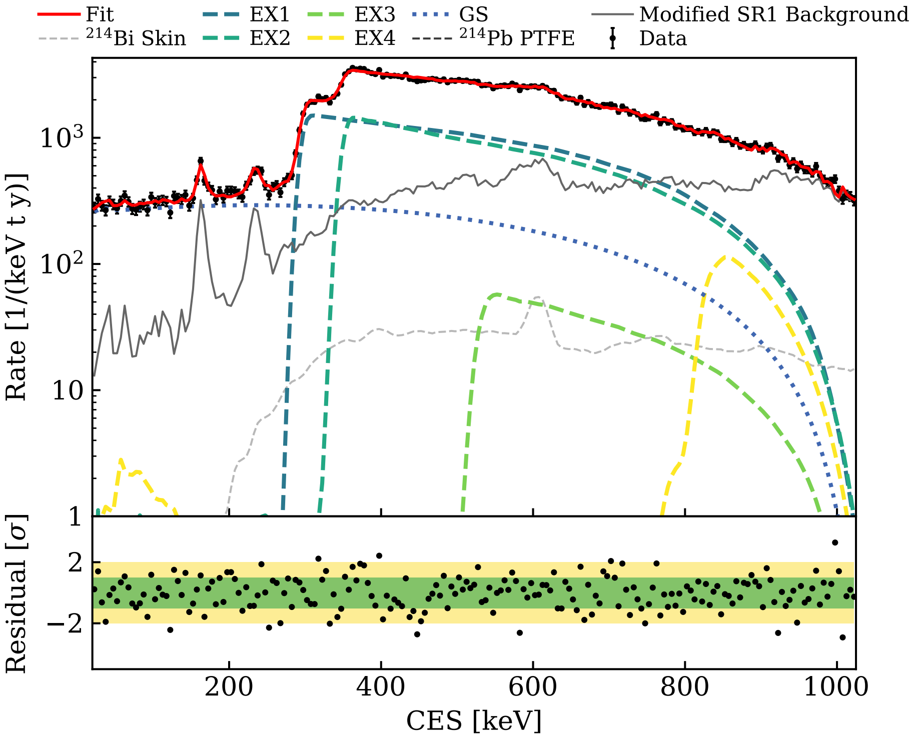

(b) ^{222}Rn binned data-set fit in y-axis log scale. Fit model components are depicted in *viridis* shades if signal contributions or in gray shades if background ones. Additionally, dashed lines represent fit model components from GEANT4 templates, the dotted line depicts the theory model (^{214}Pb ground state) and the solid one labels the data-driven template (SR1 background) subtracted from the negative contribution of activated backgrounds (^{129m}Xe, ^{121m}Xe and ^{133}Xe).

Figure 5.14: Final result of ^{214}Pb branching ratio analysis. ^{222}Rn binned data-set fit showed for linear (a) and logarithmic (b) y scale.

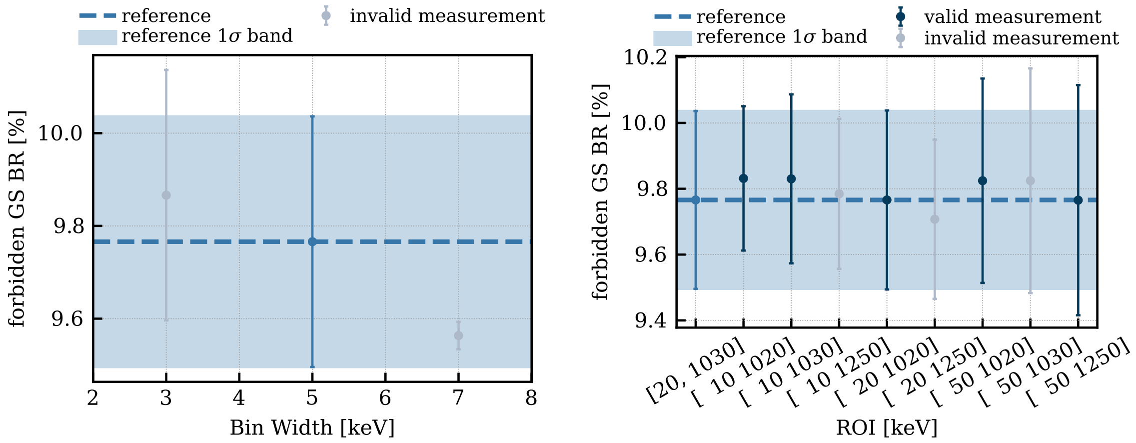

(a) GS BR measurement for different bin width.

(b) GS BR measurement for different ROI.

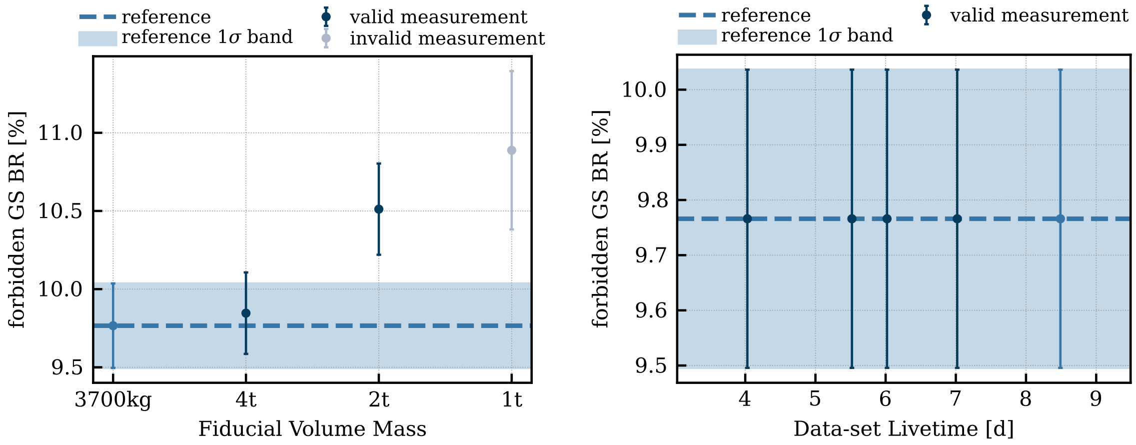

(c) GS BR measurement for different FV.

(d) GS BR measurement for different data-set livetimes.

Figure 5.15: ^{214}Pb GS branching ratios measurements with different bin width, ROI, FV and data-set livetime configurations settings for the fit (dark blue points). Reference measurements are reported as light-blue points and dashed horizontal lines, along with their light-blue 1σ band.

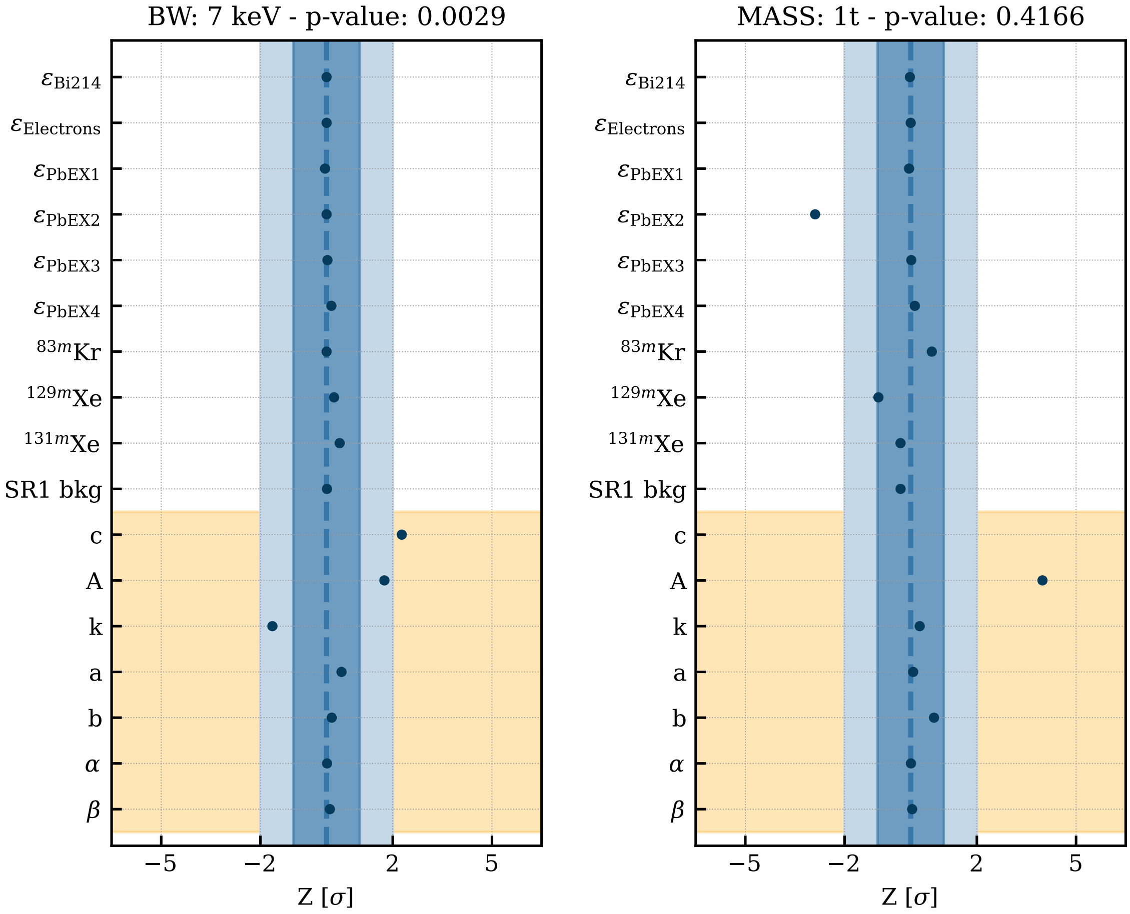

(a) 7 keV bin width.

(b) 1 t FV.

Figure 5.16: Results of ^{214}Pb fit considering 7 keV (a) bin width and 1 t (b) FV. The migration of the energy bias nuisance parameter c, above 2σ, reject the possibility of using the 7 keV bin width and 1 t FV measurements in the computation of the systematic uncertainty.

5.5.2 Discussion on Results

The results obtained in this work represent the most precise direct measurement of the ^{214}Pb branching ratios to the ^{214}Bi ground and excited states. Specifically, by directly accessing these values from the ^{222}Rn calibration data, we achieved an enhanced precision on the branching ratio to the ^{214}Bi ground state. Indeed, its relative uncertainty was reduced of about a factor 2.5, from about 7.6 % to about 3.1 %, if only considering the statistical error. If considering also the systematic uncertainty, the relative error of this measurement is found to be slightly larger than the LNHB reference.

This study represents a step ahead in the attempt of solving the tension present in the current literature, concerning the ^{214}Pb GS BR. Indeed, this study results show a strong agreement with the LNHB reference value and are in line with direct measurements, dating back to 1950s, as illustrated in Figure 5.18. This measurement represents a step forward in the possible solution concerning current literature tension, introducing the novelty of a low-background direct precision assessment. Indeed, by exploiting the XENONnT ^{222}Rn calibration data, by means of modeling and fitting technique, it is not only possible to directly measure the ^{214}Pb GS BR, but also to concurrently probe ^{214}Pb BR to every ^{214}Bi excited

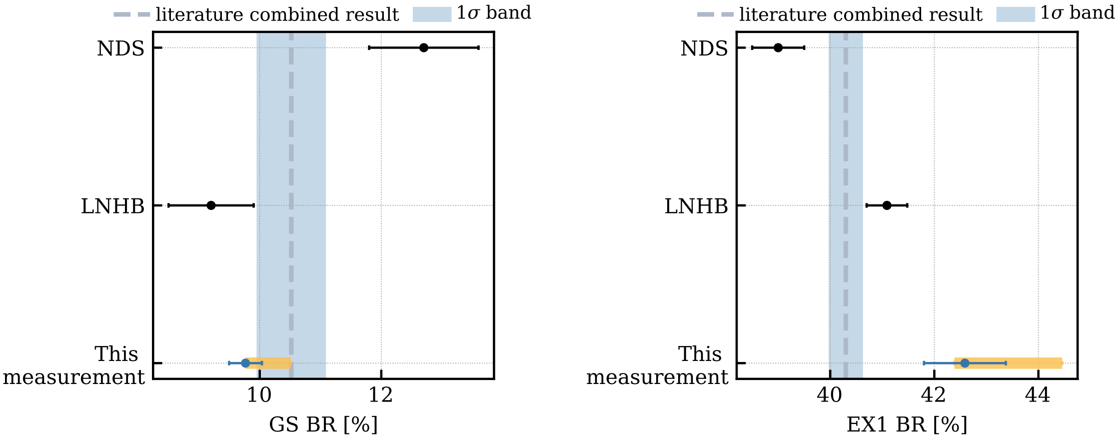

(a) GS BR literature comparison. (b) EX1 BR literature comparison.

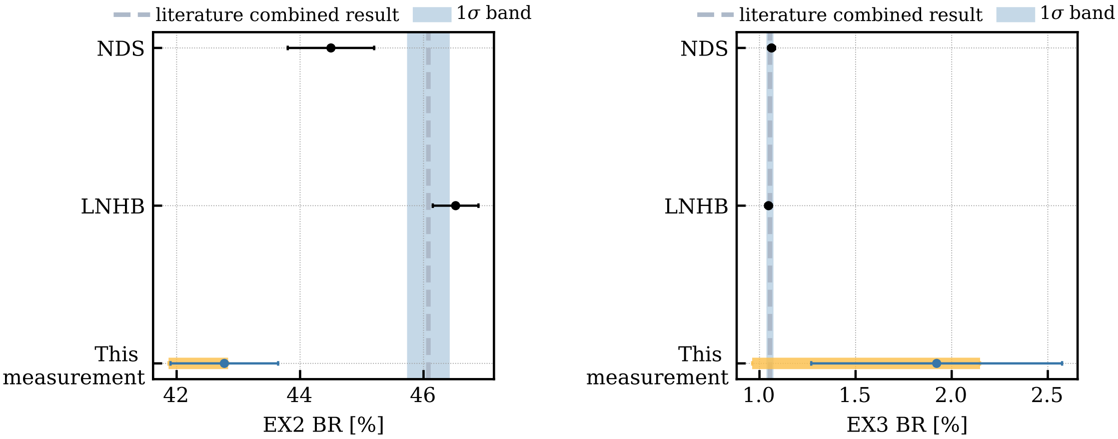

(c) EX2 BR literature comparison. (d) EX3 BR literature comparison.

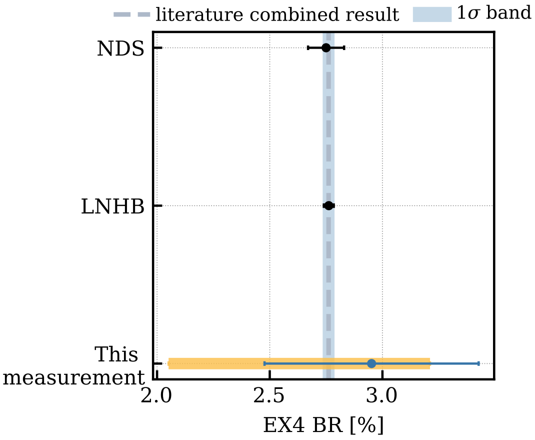

(e) EX4 BR literature comparison.

Figure 5.17: ^{214}Pb GS, EX1, EX2, EX3 and EX4 branching ratio measurements compared to the literature values of Table 5.1 (balck points). This work measurements are reported with light-blue points, light-blue statistical uncertainties and yellow error bars for systematic ones. Combined literature value, computed by means of weighted average, is represented with vertical gray dashed lines and light-blue bands for their uncertainties.

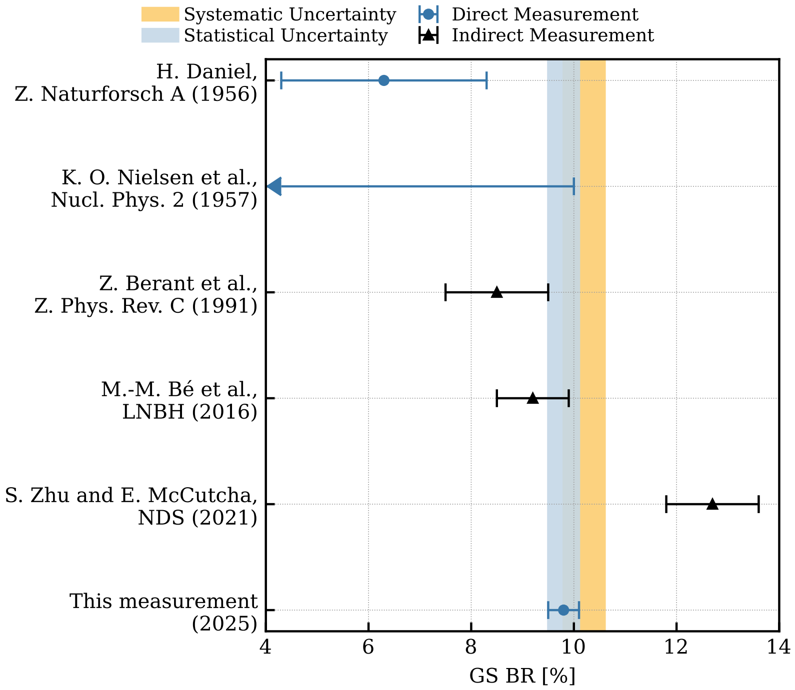

Figure 5.18: Comparison of this study ^{214}Pb GS BR measurement with the literature reference values. Y-axis reports the publications details, while the nature of the assessment, if direct or indirect is shown from the color, blue for the former, black for the latter. All reported direct measurements in the literature were conducted in the 1950s [143, 144]. Instead, indirect reference are more recent and are mainly computed starting from gamma-ray energy balances and recommended internal conversion coefficients [63, 141]. This measurement represents a step forward in the possible literature tension solution, introducing the novelty of direct precision assessment. Indeed, by exploiting the XENONnT ^{222}Rn calibration data, by means of modeling and fitting technique, it is not only possible to directly measure the ^{214}Pb GS BR, but also to concurrently probe ^{214}Pb BR to every ^{214}Bi excited state, reducing the systematic impact.

state, reducing the systematic impact. Moreover, thanks to the reproducibility of the ^{222}Rn calibration method, involving a ^{222}Rn emanation sample [100], a further refining of this measurement can easily be performed in the future, by collecting more statistics. Furthermore, improvements of the ^{214}Pb GS BR measurement can be gained once theoretical spectral shapes for ^{214}Pb decaying towards ^{214}Bi excited sates [136] will be exploited. Nevertheless, these upgrades will have a negligible impact on the precision of this measurement that can mainly be improved with new calibration data-sets.

Moreover, this study proved the feasibility of exploiting a low-background experiment, such as XENONnT, for high-precision nuclear physics measurements overcoming the standards of sensitivities of the techniques currently utilized in this field of searches. It is thus probable to expect in the near future, given the rising scientific interest, highlighted by recent publications [102, 137–139], to have access to new direct ^{214}Pb GS BR measurements. These latter would then provide more insights about the current literature tension, potentially validating this study results.

6

^{210}Pb: The TPC Surface Background

The Radon outgassing phenomenon is not the only process that introduces to the WIMP searches lead-induced background events in the LXe active volume. Indeed, PTFE panels and pillars outlining the borders of the TPC introduce the long-lived ^{210}Pb contaminant at the edges of the LXe active volume. The highly-pure PTFE panels and pillars contamination comes from the Radon daughters plate-out phenomenon occurring during the pre-commissioning phase of the XENONnT experiment.

In this chapter a comprehensive study on the ^{210}Pb induced background is illustrated. After a first introductory part about the origins of the ^{210}Pb surface background in 6.1 and the impact it has on the XENONnT WIMP searches in 6.2, the inference framework in 6.3 and the modeling of this background in 6.4 are described. Eventually, the results of this study are reported in 6.5 and a later upgrade for SR1 data is also briefly discussed in 6.6. Unless otherwise specified, all material presented in the following Chapter is original and has been produced by the author of this Thesis.

6.1 On the Origins of the ^{210}Pb Surface Background

In designing a detector which aims to unprecedented levels of sensitivity for rare-events physics searches, the selection of the structural material plays a crucial role. Generally, this choice is the result of a compromise between mechanical, thermal and optical properties of the object and the amount of background introduced in the region of interest of the experiment physics searches.

In the case of XENONnT TPC, PTFE was chosen to delimit the LXe active volume, thanks to its radio-purity and high Xenon vacuum ultraviolet light reflectivity. However, as already discussed in Chapter 3, PTFE surfaces are corrupted by Radon progeny plate-out when exposed to air during the detector construction phase [103]. This process is enhanced by both the triboelectric effect of PTFE and by the high probability that Radon progeny has to carry a positive electric charge, estimated to be larger than 85 % [113].

The continuous implantation of ^{222}Rn daughter nuclei on Teflon surfaces, when exposed to air, is interrupted at the moment in which the material is isolated. This leads to the decay of the implanted radioactive isotopes, causing the accumulation of ^{210}Pb within few hours.

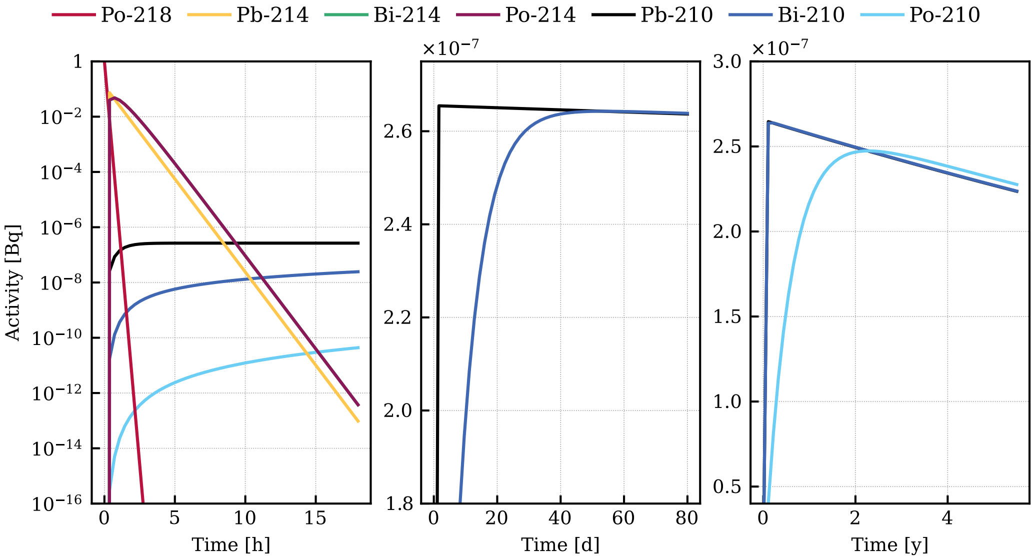

Figure 6.1: Activity trend for Radon progeny computed with radioactivedecay python package [145]. The plotted curves refer to an isolated system (no further injection of ^{218}Po after $t_0 = 0\,\mathrm{s}$) with an initial ^{218}Po activity of 1 Bq, supposing the plate-out phenomenon only involves ^{218}Po nuclei (an activity of 0 Bq at $t_0 =$ is thus assumed for the progeny isotopes). Moreover, the following isotopes half life values were used: $t_{1/2}(^{218}\mathrm{Po}) = 3.10\,\mathrm{m}$, $t_{1/2}(^{214}\mathrm{Pb}) = 26.8\,\mathrm{m}$, $t_{1/2}(^{214}\mathrm{Bi}) = 19.9\,\mathrm{min}$, $t_{1/2}(^{214}\mathrm{Po}) = 0.1643\,\mathrm{ms}$, $t_{1/2}(^{210}\mathrm{Pb}) = 22.20\,\mathrm{y}$, $t_{1/2}(^{210}\mathrm{Bi}) = 5.013\,\mathrm{d}$ and $t_{1/2}(^{210}\mathrm{Bi}) = 138.376\,\mathrm{d}$. The three panels highlight different critical moments of the isotopes activity evolution. (Left) In the first few hours after the system isolation ^{210}Pb (black solid line) reaches its maximum activity, to which its seems to stabilize given the narrow timescale, while progenitor nuclei activity quickly drop, reaching in less than 15 h values of factor 10^3 less than that of ^{210}Pb. (Center) After about 50 d ^{210}Bi (blue solid line) reaches the secular equilibrium of its parent ^{210}Pb. (Right) Given the high ^{210}Po half life, its activity (light blue solid line) stops increasing only after about 2 y and starts dropping with a rate slightly larger than that of ^{210}Pb.

The secular equilibrium between ^{210}Pb and ^{210}Bi will only be set after several weeks.

These statements are the result of a simplified model, showed in Figure 6.1, where the activities of ^{222}Rn radioactive progeny are compared. This model, based on numerical computation, assumes an initial activity of 1 Bq for ^{218}Po, as it is the only ^{222}Rn chain component implanted at the time of the system isolation. As the radioactive system evolves, after only about 50 d, ^{210}Pb and ^{210}Bi reach secular equilibrium, dictated by the long half life of ^{210}Pb of about 22.3 y, while ^{210}Po accumulates, reaching its maximum activity only after 2 y.

Although the real contamination process is more complex than the model here reported, it is still possible to assume that the order of magnitude of the time scales set still holds true, with ^{210}Pb accumulation occurring in about few hours and secular equilibrium between ^{210}Pb and ^{210}Bi and between ^{210}Pb and ^{210}Po respectively reached in a month and in few years. It is thus possible to assume that, given one year-long XENONnT commissioning phase during which the Teflon panels have been isolated from the Radon-laden air, the secular equilibrium condition for the ^{210}Pb chain was approximately met when the data-taking of the first science run started.

The obtained contamination of ^{210}Pb, characterized by a very long half life and located in direct contact with LXe sensitive volume, introduces the nearly constant background to WIMP searches known after the name of *wall* or *surface* background.

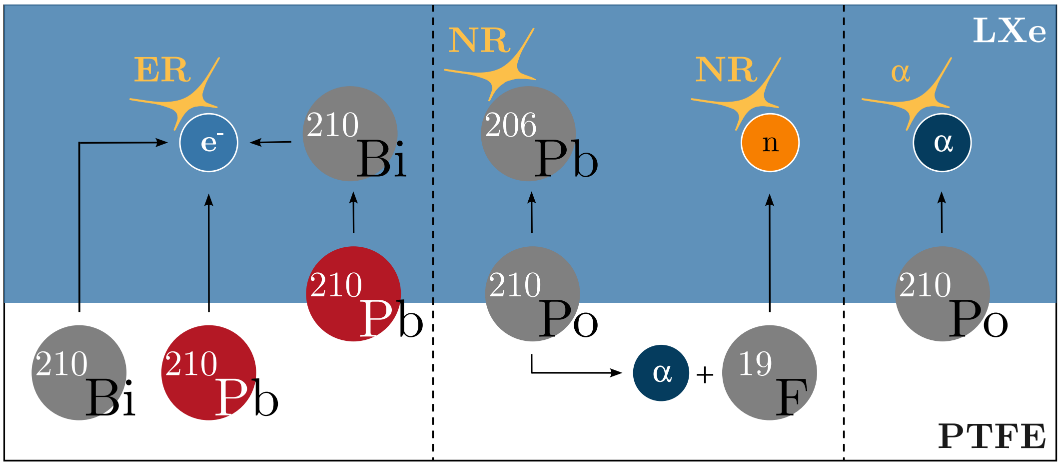

Figure 6.2: (Inspired by [112]) Decay reactions from Radon daughter plate-out on the surface of a detector wall that may produce prominent backgrounds in dark matter detectors. (Left panel) A beta decay reaction of ^{210}Bi or ^{210}Pb and of ^{210}Bi released by ^{210}Pb decay on the surface relinquishes an electron into the volume generating an electron recoil signal. (Middle panel) Generation of nuclear recoil signals via ^{210}Po decay emitting a ^{206}Pb nucleus that recoils into the detector volume or an alpha particle from ^{210}Po decay on the surface interacting with a fluorine atom in the Teflon wall causing neutron emission in the sensitive volume. (Right panel) An alpha decay of ^{210}Po on the surface releases an alpha particle into the detector volume.

6.1.1 Phenomenology of the ^{210}Pb Surface Background

Differently from ^{214}Pb, responsible for the ER background to WIMP searches (see Chapter 3 and 5), ^{210}Pb surface background is not only characterized by beta particles interacting with the atomic electrons of LXe target. Indeed, as shown in the scheme of Figure 6.2, the phenomenology of this background is more complex and triggers different classes of events: ER, NR and alpha interactions. ER events are triggered by electrons emitted in the beta decay processes of either Teflon implanted ^{210}Pb and ^{210}Bi or by ^{210}Bi nuclei released in LXe from a previous ^{210}Pb surface decay. NR events are instead generated either directly by recoiling daughter nuclei produced at the surface, that are expected to interact in a narrow neighborhood of it, or indirectly by the Fluorine-19 reaction with alpha particles, emitting neutrons in LXe. Eventually, alpha interactions occur due to the ^{210}Po decays.

As resulted from the analysis reported in this Chapter, mainly the first class of events contribute to the background referred as surface background in WIMP searches. More specifically, the electrons and gamma particles originated in both ^{210}Pb and ^{210}Bi beta decay processes represent the quasi totality of the surface background. Indeed, recoiling nuclei events are heavily suppressed by detection efficiencies while alpha interactions lay on a different energy scale. Even if not directly contributing to the surface background, alphas emitted in the ^{210}Po decays are still interesting to be studied, since carrier of valuable information about spatial distribution or activity of the ^{210}Pb contamination [116]. Neutrons emitted in the $^{19}\mathrm{F}(\alpha, \mathrm{n})^{22}\mathrm{Na}$ reaction [146] are not counted within the surface background. Contrarily to alphas, these neutrons significantly contribute to WIMP searches, but their impact is already taken into account in the neutron background, given their featureless spatial signature due to their long free path in LXe [93].

For these reasons, in this Chapter, and for the WIMP analysis case, only the ER events triggered by the electrons and photons emitted within the decay chain of ^{210}Pb in Teflon surfaces will be referred with the term *surface background*.

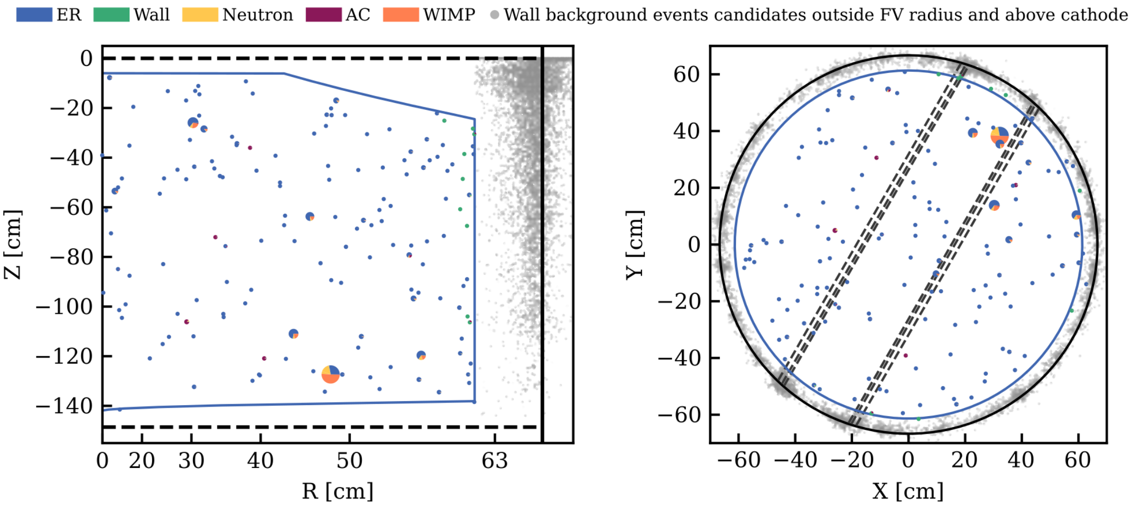

Figure 6.3: (Edited from [53]) SR0 (R, Z) and (X, Y) distributions of both the analyzed data-set for WIMP searches (colored pie charts) and the wall background events candidates (gray dots) above cathode. These latter events have been discarded in the WIMP analysis by the FV radial cut.

6.2 Surface Background in XENONnT WIMP Searches

The active region of the XENONnT TPC is outlined by 48 PTFE reflective interlocking 3 mm-thick panels installed on 24 PTFE pillars [30], forming an irregular 48-sided polygon-based prism with an inscribed diameter of 132.8 cm and an inscribed radius of 66.4 cm [66]. This geometry is the result of a compromise between three main conditions. The first is the mechanical stability, having the PTFE structure the additional role of field shaping rings holder via pillars. The second is light tightness, ensured by <1 % LXe light transmittance [147] thanks to the 48 sliding panels that overlap for few millimeters along the full height of the TPC compensating for 1.4 % thermal shrinkage of PTFE [66]. The third is the amount of Fluorine-9 nuclei introducing radiogenic neutron background due to the $^{19}\mathrm{F}(\alpha, \mathrm{n})^{22}\mathrm{Na}$ reaction [146], to be limited by means of a reduced thickness of PTFE panels [30].

As discussed in the previous paragraphs, the presence of the Teflon material in direct contact with the sensitive region of LXe introduces the ^{210}Pb radioactive contaminant at the borders of the XENONnT detector. This radioactive contamination is by far the largest source of background in the TPC for WIMP dark matter searches. Nevertheless, thanks to its very distinctive spatial signature, featuring a prominent peak at the position of the Teflon panels in the radial observable space, it is possible to reject a large amount of it by just applying a fiducial volume cut. The radius of this fiducial volume (FV) is the result of an optimization study aimed at maximizing the WIMP-signal to wall-noise ratio. The result of this study, along with those of similar analyses to limit the impact of cathode and GXe background events, is reported in Figure 6.3, where the potential wall background events candidates are plotted together with the WIMP analyzed data-set.

It is worth noting that the plots in Figure 6.3 do not show a uniform Z or azimuthal (Theta) distribution for wall events candidates. Later in this Chapter, it will be clear that the reason behind this non-uniformity is partially physical, due to both electric field lines and enhanced charge collection on PTFE pillars with respect to the panels. However, for both the two distributions, in Z and Theta, this hypothesis was demonstrated not to be enough to explain the spatial modulation. Hence, additional phenomenological ingredients had to be

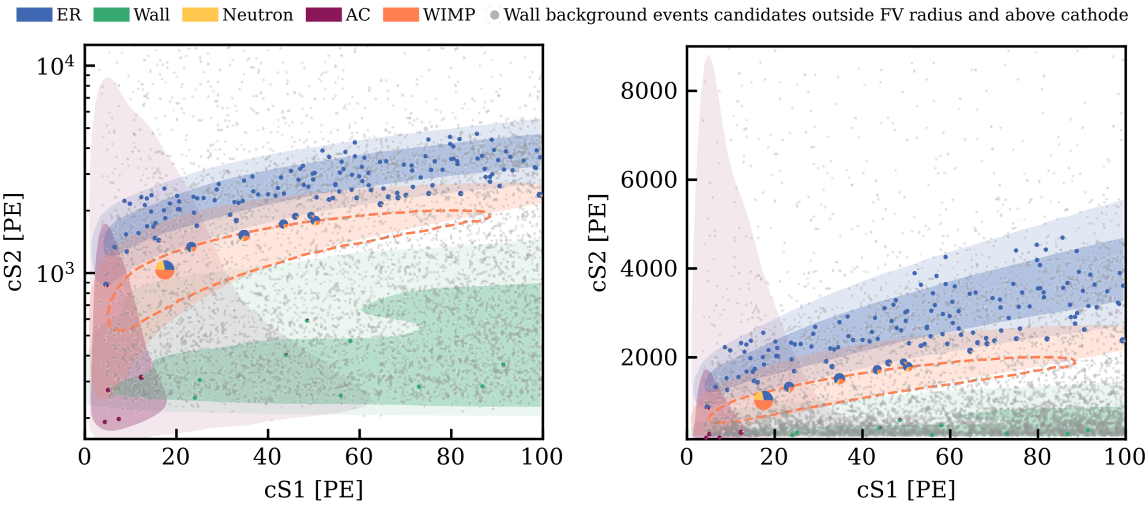

Figure 6.4: (Edited from [53]) SR0 (cS1, cS2) distributions for both analyzed data-set for WIMP searches (colored pie charts) and wall background events candidates (gray dots) above cathode, discarded in WIMP analysis by FV radial cut.

included in the model to match the data.

Beyond the strong spatial signature that characterizes the surface background, also its distribution in (cS1, cS2) observable space provides an extra handle to discriminate these events with respect to potential WIMP dark matter ones. Indeed, by observing the (cS1,cS2) space, as reported in Figure 6.4, one can easily spot a clear clustering of wall background events candidates in a cS2 region of values lower than the ones characterizing the vanilla ER band. This might trigger some questions, given that, as stated in previous Section, wall background events are, for all intents and purposes, ER events. However, the different detector response in the neighborhood of its borders causes the divergent behavior of wall events from ER ones.

6.2.1 The PTFE Charge-up Phenomenon

The XENONnT detector response in the neighborhood of the PTFE panels and pillars is not well understood as the bulk one and this is valid in general when talking about monolithic position-sensitive detectors. This happens because the outer layer is commonly more affected by external radiation backgrounds that do not represent a significant concern since they can be greatly rejected by applying a simple fiducial volume cut.

Studies aimed in better understanding the behavior of dual-phase LXe TPC detectors at the neighborhood of the Teflon panels reported already interesting results in both XENON1T [148, 149] and LUX experiments [150]. These studies revealed an additional problematic aspect of Teflon, that was observed to charge up in both the experiments. This accumulation of charge led to a distortion of the electric field lines, that from their vertical designed behavior showed a deflection in correspondence of the TPC borders.

The non-uniform distortion along Theta azimuthal coordinate observed in XENON1T reinforced the hypothesis of a charge-up effect for Teflon. Indeed, this effect was intensified at panels angular position with respect to the pillars, sustaining the field shaping rings, though which a possible charge removal process could have taken place. In order to reduce these charge-up effects, the XENONnT Teflon panels were designed to get a more efficient charge removal, because of their lower thickness and the presence of the charge collecting

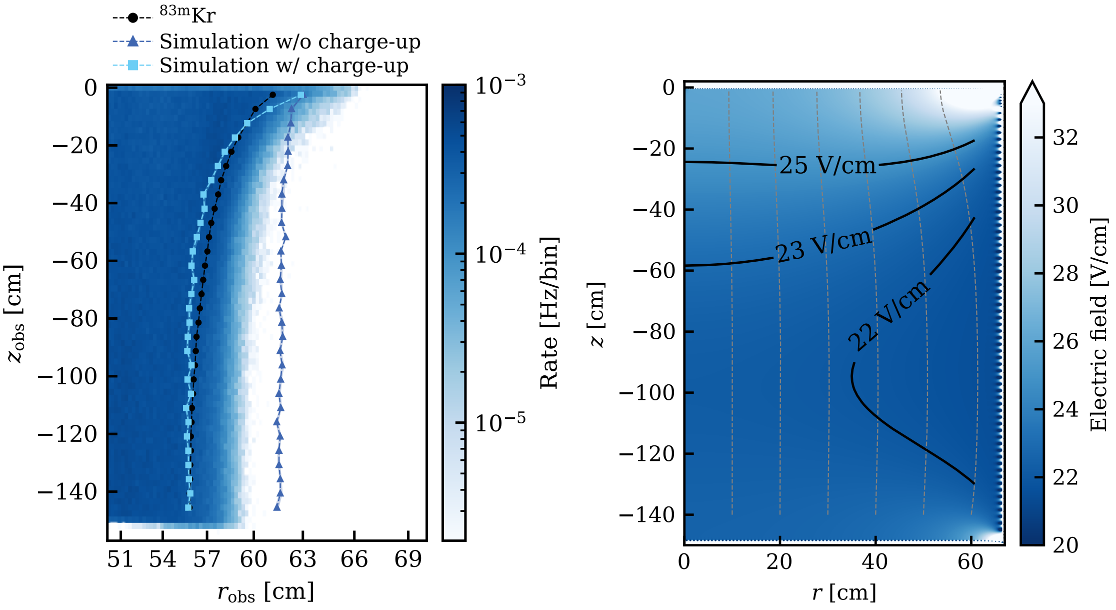

Figure 6.5: (From [130]) (Left) (r,z) distribution of ^{83m}Kr events near the walls of the TPC. The 90th percentile of the radial distribution along 30 bins of z is shown in black. The same quantities coming from the simulation with and without PTFE reflector charge-up are shown with light-blue squares and blue triangles, respectively. (Right) Electric field map determined from 2D-axisymmetric simulations including a linear charge distribution on the PTFE reflectors matched to the radial distribution of ^{83m}Kr events. The black lines indicate the contour of the electric field, while the dashed gray lines are field lines starting at different radii and same z.

holes [66]. This upgrade translated into a larger charge accumulation at the pillars with respect to the PTFE panels in XENONnT, resulting an "inverted" Theta modular structure as compared to XENON1T [66].

Moreover, differently to XENON1T, in XENONnT the analysis of the ^{83m}Kr calibration events at TPC borders highlighted an accumulation of a net positive charge towards the top part. This, as shown in Figure 6.5, causes the deflection of the electric field lines, majorly pushing inwards the position reconstruction of the events happening at the bottom. Moreover, in the bottom corners of the TPC, the electric field lines get dumped into PTFE walls, which causes the failure of drifting from these regions the ionization electrons towards the gas-liquid interface. Therefore, the XENONnT experiment results blind to any interaction occurring in this region, denominated for this reason the *charge insensitive volume* [66, 151].

Due to this effect, the events occurred in the close neighborhood of TPC borders present a suppressed S2 signal, causing the wall events (cS1, cS2) distribution to depart from the ER band one. In turn, the S2 suppression, due to PTFE charge-up phenomenon, also causes a non-uniform detection efficiency in the Z observable, which results suppressed in lower TPC region, leading to the wall events spatial distribution of Figure 6.3.

6.3 The FLAMEDISX Inference Approach

With the purpose of modeling the wall background at best by using physics assumptions, while deepening our knowledge of XENONnT detector response at TPC edges, every possible event observable has to be taken into account. The analyzed space of observable results to be six-dimensional: (cS1, cS2, R, Theta, Z, t), where t is the time at which the event occurred. Conventional fitting tools, based on template building and morphing techniques, are inadequate to perform a six-dimensional analysis [152]. Indeed, for instance, in the context of WIMP inference with XENONnT SR0 data-set, the fit is executed in the (cS1, cS2, R) limited observable space, optimizing only six background/signal rate parameters [153]. The limitation on the dimension of the SR0 WIMP analysis space arises from the demanded computational resources due to template building and morphing techniques, which increase exponentially with the dimension of the considered observable space.

To address this challenge and exploit the six-dimentional observable space while limiting the computational time to reasonable amount, the FLAMEDISX (Fast Likelihood Analysis in MorE DImensionS for Xenon TPCs) software was developed in collaboration with colleagues from the LZ experiment and made available as a python package, via pip installation. This software aims to overcome the computational limitations by building an explicit likelihood based on the LXe emission model and utilizing GPU acceleration with TensorFlow. This approach enables tensor multiplication and has been demonstrated to reduce computational costs by a factor 10 for six-dimensional analyses [153].

The novelty of the FLAMEDISX approach stands in the likelihood computation for each event, which is performed analytically [154]. This happens via factorization of the emission model of LXe quanta generation, and hence detection, which depends on several nuisance parameters and on the type of source defined in input. More precisely, the probability that an event (cS1, cS2, R, Theta, Z, t) has to be produced by a source, e.g. ^{210}Pb radioactive chain at the borders of the TPC, is computed via multiplication of the different factors fragmenting the LXe quanta emission model in steps: total number of quanta generation, the quanta splitting into photons and electrons, their detection and signal reconstruction.

6.3.1 The FLAMEDISX LXe Signals Emission Model

The base concept of FLAMEDISX LXe signals emission model is illustrated in Figure 6.6, which represents an updated version of the scheme presented in [153]. Each block of the scheme represents a conditional probability density function determined by a set of nuisance parameters (θ), that can be optimized in the fitting procedure. The multiplication of all these blocks returns the differential rate $R(\mathrm{cS1}, \mathrm{cS2}, \mathrm{R}, \mathrm{Theta}, \mathrm{Z}, \mathrm{t}|\ \theta)$ of the source in input to the model. For simplicity of writing, in the following, $\mathbf{x}$ will denote the four dimensional vector (R, Theta, Z, t).

Source Inputs and Quanta Generation

The first step to compute a source six-dimentional probability density function is the definition of its energy and spatial inputs. This is done by means of histograms that can either be generic, as happens for the WIMP ER background source that is modeled via flat spatial and energy inputs, or can be the outcome of a refined GEANT4 simulation, as occurs for the physics-driven surface background in this Chapter presented. The energy spectrum in input is, as a first step, translated into expected produced number of quanta. To do so, the input recoil differential rate spectrum $R_0(E, \mathbf{x})$ has to be convolved with the probability of generating a certain amount of quanta given a specific energy. Numerically, this happens via:

$$R_1(n_q, \mathbf{x}) = \sum_i P(n_q|E) R_0(E, \mathbf{x}) = \sum_i P(n_q|E) \Delta E \frac{\mathrm{d}R(E, \mathbf{x})}{\mathrm{d}E}, \tag{6.1}$$

where ΔE is the spectrum energy resolution and the sum runs over the bins of the input energy spectrum, approximating the integral of the convolution with $P(n_q|E)$, which represents the

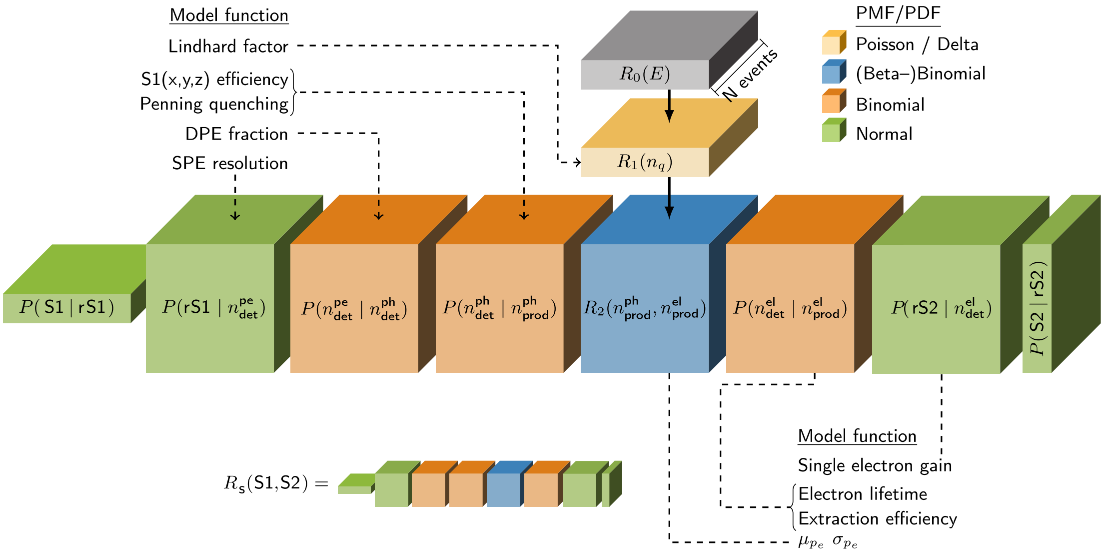

Figure 6.6: (Edited from [153]) The LXe signal emission and TPC detector response model implemented in FLAMEDISX. The differential expected signal event rate $R_s(S1, S2)$ at the observed event is computed as the matrix multiplication of the colored tensors on the lowest row. The figure also shows some model functions used in each step of the computation. The computation is "batched" over several events at once to improve performance, as indicated by the "N events" depth dimension. This is an implementation detail, since the signal differential rate is computed independently for each event. The figure describes the computation of the signal differential rate due to a single source, that has to be repeated several times for models with multiple sources.

probability of producing n_q quanta given E. In the case of an ER source, this latter is soon computed via:

$$n_q = \left\lfloor \frac{E}{W} \right\rfloor, \tag{6.2}$$

where E is the energy deposited in the electron recoil and W, as in Chapter 2, is the mean energy needed to produce a measurable quantum. Therefore, for the ER interaction the probability block takes the form of:

$$P(n_q|E)_{\text{ER}} = \delta\left(\left\lfloor \frac{E}{W} \right\rfloor\right). \tag{6.3}$$

Conversely, NR model has to take into account the energy loss in the heat channel. The energy-dependent Lindhard factor $L(E)$ is thus exploited to derive the probability distribution of n_q as:

$$P(n_q|E)_{\text{NR}} = \text{Pois}\left(n_q \middle| \left\lfloor \frac{E\,L(E)}{W} \right\rfloor\right). \tag{6.4}$$

Quanta Splitting

Once the source differential rate in terms of n_q number of quanta is computed, the next step is represented by including the probability of n_q splitting into photons and ionization electrons. The splitting n_q into n^{el}_{prod} ionization electrons and n^{ph}_{prod} scintillation photons is a Binomial process

$$P(n^{el}_{prod}|n_q) = \text{Binom}(n^{el}_{prod}|n_q, p_e), \tag{6.5}$$

where p_e is the probability of a quantum being an electron. For NR events, given n_q number of quanta, p_e is fixed. For ER events, however, the recombination phenomenon heavily contributes in the quanta splitting process. To include the ER quanta splitting dependence from the recombination factor the Thomas-Imel modified box model [81], already cited in Chapter 2, is considered. For this reason p_e is drawn from the Beta distribution:

$$P(p_e) = Beta(\alpha, \beta|E) = \frac{\Gamma(\alpha+\beta)p_e^{\alpha-1}(1-p_e)^{\beta-1}}{\Gamma(\alpha)\Gamma(\beta)}, \tag{6.6}$$

where Γ is the gamma function. The shape parameters (α,β) of the beta distribution are

$$\alpha = \langle r(E)\rangle \left(\frac{\langle r(E)\rangle}{(\Delta r(E))^2} + \left(\frac{\langle r(E)\rangle}{\Delta r(E)}\right)^2 - 1\right) \tag{6.7}$$

$$\beta = (1 - \langle r(E)\rangle) \left(\frac{\langle r(E)\rangle}{(\Delta r(E))^2} + \left(\frac{\langle r(E)\rangle}{\Delta r(E)}\right)^2 - 1\right), \tag{6.8}$$

where $\langle r(E)\rangle$ represents the mean recombination fraction computed via Thomas-Imel modified box model as:

$$\langle r(E)\rangle = \frac{n_i}{n_q}\left(1 - \frac{\ln(1 + n_i\xi_{er}/4)}{n_i\xi_{er}/4}\right)\frac{1}{1 + e^{-(E-q_0)/q_1}}, \tag{6.9}$$

where

$$\xi_{er} = \gamma_{er} e^{-E/\omega_{er}} F^{-\delta_{er}}, \tag{6.10}$$

n_i is the number of ions generated, F is the drift field in the $\mathbf{x}$ coordinate and $q_0, q_1, \gamma_{er}, \omega_{er}, \delta_{er}$ are all shape nuisance parameters that can be optimized during the inference process. $\Delta r(E)$ represents the fluctuation of the recombination fraction which takes the form:

$$\Delta r(E) = q_2(1 - e^{-E/q_3}), \tag{6.11}$$

where q_3 and q_4 are shape parameters that can be evaluated in the fit procedure as nuisance parameters. Therefore, the quanta splitting block is modeled for the ER sources as a Beta-Binomial distribution:

$$P(n^{el}_{prod}|n_q)_{ER} = \text{BetaBinom}(n^{el}_{prod}|n_q, p_e). \tag{6.12}$$

In conclusion, the differential rate for a source to produce n^{el}_{prod}, n^{ph}_{prod} quanta, given $\mathbf{x}$, is the convolution of what obtained in the previous section with the splitting quanta probability and can be written as:

$$R_2(n^{el}_{prod}, n^{ph}_{prod}, \mathbf{x}) = \sum_{n_q} P(p^{el}_{prod}|n_q) R_1(n_q, \mathbf{x}) \delta(n_q = n^{el}_{prod} + n^{ph}_{prod}). \tag{6.13}$$

Detection Efficiency

The next step takes into account any losses that might take place in the detection process. In this model block the processes of detection efficiency loss that occur for photons, such as PMT quantum efficiency, or for electrons, such as trapping by electronegative impurities, are considered. Since the detection probability for one photon (electron) is assumed to be independent of the other quanta, two Binomial distributions are considered in this step of the model:

$$P(n^{ph}_{det}|n^{ph}_{prod}) = \zeta(n^{ph}_{det})\text{Binom}(n^{ph}_{det}|n^{ph}_{prod}, \eta^{ph}), \tag{6.14}$$

and

$$P(n^{el}_{det}|n^{el}_{prod}) = \zeta(n^{el}_{det})\text{Binom}(n^{el}_{det}|n^{el}_{prod}, \eta^{el}), \tag{6.15}$$

where n_{det}^{ph} and n_{det}^{el} are the number of photons and electrons detected. Moreover, in Equations 6.14 and 6.15, $\zeta(n_{det}^{ph})$ and $\zeta(n_{det}^{el})$ account for the per-event efficiency, depending on the total number of photons and electrons detected, due for example to some constrain imposed in the reconstruction of PMT signals, where a minimum hit threshold is set in order not to avoid accidental coincidences due to PMTs dark counts. As expected from quanta statistics, $\zeta(n_{det}^{el})$ is usually very high (~ 1), while $\zeta(n_{det}^{ph})$ drops at very low n_{prod}^{ph}. The per-quanta detection efficiencies, η^{ph} and η^{el} in Equations 6.14 and 6.15, take into account different detector feature. η^{ph} depends on PMTs efficiency and the optical properties of the detector. These latter are determined via simulations and stored as efficiency maps of the $\mathbf{x}$ coordinates. η^{el} depends, instead, on the electron extraction efficiency at the liquid interface (η_{extr}), on the electron lifetime (τ_e) and the event drift time (t_d):

$$\eta^{el} = \eta_{extr} e^{-t_d/\tau_e}. \tag{6.16}$$

This per-quanta electron detection efficiency model function is modified for physics-driven wall background modeling purposes.

Signal Formation

The signal formation occurs differently for electrons and photons. Indeed, for photons, given the much lower intensity (of about one order of magnitude) of the scintillation signal with respect to the ionization one, the probability of single photons to trigger in the PMT photocathode two photo-electrons instead of one (p_{dpe}) has to be taken into account. This latter follows a binomial distribution:

$$P(n_{det}^{pe}|n_{det}^{ph}) = \text{Binom}(n_{det}^{pe} - n_{det}^{ph}|n_{det}^{ph}, p_{dpe}), \tag{6.17}$$

where n_{det}^{pe} is the number of photo-electrons detected and $n_{det}^{pe} - n_{det}^{ph}$ is used to set the domain of the distribution to $n_{det}^{pe} > n_{det}^{ph}$. The further generation of the raw signals (rS1,rS2) follows a Gaussian distribution:

$$P(rS1|n_{det}^{pe}) = f(rS1)\text{Gauss}(rS1|\mu_{rS1}(n_{det}^{pe}), \sigma_{rS1}(n_{det}^{pe})) \tag{6.18}$$

$$P(rS2|n_{det}^{el}) = f(rS2)\text{Gauss}(rS2|\mu_{rS2}(n_{det}^{el}), \sigma_{rS2}(n_{det}^{el})) \tag{6.19}$$

where $f(rS1)$ and $f(rS2)$ are the per-event quality cut efficiencies, such as those computed in Chapter 4 and $\mu_{rS1(rS2)}, \sigma_{rS1(rS2)}$ respectively represent the mean and standard deviation of rS1 (rS2) formation process as functions of n_{det}^{pe} (n_{det}^{el}), that by assuming a linear detector response, take the form:

$$\mu_{rS1}(n_{det}^{pe}) = \mu_{rS1} \times n_{det}^{pe} \qquad \sigma_{rS1}(n_{det}^{pe}) = \sigma_{rS1}\sqrt{n_{det}^{pe}} \tag{6.20}$$

$$\mu_{rS2}(n_{det}^{el}) = \mu_{rS2} \times n_{det}^{el} \qquad \sigma_{rS2}(n_{det}^{el}) = \sigma_{rS2}\sqrt{n_{det}^{el}}. \tag{6.21}$$

Commonly, μ_{rS2} and σ_{rS2} are also known after the name of single electron gain and single electron width.

Signal Reconstruction

From raw signals to observed signals one last step is needed. Indeed, noise in the PMTs waveform baseline, dark counts and afterpulses can induce biases in the S1 and S2 signal reconstruction. This effect is estimated by the signal reconstruction bias defined as:

$$R_{\text{bias}} = \frac{\text{ReconstructedArea}}{\text{TrueArea}} - 1 \tag{6.22}$$

In order to give an estimate of R_{bias}, simulations, where it is possible to access the True Area information, are exploited. These studies report a non-negligible dependence of R_{bias} on the true signals area, that is then stored as a map of S1 and S2. The final observed S1 and S2 signals are thus the result of a Gaussian process taking the form:

$$P(S1|rS1) = \text{Gauss}\left(S1|\left[R^{S1}_{\text{bias}}(rS1)+1\right]rS1, \sigma^{S1}_{bias}(rS1)\right) \tag{6.23}$$

$$P(S2|rS2) = \text{Gauss}\left(S2|\left[R^{S2}_{\text{bias}}(rS2)+1\right]rS2, \sigma^{S2}_{bias}(rS2)\right), \tag{6.24}$$

where $\sigma^{S1}_{bias}(rS1)$ and $\sigma^{S2}_{bias}(rS2)$ are the standard deviations of S1 and S2 reconstruction bias respectively.

6.3.2 The Inference Framework and Likelihood Construction

With the LXe signals emission model described in the previous paragraphs, it is possible to compute the events signals differential rate referred to the source in input to the model. More specifically, the signals differential rate as function of (S1,S2,$\mathbf{x}$) is obtained by computing the convolution of the different emission model probability density functions, by means of intra-block tensor multiplication and summation over the hidden observables (such as n^{el}_{prod}) ranges as:

$$\begin{aligned} R_s(S1,S2,\mathbf{x}) = &\sum_{rS1}\sum_{n^{pe}_{det}}\sum_{n^{ph}_{det}}\sum_{n^{ph}_{prod}}\sum_{n^{el}_{prod}}\sum_{n^{el}_{det}}\sum_{rS2} P(S1|rS1)P(rS1|n^{pe}_{det})P(n^{pe}_{det}|n^{ph}_{det})P(n^{ph}_{det}|n^{ph}_{prod}) \\ &R_2(n^{el}_{prod}, n^{ph}_{prod}, \mathbf{x})P(n^{el}_{det}|n^{el}_{prod})P(rS2|n^{el}_{det})P(S2|rS2). \end{aligned}$$

Eventually, to compute the full differential rate as function of (S1,S2,$\mathbf{x}$), also including the model-data matching in the space-time observables $\mathbf{x}$, the following multiplication is needed:

$$R(S1,S2,\mathbf{x}) = R_s(S1,S2,\mathbf{x})R_t(\mathbf{x}), \tag{6.25}$$

where $R_t(\mathbf{x})$ is the rate multiplier at the event position $\mathbf{x}$, computed by evaluating the space-time 4D probability density function at position $\mathbf{x}$. This latter is trivial for constant uniform sources, such as WIMP signal or ER background models, while it presents significant signatures in the surface background model, which shows a non-uniform and non-constant space-time 4D distribution.

The thus-obtained differential rate is analytical and its source models parameters can be optimized as nuisance parameters by means of a fit procedure against LXe TPC data. The fit extended unbinned likelihood takes the form:

$$\mathcal{L}(\theta) = \left[\text{Pois}(n|\mu(\theta))\prod_{i=1}^{\text{events}}\sum_{j}^{\text{sources}}\frac{R_j(rS1_i, rS2_i, \mathbf{x}_i;\theta)}{\mu}\right] f(\theta) \tag{6.26}$$

where n is the total number of observed events, $f(\theta)$ is the parameters constrain function, $\mu = \sum_j \mu_j$ is the total number of expected events and μ_j is the total number of expected events, after selection cuts, from the source j, defined as:

$$\mu_j = \rho\int dS1dS2d^4\mathbf{x}\, R_j(S1,S2,\mathbf{x}) \tag{6.27}$$

where ρ is the density of LXe in the detector in units of t/m^3, since $R_j(S1,S2,\mathbf{x})$ is in units of events/(t × y × PE^2), where PE stands for photo-electrons, the measure of S1 and S2 PMT signals. Similarly to the traditional WIMP analysis, the number of expected events μ_j and the differential rate $R_j(S1, S2, \mathbf{x})$ are expressed as functions of the unitless parameters r_j, known as rate multipliers:

$$\mu_j = r_j m_j(\theta) \qquad\qquad R_j = r_j M_j(\theta), \tag{6.28}$$

where $m_j(\theta)$ and $M_j(\theta)$ represent the expected number of events and differential rate for the source j chosen as references, corresponding to a unitary rate multiplier ($r_j = 1$). For instance, when modeling the WIMP signal source, the cross-section of $1 \times 10^{-47}\,\mathrm{cm}^2$ can be chosen as reference, and the rate multiplier for the WIMP source represents the renormalization to that value.

Computationally, the best fit evaluation is performed by exploiting the logarithmic form of the likelihood of Equation 6.26:

$$\log \mathcal{L}(\theta) = -\mu(\theta) + \sum_i^{\text{events}} \log\left(\sum_j^{\text{sources}} R_j(rS1_i, rS2_i, \mathbf{x}_i; \theta)\right) + \log(f(\theta)). \tag{6.29}$$

The log-likelihood optimization in the fit procedure takes place into two different steps: the analytical per-source evaluation of the events differential rate $R_j(rS1, rS2, \mathbf{x}; \theta)$ with subsequent evaluation in events coordinates, via TensorFlow tensor multiplication, and total rate $\mu(\theta)$ estimation, which takes place via grid interpolation in the parameter space, where the anchor points are estimated by means of large number of events ($\sim 10^5$) simulation.

Thanks to TensorFlow autodifferentiation, the gradient and the second derivative via Hessian matrix of the likelihood function are also computed and stored in the fitting process. This enables a faster maximization of the likelihood function, primarily driven by its gradient evaluation, and provides the direct access to the parameters uncertainty and correlations when computing the best fit.

6.4 Physics-driven Surface Background Model

Ideally, a background model for WIMP dark matter searches in the keV energy range is developed starting from physics-driven assumptions, coming from questions, such as:

- Which (radioactive) source generates this background?
- Which spatial properties does it have? Is it homogeneous in the TPC?
- Which temporal behavior does it follow? Is it stable?
- What is the detector response to this background?

Additionally, a pure enough data sample is needed to better study the background of interest.

As stated in previous paragraphs, the wall background is expected to be generated by the Radon progeny plate-out effect on PTFE panels surfaces. This would lead to an accumulation of ^{210}Pb at the borders of the TPC, which translates into a nearly constant background, characterized by an inhomogeneous spatial distribution in the TPC. Moreover, thanks to several XENONnT studies tackling electric field behavior, such as those reported in [66], the knowledge about XENONnT detector response at TPC borders has been improved so to allow a more precise assessment of the surface background. In the following paragraphs, the listed questions will be more deeply examined and eventually answered so to provide an input for the here presented physics-driven modeling of the surface background.

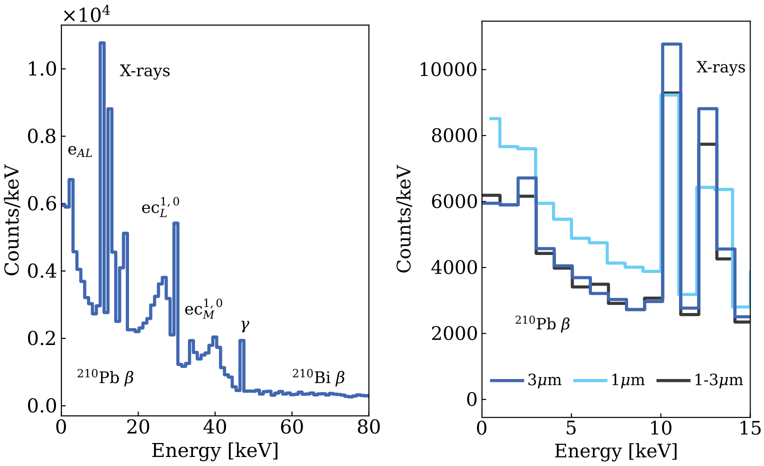

Figure 6.7: Surface background model ER energy spectrum (blue histogram) obtained by simulating 10^6 ^{210}Pb isotopes with a uniform implantation up to 3 µm from the PTFE inner surface. The left panel represents the spectrum in linear y-scale up to 80 keV so to show all the spectral features. Right panel depicts in an extended energy ROI for the WIMP searches (usually limited up to 10 keV), the comparison between the reference 3 µm spectrum and two examples of alternative implantation distributions: a uniform one up to 1 µm (light-blue histogram) and a second one uniform in 1–3 µm (dark grey histogram). Conservatively, the input energy spectrum to the surface background model is only truncated at 50 keV, in order to include any possible signal loss effect potentially shifting some high energy (>10 keV) events into the WIMP ROI.

6.4.1 Surface Background ER Energy Spectrum

The computation of the deposited energy spectrum of the full ^{210}Pb chain isotopes implanted in the PTFE surfaces represents the first step towards the modeling of the WIMP surface background. To this aim, the GEANT4-based Monte Carlo Collaboration software, whose working principle is thoroughly detailed in [155], has been exploited.

The energy deposited spectrum was hence obtained by simulating the ^{210}Pb decay chain in the PTFE panels and processing the deposited energy information with the epix [126] software so to cluster the depositions within spacetime bubbles of radii 5 µm and 10 ns. In Figure 6.7, left panel shows the deposited energy input spectrum obtained with 10^6 ^{210}Pb simulated isotopes with an implantation depth of 3 µm. The implantation depth represents the reference value up to which, from the PTFE surface, the ^{210}Pb radioactive source is uniformly distributed in the simulation. The 3 µm value allows to generate a large simulation sample, which requires increasing computational costs for smaller implantation depth, and shows a posteriori good agreement with the surface background data. However, it is worth noting that in the recent – relative to this writing – LRT2024 conference ^{210}Pb implantation depths of order 100 nm were suggested to be more reasonable [156].

A second important aspect about the simulation framework is the simplified detector geometry that might have an impact on the final evaluation of the deposited energy input spectrum. Indeed, the TPC geometry in the simulation framework is perfectly cylindrical, while in reality XENONnT presents an irregular 48-sided polygon-based prism TPC shape, whose inscribed diameter equals that of simulation geometry. Moreover, as a second (or even higher) order effect, PTFE material in the simulated geometry presents completely smooth surfaces, while in reality the surfaces roughness plays a role in the outcome of the deposited energy spectrum.

For all these reasons, beyond the fact that the FLAMEDISX software cannot accommo-

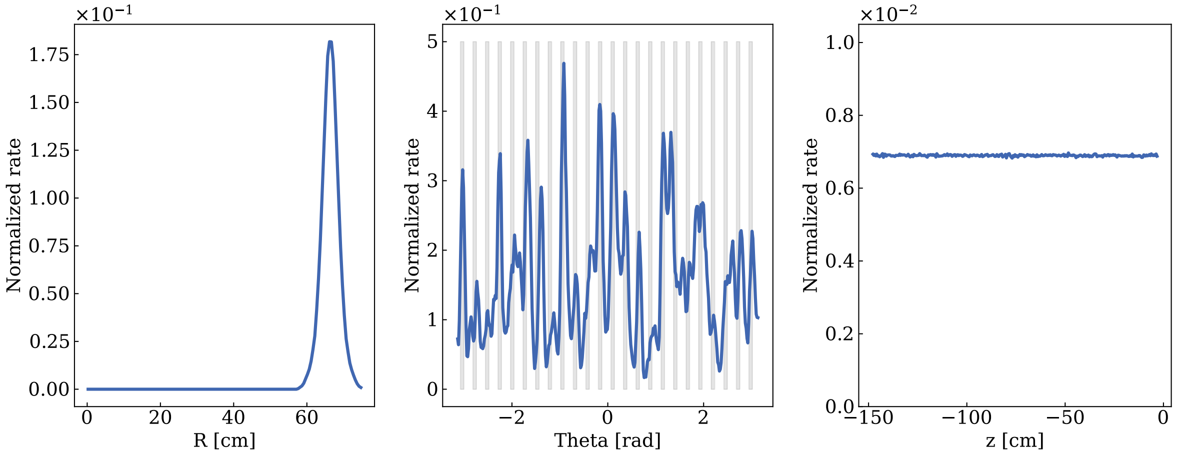

Figure 6.8: Surface background model spatial distribution inputs. The left panel shows the radial distribution which peaks at the PTFE surfaces position (at about 66.4 cm). The centeral panel reports the non-trivial Gaussian-semared azimuthal distribution of the wall events on top of gray rectangles representing the positions of the PTFE pillars structures. The right panel shows the Z distribution for the surface background assumed flat as first order approximation.

date any nuisance shape parameters for input spectra, the 3 µm implanted ^{210}Pb deposited energy spectrum of Figure 6.7, left panel, was exploited as reference. Different implantation depths have also been tested yielding similar results in terms of detector nuisance parameters optimization, and slightly distinct rate multipliers given the different Monte Carlo acceptances. For completeness, also step-wise implantation distribution have been probed, with the aim of taking into consideration the PTFE surfaces treatments, exploited also to achieve better optical property of the material, which reduce and crave part of the contaminants in the first surface layers. The deposited energy spectra for an example of this latter case, specifically for a uniform ^{210}Pb implantation ranging in 1–3 µm from the inner PTFE surfaces, and another for the uniform implantation up to 1 µm are represented in the right panel of Figure 6.7 in comparison to the 3 µm reference in the energy range of interest for the WIMP searches.

6.4.2 Spatial Distribution

One might think that the only feature present in the spatial distribution of the surface background events only characterizes the radial one. As a matter of fact also the azimuthal distribution is non-trivial. Moreover, a non-trivial distribution was also found in the Z space, even if this evidence was only used in a later refinement of the surface background model for SR1 analysis, as mentioned at the end of this Chapter.

The first attempt for a FLAMEDISX-based surface background model [154] was more close to the traditional approach, exploiting as a radial input a T-Student distribution, whose parameters were optimized with a fit procedure on data. Although this method represents a valid approach to the modeling of this background, it is not supported by any physics-driven assumptions. Thus, for the realization of the surface model here presented, the radial and azimuthal distribution were decided to be fully derived from data, by smearing the wall events distributions with a Gaussian kernel, for smoothing purposes. The results of this approach are presented in Figure 6.8, where also the flat Z distribution, assumed for the SR0 surface background model, is reported.

It is worth noting that the azimuthal distribution does not follow a strict periodical

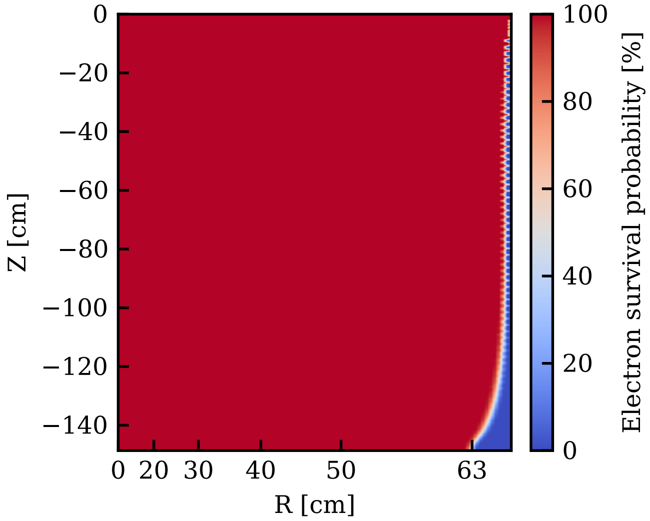

Figure 6.9: (From [66]) Electron survival probability map evaluated following the principle described in [66] [exploiting pyCOMes software]. The charge-insensitive mass of 104 kg is concentrated in the bottom corner of the active volume.

pattern highlighting the pillars-panels modulation, as clearly visible in the center panel of Figure 6.8. This might indicate that the Theta modulation visible in the data cannot be attributed to the solely possible different exposure to the Radon-laden air between the two types of materials. More interestingly, this might reveal that this contamination could be more likely enhanced by human operation, such as those performed during treatment, cleaning and handling procedures.

6.4.3 Temporal Distribution

Despite the results presented in Figure 6.1, where the numerically computed ^{218}Po chain isotopes activities are reported, the physics-driven surface background model here presented assumes a constant behavior throughout the SR0 lifetime. Indeed, even if in about 3 months of SR0 lifetime, the effects of a 22 y half-life decaying source should be slightly visible, a constant input was instead chosen so to provide an averaged effective surface background activity via rate multiplier best-fit evaluation.

In future developments of the physics-driven surface background model, if more than one science run or if a way longer science data run will be analyzed, the exponential decaying behavior of the source will be taken into account in the temporal distribution of the model.

6.4.4 Electrons Survival Probability Inclusion in Detection Efficiency Block

One of the physics-driven surface background model most important elements is the electron survival probability map [66]. This 2D map, also here reported in Figure 6.9, returns the median probability for an electron generated in (R,Z) to be detected, instead of getting trapped into the PTFE panels. In order to obtain this map, the pyCOMes [157] simulation software was developed. This map is hence drawn by exploiting the electrostatic XENONnT TPC COMSOL map and drifting 1000 electrons from different (R,Z) TPC positions, representing a very fine grid of the whole 2D surface.

The inclusion of the electron survival probability map in the FLAMEDISX software is

Table 6.1: Selection rules applied to SR0 data to obtain a pure enough surface background data-set.

Selection Cut	Description
cS1< 100 PE	WIMP ROI
S1< 100 PE	Reinforcement to WIMP ROI
cS2< 500 PE	Reduce bulk ER events contribution
S2> 100 PE	Reduce contribution from AC events
-140 cm <Z< -30 cm	Reduce contribution from non barrel PTFE events
1.2×10^5 ns< t_d <2.1×10^6 ns	Reduce contribution from AC events
R> 55 cm	Reduce contribution from ^{214}Pb ER bulk events
R< 67.25 cm	Reduce outside-TPC detector response mis-modeling impact

performed at the level of the electron detection efficiency block. To do so, the per-electron detection efficiency η^{el} model function of Equation 6.16 was modified as follows:

$$\eta^{el}(\mathbf{x}) = \eta_{extr} P^{el}_{surv}(\mathbf{x}) e^{-(t_d p_0)/\tau_e}, \tag{6.30}$$

where $P^{el}_{surv}(\mathbf{x})$ is the electron survival probability map evaluated at position $\mathbf{x}$ and p_0 is a nuisance parameter introduced as an electron lifetime τ_e suppression factor to absorb any potential mis-modeling of the detector response. The p_0 parameter was introduced once in the FLAMEDISX model to reduce the computational cost, a smoother and lighter version of the survival probability map of Figure 6.9 was exploited. In this lighter version of the map, the electron survival probability at the borders resulted artificially increased, demanding a correction factor in the model.

6.4.5 Surface Background Data Selection

In order to study a background to develop a reliable model of it, a pure enough data-set of candidate events triggered by the source of study is needed. In the surface background case, the selection of a candidate events data-set is trivially done by considering those events in the neighborhood of the TPC borders, passing some signals quality selection cuts. The signal quality selection rules exploited in this analysis are reported in Table 6.1, while the DAQ prior cuts to define an event (i.e. cut_daq_veto, cut_run_boundaries, cut_main_is_valid_triggering_peak, cut_interaction_exists and cut_s1_tightcoin_3fold detailed in Chapter 4) are omitted. By applying these selection rules in SR0 data, a data-set of 2210 events was obtained.

6.5 The Results: SR0 Physics-driven Surface Background Model

Given the limited available computational power, the SR0 physics-driven surface background model optimization was performed only considering 150 events randomly extracted from the data-set comprising 2210 events (previous paragraph for more details). Additionally, the likelihood utilized five free parameters, four of which were nuisance parameters, while the fifth was the source rate multiplier r.

The choice of the nuisance parameters to be optimized was the result of a series of simulation studies aimed to understand which model parameters were more effective in reducing the mis-modeling. For this reason, added on top of the fact that only a limited number of parameters could have been optimized, the resulted best fit values of these parameters, reported in Table 6.2, partially absorb potential mis-modeling of the surface background

Table 6.2: SR0 best-fit results of surface background model.

Parameter name	Best-fit value	Reference Equation
p_0 (τ_e suppression nuisance parameter)	20.2(2)	6.30
μ_{rS2} (single electron gain)	4.25(7) PE/electrons	6.21
σ_{rS2} (single electron width)	29.1(19) PE/electrons	6.21
σ_{rS1} (photo-electron standard deviation)	2.3(12) PE/PE	6.20
r (rate multiplier)	0.0327(18)	6.28

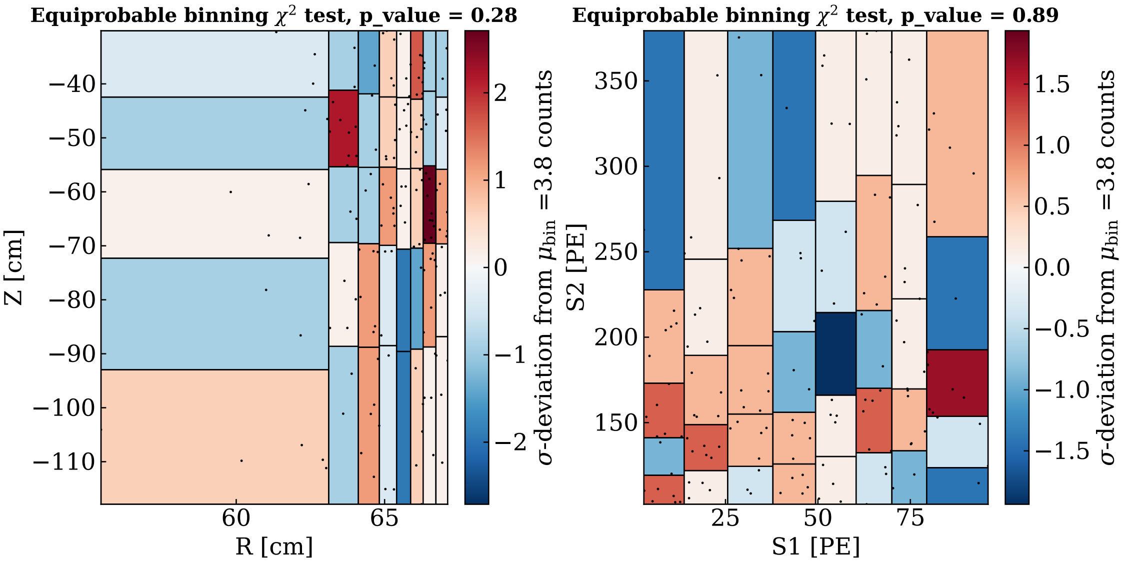

Figure 6.10: Surface background model results 2D χ^2 equiprobable binning goodness of fit tests in (R,Z), in the left panel, and (S1,S2), in the right panel. The results shown have been obtained with the *GOFevaluation* python package [101]. Red- (blue-) shifted bins highlight over- (under-) fluctuations of the data budget with respect to the model predictions.

model, while compensating for the other unoptimized models parameters values. This is indeed the case of the single electron gain μ_{rS2} parameter that as default value, suggested by other parallel XENONnT analyses, should be around 30 PE/electrons, while a value of 4.250(7) PE/electrons was found. This drastic reduction is probably the effect of fixing η_{extr} of Equation 6.30, to the value computed for the bulk events, which could be an overestimation for the detector response in the neighborhood of the PTFE.

To further support this hypothesis is the best fit value of the single electron width σ_{rS2}, 29.1(19) PE/electrons. Indeed, this value combined with the one obtained for μ_{rS2} leads to a Gaussian distribution for the signal reconstruction of Equation 6.21 which spans also negative values of $rS2$. Given, moreover, that the FLAMEDISX has been developed with an automatic rejection of negative signals, for trivial error prevention, the multiplication stage of Equation 6.21 with the found best fit values assumes the function of an efficiency step at the level of ionization raw signal generation. This in turns compensates for the potential overestimation of η_{extr}.

In order to access the goodness of the SR0 surface background fit, the *GOFevaluation* python package [101], providing also the possibility of performing 2D goodness of fit tests, has been exploited. More specifically, 2D χ^2 equiprobable binning goodness of fit tests have been performed on every combination of the six analysis dimensions. In all these cases the p-value was found to be larger than 10 %. For simplicity, here only the goodness of fit tests performed in (R,Z) and (S1,S2) are shown in Figure 6.10.

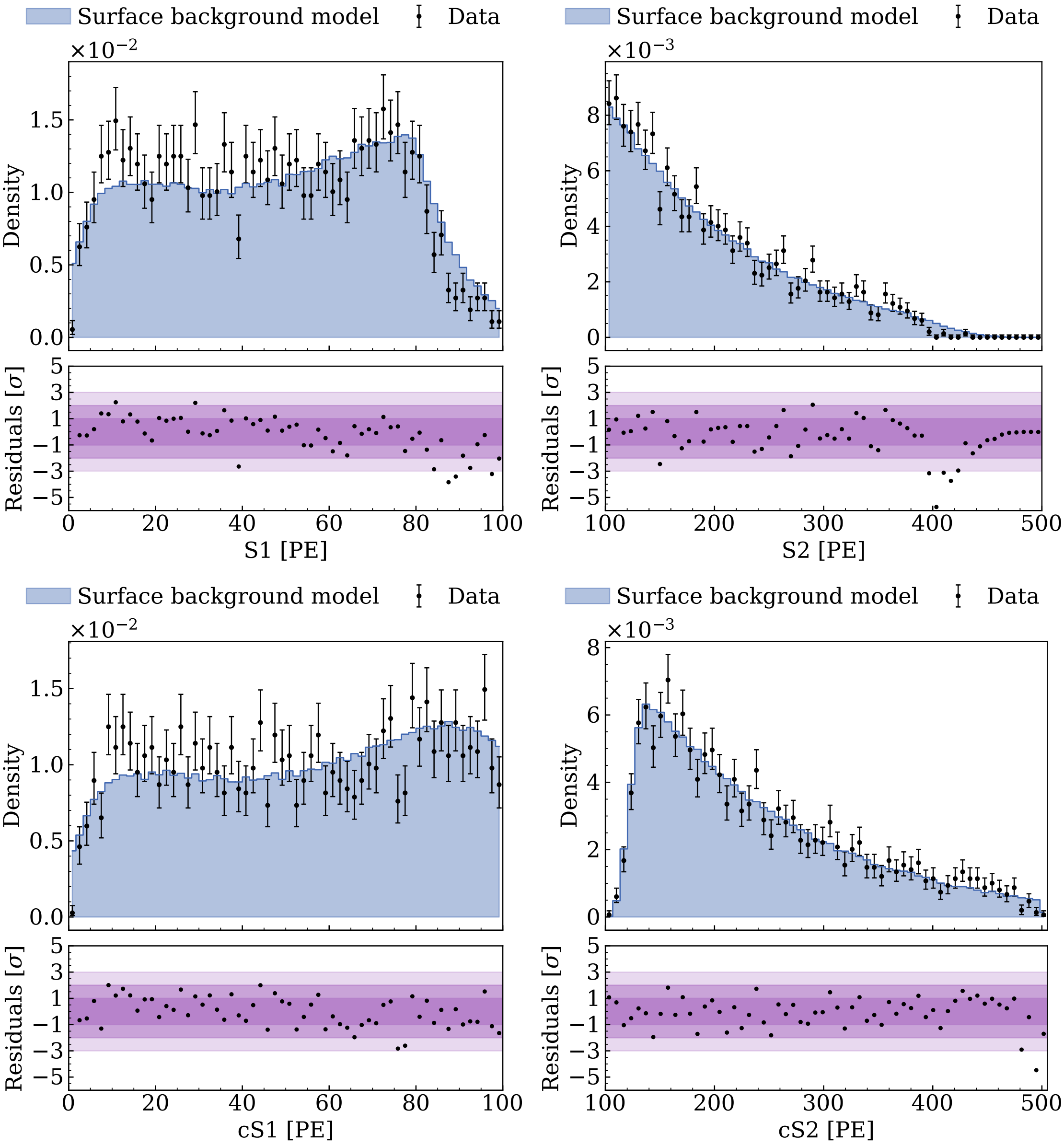

Figure 6.11: SR0 surface background model comparison with data in S1 (upper left panel), S2 (upper right panel), cS1 (lower left panel) and cS2 (lower right panel) observable spaces. Mis-modeling in low S1, cS1 regions might be due to a suboptimal choice of the ^{210}Pb implantation depth exploited in GEANT4 simulations.

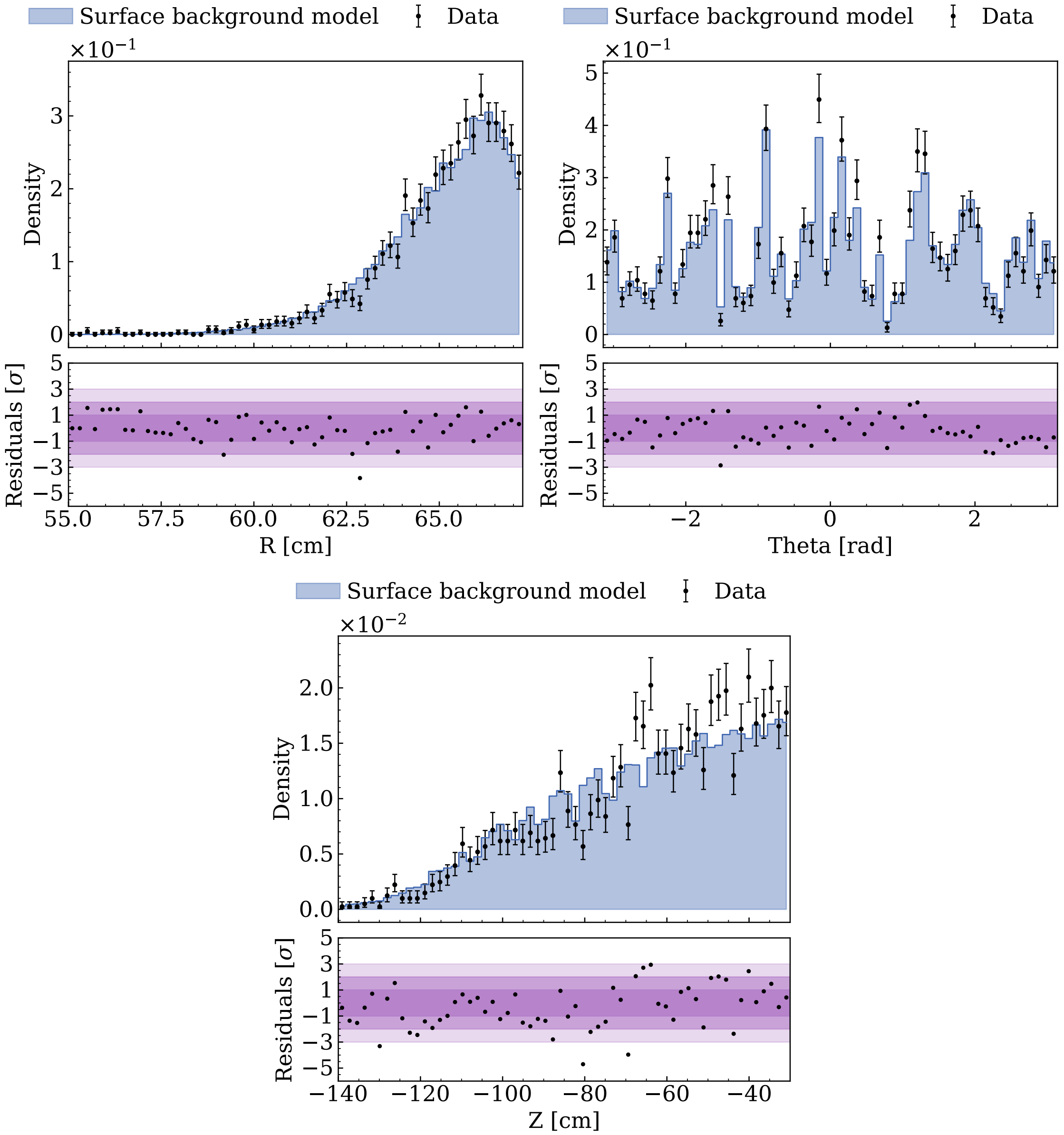

Figure 6.12: SR0 surface background model comparison with data in R (upper left panel), Theta (upper right panel) and Z (lower panel) observable spaces. Mis-modeling at high Z values might be due to the spatial distribution input assumption of Z uniformity of the ^{210}Pb PTFE contamination.

With the best-fit parameters values, it is possible to perform a simulation via FLAMEDISX of surface background events. In this way, it is possible to compare, via visual matching, the results of the fit against the full wall data-set of SR0. In Figures 6.11 and 6.12 these comparisons are shown respectively in signals observable space (S1, S2, cS1 and cS2) and in spatial coordinates (R, Theta, Z). Time observable t is here omitted, since was modeled as a constant distribution and hence does not add any extra information to the discussion, since also the observed data trend showed the same behavior. From the visual matching plots of Figures 6.11 and 6.12, it is still possible to spot some remaining mis-modeling at low S1 (cS1) values and at high values of both S2 and Z. The first can be due to the 3 µm implantation depth exploited in simulating the deposited energy spectrum in input to the surface background model, that could represent a suboptimal choice of reference for this study. The second might spot some imperfections in the reconstruction bias R_{bias} map exploited, as in Equation 6.24, to reconstruct the observed signal S2. Finally, the third highlights the necessity of a revision of the Z input distribution, that should more-likely present some non-smooth features. This latter aspect was further investigated in the attempt of modeling the SR1 surface background later mentioned in this Chapter.

From the resulting best-fit rate multiplier value r, it is possible to attempt the inference of the surface background activity. More specifically, by considering the total number of simulated ^{210}Pb decaying isotopes $N = 10^6$ generating the spectrum in input to the surface background model and multiplying it by the rate multiplier r evaluated in the fit procedure, the total number of expected ^{210}Pb decays corresponding to the number of observed event is thus obtained. By dividing this number for the SR0 lifetime (T =7.976 382 × 10^6 s) and the PTFE total surface budget (s =6.26 m^2), and scaling for the ratio of the total SR0 surface background data-set, SR0_{ds} =2210, with respect to the sub data-set used in the fit, fit_{ds} =150, an effective ^{210}Pb SR0 surface background activity is obtained. In formulae:

$$A^{effective}_{^{210}Pb} = \frac{Nr}{Ts}\frac{\text{SR0}_{\text{ds}}}{\text{fit}_{\text{ds}}} = 9.6(5)\,\text{mBq/m}^2. \tag{6.31}$$

However, after a re-examination of the deposited energy input spectrum for ^{210}Pb surface background model, a double counting mistake was spotted. More specifically, the energy deposition of every event possibly generating both S1 and S2 signals was included twice in the energy input template construction. Given that the majority of events at the borders of TPC can actually trigger both S1 and S2 signals, the scaling factor to the input energy spectrum was found to be about 1.978. By using this very same factor to scale the found ^{210}Pb activity, the following result is obtained:

$$A_{^{210}Pb} = 19.0(10)\,\text{mBq/m}^2 \tag{6.32}$$

This value was found to be in agreement with other estimates obtained via ^{210}Po alpha spectrometer material screening studies, reported in [103], of 20(3) mBq/m^2. Future studies might refine this result by exploiting a smaller implantation depth, closer to the recently suggested values [156], and an improved TPC geometry in the simulation framework.

6.6 Upgrades for the SR1 Physics-driven Surface Background Model

With the aim of improving the SR0 physics-driven surface background model, the same developed framework was also exploited for SR1 blinded data. The upgrades regarded the spatial distribution, the deposited energy spectrum and the detector response inputs.

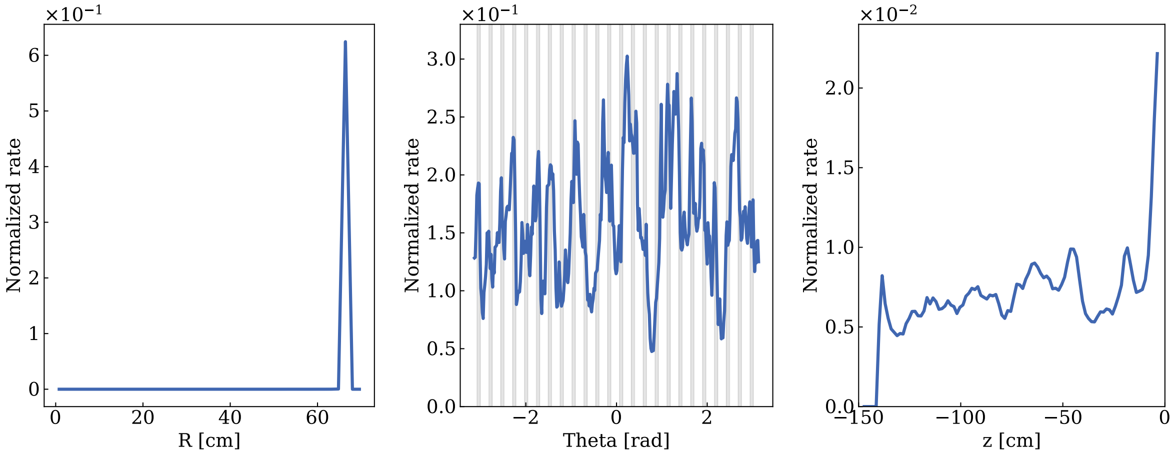

Figure 6.13: SR1 surface background model spatial distribution inputs. Left panel shows the radial distribution, obtained from epix [126] energy clustering output, peaking at the PTFE surfaces position (at about 66.4 cm). Center panel reports the Gaussian-smeared azimuthal distribution of ^{210}Po, obtained by the S1-only analysis carried out by Ying-Ting Lin, on top of gray rectangles representing the positions of the PTFE pillars structures. Right panel show the Gaussian-smeared Z distribution of ^{210}Po, obtained by always the same S1-only analysis carried out by Ying-Ting Lin.

The spatial distribution, as clearly visible in Figure 6.13, was improved so to include two different upgrades. The first concerns the radial distribution, that for SR1 was updated to the one in output of the GEANT4 ^{210}Pb radioactive chain simulation, which by using a raw binning, basically turned into a Dirac-Delta distribution. The second regards the (Theta, Z) 2D distribution that for SR1 was obtained by the S1-only study targeting ^{210}Po alpha decays. Indeed, these alpha decaying isotopes, supposing a negligible mobility of the ions in the PTFE, indicate via ionization signals, which is not affected by any field distortion detection efficiency, the position of the contaminant isotopes. This latter has found to be non-uniform in Z, as instead was supposed to be in the SR0 physics-driven wall model, and not really following a regular pattern between pillars and panels, limiting the hypothesis of a different contamination rate between the two classes of materials.

The deposited energy input spectrum for SR1 surface background model was produced starting from the SR0 Monte Carlo simulations, by correcting for the double counting mistake. The resulting spectrum used in the SR1 analysis compared to the SR0 one is reported in Figure 6.14.

The detector response is upgraded with the additional differentiation of the charge insensitive volume map into pillars and panels. Indeed, studies [66] revealed that between these two angular regions the Teflon charge-up intensity differs and hence also the deflection of the electric field lines vary and eventually the electron survival probability map is differentiated between these two regions, as shown in Figure 6.15.

With these new inputs and an updated configuration file with the SR1 specifications, while preserving the SR0 surface background best-fit values for p_0, μ_{rS2}, σ_{rS2} and σ_{rS1} nuisance parameters, it was possible to simulate the SR1 physics-driven surface background model events. Then, the outcome was compared with the SR1 unblinded wall events side-bands dataset, without a nuisance parameters optimization via fit procedure. This latter choice was driven by the complexity achieved with the SR1 physics-driven surface background model, requiring completely crazy computational costs in the attempt of performing the SR1 data fit.

This comparison, showed in Figure 6.16 where cS1 and cS2 observable spaces are omitted

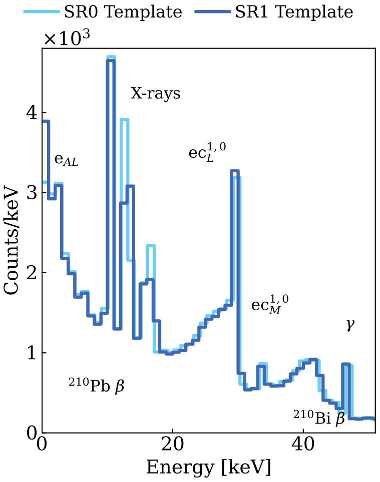

Figure 6.14: SR1 surface background model ER energy spectrum.

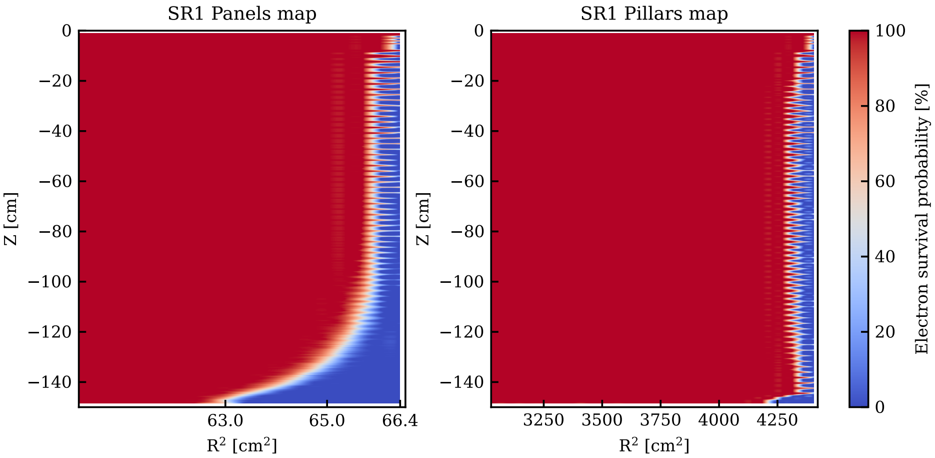

Figure 6.15: Survival probability maps for panels (left) and pillars (right) TPC regions evaluated by Francesco Toschi following the principle described in [66], exploiting pyCOMes software.

for simplicity, reports an impressing great agreement, considering the not performed optimization of detector response parameters. In particular, it is worth noting that in the R observable space, the input narrow distribution of Figure 6.13 is correctly smeared so to show a good agreement with SR1 data radial distribution.

Moreover, even if for this simulation the highly-resolved electrons survival probability maps of Figure 6.15 were exploited, the presence of the p_0 parameter and the non-physical values of the μ_{rS2} and σ_{rS2} parameters were needed to find a good match with data in S2 and Z observable spaces. This underlines that a non-yet understood mis-modeling in the detector response at the TPC borders is still present. Additionally, a sizable discrepancy is visible for high Z values. This latter might potentially suggest some imperfections in the input spatial distribution.

6.6.1 Consclusions and Outlook for Future Studies

This Chapter presented the physics-driven surface background model study. This analysis represents the first attempt of a refined model for the surface background impacting all LXe

TPC direct dark matter experiments [31, 32, 53]. Moreover, this study probed the hypothesis on the origins of such background, the Radon progeny plate-out, with results similar to those of other liquid scintillator detectors [111].

Furthermore, this study represents the first attempt to assess a precision XENONnT detector response model at its barrel edges in the neighborhood of the Teflon panels. The outcome of this analysis reinforces the hypothesis of an effective charge insensitive volume at the bottom corners of the TPC. Additionally, as visible from this study results, a non-perfect knowledge of the detector response at the level of S2 signal formation at the borders is still present, but mitigated in the model by a reduced single electron gain parameter.

Moreover, the anisotropies found in the azimuthal distribution of the surface events, that demanded a data-driven model input, might highlight that the genesis of the ^{210}Pb contamination cannot only be attributed to a physics origin. More likely, the events rate azimuthal modulation, which does not follow any geometrical structure present in the XENONnT TPC, is enhanced by human operation. This might have taken place during treatment, cleaning and handling procedures. The result of this study thus underline the importance of a careful treatment and handling of the PTFE material which radio-contamination can gain a factor up to four probably only due to a human factor. For next-generation experiments, it is thus needed to further refine the handling procedures for this material for an implanted activity reduction, which directly translates into the possibility of exploiting a larger fiducial volume for WIMP analysis, gaining in exposure and thus sensitivity.

The further attempt of refining the surface background model for SR1, led to improved insights concerning the XENONnT detector response. Indeed, the results proved that the mechanism modeling the radial position reconstruction are enough refined so to provide a nearly perfect match between data and simulations. Nevertheless, the usage of ^{210}Po alpha S1-only analysis result for a refined data-driven input for Z and Theta observables, resulted in a non-exhaustive compatibility between the model and the data. This might be due to the different activities that should characterize ^{210}Pb, real source of the surface background, and ^{210}Po, as shown at the beginning of the Chapter.

In future physics-driven surface background studies via FLAMEDISX modeling and fitting software, an improved (Z,Theta) input distribution can be obtained with the new set of statistics collected during the SR2 campaign. Other upgrades might include an improved Monte Carlo framework featuring the exact geometry of the TPC, which is currently approximated to a cylinder. More specifically, this upgrade would be necessary once the interest for more precise insights on the ^{210}Pb deposition depth in Teflon arises. Indeed, given that the treatment of PTFE for Xenon light reflectivity purposes effectively removes the first surface layer, it might be worth to exploit this technique in next-generation experiments just before the commissioning of the TPC, to reduce the temporal window for additional plate-out, while largely removing the already-corrupted layer.

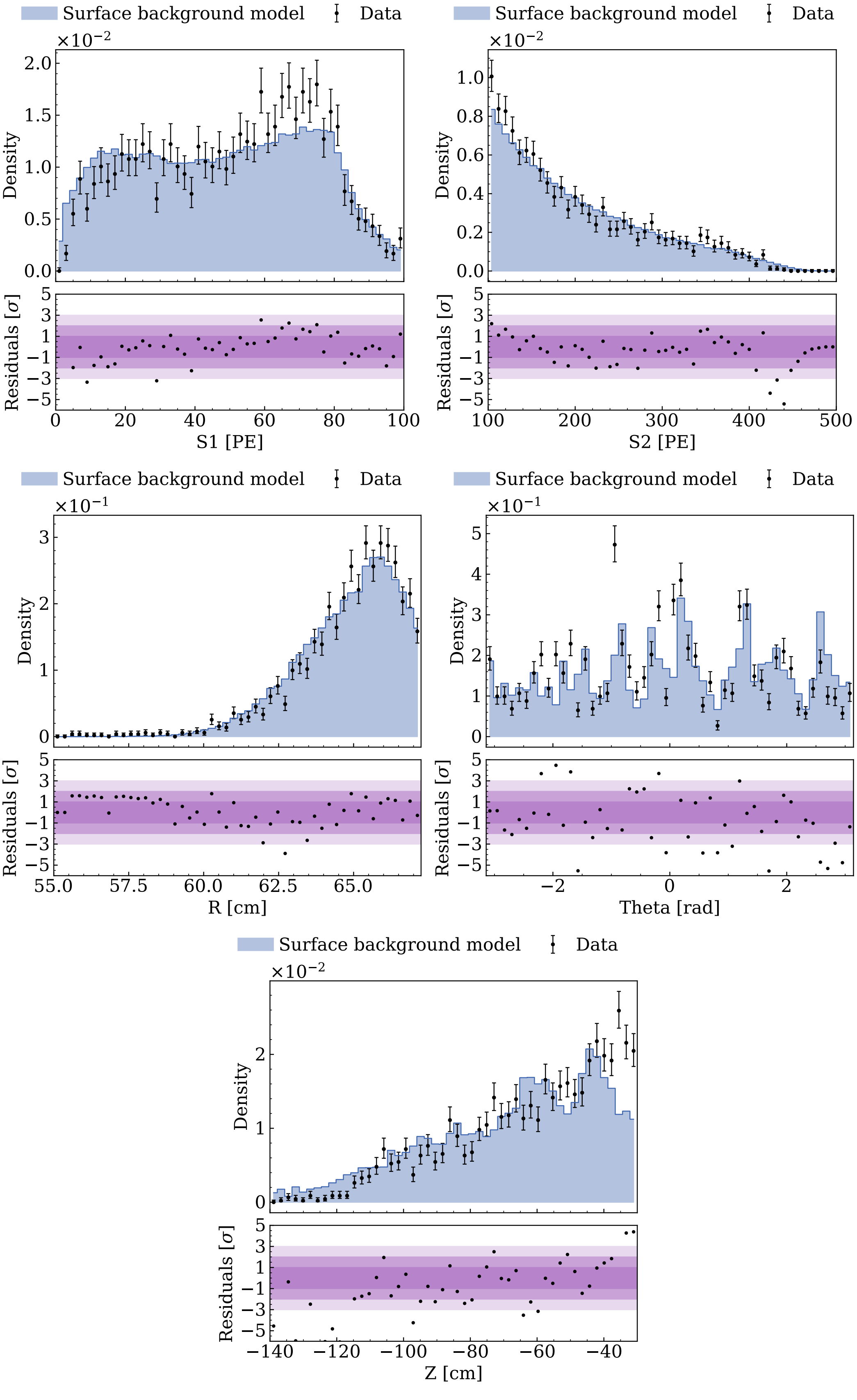

Figure 6.16: SR1 surface background model comparison with data in S1 (upper left panel), S2 (upper right panel), R (center left panel), Theta (center right panel) and Z (lower panel) observable spaces. Mis-modeling at high Z values might be due to unoptimized nuisance parameters (probably related to observed Z resolution), or an imperfect assumption in the input spatial distribution.

7

Conclusions

The search for dark matter (DM) remains one of the most compelling challenges in modern physics. While astrophysical and cosmological observations provide strong indirect evidence for its existence, direct detection efforts have yet to confirm a signal. The XENONnT experiment, a dual-phase liquid Xenon (LXe) time projection chamber (TPC), represents one of the most sensitive instruments to directly detect Weakly Interactive Massive Particle DM candidate. Such achievement is the result of two decades of technological advancements and in-depth understanding of potential background sources that could mimic WIMP interactions or more generally interfere in the search.

This Thesis focuses on this second crucial aspect of direct detection DM experiments: the precise characterization of radioactive backgrounds. In particular, the focus is directed towards Radon-induced Lead isotopes, namely ^{212}Pb, ^{214}Pb and ^{210}Pb, which represent major challenges for WIMP and other rare-events physics searches. Indeed, on the one hand, ^{212}Pb and ^{214}Pb populate the electron recoil (ER) band, contributing at low energies only when directly assessing the ground state of ^{212}Bi and ^{214}Bi respectively, and thus impacting the ER rare-events searches such as Solar-pp neutrino. On the other hand, ^{210}Pb pollutes Teflon materials surrounding the LXe active volume, introducing in the region of interest for WIMP searches the spatial-dependent background known after the name of surface or wall background.

The work presented in this Thesis addresses these three Lead backgrounds through high-precision measurements and modeling, providing valuable insights that enhance not only the sensitivity of XENONnT but also future LXe experiments, by means of improving Monte Carlo sensitivity studies with more precise nuclear transition branching ratios values and providing new insights for the definition of future materials handling and cleaning protocols. More specifically, the results of this thesis are divided into three major studies, presented in three different Chapters.

Chapter 4: Precision Measurement of ^{212}Pb Branching Ratios The first low-background direct simultaneous measurement of the ^{212}Pb branching ratios to ^{212}Bi ground and excited states was performed, achieving an unprecedented level of precision. As a result, the uncertainty on the ground-state transition was reduced by an order of magnitude statistically (from 7.7 % to 0.85 %) and by a factor of three when systematic uncertainties were included (from 7.7 % to 2.2 %). This reduction in uncertainty was facilitated by the concurrent assessment of all decay modes, which significantly mitigated systematic biases. However, a deviation of approximately 2σ was observed when comparing the measured ^{212}Pb ground state branching ratio to the relative literature values. Despite this, the study demonstrated that high-precision nuclear physics measurements are feasible within XENONnT, thanks to the detector ultra-low-background environment and refined knowledge of its detector response. Future improvements – such as additional ^{220}Rn calibration data and the inclusion of beta spectral shape theoretical models [136] in the fit – will further improve the precision of these measurements, potentially providing additional insights into the observed 2σ tension.

Chapter 5: Precision Measurement of ^{214}Pb Branching Ratios This study provided the most precise direct measurement of the ^{214}Pb branching ratios to ^{214}Bi ground state. By utilizing ^{222}Rn calibration data, the relative uncertainty on the ground-state transition was reduced by a factor of 2.5 (from 7.6 % to 3.1 %) when considering only the statistical error, marking a significant improvement over previous studies. The results demonstrated strong agreement with the value reported in the Laboratoire National Henri Becquerel reference [63], helping to resolve the 4.7σ discrepancy present in the literature, when the Nuclear Data Sheet reference [141] is also taken into account. Furthermore, the reproducibility of the ^{222}Rn calibration method opens the possibility for further refinement of these measurements, as it allows for increased statistics. The additional inclusion of ^{214}Pb beta spectral shapes, derived by means of theoretical improved-calculation [136], in the fit model could provide a further validity check for the obtained results.

Chapter 6: Physics-Driven Surface Background Model for ^{210}Pb A comprehensive study of ^{210}Pb-induced surface backgrounds was conducted, representing the first refined model of its kind for LXe TPCs. This study validated the hypothesis of Radon progeny plate-out as the origin of surface contamination, with findings consistent with results from liquid scintillator detectors [111]. Additionally, this study validated the hypothesis of the existence of a charge-insensitive volume near the TPC PTFE panels, reinforcing previous observations about detector response [66]. An unexpected azimuthal anisotropy in surface background event distributions was also observed, suggesting that the human-factor in handling and cleaning procedures significantly contributed to the ^{210}Pb contamination, potentially increasing radioactivity levels up to a factor of four. This insight underscores the importance of stricter PTFE material handling protocols for future experiments. Moreover, the ^{210}Pb activity estimated with this method, $19.0(10)\,\mathrm{mBq/m^2}$, greatly agrees with previous PTFE screening measurements conducted via alpha spectrometry methodology, reporting a contamination level of about $20(3)\,\mathrm{mBq/m^2}$ [103]. Future work in this area will involve refining the surface background model using new statistics from XENONnT SR2 dataset and improved Monte Carlo simulations.

In conclusion, this Thesis probed the feasibility of precision nuclear physics studies with low-background technique, such as those exploited in the XENONnT experiment, by refining the ^{212}Pb and ^{214}Pb branching ratios measurements. These results are in line with other recently-published analysis exploiting other low-background technologies initially developed for rare-events physics searches [102, 137–139]. The novelty of this approach for the ^{212}Pb and ^{214}Pb branching ratios estimation stands in the direct and concurrent assessment of these values by means of signal and background modeling optimized via fit procedure on calibration data. This latter aspect is of crucial importance since thanks to the reproducibility of such calibrations it allows the future refinement and validation of the measurements. Moreover, the ^{210}Pb analysis, exploiting for the first time of LXe TPC detectors a physics-driven six-dimensional model, probed and validated the hypothesis on this background origin and detector response in the neighborhood of Teflon panels. The results of this study will represent important inputs for next-generation LXe TPC optimization design studies as well as improvements in materials handling protocols. Furthermore, the methodologies developed in this Thesis will be directly applicable to upcoming multi-ton LXe experiments, such as XLZD. By refining background models and improving nuclear physics measurements, these studies will contribute to maximizing the discovery potential of future direct detection efforts.

Bibliography

[1] N. Aghanim et al. “Planck2018 results: VI. Cosmological parameters”. In: *Astronomy & Astrophysics* 641 (Sept. 2020), A6. ISSN: 1432-0746. DOI: `10.1051/0004-6361/201833910`. URL: `http://dx.doi.org/10.1051/0004-6361/201833910`.

[2] R. Bernabei et al. “The DAMA project: Achievements, implications and perspectives”. In: *Progress in Particle and Nuclear Physics* 114 (2020), p. 103810. ISSN: 0146-6410. DOI: `10.1016/j.ppnp.2020.103810`. URL: `https://www.sciencedirect.com/science/article/pii/S0146641020300570`.

[3] Marco Cirelli, Alessandro Strumia and Jure Zupan. *Dark Matter*. 2024. arXiv: `2406.01705 [hep-ph]`. URL: `https://arxiv.org/abs/2406.01705`.

[4] Particle Data Group Collaboration. “Review of Particle Physics”. In: *Phys. Rev. D* 110 (3 Aug. 2024), p. 030001. DOI: `10.1103/PhysRevD.110.030001`. URL: `https://link.aps.org/doi/10.1103/PhysRevD.110.030001`.

[5] Daniel Baumann. *Cosmology: Part III Mathematical Tripos*. 2018. URL: `https://cmb.wintherscoming.no/pdfs/baumann.pdf`.

[6] D. Baumann. *Cosmology*. Cambridge University Press, 2022. ISBN: 9781108952279. URL: `https://books.google.it/books?id=nn92EAAAQBAJ`.

[7] S. Dodelson and F. Schmidt. *Modern Cosmology*. Elsevier Science, 2020. ISBN: 9780128159484. URL: `https://books.google.it/books?id=GGjfywEACAAJ`.

[8] Y. Akrami et al. “Planck2018 results: VII. Isotropy and statistics of the CMB”. In: *Astronomy & Astrophysics* 641 (2020). ISSN: 1432-0746. DOI: `10.1051/0004-6361/201935201`.

[9] N. Aghanim et al. “Planck2018 results: V. CMB power spectra and likelihoods”. In: *Astronomy & Astrophysics* 641 (2020). ISSN: 1432-0746. DOI: `10.1051/0004-6361/201936386`. URL: `http://dx.doi.org/10.1051/0004-6361/201936386`.

[10] Volker Springel, Carlos S. Frenk and Simon D. M. White. “The large-scale structure of the Universe”. In: *Nature* 440.7088 (Apr. 2006). ISSN: 1476-4687. DOI: `10.1038/nature04805`. URL: `http://dx.doi.org/10.1038/nature04805`.

[11] F Zwicky. “Die Rotverschiebung von extragalaktischen Nebeln”. In: *Helv. Phys. Acta* 6 (1933). DOI: `10.5169/seals-110267`. URL: `http://cds.cern.ch/record/437297`.

[12] F. Zwicky. “On the Masses of Nebulae and of Clusters of Nebulae”. In: *Astrophys. J.* 86 (1937). DOI: `10.1086/143864`.

[13] Vera C. Rubin and Jr. Ford W. Kent. “Rotation of the Andromeda Nebula from a Spectroscopic Survey of Emission Regions”. In: *Astrophysical Journal* 159 (Feb. 1970), p. 379. DOI: 10.1086/150317.

[14] V. C. Rubin, Jr. Ford W. K. and N. Thonnard. “Rotational properties of 21 SC galaxies with a large range of luminosities and radii, from NGC 4605 (R=4kpc) to UGC 2885 (R=122kpc).” In: *Astrophysical Journal* 238 (June 1980), pp. 471–487. DOI: 10.1086/158003.

[15] Douglas Clowe et al. “A Direct Empirical Proof of the Existence of Dark Matter*”. In: *The Astrophysical Journal* 648.2 (Aug. 2006), p. L109. DOI: 10.1086/508162. URL: https://dx.doi.org/10.1086/508162.

[16] Tongyan Lin. *TASI lectures on dark matter models and direct detection*. 2019. arXiv: 1904.07915 [hep-ph]. URL: https://arxiv.org/abs/1904.07915.

[17] APPEC Scientific Advisory Committee. *Mid-term review of the European Astroparticle Physics Strategy 2017-2026 in preparation for the 2022 APPEC Town Meeting*. 2022. URL: https://www.appec.org/wp-content/uploads/2022/03/APPEC_Strategy_SAC_Midterm_Review_2022.pdf.

[18] M. G. Betti et al. “Neutrino physics with the PTOLEMY project: active neutrino properties and the light sterile case”. In: *JCAP* 07 (2019), p. 047. DOI: 10.1088/1475-7516/2019/07/047. arXiv: 1902.05508 [astro-ph.CO].

[19] Stefano Profumo. *TASI 2012 Lectures on Astrophysical Probes of Dark Matter*. 2013. arXiv: 1301.0952 [hep-ph]. URL: https://arxiv.org/abs/1301.0952.

[20] Howard Baer et al. “Status of weak scale supersymmetry after LHC Run 2 and ton-scale noble liquid WIMP searches”. In: *Eur. Phys. J. ST* 229.21 (2020), pp. 3085–3141. DOI: 10.1140/epjst/e2020-000020-x. arXiv: 2002.03013 [hep-ph].

[21] Mark W. Goodman and Edward Witten. “Detectability of Certain Dark Matter Candidates”. In: *Phys. Rev. D* (1985). Ed. by M. A. Srednicki. DOI: 10.1103/PhysRevD.31.3059.

[22] D. Baxter et al. “Recommended conventions for reporting results from direct dark matter searches”. In: *The European Physical Journal C* 81.10 (Oct. 2021). ISSN: 1434-6052. DOI: 10.1140/epjc/s10052-021-09655-y. URL: http://dx.doi.org/10.1140/epjc/s10052-021-09655-y.

[23] M. C. Smith et al. “The RAVE survey: constraining the local Galactic escape speed”. In: *Monthly Notices of the Royal Astronomical Society* 379.2 (Aug. 2007). ISSN: 1365-2966. DOI: 10.1111/j.1365-2966.2007.11964.x. URL: http://dx.doi.org/10.1111/j.1365-2966.2007.11964.x.

[24] A. K. Drukier, Katherine Freese and D. N. Spergel. “Detecting Cold Dark Matter Candidates”. In: *Phys. Rev. D* 33 (1986), pp. 3495–3508. DOI: 10.1103/PhysRevD.33.3495.

[25] Richard H. Helm. “Inelastic and Elastic Scattering of 187-Mev Electrons from Selected Even-Even Nuclei”. In: *Phys. Rev.* 104 (5 Dec. 1956), pp. 1466–1475. DOI: 10.1103/PhysRev.104.1466. URL: https://link.aps.org/doi/10.1103/PhysRev.104.1466.

[26] Marc Schumann. “Direct detection of WIMP dark matter: concepts and status”. In: *Journal of Physics G: Nuclear and Particle Physics* 46.10 (Aug. 2019), p. 103003. ISSN: 1361-6471. DOI: `10.1088/1361-6471/ab2ea5`. URL: `http://dx.doi.org/10.1088/1361-6471/ab2ea5`.

[27] J.D. Lewin and P.F. Smith. “Review of mathematics, numerical factors, and corrections for dark matter experiments based on elastic nuclear recoil”. In: *Astroparticle Physics* 6.1 (1996), pp. 87–112. ISSN: 0927-6505. DOI: `10.1016/S0927-6505(96)00047-3`. URL: `https://www.sciencedirect.com/science/article/pii/S0927650596000473`.

[28] A. Liam Fitzpatrick et al. “The effective field theory of dark matter direct detection”. In: *Journal of Cosmology and Astroparticle Physics* 2013.02 (Feb. 2013). ISSN: 1475-7516. DOI: `10.1088/1475-7516/2013/02/004`. URL: `http://dx.doi.org/10.1088/1475-7516/2013/02/004`.

[29] J. Aalbers et al. “A next-generation liquid xenon observatory for dark matter and neutrino physics”. In: *J. Phys. G* 50.1 (2023), p. 013001. DOI: `10.1088/1361-6471/ac841a`. arXiv: `2203.02309 [physics.ins-det]`.

[30] E. Aprile et al. “The XENONnT dark matter experiment”. In: *Eur. Phys. J. C* 84.8 (2024), p. 784. DOI: `10.1140/epjc/s10052-024-12982-5`. arXiv: `2402.10446 [physics.ins-det]`.

[31] D.S. Akerib et al. “The LUX-ZEPLIN (LZ) experiment”. In: *Nuclear Instruments and Methods in Physics Research Section A: Accelerators, Spectrometers, Detectors and Associated Equipment* 953 (Feb. 2020), p. 163047. ISSN: 0168-9002. DOI: `10.1016/j.nima.2019.163047`. URL: `http://dx.doi.org/10.1016/j.nima.2019.163047`.

[32] Yue Meng et al. “Dark Matter Search Results from the PandaX-4T Commissioning Run”. In: *Physical Review Letters* 127.26 (Dec. 2021). ISSN: 1079-7114. DOI: `10.1103/physrevlett.127.261802`. URL: `http://dx.doi.org/10.1103/PhysRevLett.127.261802`.

[33] C. E. Aalseth et al. “DarkSide-20k: A 20 tonne two-phase LAr TPC for direct dark matter detection at LNGS”. In: *The European Physical Journal Plus* 133.3 (Mar. 2018). ISSN: 2190-5444. DOI: `10.1140/epjp/i2018-11973-4`. URL: `http://dx.doi.org/10.1140/epjp/i2018-11973-4`.

[34] P. Agnes et al. “First results from the DarkSide-50 dark matter experiment at Laboratori Nazionali del Gran Sasso”. In: *Physics Letters B* 743 (Apr. 2015), pp. 456–466. ISSN: 0370-2693. DOI: `10.1016/j.physletb.2015.03.012`. URL: `http://dx.doi.org/10.1016/j.physletb.2015.03.012`.

[35] K. Abe et al. “Light WIMP search in XMASS”. In: *Physics Letters B* 719.1–3 (Feb. 2013), pp. 78–82. ISSN: 0370-2693. DOI: `10.1016/j.physletb.2013.01.001`. URL: `http://dx.doi.org/10.1016/j.physletb.2013.01.001`.

[36] R. Ajaj et al. “Search for dark matter with a 231-day exposure of liquid argon using DEAP-3600 at SNOLAB”. In: *Physical Review D* 100.2 (July 2019). ISSN: 2470-0029. DOI: `10.1103/physrevd.100.022004`. URL: `http://dx.doi.org/10.1103/PhysRevD.100.022004`.

[37] SuperCDMS Collaboration et al. *A Strategy for Low-Mass Dark Matter Searches with Cryogenic Detectors in the SuperCDMS SNOLAB Facility*. 2023. arXiv: `2203.08463 [physics.ins-det]`. URL: `https://arxiv.org/abs/2203.08463`.

[38] R. Agnese et al. “Search for low-mass dark matter with CDMSlite using a profile likelihood fit”. In: *Physical Review D* 99.6 (Mar. 2019). ISSN: 2470-0029. DOI: `10.1103/physrevd.99.062001`. URL: `http://dx.doi.org/10.1103/PhysRevD.99.062001`.

[39] CRESST collaboration. *First results on low-mass dark matter from the CRESST-III experiment*. 2017. arXiv: `1711.07692 [astro-ph.CO]`. URL: `https://arxiv.org/abs/1711.07692`.

[40] A. Aguilar-Arevalo et al. *The DAMIC dark matter experiment*. 2015. arXiv: `1510.02126 [physics.ins-det]`. URL: `https://arxiv.org/abs/1510.02126`.

[41] L. Balogh et al. “The NEWS-G detector at SNOLAB”. In: *Journal of Instrumentation* 18.02 (Feb. 2023), T02005. ISSN: 1748-0221. DOI: `10.1088/1748-0221/18/02/t02005`. URL: `http://dx.doi.org/10.1088/1748-0221/18/02/T02005`.

[42] L. Balogh et al. *Exploring light dark matter with the DarkSPHERE spherical proportional counter electroformed underground at the Boulby Underground Laboratory*. 2023. arXiv: `2301.05183 [hep-ex]`. URL: `https://arxiv.org/abs/2301.05183`.

[43] C. Amole et al. “Dark Matter Search Results from the PICO-60C_3F_8 Bubble Chamber”. In: *Physical Review Letters* 118.25 (June 2017). ISSN: 1079-7114. DOI: `10.1103/physrevlett.118.251301`. URL: `http://dx.doi.org/10.1103/PhysRevLett.118.251301`.

[44] E. Alfonso-Pita et al. *Snowmass 2021 Scintillating Bubble Chambers: Liquid-noble Bubble Chambers for Dark Matter and CEνNS Detection*. 2022. arXiv: `2207.12400 [physics.ins-det]`. URL: `https://arxiv.org/abs/2207.12400`.

[45] Teresa Marrodán Undagoitia and Ludwig Rauch. “Dark matter direct-detection experiments”. In: *Journal of Physics G: Nuclear and Particle Physics* 43.1 (Dec. 2015), p. 013001. ISSN: 1361-6471. DOI: `10.1088/0954-3899/43/1/013001`. URL: `http://dx.doi.org/10.1088/0954-3899/43/1/013001`.

[46] E. Aprile et al. “First Indication of Solar ^{8}B Neutrinos via Coherent Elastic Neutrino-Nucleus Scattering with XENONnT”. In: *Phys. Rev. Lett.* 133 (19 Nov. 2024), p. 191002. DOI: `10.1103/PhysRevLett.133.191002`. URL: `https://link.aps.org/doi/10.1103/PhysRevLett.133.191002`.

[47] Zihao Bo et al. "First Indication of Solar ^{8}B Neutrinos through Coherent Elastic Neutrino-Nucleus Scattering in PandaX-4T". In: *Phys. Rev. Lett.* 133 (19 Nov. 2024), p. 191001. DOI: `10.1103/PhysRevLett.133.191001`. URL: `https://link.aps.org/doi/10.1103/PhysRevLett.133.191001`.

[48] S. E. Vahsen et al. *CYGNUS: Feasibility of a nuclear recoil observatory with directional sensitivity to dark matter and neutrinos.* 2020. arXiv: `2008.12587 [physics.ins-det]`. URL: `https://arxiv.org/abs/2008.12587`.

[49] N. Pino et al. "Directionality for nuclear recoils in a LAr TPC". In: *EPJ Web Conf.* 280 (2023), p. 06004. DOI: `10.1051/epjconf/202328006004`.

[50] J. Angle et al. "First Results from the XENON10 Dark Matter Experiment at the Gran Sasso National Laboratory". In: *Physical Review Letters* 100.2 (Jan. 2008). ISSN: 1079-7114. DOI: `10.1103/physrevlett.100.021303`. URL: `http://dx.doi.org/10.1103/PhysRevLett.100.021303`.

[51] E. Aprile et al. "XENON100 dark matter results from a combination of 477 live days". In: *Physical Review D* 94.12 (Dec. 2016). ISSN: 2470-0029. DOI: `10.1103/physrevd.94.122001`. URL: `http://dx.doi.org/10.1103/PhysRevD.94.122001`.

[52] E. Aprile et al. "Dark Matter Search Results from a One Ton-Year Exposure of XENON1T". In: *Physical Review Letters* 121.11 (Sept. 2018). ISSN: 1079-7114. DOI: `10.1103/physrevlett.121.111302`. URL: `http://dx.doi.org/10.1103/PhysRevLett.121.111302`.

[53] E. Aprile et al. "First Dark Matter Search with Nuclear Recoils from the XENONnT Experiment". In: *Physical Review Letters* 131.4 (July 2023). ISSN: 1079-7114. DOI: `10.1103/physrevlett.131.041003`. URL: `http://dx.doi.org/10.1103/PhysRevLett.131.041003`.

[54] E. Aprile et al. "Projected WIMP sensitivity of the XENONnT dark matter experiment". In: *Journal of Cosmology and Astroparticle Physics* 2020.11 (Nov. 2020). ISSN: 1475-7516. DOI: `10.1088/1475-7516/2020/11/031`. URL: `http://dx.doi.org/10.1088/1475-7516/2020/11/031`.

[55] J. Aalbers et al. "A next-generation liquid xenon observatory for dark matter and neutrino physics". In: *J. Phys. G* 50.1 (2023), p. 013001. DOI: `10.1088/1361-6471/ac841a`. arXiv: `2203.02309 [physics.ins-det]`.

[56] Giovanni Volta. *Characterization and Monitoring of XENONnT Photosensors and Search for New Physics with the First XENONnT Science Data.* 2023. URL: `https://www.zora.uzh.ch/id/eprint/253152/`.

[57] Emanuele Angelino. *Calibration, simulation and analysis of the low-energy region in XENON project for direct dark matter search.* 2023. URL: `https://iris.unito.it/handle/2318/2017203`.

[58] CIAAW. *Xenon.* URL: `https://www.ciaaw.org/xenon.htm` (visited on 28/10/2024).

[59] AirLiquide. *Xenon Physical Properties.* URL: `https://encyclopedia.airliquide.com/xenon#properties` (visited on 28/10/2024).

[60] Ian H. Bell et al. “Pure and Pseudo-pure Fluid Thermophysical Property Evaluation and the Open-Source Thermophysical Property Library CoolProp”. In: *Industrial & Engineering Chemistry Research* 53.6 (2014), pp. 2498–2508. DOI: `10.1021/ie4033999`. eprint: `http://pubs.acs.org/doi/pdf/10.1021/ie4033999`. URL: `http://pubs.acs.org/doi/abs/10.1021/ie4033999`.

[61] I. T. Steinberger and U. Asaf. “Band-Structure Parameters of Solid and Liquid Xenon”. In: *Phys. Rev. B* 8 (2 July 1973), pp. 914–918. DOI: `10.1103/PhysRevB.8.914`. URL: `https://link.aps.org/doi/10.1103/PhysRevB.8.914`.

[62] *Particle Dark Matter: Observations, Models and Searches.* Cambridge University Press, 2010.

[63] M.-M. Bé et al. *Table of Radionuclides.* Vol. 8. Monographie BIPM-5. Pavillon de Breteuil, F-92310 Sèvres, France: Bureau International des Poids et Mesures, 2016. ISBN: 978-92-822-2264-5. URL: `http://www.bipm.org/utils/common/pdf/monographieRI/Monographie_BIPM-5_Tables_Vol8.pdf`.

[64] NIST. *Stopping-Power & Range Tables for Electrons, Protons, and Helium Ions.* 2017. URL: `https://www.nist.gov/pml/stopping-power-range-tables-electrons-protons-and-helium-ions` (visited on 01/09/2022).

[65] R.L. Platzman. “Total ionization in gases by high-energy particles: An appraisal of our understanding”. In: *The International Journal of Applied Radiation and Isotopes* 10.2 (1961), pp. 116–127. ISSN: 0020-708X. DOI: `10.1016/0020-708X(61)90108-9`. URL: `https://www.sciencedirect.com/science/article/pii/0020708X61901089`.

[66] Francesco Toschi. “Design of the field cage and charge response of the XENONnT dark matter experiment”. PhD thesis. Freiburg U., 2023. DOI: `10.6094/UNIFR/234323`.

[67] E Aprile et al. *Noble Gas Detectors.* 2007. ISBN: 978-3-527-60963-5. URL: `https://www.wiley.com/en-us/Noble+Gas+Detectors-p-9783527609635`.

[68] Ulrich Sowada, John M. Warman and Matthijs P. de Haas. “Hot-electron thermalization in solid and liquid argon, krypton, and xenon”. In: *Phys. Rev. B* 25 (5 Mar. 1982), pp. 3434–3437. DOI: `10.1103/PhysRevB.25.3434`. URL: `https://link.aps.org/doi/10.1103/PhysRevB.25.3434`.

[69] V.S. Nikolaev and I.S. Dmitriev. “On the equilibrium charge distribution in heavy element ion beams”. In: *Physics Letters A* 28.4 (1968), pp. 277–278. ISSN: 0375-9601. DOI: `10.1016/0375-9601(68)90282-X`. URL: `https://www.sciencedirect.com/science/article/pii/037596016890282X`.

[70] A. Mangiarotti et al.
“A survey of energy loss calculations for heavy ions between 1 and 100kev”.
In: *Nuclear Instruments and Methods in Physics Research Section A: Accelerators, Spectrometers, Detectors and Associated Equipment* 580.1 (Sept. 2007).
ISSN: 0168-9002. DOI: `10.1016/j.nima.2007.05.048`.
URL: `http://dx.doi.org/10.1016/j.nima.2007.05.048`.

[71] J Lindhard, M Scharff and H E Schiøtt. “RANGE CONCEPTS AND HEAVY ION RANGES (NOTES ON ATOMIC COLLISIONS, II)”.
In: *Kgl. Danske Videnskab. Selskab. Mat. Fys. Medd.* (Jan. 1963).
URL: `https://www.osti.gov/biblio/4153115`.

[72] Plante Guillaume. *The XENON100 Dark Matter Experiment: Design, Construction, Calibration and 2010 Search Results with Improved Measurement of the Scintillation Response of Liquid Xenon to Low-Energy Nuclear Recoils.* 2012.
URL: `https://inspirehep.net/literature/1515420`.

[73] D. Y. Akimov et al. *Two-Phase Emission Detectors.*
DOI: `https://doi.org/10.1142/12126`.

[74] A. Buzulutskov, A. Bondar and A. Grebenuk.
“Infrared scintillation yield in gaseous and liquid argon”.
In: *Europhysics Letters* 94.5 (May 2011), p. 52001.
DOI: `10.1209/0295-5075/94/52001`.
URL: `https://dx.doi.org/10.1209/0295-5075/94/52001`.

[75] Keiko Fujii et al. “High-accuracy measurement of the emission spectrum of liquid xenon in the vacuum ultraviolet region”.
In: *Nuclear Instruments and Methods in Physics Research Section A: Accelerators, Spectrometers, Detectors and Associated Equipment* 795 (2015), pp. 293–297.
ISSN: 0168-9002. DOI: `10.1016/j.nima.2015.05.065`. URL:
`https://www.sciencedirect.com/science/article/pii/S016890021500724X`.

[76] E. Hogenbirk et al. “Precision measurements of the scintillation pulse shape for low-energy recoils in liquid xenon”.
In: *Journal of Instrumentation* 13.05 (May 2018), P05016.
DOI: `10.1088/1748-0221/13/05/P05016`.
URL: `https://dx.doi.org/10.1088/1748-0221/13/05/P05016`.

[77] Akira Hitachi et al. “Effect of ionization density on the time dependence of luminescence from liquid argon and xenon”.
In: *Phys. Rev. B* 27 (9 May 1983), pp. 5279–5285. DOI: `10.1103/PhysRevB.27.5279`.
URL: `https://link.aps.org/doi/10.1103/PhysRevB.27.5279`.

[78] A. Mozumder. “Free-ion yield and electron-ion recombination rate in liquid xenon”.
In: *Chemical Physics Letters* 245.4 (1995), pp. 359–363. ISSN: 0009-2614.
DOI: `10.1016/0009-2614(95)01024-4`. URL:
`https://www.sciencedirect.com/science/article/pii/0009261495010244`.

[79] M. Szydagis et al.
“NEST: A Comprehensive Model for Scintillation Yield in Liquid Xenon”.
In: *JINST* 6 (2011), P10002. DOI: `10.1088/1748-0221/6/10/P10002`.
arXiv: `1106.1613 [physics.ins-det]`.

[80] Sophia Farrell et al. *NESTCollaboration/nestpy: Update to v2.4.0.* Version v2.4.0.
July 2024. DOI: `10.5281/zenodo.12773243`.
URL: `https://doi.org/10.5281/zenodo.12773243`.

[81] J. Thomas and D. A. Imel.
"Recombination of electron-ion pairs in liquid argon and liquid xenon".
In: *Phys. Rev. A* 36 (2 July 1987), pp. 614–616. DOI: `10.1103/PhysRevA.36.614`.
URL: `https://link.aps.org/doi/10.1103/PhysRevA.36.614`.

[82] Carl Eric Dahl. "The physics of background discrimination in liquid xenon, and first results from Xenon10 in the hunt for WIMP dark matter".
PhD thesis. Princeton U., 2009.

[83] G. Anton et al. "Measurement of the scintillation and ionization response of liquid xenon at MeV energies in the EXO-200 experiment".
In: *Physical Review C* 101.6 (June 2020). ISSN: 2469-9993.
DOI: `10.1103/physrevc.101.065501`.
URL: `http://dx.doi.org/10.1103/PhysRevC.101.065501`.

[84] Laura Baudis, Patricia Sanchez-Lucas and Kevin Thieme.
"A measurement of the mean electronic excitation energy of liquid xenon".
In: *The European Physical Journal C* 81.12 (Dec. 2021). ISSN: 1434-6052.
DOI: `10.1140/epjc/s10052-021-09834-x`.
URL: `http://dx.doi.org/10.1140/epjc/s10052-021-09834-x`.

[85] D.-M. Mei et al. "A model of nuclear recoil scintillation efficiency in noble liquids".
In: *Astroparticle Physics* 30.1 (2008), pp. 12–17. ISSN: 0927-6505.
DOI: `10.1016/j.astropartphys.2008.06.001`. URL:
`https://www.sciencedirect.com/science/article/pii/S0927650508000765`.

[86] XENON Collaboration et al.
XENONnT Analysis: Signal Reconstruction, Calibration and Event Selection. 2024.
arXiv: `2409.08778 [hep-ex]`. URL: `https://arxiv.org/abs/2409.08778`.

[87] Jay N. Marx and David R. Nygren. "The Time Projection Chamber".
In: *Phys. Today* 31N10 (1978), pp. 46–53. DOI: `10.1063/1.2994775`.

[88] E. Aprile et al.
"Design and performance of the field cage for the XENONnT experiment".
In: *Eur. Phys. J. C* 84.2 (2024), p. 138. DOI: `10.1140/epjc/s10052-023-12296-y`.
arXiv: `2309.11996 [hep-ex]`.

[89] XENON Collaboration et al.
XENONnT WIMP Search: Signal & Background Modeling and Statistical Inference.
2024. arXiv: `2406.13638 [physics.data-an]`.
URL: `https://arxiv.org/abs/2406.13638`.

[90] J. Aalbers et al. "The XLZD Design Book: Towards the Next-Generation Liquid Xenon Observatory for Dark Matter and Neutrino Physics". In: (Oct. 2024).
arXiv: `2410.17137 [hep-ex]`.

[91] Andrea Mancuso.
"The XENONnT neutron veto: design, construction and performance".
PhD thesis. Bologna U., 2024. DOI: `10.48676/unibo/amsdottorato/11437`.

[92] E. Aprile et al.
"The neutron veto of the XENONnT experiment: Results with demineralized water".
In: (Dec. 2024). arXiv: `2412.05264 [physics.ins-det]`.

[93] Daniel Wenz. "Commissioning of the world's first water Cherenkov neutron veto and first WIMP dark matter search results of the XENONnT experiment".
PhD thesis. Mainz U., 2023. DOI: `10.25358/openscience-9654`.

[94] Lutz Althüser. "Search for Dark Matter and other beyond the Standard Model physics with XENON1T and XENONnT". PhD thesis. Münster (Westfalen), Univ, 2023. URL: `https://nbn-resolving.de/urn:nbn:de:hbz:6-27958442020`.

[95] Maxime Pierre. "Neutrinoless double beta decay search with XENONnT". PhD thesis. Ecole nationale supérieure Mines-Télécom Atlantique, 2022. URL: `https://theses.hal.science/tel-04216774`.

[96] E. Aprile et al. *WIMP Dark Matter Search using a 3.1 tonne × year Exposure of the XENONnT Experiment*. 2025. arXiv: `2502.18005 [hep-ex]`. URL: `https://arxiv.org/abs/2502.18005`.

[97] J. Aalbers et al. "First Dark Matter Search Results from the LUX-ZEPLIN (LZ) Experiment". In: *Physical Review Letters* 131.4 (July 2023). ISSN: 1079-7114. DOI: `10.1103/physrevlett.131.041002`. URL: `http://dx.doi.org/10.1103/PhysRevLett.131.041002`.

[98] Zihao Bo et al. "Dark Matter Search Results from 1.54 Tonne · Year Exposure of PandaX-4T". In: *Phys. Rev. Lett.* 134 (1 Jan. 2025), p. 011805. DOI: `10.1103/PhysRevLett.134.011805`. URL: `https://link.aps.org/doi/10.1103/PhysRevLett.134.011805`.

[99] Florian Jörg et al. "Characterization of a 220Rn source for low-energy electronic recoil calibration of the XENONnT detector". In: *Journal of Instrumentation* 18.11 (Nov. 2023), P11009. ISSN: 1748-0221. DOI: `10.1088/1748-0221/18/11/p11009`. URL: `http://dx.doi.org/10.1088/1748-0221/18/11/P11009`.

[100] Florian Jörg, Guillaume Eurin and Hardy Simgen. "Production and characterization of a 222Rn-emanating stainless steel source". In: *Appl. Radiat. Isot.* 194 (2023), p. 110666. DOI: `10.1016/j.apradiso.2023.110666`. arXiv: `2205.15926 [physics.ins-det]`.

[101] Robert Hammann et al. *XENONnT/GOFevaluation: v0.1.0-zenodo-init.* Version v0.1.0-zenodo-init. Oct. 2021. DOI: `10.5281/zenodo.5626909`. URL: `https://doi.org/10.5281/zenodo.5626909`.

[102] Carlo Fuselli. *Measurement of the first-forbidden non-unique β-decay energy spectrum of 214-Bi to the ground state of 214-Po in XENONnT*. 2024. URL: `https://agenda.infn.it/event/37867/contributions/228330/`.

[103] E. Aprile et al. "Material radiopurity control in the XENONnT experiment". In: *The European Physical Journal C* 82.7 (July 2022). ISSN: 1434-6052. DOI: `10.1140/epjc/s10052-022-10345-6`. URL: `http://dx.doi.org/10.1140/epjc/s10052-022-10345-6`.

[104] K. S. Krane. *INTRODUCTORY NUCLEAR PHYSICS*. 1987.

[105] G. Brent Dalrymple. "The age of the Earth in the twentieth century: a problem (mostly) solved". In: *Geological Society, London, Special Publications* 190.1 (2001), pp. 205–221. DOI: `10.1144/GSL.SP.2001.190.01.14`.

[106] R.D. Evans. *The Atomic Nucleus*. McGraw-Hill, Boston., 1969.

[107] E. Aprile et al. “^{222}Rn emanation measurements for the XENON1T experiment”. In: *The European Physical Journal C* 81.4 (Apr. 2021). ISSN: 1434-6052. DOI: `10.1140/epjc/s10052-020-08777-z`. URL: `http://dx.doi.org/10.1140/epjc/s10052-020-08777-z`.

[108] S. Bruenner et al. “Radon daughter removal from PTFE surfaces and its application in liquid xenon detectors”. In: *The European Physical Journal C* 81.4 (Apr. 2021). ISSN: 1434-6052. DOI: `10.1140/epjc/s10052-021-09047-2`. URL: `http://dx.doi.org/10.1140/epjc/s10052-021-09047-2`.

[109] M. Murra et al. “Design, construction and commissioning of a high-flow radon removal system for XENONnT”. In: *The European Physical Journal C* 82.12 (Dec. 2022). ISSN: 1434-6052. DOI: `10.1140/epjc/s10052-022-11001-9`. URL: `http://dx.doi.org/10.1140/epjc/s10052-022-11001-9`.

[110] Dominick Cichon et al. “Transmission of xenon scintillation light through PTFE”. In: *JINST* 15.09 (2020), P09010. DOI: `10.1088/1748-0221/15/09/P09010`. arXiv: `2005.02444 [physics.ins-det]`.

[111] Michael Leung. “Surface Contamination From Radon Progeny”. In: *AIP Conference Proceedings* 785.1 (Sept. 2005), pp. 184–190. ISSN: 0094-243X. DOI: `10.1063/1.2060470`. eprint: `https://pubs.aip.org/aip/acp/article-pdf/785/1/184/12046593/184\_1\_online.pdf`. URL: `https://doi.org/10.1063/1.2060470`.

[112] E. S. Morrison et al. “Radon daughter plate-out onto Teflon”. In: *AIP Conference Proceedings*. Author(s), 2018. DOI: `10.1063/1.5019012`. URL: `http://dx.doi.org/10.1063/1.5019012`.

[113] P Pagelkopf and J Porstendörfer. “Neutralisation rate and the fraction of the positive 218Po-clusters in air”. In: *Atmospheric Environment* 37.8 (2003), pp. 1057–1064. ISSN: 1352-2310. DOI: `10.1016/S1352-2310(02)00997-4`. URL: `https://www.sciencedirect.com/science/article/pii/S1352231002009974`.

[114] E. Aprile et al. *Radon Removal in XENONnT down to the Solar Neutrino Level*. 2025. arXiv: `2502.04209 [physics.ins-det]`. URL: `https://arxiv.org/abs/2502.04209`.

[115] M. Yamashita. *Rn rate in various LXe dark matter experiments*. `https://github.com/masaki-yamashita/public/blob/main/Rn/experiments/plot_rn_bg_experiments.ipynb`. 2024.

[116] Florian Jörg. “From 222Rn measurements in XENONnT and HeXe to radon mitigation in future liquid xenon experiments”. PhD thesis. Heidelberg U., 2022. DOI: `10.11588/heidok.00031915`.

[117] Philipp Schulte. “Developing a cryogenic heat pump for liquid xenon radon removal systems”. LRT2024. 2024. URL: `https://indico.fais.uj.edu.pl/event/1/contributions/125/`.

[118] D. Cichon et al. “Transmission of xenon scintillation light through PTFE”. In: *Journal of Instrumentation* 15.09 (Sept. 2020), P09010–P09010. ISSN: 1748-0221. DOI: 10.1088/1748-0221/15/09/p09010. URL: http://dx.doi.org/10.1088/1748-0221/15/09/P09010.

[119] A. Singh et al. “Development of a 4π detection system for the measurement of the shape of β spectra”. In: *Nuclear Instruments and Methods in Physics Research Section A: Accelerators, Spectrometers, Detectors and Associated Equipment* 1053 (2023), p. 168354. ISSN: 0168-9002. DOI: 10.1016/j.nima.2023.168354. URL: https://www.sciencedirect.com/science/article/pii/S0168900223003443.

[120] Samuel S. M. Wong. *Introductory Nuclear Physics.* 1998. ISBN: 9783527617906. DOI: 10.1002/9783527617906.

[121] K. Auranen and E.A. McCutchan. “Nuclear Data Sheets for A=212”. In: *Nuclear Data Sheets* 168 (2020), pp. 117–267. ISSN: 0090-3752. DOI: 10.1016/j.nds.2020.09.002. URL: https://www.sciencedirect.com/science/article/pii/S0090375220300351.

[122] T. Kibédi et al. “Evaluation of theoretical conversion coefficients using BrIcc”. In: *Nuclear Instruments and Methods in Physics Research Section A: Accelerators, Spectrometers, Detectors and Associated Equipment* 589.2 (2008), pp. 202–229. ISSN: 0168-9002. DOI: 10.1016/j.nima.2008.02.051. URL: https://www.sciencedirect.com/science/article/pii/S0168900208002520.

[123] F. T. Avignone and A. G. Schmidt. “γ-ray and internal-conversion intensity studies of transitions in the decay of ^{228}Th”. In: *Phys. Rev. C* 17 (1 Jan. 1978), pp. 380–384. DOI: 10.1103/PhysRevC.17.380. URL: https://link.aps.org/doi/10.1103/PhysRevC.17.380.

[124] W.-J. Lin and G. Harbottle. “γ-ray and internal-conversion intensity studies of transitions in the decay of ^{228}Th”. In: *Journal of Radioanalytical and Nuclear Chemistry* 157 (2 Mar. 1992). DOI: 10.1007/BF02047451. URL: https://doi.org/10.1007/BF02047451.

[125] E. Aprile et al. “Energy resolution and linearity of XENON1T in the MeV energy range”. In: *The European Physical Journal C* 80.8 (Aug. 2020). ISSN: 1434-6052. DOI: 10.1140/epjc/s10052-020-8284-0. URL: http://dx.doi.org/10.1140/epjc/s10052-020-8284-0.

[126] *epix - Electron and Photon Instructions generator for XENON.* https://pypi.org/project/epix/. Version v0.3.4. 2023. DOI: 10.5281/zenodo.7777552.

[127] Diego Ramírez García. “Simulating the XENONnT dark matter experiment: backgrounds and WIMP sensitivity”. PhD thesis. Freiburg U., 2022. DOI: 10.6094/UNIFR/228338.

[128] Brian Lenardo et al. “A Global Analysis of Light and Charge Yields in Liquid Xenon”. In: *IEEE Transactions on Nuclear Science* 62.6 (2015), pp. 3387–3396. DOI: 10.1109/TNS.2015.2481322.

[129] Steve Baker and Robert D. Cousins.
"Clarification of the use of CHI-square and likelihood functions in fits to histograms".
In: *Nuclear Instruments and Methods in Physics Research* 221.2 (1984), pp. 437–442.
ISSN: 0167-5087. DOI: `10.1016/0167-5087(84)90016-4`. URL:
`https://www.sciencedirect.com/science/article/pii/0167508784900164`.

[130] E. Aprile et al.
"Design and performance of the field cage for the XENONnT experiment".
In: *The European Physical Journal C* 84.2 (Feb. 2024). ISSN: 1434-6052.
DOI: `10.1140/epjc/s10052-023-12296-y`.
URL: `http://dx.doi.org/10.1140/epjc/s10052-023-12296-y`.

[131] E. Aprile et al.
"First Dark Matter Search with Nuclear Recoils from the XENONnT Experiment".
In: *Phys. Rev. Lett.* 131 (4 July 2023), p. 041003.
DOI: `10.1103/PhysRevLett.131.041003`.
URL: `https://link.aps.org/doi/10.1103/PhysRevLett.131.041003`.

[132] P. Vischia. "Pseudosignificances as figures of merit: a systematic study and exploration of Bayesian solutions". In: *PoS Confinement2018* (2019).
DOI: `10.22323/1.336.0249`.

[133] E. Aprile et al. "Search for New Physics in Electronic Recoil Data from XENONnT".
In: *Physical Review Letters* 129.16 (Oct. 2022). ISSN: 1079-7114.
DOI: `10.1103/physrevlett.129.161805`.
URL: `http://dx.doi.org/10.1103/PhysRevLett.129.161805`.

[134] C. J. CLOPPER and E. S. PEARSON. "THE USE OF CONFIDENCE OR FIDUCIAL LIMITS ILLUSTRATED IN THE CASE OF THE BINOMIAL".
In: *Biometrika* 26.4 (Dec. 1934), pp. 404–413. ISSN: 0006-3444.
DOI: `10.1093/biomet/26.4.404`. eprint: `https://academic.oup.com/biomet/article-pdf/26/4/404/823407/26-4-404.pdf`.
URL: `https://doi.org/10.1093/biomet/26.4.404`.

[135] S. J. Haselschwardt et al. "Improved calculations of β decay backgrounds to new physics in liquid xenon detectors". In: *Phys. Rev. C* 102 (6 Dec. 2020), p. 065501.
DOI: `10.1103/PhysRevC.102.065501`.
URL: `https://link.aps.org/doi/10.1103/PhysRevC.102.065501`.

[136] M. Ramalho and J. Suhonen. "Computed total β-electron spectra for decays of Pb and Bi in the ^{220,222}Rn radioactive chains".
In: *Phys. Rev. C* 109 (1 Jan. 2024), p. 014326. DOI: `10.1103/PhysRevC.109.014326`.
URL: `https://link.aps.org/doi/10.1103/PhysRevC.109.014326`.

[137] L. Pagnanini et al. "Array of cryogenic calorimeters to evaluate the spectral shape of forbidden β-decays: the ACCESS project".
In: *Eur. Phys. J. Plus* 138.5 (2023), p. 445.
DOI: `10.1140/epjp/s13360-023-03946-x`. arXiv: `2305.01949 [physics.ins-det]`.

[138] Lucas Bodenstein-Dresler et al. "Quenching of g_A deduced from the β-spectrum shape of ^{113}Cd measured with the COBRA experiment".
In: *Phys. Lett. B* 800 (2020), p. 135092. DOI: `10.1016/j.physletb.2019.135092`.
arXiv: `1806.02254 [nucl-ex]`.

[139] Andrea Nava et al. "Measurement of the ^{14}C spectrum with Silicon Drift Detectors: towards the study of forbidden β transitions". In: (May 2024).
arXiv: `2405.07797 [physics.ins-det]`.

[140] E. Aprile et al. “Excess electronic recoil events in XENON1T”. In: *Phys. Rev. D* 102 (7 Oct. 2020), p. 072004. DOI: `10.1103/PhysRevD.102.072004`. URL: `https://link.aps.org/doi/10.1103/PhysRevD.102.072004`.

[141] Shaofei Zhu and E.A. McCutchan. “Nuclear Data Sheets for A=214”. In: *Nuclear Data Sheets* 175 (2021), pp. 1–149. ISSN: 0090-3752. DOI: `10.1016/j.nds.2021.06.001`. URL: `https://www.sciencedirect.com/science/article/pii/S009037522100034X`.

[142] V. Chisté and M. M. Bé. *^{214}Pb - Comments on evaluation of decay data*. LNHB. 2010. URL: `http://www.lnhb.fr/nuclides/Pb-214_com.pdf`.

[143] H. Daniel. In: *Zeitschrift für Naturforschung A* 11.9 (1956), pp. 759–760. DOI: `doi:10.1515/zna-1956-0914`. URL: `https://doi.org/10.1515/zna-1956-0914`.

[144] K.O. Nielsen, O.B. Nielsen and M.A. Waggoner. “Internal conversion coefficients for M1 transitions in 83Bi214, 84Po214 and 83Bi212”. In: *Nuclear Physics* 2.4 (1956), pp. 476–484. ISSN: 0029-5582. DOI: `10.1016/0029-5582(56)90035-9`. URL: `https://www.sciencedirect.com/science/article/pii/0029558256900359`.

[145] Alex Malins and Thom Lemoine. “radioactivedecay: A Python package for radioactive decay calculations”. In: *Journal of Open Source Software* 7.71 (2022), p. 3318. DOI: `10.21105/joss.03318`. URL: `https://doi.org/10.21105/joss.03318`.

[146] M.J. Carson et al. “Neutron background in large-scale xenon detectors for dark matter searches”. In: *Astroparticle Physics* 21.6 (Sept. 2004), pp. 667–687. ISSN: 0927-6505. DOI: `10.1016/j.astropartphys.2004.05.001`. URL: `http://dx.doi.org/10.1016/j.astropartphys.2004.05.001`.

[147] L. Althueser et al. “VUV Transmission of PTFE for xenon-based particle detectors”. In: *Journal of Instrumentation* 15.12 (Dec. 2020), P12021. DOI: `10.1088/1748-0221/15/12/P12021`. URL: `https://dx.doi.org/10.1088/1748-0221/15/12/P12021`.

[148] Miguel Ángel Vargas. *Data analysis in the XENON1T Dark Matter Experiment.* Ed. by Christian Weinheimer. [Electronic ed.] 2019. URL: `https://repositorium.uni-muenster.de/document/miami/619876be-47cd-4122-9ffd-b426ed212690/diss_vargas.pdf`.

[149] E. Aprile et al. “XENON1T dark matter data analysis: Signal reconstruction, calibration, and event selection”. In: *Physical Review D* 100.5 (Sept. 2019). ISSN: 2470-0029. DOI: `10.1103/physrevd.100.052014`. URL: `http://dx.doi.org/10.1103/PhysRevD.100.052014`.

[150] D.S. Akerib et al. “3D modeling of electric fields in the LUX detector”. In: *Journal of Instrumentation* 12.11 (Nov. 2017), P11022–P11022. ISSN: 1748-0221. DOI: `10.1088/1748-0221/12/11/p11022`. URL: `http://dx.doi.org/10.1088/1748-0221/12/11/P11022`.

[151] R. Hammann. *Investigation of a Charge Insensitive Volume in XENONnT, Analysis of Goodness-of-Fit Techniques, and Feasibility Studies for an Automated Krypton Assay System.* 2022. URL: `https://pure.mpg.de/pubman/faces/ViewItemOverviewPage.jsp?itemId=item_3456465`.

[152] Pueh Leng Tan. “Solar Reflected Dark Matter with XENON1T and XENONnT : Searching for sub-GeV Dark Matter using liquid xenon Time Projection Chambers”. PhD thesis. Stockholm University, Department of Physics, 2024, p. 156. ISBN: 978-91-8014-796-5.

[153] J. Aalbers et al. “Finding dark matter faster with explicit profile likelihoods”. In: *Phys. Rev. D* 102 (7 Oct. 2020), p. 072010. DOI: `10.1103/PhysRevD.102.072010`. URL: `https://link.aps.org/doi/10.1103/PhysRevD.102.072010`.

[154] Vasile Cristian Antochi. “Inference on Dark Matter in Effective Field Theories : From XENON1T towards XENONnT: Chiral effective field theory analysis of nuclear recoils, single electrons and uncommon background modelling”. PhD thesis. Stockholm University, Department of Physics, 2022. ISBN: 978-91-7911-864-8.

[155] Diego Ramírez García. “Simulating the XENONnT dark matter experiment: backgrounds and WIMP sensitivity”. PhD thesis. Freiburg U., 2022. DOI: `10.6094/UNIFR/228338`.

[156] Ali Dastgheibi Fard. “Radon daughter deposition modelling and measurement”. LRT2024. 2024. URL: `https://indico.fais.uj.edu.pl/event/1/contributions/164/`.

[157] *pyCOMes - python COMSOL electrostatic simulations*. `https://github.com/ftoschi/PyCOMes`. Version e5e6110829ded780247888ea7e94a103c1a285bd. 2022.

List of Figures

List of Tables

Acknowledgements

It's incredible how much chaotic or quite life can be. I'm now sitting in Dounia's living room on an 1976 piece of design – the IKEA POÄNG chair – starring through the window-glass at the Roio hill. Everything seems suspended and calm, even the Belvedere bridge construction works seem to proceed at the same pace. I think I'm still recovering from yesterday's elation and inebriation after PhD thesis defense at Gran Sasso Science Institute, my beloved home for the past four years. This thesis would have never been written the same way without the love, the support, the supervision and the suggestions that many people provided me during these years.

Firstly, I want to thank the XENON family, it has been a pleasure to be part of such an inspiring research group. To the current and past members of the local XENON group (Walter, Marcello, Alfredo, Alessandro, Carla, Riccardo, Valerio, Emanuele, Atul, Federico, Chiara, Andrea, Riccardino, Francesco and Lorenzo) I need to address a great recognition for having turned every bad day at LNGS into delightful moments spent together. Specially to Riccardo, I'm really grateful for the past three years as office mates: I've enjoyed every single laugh and stressed moments we experienced in that *piccionaia*, that since this March – for both of us – is no more ours. To the XENON flamedisx young fellas – Pueh Leng Tan, Cristian Antochi, Emanuele Angelino and Chiara Di Donato – among tears of despair and great expectations, I must admit that it was an incredible journey I've enjoyed to travel together. To the high-energy mates and beyond – Christian Wittweg, Maxime Pierre, Micha Weiss, Chiara Capelli, Barbara Paetsch, Giovanni Volta, Florian Jörg, Daniel Wenz, Robert Hammann, Masatoshi Kobayashi and Carlo Fuselli – thanks for all the discussions on the branching ratios analyses and for having represented the perfect team to work with: inspiring, supportive and uplifting. To the amazing LNGS people and DAQ experts that supported me during the run-coordinator fatal (for SR1) period – Jean-Marie Disdier, Federico Alfonsetti, Danilo Tatananni, Roberto Corrieri, Marco Balata, Carlo Fuselli, Maricke Fliermann and Riccardo Biondi, as Japan-based expert on vacation – I need to confess that without you the XENONnT SR1 data-taking could have lasted one month less.

To the GSSI family I am grateful for all the love and inspiration. To my AP36 mates – Alessandro, Alessio, David, Michele, Simone, Stefano and Ulyana – I must admit that together we lived an amazing journey from *day 0*, when we found friendship in a *Peperoncino* pizza slice in that November sunny day. To all the mates of PhTea Talks – Ulyana, Stefano, Alessio, Lioni, Benedetta, Arsène and Crhistian – I recognize we had lots of fun in giving birth to this nice project that I hope will survive in GSSI for many years. Thanks to the Alumni fellows – Eleonora, Carmen, Anjali, Crhistian, Giulio, Alessio and Carmelo Evoli – for having built the Association and engaging the GSSI community with great activities in these past two years, while organizing many others to come.

To my dearest friends – Francesca, Cecilia, Camilla, Lea and Ginevra – who are always there to cheer me up in bad moments and party hard in the happiest, I must thank you for the patience you had (and hopefully will continue to have) to my forgetfulness and Taurus-level stubbornness. A special recognition also goes to Dounia, Giovanni, Andrei, Riccardo (yes, you, again) and Alessio for every nice evening spent together.

After this PhD experience in L'Aquila, I'm going to fly to Boston and live new research adventures. This is only possible thanks to the support of many people. *In primis* I must thank Elena Aprile, Laura Baudis, Marcello Messina and Alfredo Ferella for having supported me via recommendation letters and having mentored me with many career suggestions. Then, I must recognize the love and support of my beloved family – Paola, Giuseppe and Lorenzo. I have no words to express my gratitude to you, but if there were, I would only use the sweetest, because you deserve them all.

Finally, I want to thank Stefano, to whom I'm more than grateful. There's no need to write down the words flowing in my mind, because in one month I'll be there, by your side, whispering them in your ear.

Vi voglio bene.
Cecilia – 16/04/25